論文 / 著書情報
Article / Book Information

題目(和文)	等原子価陽イオン置換法による機能性酸化物材料のテーラリングの研究
Title(English)	Isovalent cation substitution for tailoring functional oxide materials
著者(和文)	安川雪子
Author(English)	
出典(和文)	学位:博士（工学）, 学位授与機関:東京工業大学, 報告番号:甲第6488号, 授与年月日:2006年3月26日, 学位の種別:課程博士, 審査員:Maarit Karppinen
Citation(English)	Degree:Doctor of Engineering, Conferring organization: Tokyo Institute of Technology, Report number:甲第6488号, Conferred date:2006/3/26, Degree Type:Course doctor, Examiner:
学位種別(和文)	博士論文
Type(English)	Doctoral Thesis

Isovalent Cation Substitution for Tailoring Functional Oxide Materials

Yukiko Yasukawa

01D26114

A Thesis
Submitted to the Interdisciplinary Graduate School
of Science and Engineering through
the Department of Innovative and Engineered Materials
in Partial Fulfillment of the Requirements for
the Degree of Doctor of Engineering at
Tokyo Institute of Technology

Supervisors:
Associate Professor Maarit Karppinen
Professor Hisao Yamauchi

March 2006

ABSTRACT

For the present work, the aim was set to reveal the role of isovalent-cation substitution, *i.e.*, substituting a cation completely or partially by another cation with the same oxidation state, in controlling the distribution of charge/carriers and thereby the material properties in perovskite-related oxides of the strongly-correlated electron systems. For the target systems, the tunneling-type magnetoresistance oxides of A_2FeMoO_{6-w} with a double-perovskite structure and the high-T_c superconductive oxides of $CuBa_2RECu_2O_{7-\delta}$ with a triple-perovskite structure were selected.

For a series of fully-oxygenated cation-stoichiometric samples of $CuBa_2RECu_2O_{7-\delta}$, the dependence of the magnetic irreversibility field (H_{irr}) characteristics on the size of the rare earth element (*RE*) was systematically studied. $CuBa_2RECu_2O_{7-\delta}$ samples with the *RE* ionic radius [$r(RE^{III})$] varying from 0.982 Å (for *RE* = $Yb_{0.6}Lu_{0.4}$) to 1.066 Å (for *RE* = Eu) were synthesized. Oxygen content of the samples (7-δ) was set at a fixed level, *i.e.*, in the narrow range of 6.91 ~ 6.94. A clear dependence of the H_{irr} characteristics on the size of the *RE* constituent was revealed such that with decreasing $r(RE^{III})$ the H_{irr} characteristics were remarkably enhanced. The $CuBa_2(Yb_{0.6}Lu_{0.4})Cu_2O_{6.92}$ sample possessing the smallest *RE* constituent among the present samples exhibited a record-high H_{irr} value of ~9.0 T at 77 K. The observed trend of enhancing H_{irr} with decreasing size of *RE* was explained on the basis of a concomitant shift of holes from the charge-reservoir $CuO_{1-\delta}$ chain to the superconductive CuO_2 plane, evidence for which was revealed from bond-valence-sum calculations based on published neutron diffraction data. Since in the $CuBa_2RECu_2O_{7-\delta}$ system in general, the $CuO_{1-\delta}$ chain is more heavily doped with holes than the CuO_2 plane, such a hole shift results in a more homogeneous hole distribution over the unit cell, which was considered advantageous in terms of enhancing the H_{irr} characteristics.

According to previous ^{57}Fe Mössbauer spectroscopy data iron in Sr_2FeMoO_6 possesses a mixed-valence $Fe^{II/III}$ state owing to so-called valence-mixing phenomenon between Fe^{III} and Mo^{V}. The present Mössbauer data for a series of A_2FeMoO_{6-w} samples free from oxygen deficiency and of essentially constant grain size demonstrated that the valence value of Fe is not precisely fixed at 2.5, but the precise value of it is sensitively controlled by the average ionic radius [$r(A^{II})$] of the *A*-site constituents, *A* (= Ba, Sr or Ca). With increasing $r(A^{II})$ the valence mixing was found to be enhanced such that Fe approach the divalent state for *A* = Ba. As the valence of Fe approaches II and hence that of Mo approaches VI, the difference in charges between the Fe and Mo species increases, and parallel with this the degree of Fe/Mo order was found to increase. The Mössbauer spectroscopy results were supported by those obtained by means of Fe *L*-edge XANES spectroscopy for the same samples.

Techniques of statistical multivariate data analysis provide us with an interesting means to investigate complex systems in which - for instance - a certain important property is simultaneously controlled by multiple parameters. Here such an analysis was employed for the first time to look for relations and trends among chemical composition, redox state, precise

crystal structure (bond lengths and angles) and the magnetic properties of $A_2B'B''O_{6-w}$-type double-perovskite oxides. Tentatively, the first result of the analysis suggested that for the double-perovskite oxides the valence of the *B*' cation and the ionic radius and the valence of the *B*" cation are among the most important parameters to determine the type of magnetism and the value of T_C. Furthermore, the present analysis suggested that the structural parameters derived form *A* constituent may affect the valence of the *B*' cation and the ionic radius and the valence of the *B*" cation. This implies that the *A*-related parameters, *i.e.*, the effect of isovalent-cation substitution at *A* site, would also influence the type of magnetism and the value of T_C indirectly in the general *B*-site ordered double-perovskite system. Through out the present studies, effectiveness of isovalent-cation substitution at *A* site on the functional properties were demonstrated not only by the experimental aspects but also by the statistical analyses.

In conclusion, the present study has demonstrated the effectiveness of isovalent *A*-site cation substitution in controlling various important material characteristics of functional perovskite oxides: the size of the "spacing" *A* cation influences the charge/carrier distribution among the different electronically/magnetically active transition metal species and thereby the functional properties of the material such as superconductivity and magnetoresistance.

CONTENTS

ACKNOWLEDGEMENTS

The whole work of this thesis was carried out in the Materials and Structures Laboratory at the Tokyo Institute of Technology from April 1999 to March 2006.

First of all, my supervisors, Associate Professor Maarit Karppinen and Professor Hisao Yamauchi are gratefully acknowledged for their expert supervisions, fruitful discussions and warm supports for my study life. When I had questions, experimental problems or consultations Prof. H. Yamauchi and Assoc. Prof. M. Karppinen always gave me hearty, accurate and apparent advices. Dr. Teruki Motohashi is gratefully acknowledged, also. I appreciate for his giving me very concrete advices in terms of my research and writings. I learned from him the importance of extracting the most essential matter and expressing it with the most suitable but simple words. Under their helps and encouragements this study is possible and worthwhile.

Dr. Johan Lindén is gratefully acknowledged for his significant suggestions, discussions, writing papers and characterizations of double-perovskite samples. I am grateful to Dr. Tohru Asaka and Dr. Yoshio Matsui of National Institute for Materials Science (NIMS) for the observations of magnetic boundaries/domains and antiphase boundaries by means of Lorentz electron microscope for the double-perovskite samples. Furthermore, I would like to appreciate Professor Sunao Sugihara and Dr. Yukio Yutoh of Shonan Institute of Technology for the discussions for the double-perovskite compounds. This work was inspired by their warm collaboration. They gave me many things: not only fruitful discussions but also very warm inspiring and encouragements. I should be grateful to Professor R.S. Liu of National Taiwan University, Dr. J.M. Chen of National Synchroton Radiation Research Center for their measuring the x - ray absorption near edge spectroscopy and giving me instructions to analyze the data. I am further grateful to Dr. Terhi. Siimes of Nokia Company with the contributions of her help in multivariate data analysis. I have to describe that this study could not stand up without her appropriate advices.

The examiners of the present thesis are Associate Professor Maarit Karppinen, Professor HisaoYamauchi, Professor Yohtaro Yamazaki, Associate Professor Yoshitaka Kitamoto and Associate Professor Mamoru Yoshimoto. They also gave the appropriate advices from various standpoints. Owing to advices by them and discussions with them, this thesis got improved. I appreciate for their warm supports.

Finally, I have to thank my family. My husband and parents who gave me the chance to stay in Tokyo Institute of Technology are persons understand and support me during a long, 7 years, student life. My sweetest daughter, Shizuki, is very important person. Thanks to her, I was able to accomplish this work without forgetting smiles.

March, 2006
Yukiko Yasukawa

Y. Yasukawa

LIST OF PUBLICATIONS RELEVANT TO THIS WORK

In addition to the present thesis, the dissertation includes the following publications, which are referred to in the text by the corresponding Roman numbers:

I Y. Yasukawa, H. Yamauchi, and M. Karppinen, "Accurate oxygen-content determination method for decreased sample amounts of superconductive and other functional oxides", *Appl. Phys. Lett.* **81**, 502-504 (2002).

II Y. Yasukawa, T. Nakane, H. Yamauchi, and M. Karppinen, "Consequence of isovalent rare earth substitution to magnetic irreversibility in cation-stoichiometric $CuBa_2RECu_2O_{6.93\pm0.01}$", *Appl. Phys. Lett.* **78**, 2917-2919 (2001).

III Y. Yasukawa, T. Nakane, M. Karppinen, and H. Yamauchi, "Rare-earth-ion-size control on magnetic irreversibility field in $CuBa_2RECu_2O_{7-\delta}$", *Physica C* **357-360**, 230-233 (2001).

IV M. Karppinen, N. Kiryakov, Y. Yasukawa, T. Nakane, and H. Yamauchi, "Isovalent cation substitutions to control the intrinsic H_{irr} characteristics of superconductive copper oxides", *Physica C* **382**, 66-71 (2002).

V Y. Yasukawa, M. Karppinen, J. Lindén, T.S. Chan, R.S. Liu, and H. Yamauchi, "Iron valence in double-perovskite $(Ba,Sr,Ca)_2FeMoO_6$: isovalent substitution effect", *J. Solid State Chem.* **177**, 2655-2662 (2004).

VI M. Karppinen, H. Yamauchi, Y. Yasukawa, J. Lindén, T.S. Chan, R.S. Liu, and J.M. Chen, "Valence state of iron in the $Sr_2Fe(Mo,Ta,W)O_{6.0}$ double-perovskite system: an Fe *K*-edge and $L_{2,3}$-edge XANES study", *Chem. Mater.* **15**, 4118-4121 (2003).

VII J. Lindén, M. Karppinen, T. Shimada, Y. Yasukawa, and H. Yamauchi, "Observation of antiphase boundaries in Sr_2FeMoO_6", *Phys. Rev. B* **68**, 174415-1-5 (2003).

LIST OF SYMBOLS AND ABBREVIATIONS

Abbreviations in Chemical Formulae

A	Large metal, *e.g.*, Ca, Sr, Ba, La, in the *A* site of the perovskite structure
B	*d*-block transition metal, *e.g.*, Mn, Fe, Co, Ni, Cu, in the *B* site of the perovskite structure
RE	Rare-earth element (Sc, Y and the lanthanides from La to Lu)
Q	Intermediate-size metal, *e.g.*, *RE*, Ca
M	Metal, *i.e.*, Cu, Pb, Bi, Hg, in the charge reservoir block of superconductive copper oxides
m	Stoichiometry of the metal (*M*) in the charge reservoir block of superconductive copper oxides
n	Number of superconducting CuO_2 planes
δ	Amount of oxygen deficiency of the superconductive materials
w	Amount of oxygen deficiency of the double-perovskite materials

Other Abbreviations and Symbols

T_c	Superconductivity transition temperature
T_C	Curie temperature
T_N	Néel temperature
M_S	Saturation magnetization
XRD	x-ray powder diffraction
NPD	neutron powder diffraction
redox	Reduction-oxidation
XANES	X-ray Absorption Near-Edge Structure
BVS	Bond Valence Sum
R^0_{ij}	BVS scaling parameter for the *i*-*j* bond
d_{ij}	Bond length between *i* and *j*
$p(CuO_2)$	Hole concentration of an individual CuO_2 plane
H_{irr}	The magnetic-field irreversibility of high-T_c superconductors
CN	Coordination number
MR	Magnetoresistivity
S	Degree of order
V	Valence of a specimen of metal
HS	High spin state of a specimen of *d*-block transition metal

APB	A crystallographic boundary at which the phase shift of the *B*-site ordering occurs of the double-perovskite compounds, *i.e.*, antiphase boundary
SIMCA	Simple Classification Analysis
PC	Principal Component
PCA	Principal Component Analysis
PLS	Projections to Latent Structures by means of partial least squares
PLSDA	PLS Discriminant Analysis
LDA	Local Density Approximation
DOS	Density of State

Note

The oxidation state of the element is expressed for, *e.g.*, divalent iron, as follows:

Fe^{II}	in solids
Fe^{2+}	in solutions

In the general *B*-site ordered double-perovskite $A_2B'B''O_{6-w}$ compound without evaluating the accurate value of the oxygen content, the compound is assumed to be the stoichiometry, *i.e.*, the oxygen content (6-*w*) of 6 is assumed. On the other hand, precise values of the oxygen content are determined for the samples synthesized by the present study. Thus, in order to denote the present prepared samples, the oxygen content is expressed for (6-*w*), *i.e.*, $A_2B'B''O_{6-w}$, is utilized in this thesis.

1. INTRODUCTION

1.1. Background of the Present Work

1.1.1. Historical Studies and Potentials of Perovskite Compounds

Most of the compounds with the general formula ABO_3 have a perovskite structure, where the A cation is surrounded by 12 oxygen atoms and the B cation forms an octahedron with 6 oxygen atoms. This is called a single-perovskite structure. Since 1945, when the ferroelectric properties of $BaTiO_3$ were reported by von Hippel, perovskite compounds have been studied extensively [1,2]. Until 1955 most of the possible combinations of large A and smaller B cations satisfied to form perovskite-type compounds had been discovered. At the same time, not only interests in ferroelectric materials but also expectations for laser host materials, laser modulation, thermistors, superconductors and infrared windows were generated in perovskite compounds [2].

The single perovskites were widely studied for $A^{I}B^{V}O_3$, $A^{II}B^{IV}O_3$ and $A^{III}B^{III}O_3$. The $A^{I}B^{V}O_3$ and $A^{II}B^{IV}O_3$ types are of particular interest because of their ferroelectric properties. Among the $A^{II}B^{IV}O_3$-type compounds the titanates were of the highest interested because the barium and lead titanates show the ferroelectric properties exhibiting high dielectric constants. Thus, $BaTiO_3$ has been studied for energy converter and capacitor applications [2,3]. Perovskite-derived compounds such as Pb_2ScNbO_6 and Pb_2ScTaO_6 were also found to be ferroelectric materials [2,4]. The most widespread applications of ferroelectric materials are capacitors and the secondly dielectric amplifiers. The hysteresis loop of ferroelectric single crystal makes them of potential use for information storage in electric computers. $BaTiO_3$ also exhibits piezoelectric properties. Piezoelectric materials are mainly applied for measuring dynamic pressures in blast gauges, accelerometers, sound transmission/reception and ultrasonic cleaning devices. Furthermore, $BaTiO_3$ and $SrTiO_3$ have been considered for high-temperature infrared windows.

In recent years there has been considerable interest in materials represented by chemical formula of $A^{III}B^{III}O_3$ for laser application. Since the enhancement of lifetimes observed for an activating ion in laser host materials with perovskite structure, an extensive search was carried out for cubic-perovskite compounds which would accept trivalent rare-earth ions [2,5]. In fact, some improvement of Ni^{III} lifetimes in perovskite-derived Ba_2LuTaO_6 compound as a laser host material was observed.

Application as catalysts is also possible for perovskite compounds. Perovskite-related compounds consisting of two different elements of the B site were evaluated for fuel cell application. The B cations were selected from those which are known to have catalytic properties and the B' cations were selected for the corrosion resistance they impart to a compound. The most satisfactory catalysts were Mn-based perovskites possessing more than one valence state of

manganese [2].

1.1.2. Single-, Double- and Triple-Perovskite Structures

In a single-ABO_3 perovskite structure, A is the largest metal ion thus CN is preferred rather large. On the other hand, B is the smaller metal ions with oxygen-deficiency and thereby a smaller CN is more preferable. In the most of perovskite compounds, B is the transition metals inducing the mixed-valence states thereby the oxygen non-stoichiometry is generated in a compound. From the basic single perovskite ABO_3, it is possible to build up ordered-perovskite compounds by occupying multiplly the one or both of the two cation sites, *i.e.*, A or B. The cation substituent may be randomly distributed, clustered or ordered. The double-perovskite compounds consist of the double-ordered lattices, obtained with one-to-one stoichiometry of the two A site, *i.e.*, A' and A'' or B site, *i.e.*, B' and B'' constituents. In the case of B-site ordered perovskites, *i.e.*, $A_2B'B''O_6$, the two different octahedral B-cation sites consisting of B' and B'' are alternatively ordered resulting in 8 times ($2 \times 2 \times 2 = 8$) larger than the basic cubic cell of the simple perovskite. It is shown in Fig. 1.1.2.-1 [6]. One of the first double-perovskite compounds with the $A^{II}{}_2B'^{III}B''^{VI}O_6$ formula, *i.e.*, $Ba_2Sc_{0.67}W_{0.33}O_6$ was synthesized by Fresia *et al.* [2,7]. $A^{II}{}_2B'^{II}B''^{V}O_6$ double-perovskite compounds were commonly synthesized containing Nb and Ta as B'' constituent. However, a decrease in the ordering with decreasing the difference in the size of the B'^{II} and Ta^{V} ions was found [2,8]. For $A^{II}{}_2B'^{III}B''^{V}O_6$, $A^{II}{}_2B'^{II}B''^{VI}O_6$, $A^{II}{}_2B'^{I}B''^{VII}O_6$ and $A^{III}{}_2B'^{II}B''^{IV}O_6$ double-perovskite compounds it was found that when the structure of these compounds is ordered, and mostly they are, they adopt the structure shown in Fig. 1.1.2-1. It was postulated by Galasso *et al.* [2,9] that an ordered distribution of B ions is most probable when a large difference existed in either their charges or ionic radii. Fresia *et al.* [2,7] revealed that other ions such as Zn^{II}, Fe^{II}, Co^{II} and Ni^{II} could be adopted as B'' ions in the double-perovskite structure were not distorted. However, in studies of $A_2B'^{II}UO_6$ [2,10], $A_2B'^{II}WO_6$ and $A_2B'^{II}MoO_6$ it was found that all of the compounds containing Sr in the A site had distorted structures, while a number of compounds with Ba in the A site should form the cubic structure. Goldschmidt [2,11] has shown that the cubic perovskite structure is stable only if a tolerance factor, t, has an approximate range of $0.8 < t < 0.9$ and somewhat larger range for distorted perovskite structures. However, for higher B-site ordered perovskite such as $(A',A'',A''')_3B'B''_2O_9$ triple-perovskite compound has not been established, yet.

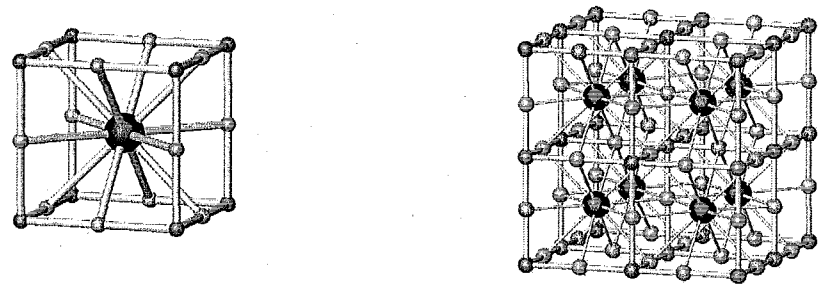

(a) (b)

Fig. 1.1.2.-1 Derivation of the *B*-site ordered ($A_2B'B''O_6$) double-perovskite structure from the single-perovskite (ABO_3) structure.

In the case of *A*-site ordered perovskites consisting of two different metals, *e.g.*, larger *A*' and smaller *A*", it is possible to build up different layered ordered-oxygen-vacancy perovskite structures deriving from *A*'O, *A*"O_δ and BO_2 layers by varying the ratio of *A*':*A*" [12]. With 1:1 and 2:1 ratios, for instances, oxygen-deficient $A'A''B_2O_{5+\delta}$ double perovskite and $A'_2A''B_3O_{8\pm\delta}/A'_2A''B_3O_{7-\delta}$ triple perovskites would form [13] as shown in Fig. 1.1.2.-2. For example, $Ba_2REFe_3O_{8\pm\delta}$ [12,14,15-17] and $Ba_2RECu_3O_{7-\delta}$ [12,18] deriving from the triple-perovskite structure are the fundamental high-T_c superconducting materials with *B* = Cu and Fe, respectively. The higher-ordered perovskite structures such as quadruple- and quintuple-perovskite compounds have been established for the case of Cu for *B*-cation constituent, only. These compounds are known as the ultra-high-pressure-synthesized high-T_c superconductors, *i.e.*, $Ba_2Ca_2Cu_4O_{8+\delta}$ and $Ba_2Ca_3Cu_5O_{10+\delta}$. One of the features of higher-ordered perovskite structures, they are heavily-oxygen deficient compounds exhibiting various oxygen-coordination polyhedra for the *B* cation even for phases with $\delta = 0$. For instance, in the quadruple-perovskite structure of $Ba_2Ca_2Cu_4O_8$ ($CuBa_2Ca_2Cu_3O_8$) with the layer sequence of BaO-Cu-BaO-CuO_2-Ca-CuO_2-Ca-CuO_2 the *CN* of Cu is 2, 5 (pyramidal), 4 (square planar) and 5, respectively [12].

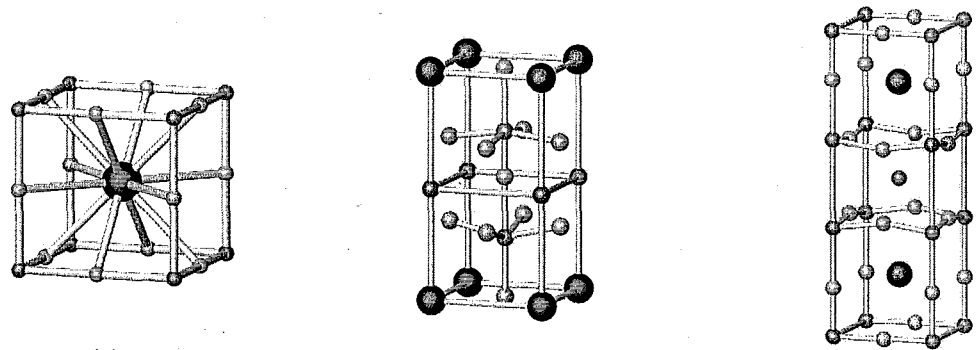

(a) (b) (c)

Fig. 1.1.2.-2 Derivation of the *A*-site ordered double- and triple-perovskite structures.
(a) Single-perovskite (ABO_3) structure. (b) Double perovskite ($A'A''B_2O_{5+\delta}$) and (c) triple-perovskite ($A'_2A''B_3O_{7-\delta}$) structures.

1.1.3. Non-stoichiometry and Cation Valences in Perovskites

Mixed-valence states are possible for transition metal/few heavy metals and it is the origin of metallic conductivity. For tuning the transition-metal valence, structures allowing for oxygen non-stoichiometry are advantageous. Thus, cation/oxygen non-stoichiometry derived from mixed-valence states and/or various coordination states of transition metals is common in peorvskite structures. Concerning to the oxygen non-stoichiometry, the "oxygen engineering" is one of the most crucial/interesting research topics in the functional perovskite-related compounds in strongly-correlated electrons [19,I].

The non-stoichiometry affects the charges over the crystal and influences not only the structures but also the properties. Na_xWO_3 and Li_xWO_3 are well known as cation non-stoichiometric compounds. The cation deficiencies can be tolerated over ranges of composition maintaining the perovskite structure. The phases $SrBO_{3-x}$ where B is Ti or V, $SrFeO_{3-x}$ [2,20-22], $CaFeO_{3-x}$ [6,22,23] and $SrCoO_{3-x}$ [6,22] systems exhibit the oxygen deficiency keeping perovskite structures. Various strongly-correlated-electron oxides such as high-T_c superconductive copper oxides and magnetoresistance manganese, cobalt and iron oxides possess a strong tendency for oxygen non-stoichiometry. Tuning the oxygen content provides us with a means of controlling the valence state of the transition metal and thereby the carrier concentration/electromagnetic properties of the active transition metal oxide layers [19,I]. Superconductivity occurs in the oxygen content range $0 < \delta < 0.55$ with the value of T_c increasing in accordance with decreasing oxygen deficiency for the $CuBa_2RECu_2O_{7-\delta}$ phase [13]. Also in the case of MR cobalt and iron oxides small changes in the oxygen content have been shown to sensitively affect the MR characteristics [24,25,I]. However, tuning the oxygen stoichiometry in the double- and triple-perovskite structures has a different effect. For the $A_2B'B''O_{6-w}$ double perovskite for example, the oxygen non-stoichiometry has not been reported, or at least, extremely small amount of oxygen deficiency exists in the compound [26]. Thus, the oxygen non-stoichiometry is not a dominant factor in terms of the physical properties in this system. On the other hand, varying the oxygen non-stoichiometry in a triple-perovskite structure such as $CuBa_2RECu_2O_{7-\delta}$ is a direct technique to control the oxidation state of transition metal thus the superconductivity properties can be controlled by changing the oxygen content in the CuO_δ layer. For the high-T_c superconductors, it has been well established that both T_c value and the H_{irr} characteristics strongly depend on the hole concentration and thereby on the oxygen content [13,I].

In the perovskite compounds, non-stoichiometry and resistivity/magnetic behaviour, correlate closely. In general, perovskites are found to possess high electrical resistivities but some of them containing B ions in lower than their most stable oxidation state or compounds consisting of the B ions in two valence states are considered to be fairly good conductors or semiconductors. Na_xWO_3 with $0.3 \leq x \leq 0.5$ and low-temperature phase of Li_xWO_3 with $x \approx 0.4$ are highly conducting. Superconductivity has been observed phases in the systems $(Ba_{1-x}Sr_x)TiO_3$ and $(Ca_{1-y}Sr_y)TiO_3$ when $x \geq 0.9$ and $y \geq 0.7$ [2,27]. Moreover, the presence of

oxygen deficiencies such as (Ba,Sr,Ca)TiO_{3-x} phases reduce the resistivity of the stoichiometric phases producing semiconductors [2,28]. Concerning with the magnetic properties, many of the perovskites are magnetic compounds derived by the super-exchange interaction which influences their conduction. The electron transfers are easier if the spin moments are parallel. For instance, ferromagnetic (La,Sr)CoO_3 exhibits nearly metallic conductivity [2,23], while antiferromagnetic (La,Sr)FeO_3 and (La,Sr)CrO_3 have a much higher resistivity [2,21]. The energy between spins of neighboring metal ions in the perovskite structure is often found to be negative so that antiparallel alignment has the lowest energy. In the $A_2B'B''O_6$ magnetic-ordered perovskite compounds where B' is W^V, Mo^V or Re^{VI} and B'' is a paramagnetic ion, it was proposed that a negative interaction between the B' and B'' exists [2,29]. On the other hand, La$B'MnO_6$ perovskites where B' is Mg, Co, Ni or Cu found that the magnetic exchange interactions between B' and Mn^{IV} ions in ferromagnetic compounds appear to be positive [2,30]. In the double-perovskite compounds, the combination of B'/B'' cations determines the magnetic interaction between B'-B'' cations. Furthermore, structural changes often induce changes in behaviours of magnitude of saturation magnetization [2,31] in magnetic perovskites.

Not only the non-stoichiometry but also mixed-valence states, *i.e.*, the versatile coordination states of transition metals and structural distortions are outstanding features in perovskite structures. In the superconductors such as $NbO_{1-\delta}$ [13,32], $SrTiO_{3-\delta}$ [13,33], $(Na,K)_xWO_3$ [13,34], $Li_{1+x}Ti_{2-x}O_4$ [13,35], $BaBi_{1-x}Pb_xO_3$ [13,36], $Ba_{1-x}K_xBiO_3$ [13,37] and the high-T_c copper oxides, all of them are mixed-valence compounds. Since the transition metal at B site has a prominent role in determining the electrical, magnetic and catalytic [38-40] properties, the valence value of B cation is an influential parameter of properties in the perovskite materials. For instance, the important role of the mixed-valence state of copper, *i.e.*, copper atoms normally show a valence value between II and III in the CuO_2 planes, have revealed to be essential for high-T_c superconductivity. Besides, in the magnetoresistive manganites, cobalt and iron oxides the mixed-valence state of the transition metal with $Mn^{III/IV}$ [40-42], $Co^{II/III/IV}$ [24,40,42] and $Fe^{II/III/IV/V}$ [40,43,44] is believed to be origins of MR behaviour.

The coordination state of the transition metal is also an essential factor for properties because the valence value of B cation is affected by the coordination numbers/states in the perovskite structure. Among the transition metals, copper is one of the most flexible elements owing to its many possible oxidation states and coordination polyhedra. In terms of the coordination polyhedron, $CN = 2$ is typical for Cu^I, while Cu^{II} may be realized when $CN = 4$, 5 and 6 (octahedral) coordinations. For the cases of $CN = 4$ and 6, it is possible to be Cu^{III}. Cu^{IV} has been stabilized only at $CN = 6$ [13].

Other important feature of the perovskite compounds is the Jahn-Teller effect induced by the 3*d* transition metal. In general, the ideal cubic structure possesses equivalent 3*d* orbitals, while it separates as t_{2g} and e_g orbitals with inequivalent energies for perovskite structure. Further structural distortion through the Jahn-Teller effect from a cubic perovskite structure induces separations of t_{2g} and e_g orbitals, *i.e.*, $3d_{xy}/3d_{yz}/3d_{zx}$ (t_{2g}) and $3d_{x^2-y^2}/3d_{z^2}$ (e_g). When the 3*d* transition metal forms octahedral coordination, two anions existing in out-of-plane of

octahedron are mostly influenced by the *z*-oriented orbital, *i.e.*, $3d_z^2$. Since the "electron clouds" stretches *z* direction in the case of $3d_z^2$ orbital, a force of repulsion works between an anion and the electron existing in $3d_z^2$ orbital. Therefore, the bond length of out-of-plane is elongated compared to that of in-plane, usually. For example, the four in-plane Cu^{II}-O bonds (Cu^{II}: either $3d_{z2}^{2}3d_{x2-y2}^{1}$ or $3d_{z2}^{1}3d_{x2-y2}^{2}$) are typically shorter than the out-of-plane Cu^{II}-O bond (Cu^{II}: $3d_{z2}^{2}3d_{x2-y2}^{1}$) in the high-$T_c$ superconductor.

1.1.4. Perovskite Compounds as Electro-Functional Materials

Perovskite oxides with 3*d* transition metals are examples of so-called "strongly-correlated electron systems" and have been studied extensively, since they present interesting and frequently unexpected magnetic and transport properties. Representative examples are the superconducting mixed-valent copper oxides and the mixed-valent manganese perovskites exhibiting CMR [45,46]. The origin of both materials is antiferromagnetic insulator. By doping a carrier in the antiferromagnetic insulating mother compounds, it is possible to obtain high-T_c copper oxides/CMR manganites.

Since the 3*d* band widths are narrow and the 3*d* electrons in the transition-metal oxides are extremely sensitive to crystal field, 3*d* orbitals and electrons/structures interacts each other, strongly. Thus, it is possible to consider that the interaction between 3*d* orbitals and spins/charges generates many quantum-mechanical states, such as superconductivity and magnetoresistance [47,48]. The superconductivity and MR are representative examples of conductivity induced by mixed-valence state of transition metals in perovskites. On the other hand, the most prominent natures in terms of superconductivity and magnetoreisistance are different. The dominant origins are degree of freedom of spins/charges in the two-dimensional CuO_2 planes for superconducting properties but MR properties are derived from degree of freedom of spins/orbitals/charges [49].

Moreover, perovskite compounds consisting of other 3*d* transition-metals have also attracted considerable attention owing to their interesting phenomena and physics. Not only copper and manganese but also cobalt is well known to exhibit a range of different valence states [46]. Due to the flexible valence states of cobalt there exists a great variety of cobalt-based perovskites showing a wide range of magnetic properties, *e.g.*, antiferromagnetism, ferromagnetism, spin-glass behaviour, or MR behaviour [46]. The combinations of *B*' and *B*'' cations in double perovskites also lead to various properties. For $A_2B'ReO_6$ (*A* = Ba, Sr, Ca and *B*' = first row transition metal) system with *A* = Ba members revealed that several members of the series, *i.e.*, compounds with *B*' = Mn, Fe and Ni, are ferrimagnetic compounds. However, the *B*' = Fe member is unique because it possesses both metallic and ferromagnetism [29,50-52].

In the single-perovskite iron oxides, *e.g.*, $CaFeO_3$ and $RE_{1-x}Sr_xFeO_3$, the charge disproportionation (CD) phenomenon represented by $2Fe^{IV}$ (higher temperature) $\leftrightarrow$ Fe^{III} + Fe^{V} (lower temperature) occurs [53-57]. In this compound, negative MR was observed in the

temperature regime where CD/charge ordering (CO) transition takes place [44]. In the case of $La_{1/3}Sr_{2/3}FeO_{3-w}$ perovskite [40,44], it has been found to show the MR peak appears at the temperature where Fe^{IV} disproportionates to Fe^{III} and Fe^{V}. This disproportionation leads to CO and to magnetic transition from paramagnetic to antiferromagnetic state. These interesting physical phenomena and properties lying in 3*d*-trantision metal perovskite compounds have attracted intense attention expecting as new functional materials.

1.2. Isovalent Cation Substitution

Isovalent-cation substitution is a substitution replacing a cation by another cation with the same oxidation state. By means of this substitution, a change in ionic radius of substituted cation only affects the structural parameters/physical properties of the compounds. Therefore, the substitution is regarded as "size-only-dependent". This substitution technique is often discussed as "chemical pressure [58,59,II,III,IV]", to the application of external mechanical pressure. The chemical pressure effect is associated with an internal pressure mechanism within the crystal. For instance, if a cation is replaced by smaller isovalent cation, the overall unit cell will be suppressed and bond lengths between substituted cation-anions will be changed. Some bond lengths may be shortened but others may be elongated. In the layered superconductive $-A$O-CuO_2-(Q-CuO_2)$_{n-1}$-AO-$M_mO_{m\pm\delta}$- structure for example [IV], when the A site is substituted by a smaller isovalent cation the lattice shrinks such that bond lengths from the A and O atoms in the AO layer to neighbouring CuO_2-plane O and Cu atoms, respectively, become shorter. On the other hand, Q-site substitutions with smaller isovalent cations shorten the bond length from the Q atom to the CuO_2-plane O atom. As compared to the high-pressure synthesized samples, an essential difference related to the isovalent-substituted samples is that such substitutions do not necessarily decrease the effective A/Q-O bond length. That is, the structure is often rigid enough to somewhat resist against the strive in decreasing the bond length. Therefore, the effective bond length rather increases.

The changes in cation-anion bond lengths will also induce the variation of charge/carrier distribution, since the effective cation-anion bond lengths are altered through the chemical pressure. For the layered M-$m^{(A)}2^{(Q)}(n\text{-}1)n$ copper oxides increasing/decreasing the effective A/Q-O bond length is believed to increase/decrease the charge/carrier concentration in the CuO_2 plane, while increasing/decreasing the Cu-O bond length results in an decrease/increase in the CuO_2-plane charge/carrier concentration [60-62,II,III,IV]. The overall direction and extension of charge transfer depend on the balance of these two effects [IV].

Thus, the isovalent substitutions provide us with interesting possibilities as such substitutions maintain the overall charge/carrier concentration constant but are likely to influence the distribution of charge/carriers over the unit cell [60,61,II,III,IV]. If we can control the distribution of charge/carriers it may be possible to obtain the desirable materials possessing the desirable properties. Therefore, a tailoring new functional material can be expected through the

isovalent-cation substitution.

1.2.1. Chemical Pressure *versus* Physical Pressure

In the material science, two kinds of "pressures" have been commonly recognized as powerful way to bring out unique properties of materials. That is, chemical pressure and physical pressure. As described in above, the chemical pressure is owing to isovalent substitutions. On the other hand, the physical pressure induced by an external mechanical pressure is a pure size perturbation and is free from the randomness of the potential introduced by chemical substitution.

In accordance with thermal expansion measurements on single crystals of $CuBa_2YCu_2O_x$ confirmed [63], the complexity of the dT_c/dp dependence on the direction of the lattice axes of $CuBa_2YCu_2O_x$ has been revealed [64]. They observed anisotropic effects on the lattice axes through the hydrostatic pressure. According to their calculation, the pressure effects in the *a*, *b* and *c*-directions were -1.9 K/GPa, +2.2 K/GPa and 0 K/GPa, respectively. Thus, value of T_c is expected to increase/decrease for uniaxial pressure along *b*/*a* axes, and to be insensitive to *c*-axis uniaxial pressure. By applying either physical or chemical pressure in the $Cu(Ba_{1-x}Sr_x)_2YCu_2O_{7-\delta}$ system, it was demonstrated [58] the disparities of chemical/physical pressure as follows: (*i*) the shrinkage of the lattice parameters resulting from the chemical pressure is almost isotropic along the three directions, whereas that induced by the physical pressure is highly anisotropic. (*ii*) most of the structural parameters decreased with x just as they decrease when the un-substituted compounds is subjected to physical pressure. However, in the latter case an increase of T_c values is observed. The only structural parameter that shows opposite behaviour with respect to the application of physical and chemical pressure, is the thickness of the superconducting block. (*iii*) in $Cu(Ba_{1-x}Sr_x)_2YCu_2O_{7-\delta}$ compound, the chemical pressure induces a displacement δ of O4 chain site from the *b* axis. This displacement which does not occur under a physical pressure, is mainly due to the size difference of Sr and Ba results in the depression of T_c value.

In contrast to afore-mentioned different effects between two kinds of pressures, similar trends were reported [65] as in the case of chemical- and physical-pressure consequence in the $Ba_2FeMoO_{5.9}$ sample. Namely, the investigation revealed that the T_C value of the sample increased linearly and the resistivity was depressed with the hydrostatic pressure showing metal-like behaviour. These results were consistent with a tendency induced by chemical pressure.

1.2.2. Isovalent Cation Substitution in High-T_c Superconductive Layered Copper Oxide Systems

In the high-T_c superconductive copper oxides such as Cu-$1^{(A)}2^{(Q)}12$, researches related to the isovalent-cation substitution have been widely carried out. One of the most general examples by means of the isovalent substitutions in this system is replacing Ba by smaller Sr.

In general, the application of physical pressure on high-T_c superconductive layered copper oxides increases T_c values [58]. It is well known that the substitution of Ba by Sr in $Cu(Ba_{1-x}Sr_x)_2YCu_2O_{7-\delta}$ induces a decrease of T_c value and ultimately makes the phase unstable [58,66-69]. In order to obtain x =1 sample, *i.e.*, $CuSr_2YCu_2O_{7-\delta}$, it is necessary to carry out the synthesis under high pressure [70]. For the purpose of revealing the structural mechanisms associated with T_c variations induced by either physical or chemical pressure, a series of samples of the $Cu(Ba_{1-x}Sr_x)_2YCu_2O_{7-\delta}$ with $0 \leq x \leq 1$ possessing various oxygen contents, have been prepared and characterized [58]. Through out the work, it was found: (*i*) T_c values were connected with the Sr concentration, x. As x increases, T_c decreases monotonically from 92.5 K for x = 0 to 78 K for x = 0.75. (*ii*) the complete substitution of Ba with Sr (x = 1) would induce an extrapolated value of the lattice parameters equivalent to the application of a physical pressure of about 10 GPa. (*iii*) the shrinkage of the lattice parameters by the chemical pressure is almost isotropic along the three directions. (*iv*) with increasing x concentration, most of the structural parameters decreased. Besides, the substitution of Ba by Sr in $Cu(Ba_{1-y}Sr_y)_2YbCu_2O_{6.95(2)}$ sample series ($0 \leq y \leq 0.4$) was studied [71] with respect to the effect of Sr substitution. The amount of oxygen and the overall hole are precisely controlled to be constant upon the Sr substitution for all the samples studied. As a result, it was demonstrated that the thickness of non-superconductive blocking block (BB) might be decreased through the substitution of the larger Ba by the smaller Sr. Furthermore, NPD analysis revealed that Sr substitution induces a disarrangement of the conductive CuO chains in BB by shifting part of the excess oxygen atoms from the *b*-axis lattice site to the *a*-axis site. Therefore, the destruction of CuO chain would induce the decrease in the concentration of mobile holes in the BB, as supported by the results of TEP measurements.

Similar behaviour has been observed for the Hg-based copper oxides. If Sr is substituted for Ba sites, T_c decreases [58,72] and the synthesis of single-phase samples necessitates the application of the high pressure [58,73]. The lattice parameters of this compound decreases with respect to those of fundamental compounds with no substitutions same as that observed by applying physical pressure [58,74].

In contrast to isovalent substitutions, the effect of physical pressure on T_c value of Cu-$1^{(Ba)}2^{(Y)}12$ system is unique. It was studied [75] the AC-susceptibility of $CuBa_2YCu_2O_{7-\delta}$ polycrystals with various oxygen contents under hydrostatic pressure up to 0.8 GPa. The T_c values for nine samples possessing various oxygen contents as a function of the pressure showed increasing T_c values linearly with pressure.

1.2.3. Isovalent Cation Substitution in *B*-site Ordered Double-Perovskite Systems

Historically, the effectiveness of isovalent substitutions in the single Mn-based perovskite system was first realized then the investigations of *B*-site ordered double perovskites employing isovalent substitutions followed. However, in the *B*-site ordered double-perovskite compounds, the effects of the aliovalent substitutions at *B* site were more highlighted compared to isovalent effects. Thus, in the contrast to the high-T_c superconductive layered copper oxide system, systematic researches through the chemical pressure has not been established yet, in this system.

It was revealed that the isovalent-cation substitution into *A* site in $AMnO_3$ compound exerts a chemical pressure on the system. In several single perovskites, the overlap between *d* orbitals in *B* site and oxygen *p* orbitals forms the electronically active band. Thus, this overlap can be strongly influenced by the internal pressure generated by isovalent substitutions at *A* site [76,77]. Based on this notion, a study of physical properties [77] as a function of average ionic radius of *A* site, *i.e.*, $r(A^{II})$, in $LaMnO_3$ sample substituted La by *A* (alkaline-earth elements) found that with decreasing $r(A^{II})$, T_C decreased and the magnitude of MR near T_C enhanced drastically. Besides, the magnetic properties seemed to be influenced by $r(A^{II})$. It was proposed that the principal effect of decreasing $r(A^{II})$ is to decrease the Mn-O-Mn bond angle thereby reducing electron hopping between Mn sites. In this work it was concluded that the most influential parameter in determining T_C value for a given carrier concentration was $r(A^{II})$.

After a number of searches of chemical pressure at *A* site in single-perovskite compounds, the application of isovalent-cation substitution at *A* site in the *B*-site ordered double-perovskite compounds has been tried similar way. For example, in the case of $(Ca,Sr,Ba)_2FeMoO_6$ samples [78], the magnitude of low-field MR at room temperature was optimized in $(Sr_{0.2}Ba_{0.8})_2FeMoO_6$. On the other hand, $(Sr_{0.95}Ca_{0.05})_2FeMoO_6$ exhibited the largest MR value at high field such as 1 T. This study also reported that T_C values as a function of $r(A^{II})$. In $(Sr_{1-y}Ba_y)_2FeMoO_6$ samples T_C values showed decreasing monotonically with increasing Ba concentration. For the $(Sr_{1-x}Ca_x)_2FeMoO_6$ system, there existed a broad increase in T_C as Ca concentration increased. Moreover, another research suggested [52] that the electronic structure of A_2FeMoO_6/A_2FeReO_6 primarily depends on the number of electrons in the ordered $FeMoO_6/FeReO_6$ sublattice but the influence of the *A* cation on the structure and properties was clearly observed. That is, the compounds with *A* = Ca of both series, *i.e.*, Ca_2FeMoO_6 and Ca_2FeReO_6, have a monoclinic ordered-perovskite structure [52,79,80] whereas the *A* = Ba and Sr members have cubic/tetragonal structures for both series. For A_2FeReO_6 oxides, changes in T_C values associated with chemical pressure at *A* site were revealed, *i.e.*, the T_C value increased in the order Ca, Sr and Ba [52,81]. Besides, the electrical property of A_2FeReO_6 indicated that *A* = Ba and Sr samples were conducting, while the *A* = Ca sample was an insulator [*e.g.*,81]. Similar to the A_2FeReO_6 system, studies in A_2FeMoO_6 have revealed that the Curie temperature seems to be controlled by structural parameters [82] which are affected by the chemical pressure at *A* site. It is because through the change of structural parameters such as the bond lengths and bond

angles of Fe-O-Mo and Mo-Mo [78,82] by the isovalent substitution, the degree of electron hopping and further the electronic bandwidth might be influenced.

1.3. Objectives and Significance of the Present Work

From a historical point of view, researches associated with the aliovalent-cation substitution began first in the 3*d* functional-perovskite materials then studies related to the isovalent-cation substitution followed in this system. Furthermore, interests of novel functional materials and explores of obtaining unstable materials under ambient environment have arisen recently. Thus the external-mechanical pressure effect was highlighted more. The consequences of isovalent-cation substitutions are much less understood resulting in numerous research subjects to be solved so that it is crucial and interesting to establish the effects of isovalent substitutions.

Isovalent substitution or "size-only-dependent" cation substitution provides us with an interesting tool to control material properties, *i.e.*, "chemical pressure" effect. In an ideal case, the overall charge/carrier concentration remains constant, whereas the distribution of charge/carriers is rather likely to be affected. The purpose of the present research was set so as to creatively utilize such substitution in tailoring functional oxide systems with strongly-correlated electrons. For the two target systems high-T_c superconductive (HTSC) compounds of $CuBa_2RECu_2O_{7-\delta}$ and tunneling-type magnetoresistance (TMR) compounds of A_2FeMoO_{6-w} were chosen.

For HTSCs the magnetic irreversibility-field line [$H_{irr}(T)$] determines the limit of high-field application. It was known that the H_{irr} characteristics of $CuBa_2YCu_2O_{7-\delta}$ of the Cu-1212:P phase are most superior among the known HTSC materials [13]. However, the dependence of H_{irr} on the size of rare earth ion [$r(RE^{III})$], that is, the consequences of isovalent-cation substitution at the *RE* site, has not been established yet for the $CuBa_2RECu_2O_{7-\delta}$ system.

Among a number of *B*-site ordered double-perovskite compounds, A_2FeMoO_6 and A_2FeReO_6 systems are particular interest since they have found to be giant TMR materials [79,83,84]. Sr_2FeMoO_6 had been known as a ferrimagnet with a high T_C value [85,86] until TMR behaviour [83] having its origin in the halfmetallic ground state was recently revealed. It was later found that iron in this compound, as seen by ^{57}Fe Mössbauer spectroscopy, possesses a mixed-valence $Fe^{II/III}$ state [87,88]. Therefore, it is worthwhile to investigate the relationship between the Fe valence state (V_{Fe}) and isovalent substitution at the *A* site.

Through controlling the distribution of charge/carriers the oxidation state of the rare-earth elements/transition metals will be influenced for both double- and triple-perovskites. Since the changes in the valence values of the rare-earth elements/transition metals may induce novel properties, controlling the distribution of charge/carriers and tailoring/designing desirable functional materials are the final purpose in this work.

References

1. B. Matthias and A. von Hippel, *Phys. Rev.* **73**, 268 (1948).; B. Matthias and A. von Hippel, Phys. Rev. **73**, 1378 (1948).
2. F.S. Galasso, *Structure, properties and preparation of perovskite-type compounds*, Pergamon, Oxford (1969).
3. S.H. Hoh and F.E. Pirigy, *J. Am. Ceram. Soc.* **46**, 516 (1963).
4. G.A. Smolenskii, A.I. Agranovskaya and V.A. Isupov, *Sov. Phys. Solid State* **1**, 907 (1959).
5. F.S. Galasso, G. Layden and D. Flinchbaugh, *J. Chem. Phys.* **44**, 2703 (1966).
6. M. Karppinen and H. Yamauchi, *Chemistry of halfmetallic and related cation-ordered double perovskites*, In: *Frontiers in Magnetic Materials*, A.V. Narlikar (Ed), Springer Verlag, Berlin 2005, p. 3.
7. F.J. Fresia, L. Katz, and R. Ward, *J. Am. Chem. Soc.* **81**, 4783 (1959).
8. F.S. Galasso, and J. Pyle, *Inorg. Chem.* **2**, 482 (1963).
9. F.S. Galasso, L. Katz, and R. Ward, *J. Am. Chem. Soc.* **81**, 820 (1959).
10. A.W. Sleight, and R. Ward, *Inorg. Chem.* **1**, 790 (1962).
11. V.M. Goldschmidt, Skrifter Norske Videnskaps-Akad. Oslo, I. Mat.-Naturv. Kl., No. 8 (1926).
12. M. Karppinen and H. Yamauchi, *Chemistry of halfmetallic and related cation-ordered double perovskites*, In: *Frontiers in Magnetic Materials*, A.V. Narlikar (Ed), Springer Verlag, Berlin 2005, p. 4.
13. M. Karppinen and H. Yamauchi, *Mater. Sci. Eng. R* **26**, 51 (1999).
14. S.H. Lee, W.T. Kim, and D.J. Jung, *Sae Mulli* **29**, 614 (1989); Y. Matsumoto and J. Hombo, *J. Solid State Chem.* **93**, 395 (1991); M. Elmassalami, A. Elzubair, H.M. Ibrahim, and M.A. Rizgalla, *Physica C* **183**, 143 (1991).
15. Q. Huang, P. Karen, V.L. Karen, A. Kjekshus, J.W. Lynn, A.D. Mighell, N. Rosov, and A. Santoro, *Phys. Rev. B* **45**, 9611 (1992).
16. P. Karen, A. Kjekshus, Q. Huang, J.W. Lynn, N. Rosov, I. Natali Sora, V.L. Karen, A.D. Mighell, and A. Santoro, *J. Solid State Chem.* **136**, 21 (1998).
17. J. Lindén, M. Lippmaa, P. Karen, A. Kjekshus, and M. Karppinen, *J. Solid State Chem.* **138**, 87 (1998); J. Lindén, A. Kjekshus, P. Karen, J. Miettinen, and M. Karppinen, *J. Solid State Chem.* **139**, 168 (1998); J. Lindén, P. Karen, A.Kjekshus, J. Miettinen, and M. Karppinen, *J. Solid State Chem.* **144**, 398 (1999).
18. M.K. Wu, J.R. Ashburn, C.J. Torng, P.H. Hor, R.L. Meng, L. Gao, Z.J. Huang, Y.Q. Wang, and C.W. Chu, *Phys. Rev. Lett.* **58**, 908 (1987).
19. M. Karppinen and H. Yamauchi, *Oxygen Engineering for Functional Oxide Materials*, In: *International Book Series: Studies of High Temperature Superconductors*, Vol. 37, A.V. Narlikar (Ed.), Nova Science Publishers, New York 2001, pp. 109-143.
20. C. Brisi, *Ricerca Sci.* **24**, 1858 (1954).
21. G.H. Jonker, *Physica* **20**, 1118 (1954).
22. H.L. Yakel, *Acta Cryst.* **8**, 394 (1955).
23. G.H. Jonker and J.H. Van Santen, *Physica* **16**, 337 (1950).
24. A. Maignan, C. Martin, D. Pelloquin, N. Nguyen, and B. Raveau, *J. Solid State Chem.* **142**, 247 (1999).
25. J. Nakamura, J. Lindén, M. Karppinen, and H. Yamauchi, *Appl. Phys. Lett.* **77**, 1683 (2000).
26. T. Yamamoto, J. Liimatainen, J. Lindén, M. Karppinen, and H. Yamauchi, *J. Mater. Chem.* **10**, 2342 (2000).
27. A.R. Mackintosh, *J. Chem. Phys.* **38**, 1991 (1963).
28. D.D. Glower and R.C. Heckman, *J. Chem. Phys.* **41**, 877 (1964).
29. J. Longo and R. Ward, *J. Am. Chem. Soc.* **83**, 2816 (1961).
30. G. Blasse, *J. Phys. Chem. Sol.* **26**, 1969 (1965).
31. G.H. Jonker, *Physica* **22**, 707 (1956).
32. W. Meissner, H. Franz, and H. Westerhoff, *Ann. Phys.* **17**, 593 (1933).
33. J.F. Schooley, W.R. Hosler, and M.L. Cohen, *Phys. Rev. Lett.* **12**, 474 (1964).
34. Ch.J. Raub, A.R. Sweedler, M.A. Jensen, S. Broadston, and B.T. Matthias, *Phys. Rev. Lett.* **13**, 746 (1964).
35. D.C. Johnston, H. Prakash, W.H. Zachariasen, and R. Viswanathan, *Mater. Res. Bull.* **8**, 777 (1973).
36. A.W. Sleight, J.L. Gillson, and P.E. Bierstedt, *Solid State Commun.* **17**, 27 (1975).
37. R.J. Cava, B. Batlogg, J.J. Krajewski, R. Farrow, L.W. Rupp Jr., A.E. White, K. Short, W.F. Peck, and T. Kometani, *Nature* (London) **332**, 814 (1988).
38. W.F. Libby, *Science* **171**, 499 (1971).
39. M.A. Pena and J.L.G. Fierro, *Chem. Rev.* **101**, 1981 (2001).
40. K. Lehmus, Ph. D. Thsesis, Helsinki University of Technology, Espoo 2002, p. 12.
41. Y. Tokura and Y. Tomioka, *J. Magn. Magn. Mater.* **200**, 1 (1999).
42. A. Maignan, C. Martin, and B. Raveau, *J. Supercond.* **13**, 313 (2000).

43. J. Lindén, P. Karen, A. Kjekshus, J. Miettinen, T. Pietari, and M. Karppinen, *Phys. Rev. B* **60**, 15251 (1999).
44. V.P.S. Awana, J. Nakamura, J. Lindén, M. Karppinen, and H. Yamauchi, *Solid State Commun.* **119**, 159 (2001).
45. Y. Minet, V. Lefranc, N. Nguyen, B. Domengès, A. Maignan, and B. Raveau, *J. Solid State Chem.* **121**, 158 (1996).
46. V. Primo-Martín, and M. Jansen, *J. Solid State Chem.* **157**, 76 (2001).
47. S. Maekawa, Kotaibutsuri **34**, 935 (1999). (*in Japanese*)
48. S. Maekawa, Kotaibutsuri **32**, 876 (1997). (*in Japanese*)
49. S. Maekawa, Kotaibutsuri **32**, 25 (1997). (*in Japanese*)
50. A.W. Sleight and R. Ward, *J. Am. Chem. Soc.* **83**, 1088 (1961); A.W. Sleight, J.M. Longo, and R. Ward, *Inorg. Chem.* **1**, 245 (1962).
51. A.W. Sleight and J.F. Weiher, *J. Phys. Chem. Solids* **33**, 679 (1972).
52. K. Ramesha, L. Sebastian, B. Eichhorn, and J. Gopalakrishnan, *Chem. Mater.* **15**, 668 (2003).
53. M. Takano, N. Nakanishi, Y. Takeda, S. Naka, and T. Takeda, *Mtaer. Res. Bull.* **12**, 923 (1977).
54. Y. Takeda, S. Naka, and M. Takano, *J. de Physique* **40**, C2 331 (1979).
55. M. Takano, J. Kawauchi, N. Nakanishi, and Y. Takeda, *J. Solid State Chem.* **39**, 75 (1981).
56. Y. Takdeda, K. Kajiura, S. Naka, and M. Takano, *Froc. Inter. Conf.* Kyoto, 929 (1980).
57. J. Nakamura, Ph. D. Thsesis, Tokyo Institute of Technology, Tokyo 2003, p. 7.
58. F. Licci, A. Gauzzi, M. Marezio, G. Radaelli, R. Masini, and C. Chaillout-Bougerol, *Phys. Rev. B* **58**, 15208 (1998).
59. Karpinski, S.M. Kazakov, M. Angst, A. Mironov, M. Mali, and J. Roos, *Phys. Rev. B* **64**, 94518 (2001).
60. M. Karppinen and Y. Yamauchi, *Philos. Mag. B* **79**, 343 (1999).
61. M. Karppinen, and Y. Yamauchi, *Int. J. Inorg. Mater.* **6**, 589 (2000).
62. J.L. Tallon, *Physica C* **168**, 85 (1990).
63. C. Almassan, S. Han, B. Lee, L. Paulius, M. Maple, B. Veal, J. Downer, A. Paulikas, Z. Fisk, and J. Schirber, *Phys. Rev. Lett.* **69**, 680 (1992).
64. C. Meingast, O. Kraut, T. Wolf, H. Wühl, A. Erb, and G. Müller-Vogt, *Phys. Rev. Lett.* **67**, 1634 (1991).
65. R. Wang and M. Itoh, *Solid State Ionics* **108**, 269 (1998).
66. T. Wada, S. Adachi, T. Mihara, and R. Inaba, *Jpn. J. Appl. Phys.*, Part 2 **26**, L706 (1987).
67. B.W. Veal, W.K. Kwok, A. Umezawa, G.W. Crabtree, J.D. Jorgensen, J.W. Downey, L.J. Nowicki, A.W. Mitchell, A.P. Paulikas, and C.H. Sowers, *Appl. Phys. Lett.* **51**, 279 (1987).
68. A. Ono, T. Tanaka, H. Nozaki, and Y. Ishizawa, *Jpn. J. Appl. Phys.*, Part 2 **26**, L1687 (1987).
69. R.S. Roth, C.J. Rawn, J.D. Whitler, C.K. Chiang, and W.K. Wong-ng, *J. Am. Ceram. Soc.* **72**, 395 (1989).
70. B. Okai, Jpn. *J. Appl. Phys.*, Part 2 **29**, L2180 (1990).
71. T. Nakane, K. Isawa, R.S. Liu, J.M. Chen, H. Yamauchi, and M. Karppinen, *J. Solid State Chem.* **177**, 1925 (2004).
72. D.E. Morris, K.K. Singh, V. Kirtikar, and A.P.B. Sinha, *Physica C* **235-240**, 903 (1994).
73. M.A. Subramanian and M.-H. Whangbo, *J. Solid State Chem.* **109**, 410 (1994).
74. M. Marezio and F. Licci, *Physica C* **282**, 51 (1997).
75. R. Benischke, T. Weber, W. Fietz, J. Metzger, K. Grube, T. Wolf, and H. Wühl, *Physica C* **203**, 293 (1992).
76. J.B. Goodenough, and J.M. Longo, *Landolt-Börnstein Tabellen*, Springer, Berlin 1970, Vol. III/4a.
77. H.Y. Hwang, S.-W. Cheong, P.G. Radaelli, M. Marezio, and B. Batlogg, *Phys. Rev. Lett.* **75**, 914 (1995).
78. B.-G. Kim, Y.-S. Hor, and S.-W. Cheong, *Appl. Phys. Lett.* **79**, 388 (2001).
79. J. Gopalakrishnan, A. Chattopadhyay, S.B. Ogale, T. Venkatesan, R.L. Greene, A.J. Millis, K. Ramesha, B. Hannoyer, G. Marest, *Phys. Rev. B* **62**, 9538 (2000).
80. J.A. Alonso, M.T. Casais, M.J. Martínez-Lope, J.L. Martínez, P. Velasco, A. Muňoz, and M.T. Fernández-Díaz, *Chem. Mater.* **12**, 161 (2000).
81. S.E. Lofland, T. Scabarozi, S. Kale, S.M. Bhagat, S.B. Ogale, T. Venkatesan, R.L. Greene, J. Gopalakrishnan, and K. Ramesha, *IEEE Trans. Magn.* **37**, 2153 (2001).
82. C. Ritter, M.R. Ibarra, L. Morellon, J. Blasco, J. García, and J.M. De Teresa, *J. Phys.: Condens. Matter* **12**, 8295 (2000).
83. K.-I. Kobayashi, T. Kimura, H. Sawada, K. Terakura, and Y. Tokura, *Nature* (London) **395**, 677 (1998).
84. S.B. Kim, B.W. Lee, and C.S. Kim, *J. Magn. Magn. Mater.* **242-245**, 747 (2002).
85. F.K. Patterson, C.W. Moeller, and R. Ward, *Inorg. Chem.* **2**, 196 (1963).
86. F.S. Galasso, F.C. Douglas, and R.J. Kasper, *J. Chem. Phys.* **44**, 1672 (1966).
87. J. Lindén, T. Yamamoto, M. Karppinen, H. Yamauchi, and T. Pietari, *Appl. Phys. Lett.* **76**, 2925 (2000).
88. O. Chmaissem, R. Kruk, B. Dabrowski, D.E. Brown, X. Xiong, S. Kolesnik, J.D. Jorgensen, and C.W. Kimball, *Phys. Rev. B* **62**, 14197 (2000).

2. OXYGEN CONTENT AND METAL VALENCE

Mixed-valence states can be often observed for transition metal/few heavy metals in the perovskite compounds so that the oxygen non-stoichiometry derived from the mixed-valence states and/or various coordination states of transition metals for tuning the transition-metal valence is common in the peorvskite-related compounds. Therefore, the precise evaluation of the oxygen content of compounds and further, the fine tuning of the oxygen content and controlling the material properties, *i.e.*, "oxygen engineering", is one of the most crucial research topics from a standpoint of material science [I]. It is because small differences in the oxygen contents among samples exert unique material properties, *e.g.*, quite different T_c/H_{irr} values can be obtained by varying the oxygen content in the high-T_c superoconductive materials.

2.1. Oxygen Content Analyses

Several techniques of chemical analysis have been employed to establish the oxygen content in 3*d* transition metal oxides [1-3] such as volumetric methods utilizing a thermobalance and thermogravimetric (TG) reduction and so on. Among the different techniques, wet-chemical redox [4] analysis methods are often found the most accurate [2,5]. The wet-chemical redox methods are based on the oxidation-reduction reaction between the high-valent metal species that exist in the sample and a suitable reductant. After the high-valent metal ions are reduced by a reductant completely, it is possible to calculate the oxygen content by determining either the amount of reductant remained or the amount of oxidized species formed from reductant. Iodometric titration [6] utilizing I^- as a reductant is the most common method for copper and cobalt oxides but due to small difference values of the standard reduction potential between the Fe^{III}/Fe^{II} and I^0/I^{-I} redox couples [1], this method is not appropriate for iron oxides. In terms of iron oxides, cerimetric titration using a redox power of divalent iron can be adopted. It is possible to determine the oxygen content of the iron oxides by estimating the amount of remained Fe^{2+} ions derived from the reaction between high-valent iron ions and divalent iron with Ce^{4+} ions [1,7]. Cobalt oxides also can be analyzed by this method [5], but copper oxides is not applicable due to the incomplete reaction of Cu^{III} with Fe^{2+} ions [1]. Therefore, the most powerful and the most convenient redox method applicable to Cu, Co and Fe oxides [1] can be considered as utilizing the reduction capability of monovalent copper. The oxygen content of oxide samples are evaluated by determining the remaining amount of the reductant of Cu^+ ions by means of electrochemical oxidation, *i.e.* coulometric titration [8-10] or constant-potential electrolysis [11].

Coulometric titration is based on the reduction of high-valent cations existing in a sample with a known excess of monovalent copper (Cu^+/Cu^{2+} titration) or divalent iron (Fe^{2+}/Fe^{3+} titration) in an acidic solution [2]. The un-reacted Cu^+ or Fe^{2+} is oxidized by applying

a constant current and the amount of the species titrated is calculated from the time required for the oxidation according to Faraday's law. Due to its accuracy and versatility coulometric Cu^{+}/Cu^{2+} and Fe^{2+}/Fe^{3+} titrations were applied in the present study for the determination of the oxygen contents in the $CuBa_2RECu_2O_{7-\delta}$ triple perovskites [II,III] and the A_2FeMoO_{6-w} double perovskites [V] with A elements are Ba, Sr and Ca, *i.e.*, the most fundamental members of A_2FeMoO_6 system.

In perovskite structures with the same element but locating in different atomic positions, the oxidation and coordination states at a distinct position are crucial factor. This is particularly essential with high-T_c superconductive copper oxides because the distribution of holes among the different copper-oxide layers is likely to affect the superconductivitiy properties [12]. However, chemical methods for oxygen content analysis only give the average oxidation state of the metals. Therefore, other methods are needed to obtain information in the oxidation states of distinct metal atoms in the structure, *e.g.*, XANES [13-21] and ^{57}Fe Mössbauer spectroscopies [22-27]. Since they are of great advantage owing to the possibility to selectively examine the chemical environment of each distinct element, the combination of the wet-chemical redox analysis methods and XANES and/or ^{57}Fe Mössbauer techniques would provide us with the most reliable information in terms of the oxygen content, and further with the influential factors of compounds derived from chemical environment of cations.

2.1.1. Cu^{+}/Cu^{2+} Coulometric Titration [I]

In the Cu^{+}/Cu^{2+} redox analysis the highly oxidized transition metal species in a sample are first reduced with an excess of Cu^{+} ions. For Cu^{III} in $CuBa_2RECu_2O_{7-\delta}$ the reduction occurs according to reaction:

$$Cu^{III} + Cu^{+} \rightarrow 2\,Cu^{2+}. \qquad (2.1.1.\text{-}1)$$

Then the amount of non-reacted Cu^{+} ions is determined with coulometric titration (anodic oxidation) as follows:

$$Cu^{+} \rightarrow Cu^{2+} + e^{-}. \qquad (2.1.1.\text{-}2)$$

The excess amount of Cu^{+}, $n(Cu^{+}_{tit})$, is calculated from the titration time, t, according to Faraday's law:

$$n(Cu^{+}_{tit}) = \frac{I \times t}{F}, \qquad (2.1.1.\text{-}3)$$

where I is constant dc current applied and F is Faraday's constant. As the source of Cu^{+} ions CuCl was utilized in the present study. The actual amount of monovalent copper in the CuCl powder used was checked by coulometric titration, and the result was taken into account through a correction parameter, f, calculated as

$$f = \frac{I \times t \times M(\mathrm{CuCl})}{F \times m(\mathrm{CuCl})}, \qquad (2.1.1.\text{-}4)$$

where m(CuCl) is the mass of CuCl used for the experiment and M(CuCl) is the molecular weight of CuCl. The amount of highly oxidized transition metal species in the sample is calculated from the titration result, *i.e.*, $n(\mathrm{Cu^{III}})$, for the present $CuBa_2RECu_2O_{7-\delta}$ reference sample is:

$$n(\mathrm{Cu^{III}}) = \frac{f \times m(\mathrm{CuCl})}{M(\mathrm{CuCl})} - n(\mathrm{Cu^{+}_{tit}}). \qquad (2.1.1.\text{-}5)$$

Therefore, the oxygen non-stoichiometry in the case of $CuBa_2RECu_2O_{7-\delta}$ is then obtained as

$$\delta = \frac{m(\mathrm{CuBa_2RECu_2O_{7-\delta}}) - n(\mathrm{Cu^{III}}) \times M(\mathrm{CuBa_2RECu_2O_7})}{2m(\mathrm{CuBa_2RECu_2O_{7-\delta}}) - n(\mathrm{Cu^{III}}) \times M(\mathrm{O})}, \qquad (2.1.1.\text{-}6)$$

where $m(CuBa_2RECu_2O_{7-\delta})$ is the mass of the analyzed sample and $M(CuBa_2RECu_2O_7)$ and M(O) are the molecular weight of $CuBa_2RECu_2O_7$ and the atomic weight of oxygen, respectively.

The present coulometric titration experiments were performed in 1 M HCl cell solution (*ca.* 200 ml) and the potential of the solution was measured with an Ag/AgCl reference electrode (Horiba: pH meter F-22) as a function of the anodic oxidation time. Platinum plates were used for both cathode and anode, and the cathode was separated from the cell solution with a salt bridge. To prevent oxidation of Cu^{+} ions by oxygen during the titration analysis, the cell solution was freed from dissolved oxygen by Ar-gas bubbling before adding reagents and titration was carried out in an air-tight cell under an Ar-gas flow. Furthermore, for every sample analysis, a pre-titration was performed by dissolving 2 ~ 3 mg of CuCl in the cell solution and applied current using a constant-current source (Advantest: R6144) until the potential against the Ag/AgCl electrode reached 930 mV. The purpose of pre-titration was to standardize the initial redox-power of the cell. Actual analysis of the sample was carried out immediately after a pre-titration in the same cell. The titration time was detected at the titration end-point at 930 mV. The proper end-point is found within the range of the fastest change in the cell potential. The presently applied conventional coulometric analysis method (with the end-point detection at 930 mV) agreed with a number of previous studies on various 3*d* transition metal oxide systems

determined for the same materials by means of iodometric titration, cerimetric titration and/or thermogravimetric reduction [*e.g.*,5].

The amount of sample used for a single experiment of a conventional wet-chemical redox analysis is typically 50 ~ 100 mg [1,2]. Furthermore, several parallel experiments are required to guarantee the reliability of the obtained result. As some important synthesis techniques of functional oxides, *e.g.* ultra-high pressure synthesis and single-crystal growth, yield samples with a mass that is insufficient for a conventional oxygen content analysis, a reliable technique enabling us to analyze samples of smaller amounts is indispensable for further development of functional oxide materials. In this section, the development of a Cu^{+}/Cu^{2+} coulometric titration technique, *i.e.*, henceforth called "micro-titration" that can be applied to sample amounts considerably smaller than those required for conventional wet-chemical redox analysis techniques, is described [I].

A high-quality fully-oxygenated $CuBa_2YCu_2O_{7-\delta}$ sample was used as a reference material to reveal the reliability of Cu^{+}/Cu^{2+} coulometric titration through the comparison of both conventional- and micro-titration techniques. To make the Cu^{+}/Cu^{2+} coulometric titration analysis as efficient as possible in terms of the time required for a single experiment, the accuracy of the method was first investigated against the titration time. For these experiments the current applied was fixed at 5 mA, *i.e.* the value that has typically been employed for analyses of superconductive oxides [2,8-10]. If the titration time becomes too short, *i.e.* $n(Cu^{+}_{tit})$ is too small (Eq. 2.1.1.-3), possible error in determining the end-point becomes dominant for the accuracy of the analysis. From several repeated experiments with varying $n(Cu^{+}_{tit})$ it was concluded that a titration time of $t > 8$ min is needed for accurate analysis. For the further experiments, the titration time was fixed in the range of 9 ~ 12 min to reduce the time required for one experiment as much as possible but at the same time to guarantee high enough accuracy for the analysis.

With another set of experiments, an optimum range for the ratio $n(Cu^{+}_{tit}) / n(Cu^{III})$ was searched for. As a result, it was revealed that both the accuracy and the reproducibility of the analysis are highest at $n(Cu^{+}_{tit}) / n(Cu^{III}) = 1/2 \sim 3/2$. For further experiments, ratio, $n(Cu^{+}_{tit}) / n(Cu^{III}) \approx 1/2$, was selected. This means that for the present fully-oxygenated $CuBa_2YCu_2O_{7-\delta}$ reference material $m(CuCl)/m(CuBa_2YCu_2O_{7-\delta})$ ratio must be around 1/5. In the final experiments, not only the micro-titrations but also the conventional titrations performed for comparison were carried out at the mass ratio of 1/5 for the CuCl powder and the sample. For the conventional titration performed at $I = 5$ mA, about 10 mg of CuCl and 50 mg of the $CuBa_2YCu_2O_{7-\delta}$ reference sample were used for a single experiment to satisfy the two criteria discussed above, *i.e.* (*i*) $t = 9 \sim 12$ min, and (*ii*) $n(Cu^{+}_{tit}) / n(Cu^{III}) \approx 1/2$ (Eqs. 2.1.1.-3 and

2.1.1.-5).

In order to apply the Cu^{+}/Cu^{2+} coulometric titration method to the analysis of small amounts of sample, the current applied for the titration needs to be decreased. If we like to apply the method to a $CuBa_2YCu_2O_{7-\delta}$ sample of *ca.* 10 mg, application of a current of 1 mA satisfies the afore-given criteria (*i*) and (*ii*). The amount of CuCl used for such micro-titration was accordingly set at *ca.* 2 mg. In Table 2.1.1.-1, the results of five parallel micro-titrations for the $CuBa_2YCu_2O_{7-\delta}$ reference sample are summarized. Based on the micro-titration analysis, the oxygen content 7-δ is determined at 6.937 with a standard deviation of ± 0.007. An excellent agreement is seen between this result and the one, *i.e.* 6.941 ± 0.009, calculated for the same $CuBa_2YCu_2O_{7-\delta}$ reference material from five parallel experiments of conventional Cu^{+}/Cu^{2+} coulometric titration using samples of ~50 mg (Table 2.1.1.-1). Further reduction in the amount of sample used is in principle possible by decreasing the current accordingly. However, for samples with a mass considerably less than *ca.* 2 mg the weighing error becomes a dominant factor for the accuracy of the analysis. The same applies when amounts smaller than *ca.* 2 mg of CuCl need to be weighed.

Table 2.1.1.-1 Oxygen-content values and corresponding coulometric Cu^{+}/Cu^{2+} titration data obtained for the $CuBa_2YCu_2O_{7-\delta}$ reference sample from five parallel experiments of conventional Cu^{+}/Cu^{2+} coulometric titration and from five parallel micro-titration experiments [I].

Conventional titration	**Exp. 1**	**Exp. 2**	**Exp. 3**	**Exp. 4**	**Exp. 5**
f	0.97726	0.97227	0.97414	0.97414	0.98673
m (CuCl) [mg]	14.5	16.82	10.49	10.48	9.47
m ($CuBa_2YCu_2O_{7-\delta}$) [mg]	42.67	54.59	49.8	49.44	50.23
t [s]	1686	1772	679	748	548
$n(Cu^{+}_{tit})$ [mmol]	0.087369	0.091826	0.035186	0.038762	0.028398
$n(Cu^{III})$ [mmol]	0.055766	0.073364	0.068034	0.06436	0.065991
δ	0.06535	0.05292	0.04544	0.06708	0.06305
Oxygen content (7-δ)	6.935	6.947	6.955	6.933	6.937
Aver. (7-δ) and Std.	6.941 ± 0.0093				
"Final titration result"	6.94 ± 0.01				
Micro-titration	**Exp. 1**	**Exp. 2**	**Exp. 3**	**Exp. 4**	**Exp. 5**
f	0.96342	0.96342	0.9709	0.9709	0.9709
m (CuCl) [mg]	2.14	2.41	2.07	2.01	2.11
m ($CuBa_2YCu_2O_{7-\delta}$) [mg]	10.62	10.56	10.11	10.18	9.88
t [s]	672	904	710	606	728
$n(Cu^{+}_{tit})$ [mmol]	0.006965	0.009369	0.007359	0.006281	0.007545
$n(Cu^{III})$ [mmol]	0.013861	0.014084	0.012942	0.013432	0.013148
δ	0.06594	0.05634	0.07435	0.06115	0.05733
Oxygen content (7-δ)	6.934	6.944	6.926	6.939	6.943
Aver. (7-δ) and Std.	6.937 ± 0.0074				
"Final titration result"	6.94 ± 0.01				

In Figs. 2.1.1.-1(a) and (b), typical titration curves are shown for the $CuBa_2YCu_2O_{7-\delta}$ reference sample obtained with the conventional titration and our micro-titration, respectively. At point A, about 3 mg of CuCl is dissolved in the cell solution for the pre-titration. After the potential of the cell solution is stabilized, constant dc current of 5 mA is applied [Eq. (2.1.1.-2)] starting from point B. Point C is the end-point of the pre-titration. At point C the cell potential is 930 mV, *i.e.* the purpose of the pre-titration to standardize the initial redox power of the cell solution is fulfilled. At point D, an excess amount of CuCl is added. As a consequence the cell potential decreases drastically. After CuCl is dissolved completely, *i.e.* the cell potential is stabilized, the sample is dissolved in the cell solution at point E. From point E to F, Cu^{III} from the sample is reduced spontaneously to Cu^{2+} by Cu^{+} [Eq. (2.1.1.-1)] and accordingly the cell potential increases. From point F the constant dc current (5 mA for conventional titration and 1 mA for micro-titration) is applied in order to oxidize the remained Cu^{+} ions to Cu^{2+} [Eq. (2.1.1.-2)]. All Cu^{+} ions are oxidized to Cu^{2+} and the titration is finished at point G. It is clearly seen from Figs. 2.1.1.-1(a) and (b), that the two titration experiments, *i.e.* conventional titration and micro-titration, occur in a perfectly parallel way. In both experiments, each step is clearly distinguishable and sharp. This feature is an essential requirement for a successful analysis.

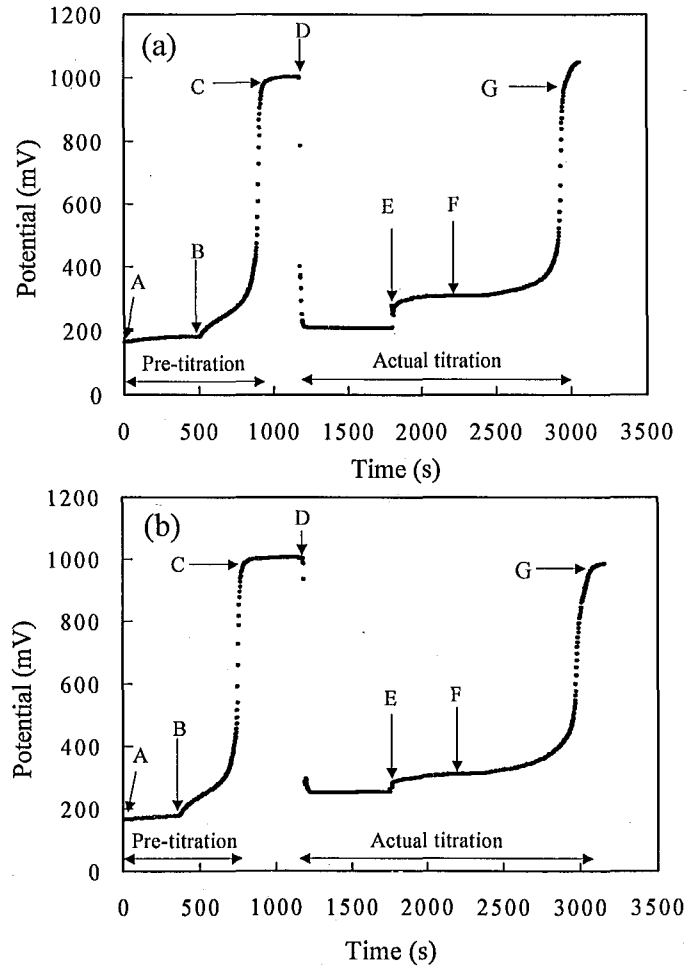

Fig. 2.1.1.-1 Typical coulometric titration curves, *i.e.* cell potential *versus* time, obtained for (a) conventional titration (Exp. 5 in Table 2.1.1.-1), and (b) micro-titration (Exp. 1 in Table 2.1.1.-1). In both figures, pre-titration corresponds to points A to C and actual sample titration starts from point D. More detailed explanations for points A-G are given in the text. Note that, for conventional titration/micro-titration, the amount of CuCl added was about 10 mg/2 mg, the amount of sample was about 50 mg/10 mg, and the applied constant dc current was 5 mA/1 mA [I].

In conclusion, it was demonstrated that an improved coulometric titration method works to precisely analyze oxygen contents of decreased amounts of various mixed-valent oxides containing, *e.g.*, copper, cobalt or iron. By means of micro-titration method the oxygen content can be determined for employed $CuBa_2YCu_2O_{7-\delta}$ reference with high reproducibility, *i.e.* $|\Delta\delta| < 0.01$, for samples with a mass of only ~10 mg.

2.1.2. Fe^{2+}/Fe^{3+} Coulometric Titration

Cerimetric titration is commonly applied for the determination of the oxygen content in iron oxides where an excess of the reducing agent Fe^{2+} is added to the sample solution and the remaining Fe^{2+} is titrated with Ce^{4+}. However, in the case of double-perovskite compounds consisting of Fe and Mo as *B*'/*B*" cations, the behaviour of Mo ion in the cerium dissolved solution is not obvious. Thus, Fe^{2+}/Fe^{3+} coulometric titration was applied in the present study for the determination of the oxygen contents in the A_2FeMoO_{6-w} double perovskites in stead of applying cerimetric titration.

In the Fe^{2+}/Fe^{3+} coulometric titration for the A_2FeMoO_{6-w} samples, not only Fe^{II} in each sample but also Mo^{V} species is determined by coulometric titration through the oxidation reaction. The reactions are as follows:

$$Fe^{II} \rightarrow Fe^{3+} + e^- \quad . \qquad (2.1.2.\text{-}1)$$

$$Mo^{V} \rightarrow Mo^{6+} + e^- \quad . \qquad (2.1.2.\text{-}2)$$

Then the total quantity of Fe^{II} and/or Mo^{V} in the sample titrated, *i.e.*, $n(Fe^{II}{}_{tit})$ and/or $n(Mo^{V}{}_{tit})$, was calculated based on Faraday' s law:

$$n(Fe^{II}{}_{tit}) = \frac{I \times t}{F} \quad . \qquad (2.1.2.\text{-}3)$$

$$n(Mo^{V}{}_{tit}) = \frac{I \times t}{F} \quad . \qquad (2.1.2.\text{-}4)$$

The oxygen deficiency in the A_2FeMoO_{6-w} is then obtained as

$$w = \frac{n(Fe^{II}{}_{tit}) \times M(A_2FeMoO_6) - m(A_2FeMoO_{6-w})}{2m(A_2FeMoO_{6-w}) + n(Fe^{II}{}_{tit}) \times M(O)} \quad , \qquad (2.1.2.\text{-}5)$$

where $m(A_2FeMoO_{6-w})$ is the mass of the analyzed sample, and $M(A_2FeMoO_6)$ and $M(O)$ are the molecular weight of A_2FeMoO_6 and the atomic weight of oxygen, respectively. Note that the amounts of titrated Fe^{II} and Mo^{V} are equivalent, *i.e.*, $n(Fe^{II}{}_{tit})$ equals to $n(Mo^{V}{}_{tit})$, here. Moreover,

the excess reductant was not required to be added in the present titration because the amount of Fe^{II} and/or Mo^{V} is expected to satisfy in order to determine the oxygen content for the present samples. Namely, the iron/molybdenum valences are expected to be II/VI or at least they are in between II/VI and III/V in the case of A_2FeMoO_6 system. Therefore, all the amount of Fe^{II} and/or Mo^{V} in each sample is determined by coulometric titration through the oxidation reaction.

The present titrations were performed in 200 ml of 3 M HCl cell solution and all the experimental conditions and procedures were carried out in the same manner as Cu^{+}/Cu^{2+} coulometric titration. For the titration, about 25 mg of the A_2FeMoO_{6-w} samples were used for a single experiment. For every sample analysis, a pre-titration was performed by dissolving 2 ~ 3 mg of $FeCl_2{\cdot}4H_2O$ as Fe^{2+} source and applied current in order to standardize the initial redox-power of the cell. The current was applied until the potential reached 820 mV. Actual analysis of the sample was carried out immediately after a pre-titration in the same cell. The proper end-point was found at 820 mV and the applied current was fixed at 3 mA.

Fig. 2.1.2.-1 shows a typical Fe^{2+}/Fe^{3+} coulometric titration curve obtained by the present experiment. Comparing Cu^{+}/Cu^{2+} and Fe^{2+}/Fe^{3+} curvatures it is obvious that each titration step is distinguishable but dull for Fe^{2+}/Fe^{3+} titration. This tendency is quite reasonable and is resulted in smaller difference in the standard-reduction potential values between the Fe^{II}/Fe^{III} couples than Cu^{I}/Cu^{II} couples.

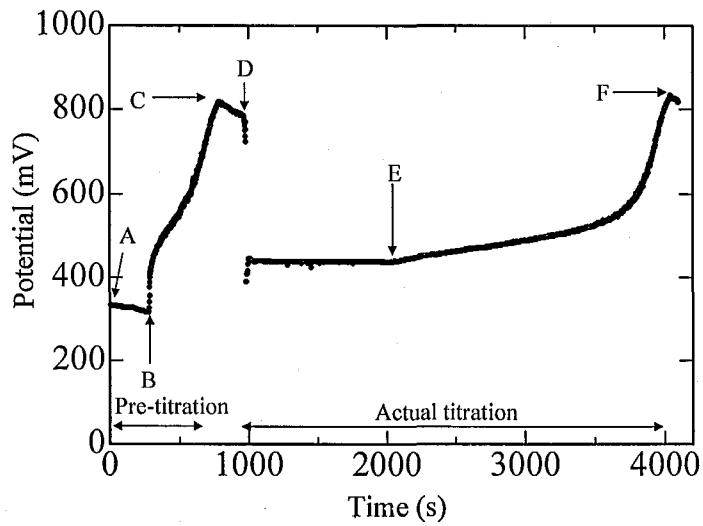

Fig. 2.1.2-1 Experimentally obtained $Fe^{2+/3+}$ coulometric titration curve. Pre-titration corresponds to points A to C and actual sample titration starts from point D. At point D, the sample is dissolved thus the cell potential decreases. After the sample is dissolved completely and cell potential is stabilized (point E), the constant dc current is applied for oxidization of Fe^{II} to Fe^{3+}/Mo^{V} to Mo^{6+} [Eqs. (2.1.2-1) and (2.1.2.-2)]. The titration is finished at point F. The titration curve is distinguishable but dull due to a small difference in the standard-reduction potential values between the Fe^{II}/Fe^{III} couples.

Since iron and molybdenum take mixed-valence states in A_2FeMoO_6, an estimation of the absolute valence value for each species is impossible from the overall-oxygen content determined by Fe^{2+}/Fe^{3+} coulometric titration. If the valence of iron increases the molybdenum valence decreases and *vice versa*.

2.2. Individual Metal Valence Analyses

Since perovskite structures often take oxygen non-stoichiometry for tuning the transition-metal valence, the oxygen non-stoichiometry and metal valence of perovskite-related compounds are correlated strongly. So far, it is known that the aliovalnet-/isovalnt-cation substitution and temperature *etc.* control the metal valence in these compounds. Furthermore, the transition metal often exhibits in distinct atomic sites resulting in different oxidation states and coordination numbers in the perovskite compounds. For example, the superconductive $CuBa_2RECu_2O_{7-\delta}$ possesses two different Cu sites, *i.e.*, Cu(1) in the charge-reservoir block and Cu(2) in the superconductive block representing different valence of Cu, respectively. In the *B*-site ordered double-pervskite A_2FeMoO_6, two transition metals of Fe and Mo take mixed valency. Thereby the determination of the overall-oxygen content is indispensable for the perovskite-related compounds but it is not sufficient. It is because the overall-oxygen content can evaluate the overall-metal valence only, whereas it can not determine each individual valence of metal at different sites/individual valence of metals with different species. Also, the oxidation state and coordination number of the transition metal are crucial role for the electromagnetic properties of the perovskite-related oxides. Thus, not only the oxygen content analysis but also the precise evaluation of individual-metal valence and its controlling are important.

2.2.1. Bond-Valence-Sum (BVS) Calculation

The BVS rule gives the correlation between the bond length and the bond valence. The concept of BVS provides us with a quantitative means by converting the detailed structure into a valence value for each structurally distinct atom. The bond valence, s_{ij}, of the bond between atom/ion i and j is calculated based on a parameter R^0_{ij} proposed by Brown [28]. The values of R^0_{ij} were empirically determined specific for each different type of i-j pairs. Calculating from the experimentally obtained bond length d_{ij} (in Å) and R^0_{ij} values, the bond valence is then obtained as

$$s_{ij} = \exp\left\{\frac{\left(R^0_{ij} - d_{ij}\right)}{0.37}\right\}, \qquad (2.2.1.\text{-}1)$$

Summing over the bond valences for all the nearest-neighbouring counter atoms/ions j gives the bond-valence sum around species i, described:

$$V_i = \pm\sum_j s_{ij} \qquad (2.2.1.\text{-}2)$$

The calculated bond-valence sum V_i represents the oxidation state of ion *i*. The BVS method allows for an estimation of the oxidation state of an ion affected by the structural environment, *i.e.*, the coordination state and the nearest-neighbouring atoms. BVS results can also be used for indicating tensile or compressive strain directed to an atom in a structure. Structural strains are indicative of the tendency of a structure to bind more oxygen or to release an oxygen atom since the strain can be influenced by changes of bond length [29].

The combination of precise structural data obtained from neutron diffraction measurements with the BVS method has been found to be the most powerful tool in order to establish the valence values for copper atoms at the $CuO_{1-\delta}$ site and the CuO_2 plane site in the $CuBa_2RECu_2O_{7-\delta}$ system [29-32]. Note that, considering not only the copper valence but also the valence of the oxygen atom in the CuO_2 plane, *i.e.* employing the following P_{BVS} parameter,

$$P_{BVS} = V_{Cu} + V_{Oa} + V_{Ob} + 2 \qquad (2.2.1.\text{-}3)$$

is important. The P_{BVS} values are obtained by summing the holes on copper and on oxygen in one CuO_2 unit. O_a and O_b indicate the oxygen atoms along the *a* and *b* axes, respectively. By employing this P_{BVS} parameter, a reasonable explanation for the T_c *versus* δ relation for the $CuBa_2RECu_2O_{7-\delta}$ system has been accomplished [32-34]. The P_{BVS} parameter must reflect the actual local hole concentration, $p(CuO_2)$, better than the value of V_{Cu} alone [33,34]. It is because the appearance of superconductivity is often associated with high-valent copper in the superconductive CuO_2 planes but the holes may also exits in oxygen or be distributed in between the copper-oxygen bond.

Although the BVS method has been studied and a lot of data based on this method have been collected, the BVS calculation may sometimes reveal somewhat shifted valence value in the absolute scale, but it is possible to consider that the calculation gives relatively comparable values within a certain system. Moreover, by detecting changes rather than absolute values of P_{BVS} with increasing dopant concentration, the more reliable estimation for the local hole concentration is believed to be obtained [32,33]. The BVS calculation for the present $CuBa_2RECu_2O_{7-\delta}$ samples were not studied and discussed in this study since the precise structural data, *i.e.* neutron diffraction data is in progress. However, a reliable structural data obtained form neutron diffraction experiments by other group was utilized for a discussion in terms of valence value of *RE* and thereby hole concentration in the CuO_2 plane(s) through the BVS method for the $CuBa_2RECu_2O_{7-\delta}$ system, in the present study. In the fully-oxygenated $CuBa_2RECu_2O_{7-\delta}$ system studied in the present work, there are two CuO_2 planes and they form pyramidal structure. Therefore, the P_{BVS} value was evaluated by developing the Eq.(2.2.1.-3) as [12]

$$\begin{aligned} P_{BVS} &= V_{Cu(2)} + V_{O(2)} + V_{O(3)} + 2 \\ &= V_{Cu(2)} + 2\,V_O + 2. \end{aligned} \qquad (2.2.1.\text{-}4)$$

Furthermore, in order to estimate bond valences in the *B*-site ordered double-perovskites, the BVS method was applied in the present study. So far, over 300 *B*-site ordered double-perovskite compounds represented in $A_2B'B''O_6$ were found and it was revealed that its physical properties are surprisingly various. This system exhibits magnetism/non-magnetism, conducting/non-conducting and shows various values of magnetic transition temperatures but successful theoretical explanations of origins for these various properties have not been provided. Thus, in order to reveal derivations of these properties, we tried to approach the problems from the structural point of view. For instance, correlations between bond valence of *B*'/*B*'' ions, other structural parameters and transition temperature value/the magnetism of *B*-site ordered double-perovskite compounds were investigated by means of statistical based multivariate data analysis. Since it was required a numerous number of reliable structural data, precise structural data in literatures obtained by neutron diffraction by many groups, were used for this analysis. For the estimation of these bond-valence values of *B*'/*B*'' constituents, BVS derived Eqs. (2.2.1.-1) and (2.2.1.-2) were applied in the present study.

2.2.2. ^{57}Fe Mössbauer Spectroscopy

The ^{57}Fe Mössbauer spectroscopy measurement enables to study the chemical environment of a distinct element with high resolution, being thus one of the most reliable measurement ways to reveal the valence state of Fe. Mössbauer spectroscopy is based on emission and absorption between the ground state and the excited state of an atom with recoilless γ radiation by a Mössbauer active nucleus [35,36]. In general, ^{57}Fe is the most widely utilized as Mössbauer active nucleus [35,36]. Mössbauer effect provides information on the local environment of the Mössbauer active nucleus in the structure since the energy levels of a nucleus depend on the surrounding lattice. The changes in the interaction between the nucleus and its environment are detected as small changes in the energies absorbed by the nucleus. The main interactions are (*i*) chemical interaction (*ii*) electric quadrupole interaction and (*iii*) magnetic hyperfine interaction. As a consequence of a change in the binding or oxidation state of the nucleus, the chemical interaction is changed and the peak positions are shifted in the spectrum. This parameter is known as an isomer shift. Isomer shift is the best parameter to judge the valence of the atom concerned. Atomic nucleus which has nuclear spin I ($I \geq 1$) shows a quadrupole moment. The energy level of the quadrupole is split by the interaction with an electric field gradient at the nucleus. This observed quadrupole splitting value is affected by the electric field gradient at the nucleus. Thus the quadrupole interaction is related to the symmetry of the nucleus and therefore is indicative of the coordination states of the nucleus. Interaction between the magnetic moment of the nucleus and the external magnetic field effective at the nucleus is seen as splitting of the energy states which thus provides information on magnetic ordering of the material [35,36]. Among the elements having a Mössbauer active nucleus, ^{57}Fe and ^{151}Eu are the most widely utilized in studying perovskite oxides [35,36].

In the present work, the valence state of iron was investigated by ^{57}Fe Mössbauer spectroscopy measurement for all the *B*-site ordered double-perovskite samples [V]. Mössbauer spectra measured at 77 K were analyzed using four spectral components for the present A_2FeMoO_{6-w} system. A typical fitted spectrum for A_2FeMoO_{6-w} is shown in Fig. 2.2.2.-1.

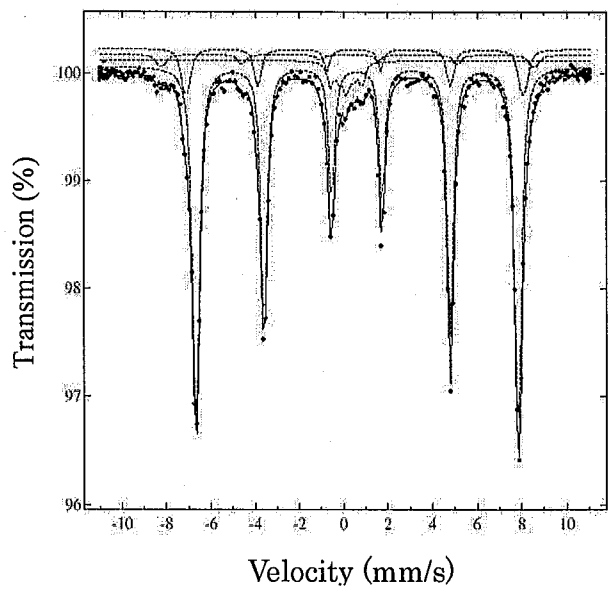

Fig. 2.2.2.-1 Typical fitted 77-K ^{57}Fe Mössbauer spectrum for an A_2FeMoO_{6-w} sample. The spectral components used in the fit are displayed above the data points. Starting from the topmost they are: M2, AS, AP, and M1 [V].

2.2.3. X-ray Absorption Near-Edge Structure (XANES) Spectroscopy

The energy region just below an absorption edge in the X-ray absorption spectrum contains information about the excitations of the inner-core electrons to the empty states in outer orbitals. Thus, it is possible to obtain the extract information on the local electronic structure of individual atoms in the structure by using this pre-edge absorption region in the XANES study. Experimentally XANES technique is commonly applied in order to reveal the oxidation state of cations so that carrier concentration is also detectible. Fe *K*- and $L_{2,3}$-edge XANES methods provide the information of oxidation state of Fe thus these techniques were utilized to reveal the valence state of Fe of the present series of samples of the A_2FeMoO_{6-w} system. A typical Fe L_3 edge XANES spectrum for the A_2FeMoO_{6-w} sample is shown in Fig. 2.2.3.-1.

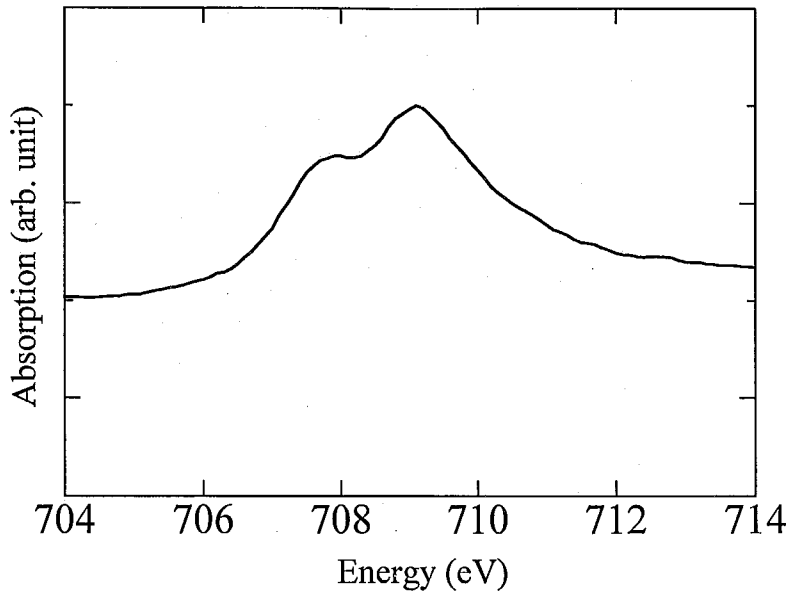

Fig. 2.2.3.-1 Typical Fe L_3 edge XANES spectrum for A_2FeMoO_{6-w} in the energy range of 704-714 eV [VI]. Two outstanding peaks can be seen at ~707 eV and at ~709 eV. Both peaks represent orbital states, *i.e.*, Fe t_{2g} and Fe e_g orbitals, respectively. Even though it is impossible to determine the absolute "number" of oxidation state for a specific atom by this technique, it is deducible that the relative correlation of valence of atom by comparing area and intensity of peaks for a series of samples. In the case of A_2FeMoO_{6-w} sample, when the contribution of Fe^{III} is stronger than that of Fe^{II} in a sample, the intensity and area of peak at ~709 eV are intensified, while those of peak at ~707 eV are weakened and *vice versa* [VI].

References

1. M. Karppinen and H. Yamauchi, *Oxygen Engineering for Functional Oxide Materials*, In: *International Book Series: Studies of High Temperature Superconductors*, Vol. 37, A.V. Narlikar (Ed.), Nova Science Publishers, New York 2001, pp. 109-143.
2. M. Karppinen, A. Fukuoka, L. Niinistö, and H. Yamauchi, *Supercond. Sci. Technol.* **9**, 121 (1996).
3. M. Karppinen, L. Niinistö, and H. Yamauchi, *J. Therm. Anal.* **48**, 1123 (1997).
4. Redox stands for reduction-oxidation. Note also that here we use Roman numerals for the valence states of atoms in a solid structure, while the charges of ions in solution are given by Arabic numerals.
5. M. Karppinen, M. Matvejeff, K. Salomäki, and H. Yamauchi, *J. Mater. Chem.* **12**, 1761 (2002).
6. A.I. Nazzal, V.Y. Lee, E.M. Engler, R.D. Jacowitz, Y. Tokura, and J.B. Torrance, *Physica C* **153-155**, 1367 (1988).
7. P. Karen and P.M. Woodward, *J. Mater. Chem.* **9**, 789 (1999).
8. G. Kawamura and M. Hiratani, *J. Electrochem. Soc.* **134**, 3211 (1987).
9. K. Kurusu, H. Takami, and K. Shintomi, *Analyst* **114**, 1341 (1989).
10. M. Karppinen, H. Yamauchi, and S. Tanaka, *J. Solid State Chem.* **104**, 276 (1993).
11. M. Karppinen, A. Fukuoka, T. Kaneko, and H. Yamauchi, *Supercond. Sci. Technol.* **6**, 265 (1993).
12. M. Karppinen and H. Yamauchi, *Mater. Sci. Eng. R* **26**, 51 (1999).
13. N. Nücker, E. Pellegrin, P. Schweiss, J. Fink, S.L. Molodtsov, C.T. Simmons, G. Kaindl, W. Frentrup, A. Erb, and G. Müller-Vogt, *Phys. Rev. B* **51**, 8529 (1995).
14. J.M. Chen, R.G. Liu, S.C. Chung, R.S. Liu, M.J. Kramer, K.W. Dennis, and R.W. McCallum, *Phys. Rev. B* **55**, 3186 (1997).
15. M. Merz, N. Nücker, E. Pellegrin, P. Schweiss, S. Schuppler, M. Kielwein, M. Knupfer, M.S. Golden, J. Fink, C.T. Chen, V. Chakarian, Y.U. Idzerda, and A. Erb, *Phys. Rev. B* **55**, 9160 (1997).
16. J.M. Chen, R.S. Liu, J.G. Lin, C.Y. Huang, and J.C. Ho, *Phys. Rev. B* **55**, 14586 (1997).
17. R.S. Liu, C.Y. Chang, and J.M. Chen, *Inorg. Chem.* **37**, 5527 (1998).
18. R.S. Liu, C.Y. Chang, J.M. Chen, and R.G. Liu, *J. Supercond.* **11**, 563 (1998).
19. J.M. Chen, R.S. Liu, P. Nachimuthu, M.J. Kramer, K.W. Dennis, and R.W. McCallum, *Phys. Rev. B* **59**, 3855 (1999).
20. A. Bianconi, M. DeSantis, A. Di Ciccio, A.M. Flank, A. Fronk, A. Fontaine, P. Legarde, H.K. Yoshida, A. Kotani, and A. Marcelli, *Phys. Rev. B* **38**, 7196 (1988).
21. J.-H. Choy, D.-K. Kim, S.-H. Hwang, and G. Demazeau, *Phys. Rev. B* **50**, 16631 (1994).
22. J. Lindén, Ph. D. Thsesis, Helsinki University of Technology, Espoo 1994, p. 41.
23. J. Lindén, J. Hietaniemi, E. Ikonen, M. Lippmaa, I. Tittonen, T. Karlemo, M. Karppinen, L. Niinistö, and K. Ullakko, *Phys. Rev. B* **46**, 8534 (1992).
24. J. Lindén, M. Lippmaa, J. Miettinen, I. Tittonen, T. Katila, A. Kareiva, M. Karppinen, L. Niinistö, J. Valo, and M. Leskelä, *Phys. Rev. B* **50**, 4154 (1994).
25. J. Lindén, M. Lippmaa, J. Miettinen, I. Tittonen, T. Katila, M. Karppinen, and L. Niinistö, *Phys. Rev. B* **50**, 16040 (1994).
26. J. Lindén, M. Lippmaa, P. Karen, A. Kjekshus, and M. Karppinen, *J. Solid State Chem.* **138**, 87 (1998).
27. J. Lindén, A. Kjekshus, P. Karen, J. Miettinen, and M. Karppinen, *J. Solid State Chem.* **139**, 168 (1998).
28. I.D. Brown, and D. Altermatt, *Acta Cryst. B* **41**, 244 (1985).
29. I.D. Brown, *J. Solid. State Chem.* **82**, 122 (1989).
30. J.D. Jorgensen, B.W. Veal, A.P. Paulikas, L.J. Nowicki, G.W. Grabtree, H. Claus, and W.K. Kwok, *Phys. Rev. B* **41**, 1863 (1990).
31. R.J. Cava, A.W. Hewat, E.A. Hewat, B. Batlogg, M. Marezio, K.M. Rabe, J.J. Krajewski, W.F. Peck Jr., and L.M. Rupp Jr., *Physica C* **165**, 419 (1990).
32. M. Karppinen, H. Yamauchi, K. Fujinami, T. Nakane, K. Peitola, H. Rundlöf, and R. Tellgren, *Phys. Rev. B* **60**, 4378 (1999).
33. M. Karppinen and H. Yamauchi, *Philos. Mag. B* **79**, 343 (1999).
34. J.L. Tallon, *Physica C* **168**, 85 (1990).
35. H. Sano, *Mössbauer spectroscopy-The applications for chemistry-*, Kodansha, Tokyo (1972). (*in Japanese*)
36. H. Sano and M. Katada, *Mössbauer spectroscopy-The bases and applications-*, Gakkai Shuppan Centre, Tokyo (1996). (*in Japanese*)

3. ENHANCEMENT IN THE H_{irr} CHARACTERISTICS OF $CuBa_2RECu_2O_{7-\delta}$

3.1. Introduction

3.1.1. Superconductive Materials

In 1986, the first superconductive copper oxide was discovered and this induced new aspects to the field of superconductive materials. Soon after the discovery of $(La_{1-x}Ba_x)_2CuO_4$ or so-called (La,Ba)-214, [1,2] the same compounds partially substituted La by Sr/Ca were discovered [3] with T_c values of 30 K, 40 K and 20 K, respectively. Even though these discoveries were scientifically very important they were not yet considered for industrial applications because of their low values of T_c. Soon $CuBa_2YCu_2O_y$ (Cu-1212) or so-called Y-123 [4] with T_c above the liquid nitrogen boiling point, *i.e.* 77 K was discovered. This discovery provided us with a breakthrough in the field of superconductivity.

Looking back the history of superconductive copper oxides it may be possible to classify into three periods. During the first period, increasing the value of T_c was the main aim for superconductive material research. In order to improve values of T_c, not only Cu-based materials but also non-copper oxides were studied. It was found that for superconductivity to occur change carrier doping in the superconductive materials was essential. During the second period, the Bi- and Tl-based homologous series of $Bi_2Sr_2Ca_{n-1}Cu_nO_y$ (n = 1, 2, ...) and $Tl_mBa_2Ca_{n-1}Cu_nO_y$ (m = 1, n = 1, 2, ...) were established [5-8] and it was somehow established that the layered structure containing CuO_2 plane(s) was essential to induce high-T_c superconductivity. Also it was reported that when the number of CuO_2 planes, n, equals to 3 or 4, the highest T_c among the members of the same superconductive series would be obtained. Moreover, single crystals of Cu-1212 and Bi-2212 by the technique of flux method and (La,Sr)-214 single crystals by the floating zone method were successfully synthesized. These discoveries enabled the studies of anisotropy of superconductivity properties, resulting in finding that superconductive copper oxides have a large electrical-magnetic anisotropy because of their layered structure. During the second period, the solid-state reaction under normal pressure was the most common synthesis technique.

During the third period that is still going on, the high-pressure synthesis method and thin film synthesis techniques have been established. The advantage of the high pressure synthesis technique is to be able to stabilize high-density but unstable phases. Moreover, through the atomic-layer-controlled thin film deposition methods, there are possibilities to obtain superconductive structures that are un-stable from the stand point of thermodynamics.

As a conclusion so-far, it has been revealed that superconductors which have

possibilities to be applied in industry are only Cu-based materials, *i.e.* $CuBa_2RECu_2O_{7-\delta}$ or Cu-1212:P system, and Bi-based homologous series. This is because among the high-T_c superconductive materials with T_c above liquid N_2 boiling point, these are the few systems that can be synthesized under normal pressure.

3.1.2. Homologous Series

All the superconductive copper oxide materials possess a layered structure including CuO_2 plane(s) except the superconductor with a ladder structure, *i.e.* $(Sr,Ca)_{14}Cu_{24}O_{41}$ [9]. In the case of the copper oxide superconductors, the superconductivity electrons are collected on the CuO_2 plane(s) and the electrons is much less along the *c* axis direction than the *ab* plane direction. Therefore, the CuO_2 plane(s) is called "superconductive block" and the other layers are called "blocking block" [10]. More than several hundred kinds of copper oxide superconductors have been discovered, all the compounds consisting of the superconductive block and the blocking block except the superconductor with the ladder structure.

There are three types of superconductive block of CuO_2 planes. Fig. 3.1.2.-1 shows the change of the local structure as a function of the number of CuO_2 plane(s), *n*. In the case of $n = 1$, O or F or Cl ion is located above and below the CuO_2 plane, resulting in a CuO_6 octahedron. This structure, *i.e.* CuO_2 plane and the upper and lower plane to CuO_2 plane (*A*O layer) is the same as that of the perovskite structure. In the case of $n = 2$, the two sheets of CuO_2 planes form the CuO_5 pyramidal structure and their bases confront each other. Therefore, one sheet which consists of metal layer (*Q* layer) exists between these two CuO_5 pyramids. For $n = 3$ case, one CuO_2 plane is inserted in the structure of that of the $n = 2$ case. Thus two *Q* layers exit in this structure. Moreover, two types of CuO_2 planes consist of this structure, *i.e.* two of pyramidal CuO_5 structures and one CuO_2 plane. When *n* increases more than four, there are (*n*-2) sheets of CuO_2 planes and (*n*-1) sheets of *Q* layers between the two of CuO_5 pyramidal structures.

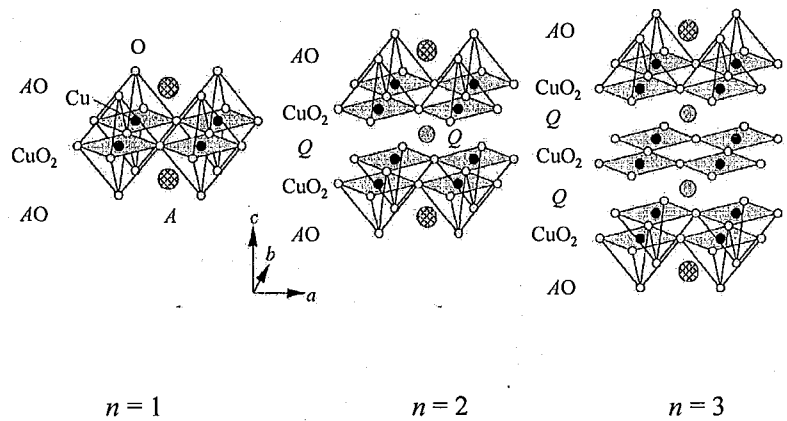

Fig. 3.1.2.-1 Local structures of the superconductive block with $n = 1 \sim 3$.

The structure of the blocking block is more complicated than that of the

superconductive block. In Fig. 3.1.2.-2, the typical structures of the blocking block are shown. The intermediate layer of the blocking block (*M*O layer) between the *A*O layer determines the structure type of the blocking block. The thickness of the blocking block affects the anisotropy of electrical-magnetic properties of the superconductor, while the local structure of the CuO_2 plane which affects the T_c value of the compound is closely related to the blocking block structure. Therefore, the constituent *M* controls the properties of superconducting materials.

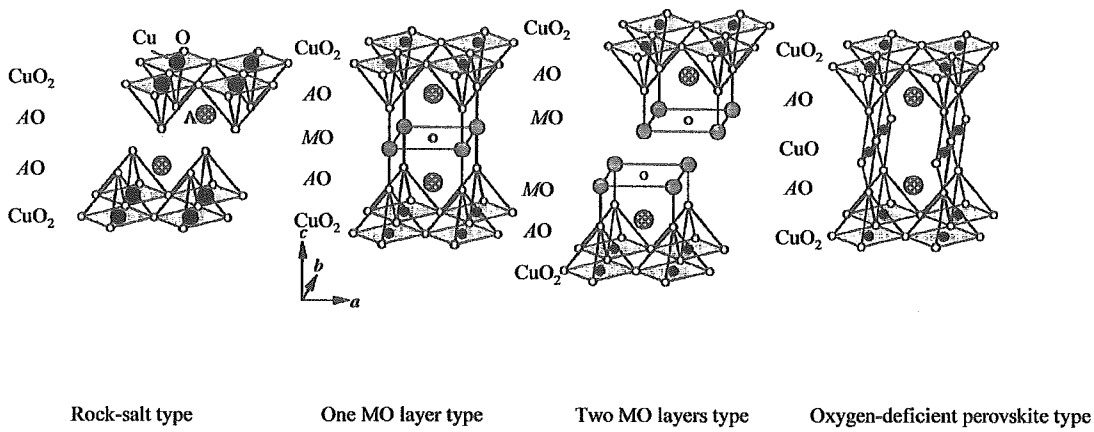

Fig. 3.1.2.-2 Typical structures of charge-reservoir block.

Based on these types of structures, it is convenient to categorize accordingly the structure types. This categorization is called "Homologous series" of superconductors. Depending on the involvement of various structural elements the existing superconductive copper-oxide phases are categorized into two main categories [11]: category-A (Fig. 3.1.2.-3(a)) contains the structures built up with oxygen-deficient-perovskite and rock-salt layers only, while the structures of category-B (Fig. 3.1.2.-3(b)) contain fluorite layers as well. In both categories, the phases as best described as members of various homologous series [12-14].

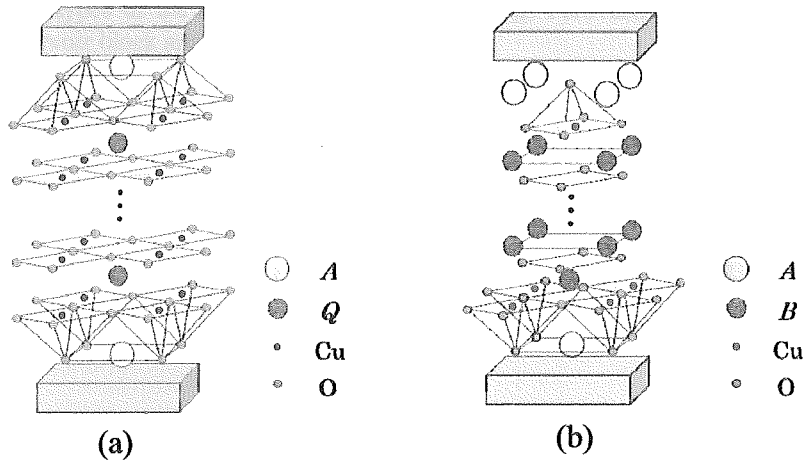

Fig. 3.1.2.-3 Schematic representations of multi-layered copper-oxide structures. (a) $M_mA_2Q_{n-1}Cu_nO_{m+2+2n\pm\delta}$ of category-A. Category-A consists of a perovskite-type block ($Q_{n-1}Cu_nO_{2n}$), two rock-salt-type layers (*A*O) and a charge-reservoir block ($M_mO_{m\pm\delta}$). (b) $M_mA_2B_sCu_2O_{m+4+2s\pm\delta}$ of category-B. Category-B is composed of two perovskite-type blocks (CuO_2), two rock-salt type layers (*A*O), a fluorite-type block ($B(O_2B)_{s-1}$) and a charge-reservoir block ($M_mO_{m\pm\delta}$) [15].

In the structures of superconductive copper oxides, an ordered-oxygen-vacancy perovskite block $Q_{n-1}Cu_nO_{2n}$ is connected to an AO layer and in most cases further to a non-stoichiometric $M_mO_{m\pm\delta}$ charge-reservoir block to form multi-layered structures with a $(MO_{1\pm\delta})_m$-AO-CuO_2-$(Q$-$CuO_2)_{n-1}$-AO, along the c axis. As schematically shown in Fig. 3.1.2.-4, the structures of the category-A phases contain alternating $M_mO_{m\pm\delta}$ charge-reservoir blocks with $mMO_{1\pm\delta}$, oxide layers (M = *e.g.* Cu, Bi, Pb, Tl, Hg, Al, Ga, C, B) and superconductive $Q_{n-1}Cu_nO_{2n}$ blocks with n CuO_2 phases and n-1 Q metal layers. The $M_mO_{m\pm\delta}$ and $Q_{n-1}Cu_nO_{2n}$ blocks are separated from each others by a single AO layer that the stoichiometry of the phase is given by $M_mA_rQ_{n-1}Cu_nO_{m+r+2n\pm\delta}$. Each $M_mA_rQ_{n-1}Cu_nO_{m+r+2n\pm\delta}$ phase is denoted in an unambiguous way by M-$m^{(A)}r^{(Q)}(n$-1$)n[X]$:RS/P, where RS/P stands for the crystallographic structure of the charge-reservoir block, either rock-salt type or perovskite type. The possible halogen-substituent X is induced by [X]. However, the well-established shorter scheme, *i.e.* M-$mr(n$-1$)n$, to refer to the $M_mA_rQ_{n-1}Cu_nO_{m+r+2n\pm\delta}$ phases, is commonly used as a expression of chemical formulae in category-A [15].

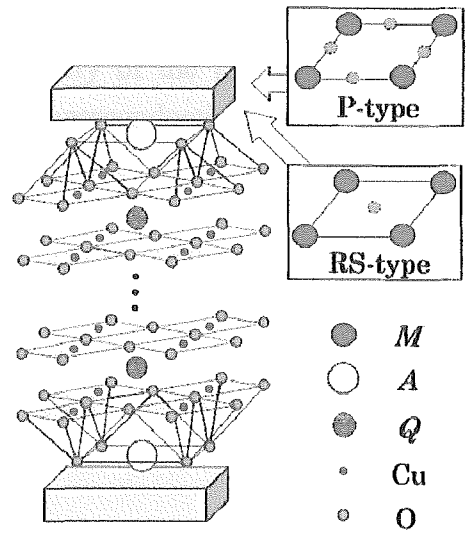

Fig. 3.1.2.-4 Structure types of the charge-reservoir block, $MO_{1\pm\delta}$. Perovskite and rock-salt types. The oxygen atoms in the charge-reservoir block are removable [15].

In Table 3.1.2.-1, the multi-layered copper-oxide structures of category-A, *i.e.* M-$mr(n$-1$)n$ copper-oxide structures together with some representative compounds are arranged in order of increasing m (0~3), r (1~2) and n (1~4). Note that, as far as the structures known to exist at the moment are concerned the table could be continued up to n = 8 [15].

Table 3.1.2.-1 Multi-layered copper-oxide structures of category-A, *i.e.*, $M_mA_rQ_{n-1}Cu_nO_{m+r+2n\pm\delta}$ or *M-mr*(*n*-1)*n*, together with representative compounds [15].

01(*n*−1)*n*	02(*n*−1)*n*	M-12(*n*−1)*n*	M-22(*n*−1)*n*	M-32(*n*−1)*n*
0101 $LaCuO_3$	0201 $(La,Sr,Ba)_2CuO_4$ Sr_2CuO_4 $Sr_2CuO_2F_2$	M-1201 $HgBa_2CuO_4$:RS $Tl(Ba,Y)_2CuO_5$:RS	M-2201 $Bi_2Sr_2CuO_6$:RS $Tl_2Ba_2CuO_6$:RS	M-3201 $(Pb_{2/3}Cu_{1/3})_3(Sr,La)_2CuO_6$:P
0112 $(Ba,La)Y(Cu,Fe)_2O_5$	0212 $La_2SrCu_2O_6$ $Sr_2CaCu_2O_6$ $Ba_2CaCu_2O_6$ $Sr_2CaCu_2O_4F_2$	M-1212 $HgBa_2CaCu_2O_6$:RS $TlBa_2CaCu_2O_7$:RS $CuBa_2YCu_2O_7$:P	M-2212 $Bi_2Sr_2CaCu_2O_8$:RS $Tl_2Ba_2CaCu_2O_8$:RS	M-3212 $(Pb_{2/3}Cu_{1/3})_3Sr_2(Y,Ca)Cu_2O_8$:P
	0223 $Sr_2Ca_2Cu_3O_8$ $Ba_2Ca_2Cu_3O_8$ $Sr_2Ca_2Cu_3O_6F_2$	M-1223 $HgBa_2Ca_2Cu_3O_8$:RS $TlBa_2Ca_2Cu_3O_9$:RS $CuBa_2Ca_2Cu_3O_8$:P	M-2223 $Bi_2Sr_2Ca_2Cu_3O_{10}$:RS $Tl_2Ba_2Ca_2Cu_3O_{10}$:RS	M-3223 $(Cu,C,Ba)_3Ba_2Ca_2Cu_3O_9$:P
	0234 $Sr_2Ca_3Cu_4O_{10}$ $Ba_2Ca_3Cu_4O_{10}$	M-1234 $HgBa_2Ca_3Cu_4O_{10}$:RS $TlBa_2Ca_3Cu_4O_{11}$:RS $CuBa_2Ca_3Cu_4O_{10}$:P	M-2234 $Tl_2Ba_2Ca_3Cu_4O_{12}$:RS	M-3234 $(Cu,C,Ba)_3Ba_2Ca_3Cu_4O_{11}$:P

Soon after the discovery of the first high-T_c copper-oxide, $(La,Ba)_2CuO_4$ (0201 or so-called "*T*") phase, another superconductive phase with a "214" stoichiometry was discovered by replacing La by Nd and Ba by (Sr,Ce), *i.e.* $(Nd,Sr,Ce)_2CuO_4$ [16]. As illustrated in Fig. 3.1.2.-5, the multi-layered structure of $(Nd,Sr,Ce)_2CuO_4$ with a layer sequence, CuO_2(P)-[(Nd,Ce)-O_2-(Nd,Ce)](F)-CuO_2(P)-[(Sr,Nd)O-(Sr,Nd)O](RS), contains, besides the two types of structural elements constructing the category-A phases, *i.e.* P and RS, also a third structural element, *i.e.* the fluorite structure F adapted by *e.g.* CeO_2. This "214" phase was called as the "*T**" phase. Later the third "214" structure, named the "*T*'" phase, was obtained for a $(Nd,Ce)_2CuO_4$ compound [17].

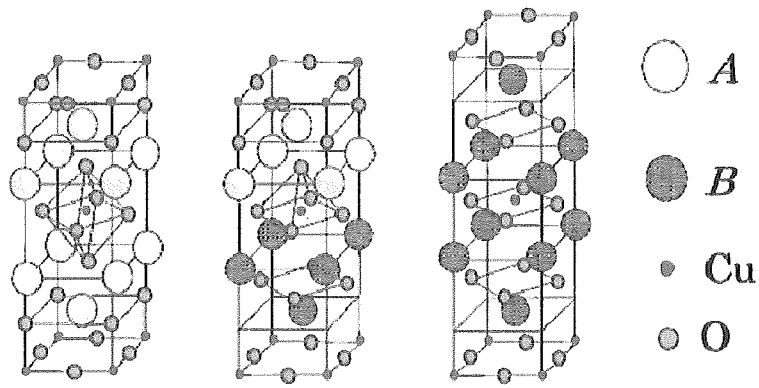

Fig. 3.1.2.-5 The *T*-, *T**- and *T*'- structures of $(La,Ba)_2CuO_4$, $(Nd,Sr,Ce)_2CuO_4$ and $(Nd,Ce)_2CuO_4$, respectively [15].

Copper-oxide structures containing a fluorite block $B(O_2B)_{s-1}$ are defined to form category-B [11]. All the category-B phases obey a general formula, $M_mA_{2k}B_sCu_{1+k}O_{m+4k+2s}$ where

$m = 0, 1, 2, 3, \ldots$, $s \geq 1$ and $k = 0$ or 1, with the conditions that for $k = 0$, $m = 0$ and for $k = 1$, $m \geq 0$ [12-14]. A phase obeying the $M_mA_{2k}B_sCu_{1+k}O_{m+4k+2s}$ formula is denoted by M-$m(2k)s(1+k)$. Examples of the systematic naming of various representative category-B phases are given in Table 3.1.2.-2. The naming schemes for the both categories, A and B, are consistent at common limits, *i.e.* the phases with $s = 1$ including the infinite-layer phase as a 0011 structure.

Table 3.1.2.-2 Schematic names for representative layered copper-oxides of category-B [15].

Formula	Trivial name	Systematic name
$(Sr,Nd)CuO_2$	infinite-layer phase	0011
$(Nd,Ce)_2CuO_4$	T′	0021
$(Nd,Sr,Ce)_2CuO_4$	T*	0222
$(Pb,Cu)(Sr,Eu)_2(Eu,Ce)_2Cu_2O_9$	–	(Pb,Cu)-1222
$Cu(Ba,Eu)_2(Eu,Ce)_2Cu_2O_9$	223 or 446	Cu-1222
$Bi_2Sr_2(Gd,Ce)_2Cu_2O_{10}$	–	Bi-2222
$(Pb_{2/3}Cu_{1/3})_3Sr_2(Eu,Ce)_2Cu_2O_{11}$	–	$(Pb_{2/3}Cu_{1/3})$-3222
$(Pb,Cu)Sr_2(Ho,Ce)_3Cu_2O_{11}$	–	(Pb,Cu)-1232

3.1.3. Hole-Doping Routes

In the $M_mA_2Q_{n-1}Cu_nO_{m+2+2n\pm\delta}$ phase in general, as previously mentioned in section 2.2.1., the P_{BVS} values as calculated according to Eqs. 2.2.1.-1, 2.2.1.-2 and 2.2.1.-3, only the out-of-plane bonds from Cu to the apical oxygen, O_{api}, and from the in-plane O to cations A and Q have contributions to the hole concentration in the CuO_2 plane.

For an octahedral CuO_2 plane, in the case of CuO_2 plane number, $n = 1$, P_{BVS} is calculated by [15]:

$$\begin{aligned} P_{BVS} &= V_{Cu} + 2\,V_O + 2 \\ &= 2\,s_{Cu\text{-}Oapi} + 4\,s_{Cu\text{-}O} - 2\,(2\,s_{Cu\text{-}O} + 4\,s_{A\text{-}O}) + 2 \\ &= 2\,s_{Cu\text{-}Oapi} - 8\,s_{A\text{-}O} + 2. \end{aligned} \qquad (3.1.3.\text{-}1)$$

For a pyramidal CuO_2 plane of the $n = 2$ phase and an outermost CuO_2 plane of the $n \geq 3$ phase, P_{BVS} is given by:

$$\begin{aligned} P_{BVS} &= V_{Cu} + 2\,V_O + 2 \\ &= s_{Cu\text{-}Oapi} + 4\,s_{Cu\text{-}O} - 2\,(2\,s_{Cu\text{-}O} + 2\,s_{A\text{-}O} + 2\,s_{Q\text{-}O}) + 2 \\ &= s_{Cu\text{-}Oapi} - 4\,s_{A\text{-}O} - 4\,s_{Q\text{-}O} + 2. \end{aligned} \qquad (3.1.3.\text{-}2)$$

For a square-planar CuO_2 plane, *i.e.* the inner planes of the $n \geq 3$ phase, P_{BVS} is given by:

$$\begin{aligned} P_{BVS} &= V_{Cu} + 2\,V_O + 2 \\ &= 4\,s_{Cu\text{-}O} - 2\,(2\,s_{Cu\text{-}O} + 4\,s_{Q\text{-}O}) + 2 \\ &= -8\,s_{Q\text{-}O} + 2. \end{aligned} \qquad (3.1.3.\text{-}3)$$

According to these observations, there are three different distinguishable ways of increasing the hole-doping level of a CuO_2 plane as illustrated in Fig. 3.1.3.-1 [18,19]: (*i*) shortening the Cu-O_{api} bond, *i.e.* hole-doping route Π(1), (*ii*) lengthening the effective O-*A* bond, *i.e.* hole-doping route Π(2), and (*iii*) lengthening the effective O-*Q* bond, *i.e.* hole-doping route Π(3). It is important to note that not only the bond length d_{ij} but also the corresponding R^0_{ij} value contribute to the "effective" length of a bond. Moreover, the R^0_{ij} value for an O-*A*/*Q* bond depends on both the valence and size of the cation *A*/*Q*. Therefore, not only the valence but also the size of the cation *A*/*Q* affects the hole-doping level of the CuO_2 plane. Replacing the *A*/*Q* site for an isovalent cation but with a smaller ionic radius the change would decrease the R^0_{ij} value of the O-*A*/*Q* bond. Note that the changes in the effective bond length, *i.e.* $(d_{ij} - R^0_{ij})$, depends on the rigidity of the structure. In the case the structure is rigid enough to resist against the decrease in the bond length d_{ij}, the value of $(d_{ij} - R^0_{ij})$ and thereby the hole concentration of the CuO_2 plane increase.

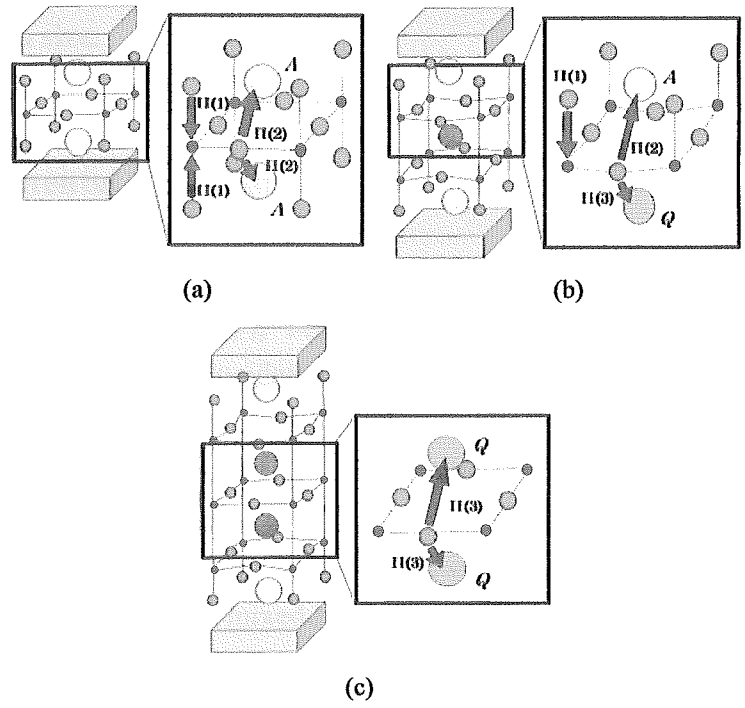

Fig. 3.1.3.-1 (a) Hole-doping routes, Π(1) and Π(2), into the CuO_2 plane in the *M*-*m*201 structure. When the out-of-plane O atom approaches towards the in-plane Cu atom holes are introduced through route Π(1), and also through Π(2) if the effective distance between the in-plane O atom and *A* atom increases. (b) Hole-doping routes, Π(1), Π(2) and Π(3), into the CuO_2 plane in the *M*-*m*212 structure. Holes are introduced through route Π(1) when the out-of-plane O atom approaches towards the in-plane Cu atom, through Π(2) as the effective distance between the in-plane O atom and *A* atom increases, and also through Π(3) if the effective distance between the in-plane O atom and *Q* atom increases. (c) Hole-doping route, Π(3), into the inner CuO_2 plane in the *M*-*m*223 structure. As the effective distance between the in-plane O atom and *Q* atom increases, holes are introduced through Π(3) [15].

3.1.4 Irreversibility Characteristics of High-T_c Superconductors

The irreversibility-field line, $H_{irr}(T)$, is a boundary between the magnetically reversible

region ($J_c = 0$) and the irreversible region ($J_c \neq 0$) in the H_{irr}-*vs*-T phase diagram. The absolute values of H_{irr} depend on the experimental apparatus, measurement method, analysis method and H_{irr} determination criteria *etc*. Thus, when comparing the absolute values of H_{irr} among different sample systems, it is required to fix them. Since the magnetization of magnetic-related compounds is influenced by "the magnetic relief time", even the measurement rate should be fixed. It is also because the value of H_{irr} is affected by the vortex creep that depends on the measurement rate, *i.e.* vortex invasion rate.

It is very crucial to keep the grain size constant when the H_{irr} characteristics are determined since J_c *via* Bean's model is applied in the present work and the model depends on the size of the grains. Although the Bean's model standardizes the grain size among the samples when it determines the absolute values of J_c, the grain-size standardization affects just the figure. Determination of J_c values for samples with various grain sizes is worthless even though the grain-size effect among the samples is taken into account by using Bean's model. Therefore, in order to compare the H_{irr} characteristics *via* Bean's model, it is needed to synthesize samples with the same grain size.

3.2. Experimental Procedure

The fully-oxygenated $CuBa_2RECu_2O_{7-\delta}$ sample series, *i.e.*, *RE* = Eu, Gd, Y, $Yb_{0.6}Y_{0.4}$, $Yb_{0.8}Y_{0.2}$, Yb, $Y_{0.18}Lu_{0.82}$, $Yb_{0.9}Lu_{0.1}$, $Yb_{0.8}Lu_{0.2}$, $Yb_{0.7}Lu_{0.3}$ and $Yb_{0.6}Lu_{0.4}$ were synthesized by solid-state reaction in order to elucidate the dependence of the H_{irr} characteristics on the ionic radius of the rare-earth element [20]. Since the method of solid state reaction is the most conventional and popular method for synthesizing high-T_c superconductors and other ceramics, the present $CuBa_2RECu_2O_{7-\delta}$ samples were synthesized by this technique. RE_2O_3, $BaCO_3$ and CuO mixture of high-purity (99.9 or 99.99 %) powders were selected as cation sources in this study. The starting materials were mixed into the atomic ratio *RE*:Ba:Cu = 1:2:3 and the obtained powder mixture was sintered (first sintering). After the first sintering, the samples were reground and the powders were pressed into pellets. The pellets were sintered again (second sintering) in the oxygen atmosphere in order to obtain fully-oxygenated samples. The precise sintering conditions are shown in Table 3.2.-1. The absolute values of the oxygen content were determined by the $Cu^{+/2+}$ coulometric titration method. Throughout the careful controlled oxygen annealing, all the samples possess fixed level of the oxygen contents, *i.e.*, 7-δ ranging from 6.91 to 6.94 (except for the sample with *RE* = Gd).

Table 3.2.-1 Synthesis conditions of a series of fully-oxygenated $CuBa_2RECu_2O_{7-\delta}$ samples.

RE	Ionic radius (Å)	Sintering (in Air)	Oxygen annealing	Oxygen content 7 - δ
Eu	1.066	950°C,120h	350°C, 48h	6.94
Gd	1.053	900°C, 24h	400°C, 48h	6.98
		910°C, 12h	350°C, 48h	
Y	1.019	900°C, 24h	350°C, 48h	6.93
		905°C, 24h		
		905°C, 24h		
$Y_{0.4}Yb_{0.6}$	0.999	900°C, 12h	350°C, 48h	6.93
$Y_{0.2}Yb_{0.8}$	0.992	900°C, 12h	350°C, 48h	6.91
Yb	0.985	900°C, 24h	350°C, 48h	6.93
		905°C, 24h		
		905°C, 24h		
$Y_{0.18}Lu_{0.82}$	0.985	900°C, 24h	400°C, 48h	6.93
			350°C, 48h	
$Yb_{0.9}Lu_{0.1}$	0.984	900°C, 12h	400°C, 48h	6.92
			350°C, 48h	
$Yb_{0.8}Lu_{0.2}$	0.983	900°C, 12h	400°C, 48h	6.94
			350°C, 48h	
$Yb_{0.7}Lu_{0.3}$	0.983	900°C, 12h	400°C, 48h	6.91
			350°C, 48h	
$Yb_{0.6}Lu_{0.4}$	0.982	900°C, 12h	400°C, 48h	6.92
			350°C, 48h	

In the present work the magnetic property measurements were performed by a dc SQUID magnetometer (Quantum Design MPMSR-5S). For the present $CuBa_2RECu_2O_{7-\delta}$ samples, the T_c value is estimated by measuring the magnetic susceptibility (χ) as a function of temperature. The method to measure the susceptibility as a function of the temperature by a SQUID magnetometer consists of the zero-field-cooling and field-cooling measurements. In the zero-field-cooling method the superconductor is first cooled below its T_c and then the magnetic field is applied. Thus volume fraction of the superconductor is estimated larger than the true one. On the other hand, in the field-cooling method the magnetic field is applied before the superconductor is cooled below the T_c. Therefore, the volume fraction of the superconductor is estimated smaller than the true one. Consequently the true volume fraction of the superconductor is in between the values revealed from the zero-field-cooling and field-cooling measurements. In the present work the temperature-dependence of magnetic susceptibility was measured for pelletized samples under a fixed external field (H) of 10 Oe from room temperature down to 5 K. The "effective" superconductivity transition temperature, $T_c^{(e)}$, value for each sample was estimated by extrapolating the obtained diamagnetic portion of the χ-*vs*-T curves to the χ= 0 level [21]. This $T_c^{(e)}$ value is somewhat lower than the onset temperature of the Meissner signal, that is commonly referred to as the T_c value. The $T_c^{(e)}$ values are almost the same with the T_c

values estimated from the curve fitting of measured χ-*vs*-T curves [21,22].

The irreversibility-field line, $H_{irr}(T)$, has been determined by several techniques [23,24] so far. In the present study, the M-*vs*-H curve were measured for H up to 5 T then the H_{irr} value was determined from the magnetization (M)-*vs*-H curve as the limit of H where the hysteresis in the difference of magnetization, ΔM, becomes zero:

$$H_{irr} = H\,(\Delta M \rightarrow 0)\,. \qquad (3.2.\text{-}1)$$

Actually, the following relationship that satisfies the definition was employed [25]:

$$\log H = \log H_{irr} + b\,\Delta M\,. \qquad (3.2.\text{-}2)$$

The values of parameters, H_{irr} and b, were determined by a least-square method applied to the experimental plot of log H-*vs*-ΔM. Note that, the ΔM data points which correspond to J_c values in the range of 500 to 1000 A/cm^2 (according to Bean's model) were employed in this procedure. Moreover, to be able to compare the H_{irr} characteristics of different superconductors, the experimentally measured irreversibility-field lines are typically plotted against the reduced temperature, $1\text{-}T/T_c$.

In the magnetization measurements, the sample amount was kept relatively large and essentially constant, *i.e.* at 350 ± 10 mg in order to obtain sufficient magnetization signal. The sufficient magnetization signal enables to avoid the deviation in the measured magnetization values due to the difference in the sample mass.

For the study of H_{irr} characteristics of $CuBa_2RECu_2O_{7-\delta}$ samples, it is very crucial to fix the grain size since J_c *via* Bean's model is applied and the model strongly depends on the size of the grains. Although the Bean's model standardizes the grain size among the samples when it determines the absolute values of J_c, the grain-size standardization affects just the figure. Determination of J_c values for samples with various grain sizes is worthless even though the grain-size effect among the samples is taken into account by using Bean's model. Therefore, in order to compare the H_{irr} characteristics *via* Bean's model, it is needed to synthesize samples with the same grain size. Besides, the homogeneity of the oxygen content from grain to grain is another essential requirement for the precise estimation of H_{irr} characteristics. If the grains have different particle sizes, the oxygen content may vary among the grains within the same sample and it is worthless to confirm the H_{irr} characteristics because the absolute value of H_{irr} is strongly affected by the oxygen content.

Thus to confirm the particle size and to check whether the sample grains are melt-grown or not, the field-emission scanning electron micrographs (SEM; Hitachi FE-SEM S-45500) with EDS were taken for the $CuBa_2RECu_2O_{7-\delta}$ samples at an accelerated voltage of 15 kV. From these observations, the longest distance of each grain was determined as a grain size of one particle since the anisotropic of grain size is stronger for the superconductive compound.

The average of grain size was determined at 3.0±0.5 μm for a series of $CuBa_2RECu_2O_{7-\delta}$ samples thus it is reasonable to assume that all the grains had the same oxygen content.

Moreover, for the observation of the crystal microstructure and twinning, and to reveal the existence of possible atomic disorder or concentration modulation in the crystal structure, transmission electron microscopy (TEM; HITACHI H-9000NAR) was performed at an accelerating voltage of 300 kV for $CuBa_2RECu_2O_{7-\delta}$ samples. The observations of particles, electron diffraction and high resolution observations were performed.

3.3. Results and Discussion

Through a study in the influence of oxygen content on the H_{irr} characteristics, the importance of the oxygen content of the samples on the H_{irr} characteristics was clearly revealed. With increasing the oxygen content, the superb H_{irr} characteristics were obtained for the $CuBa_2RECu_2O_{7-\delta}$ (*RE* = Gd, Yb) system. Since the fully-oxygenated samples possess superior H_{irr} characteristics, the oxygen content was fixed at full for the study aiming at clarifying the *RE* size-only-dependent effects, *i.e.* isovalent-cation-substitution effects on the H_{irr} characteristic. A systematic study on the $CuBa_2RECu_2O_{7-\delta}$ sample series (*RE* = Eu, Gd, Y, $Yb_{0.6}Y_{0.4}$, $Yb_{0.8}Y_{0.2}$, Yb, $Y_{0.18}Lu_{0.82}$, $Yb_{0.9}Lu_{0.1}$, $Yb_{0.8}Lu_{0.2}$, $Yb_{0.7}Lu_{0.3}$ and $Yb_{0.6}Lu_{0.4}$) with an oxygen content fixed at full is reported in this chapter.

3.3.1. Confirmations of Synthesized Samples

Fig. 3.3.1.-1 shows the XRD patterns of the fully-oxygenated $CuBa_2RECu_2O_{7-\delta}$ samples with various *RE* constituents. From the XRD data, it was found that with decreasing the ionic radius of *RE*, $r(RE^{III})$, it became more difficult to obtain the $CuBa_2RECu_2O_{7-\delta}$ phase in a single-phase form. For the samples with the $r(RE^{III})$ smaller than that of Yb, small amounts of impurity phases of RE_2BaCuO_5 and $BaCuO_2$ were detected. It has been reported that with the smallest *RE*'s, *e.g.* Yb or Lu, the mechanism of $CuBa_2RECu_2O_{7-\delta}$ phase formation is different from that of the conventional $CuBa_2YCu_2O_{7-\delta}$. Since the $CuBa_2RECu_2O_{7-\delta}$ phase with smaller *RE*'s forms nucleus of RE_2BaCuO_5 and $BaCuO_2$ first then superconductive phase forms, the RE_2BaCuO_5 phase is detected even when applying synthesis temperatures lower than the appropriate synthesis temperature [26,27]. Furthermore, it has been reported that the smallest *RE*'s can not form the $CuBa_2RECu_2O_{7-\delta}$ phase since with the too small *RE* the lattice is extremely highly strained [28]. In terms of polycrystalline $CuBa_2LuCu_2O_{7-\delta}$, a number of research groups found that they could not obtain the single-superconductivity phase [20,29-35]. An extensive investigation on the phase diagram of $CuBa_2LuCu_2O_{7-\delta}$ has been reported and the study claims that the $CuBa_2LuCu_2O_{7-\delta}$ phase can not form in the polycrystalline samples [36] owing to the existence of a lower limit of the $r(RE^{III})$ that the $CuBa_2RECu_2O_{7-\delta}$ structure can be

tolerated [34,35]. Also, the synthesis difficulty of $CuBa_2LuCu_2O_{7-\delta}$ was ascribed to the very low peritectic melting temperature of this compound [37]. On the other hand, a single-crystal specimen of $CuBa_2LuCu_2O_{7-\delta}$ compound with T_c value of 90 K [38] was reported. The stabilization of the $CuBa_2LuCu_2O_{7-\delta}$ phase in single-crystal form may be due to the enhanced temperature, *i.e.*, about 100 to 200 °C higher than the sintering temperature of bilk samples, and the extremely off-nominal starting composition, *e.g.*, Lu:Ba:Cu = 1:23:9 [29]. $CuBa_2LuCu_2O_{7-\delta}$ single crystals were also obtained by the flux method in alumina crucibles [39] with a mixture containing the stoichiometric $CuBa_2LuCu_2O_{7-\delta}$ powder and flux components, *i.e.*, BaO and CuO. After the heat treatment, the crystal was slowly cooled at a constant rate of 4-10 °C a day in the temperature interval 960-870 °C with subsequent decanting of the residual flux. The obtained crystals oxygenated in flowing oxygen at 475 °C exhibited T_c value of 90.0-90.5 K with ΔT_c = 0.2-0.4 K and the resistivity value in the *ab* plane implied the characteristics of high-quality single-crystals. Single phase $CuBa_2LuCu_2O_{7-\delta}$ thin-epitaxial films were recently obtained by PLD [40,41] and MOCVD [42] methods. A single phase of the polycrystalline $CuBa_2Y_{1-x}Lu_xCu_2O_{7-\delta}$ sample exhibiting the T_c value in a range of 92.1 to 86.7 K was synthesized up to $x \leq 0.5$ through a solid-state reaction method [32]. Pure $CuBa_2Y_{1-x}Lu_xCu_2O_{7-\delta}$ samples were successfully yielded up to $x \leq 0.75$ (T_c = 88 ~ 89 K) by adding 8 % of excess copper in the initial starting composition [34]. Furthermore, partial substituting Ca for Lu stabilizes the superconducting phase. $CuBa_2Lu_{1-x}Ca_xCu_2O_{7-\delta}$ for example, the superconductivity phase is mainly obtained due to Ca with x = 0.1 composition although sample contains a small amount of impurity phases. On the other hand, Ca rich sample such as x = 0.4 again contains impurity phases implying the solubility limit of Ca in this system. Intermediate compositions such as $x \approx 0.3 \sim 0.4$ were reported to be free from impurities [28].

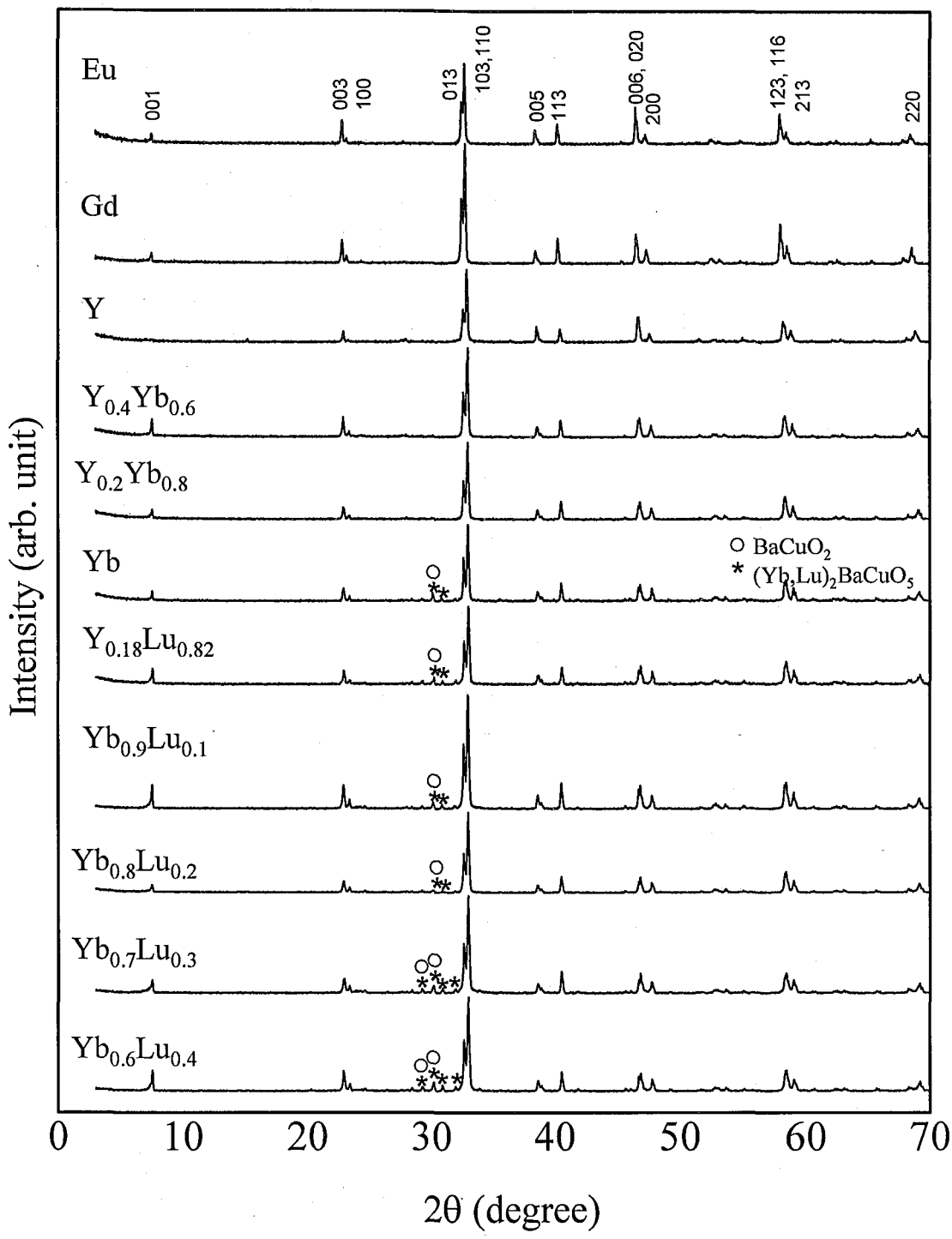

Fig. 3.3.1.-1 XRD patterns for the $CuBa_2RECu_2O_{7-\delta}$ ($6.91 \leq 7-\delta \leq 6.94$) samples. All the patterns were obtained after the oxygen annealings.

It has been believed that the RE_2BaCuO_5 phase appears when the applied synthesis temperature is higher than the optimum temperature, while $BaCuO_2$ forms when the synthesis temperature is lower than the optimum synthesis temperature. However, from the experimental facts in present study the situation in reality may be more complicated. Fig. 3.3.1.-2 shows the XRD patterns of the $CuBa_2(Yb_{0.6}Lu_{0.4})Cu_2O_{7-\delta}$ samples synthesized at various temperatures. The optimum temperature for synthesizing this sample was determined at 900 °C, in this work. However, in the XRD patterns, $(Yb,Lu)_2BaCuO_5$ and $BaCuO_2$ are detected even at higher and

lower temperatures than the optimum synthesis temperature. For the $CuBa_2(Yb_{0.6}Lu_{0.4})Cu_2O_{7-\delta}$ sample synthesized at 890 °C the detected impurity phases were $(Yb,Lu)_2BaCuO_5$, $BaCuO_2$ and very small amount of CuO. On the other hand, at 910 °C, in spite of the fact that the temperature was higher than the optimum temperature, both $(Yb,Lu)_2BaCuO_5$ and $BaCuO_2$ were detected as impurity phases.

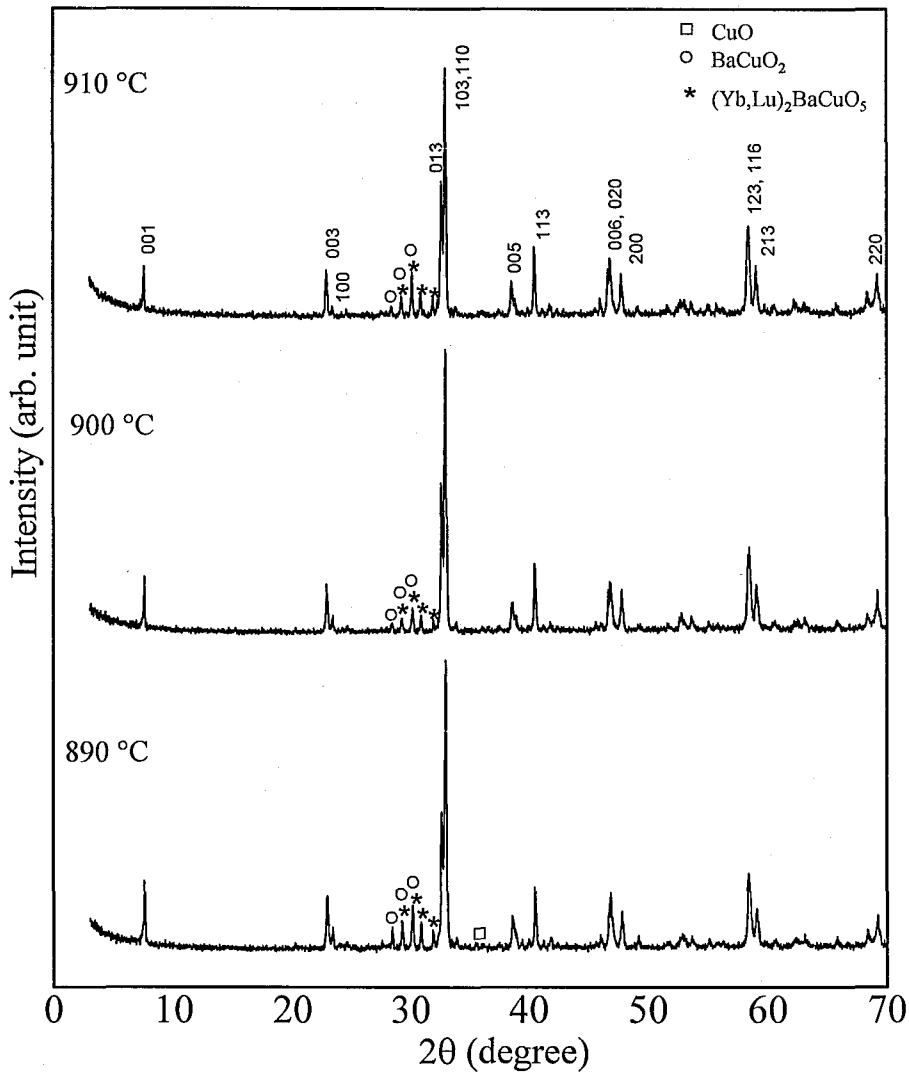

Fig. 3.3.1.-2 XRD patterns for the as-synthesized $CuBa_2(Yb_{0.6}Lu_{0.4})Cu_2O_{7-\delta}$ samples heated at various temperatures.

Fig. 3.3.1.-3 shows the XRD patterns of the $CuBa_2(Yb_{1-x}Lu_x)Cu_2O_{7-\delta}$ (x = 0.5, 0.6 and 1.0) samples. The main phase in the sample with x = 0.5 is the superconductive phase but it includes larger amounts of the impurity phases of $(Yb,Lu)_2BaCuO_5$ and $BaCuO_2$, than the $CuBa_2(Yb_{0.6}Lu_{0.4})Cu_2O_{7-\delta}$ sample. However, the synthesis temperatures of both *RE* = $Yb_{0.5}Lu_{0.5}$ and $Yb_{0.6}Lu_{0.4}$ samples were the same, *i.e.* 900 °C. Moreover, Lu content increases more, *i.e.* in the case of the sample with x = 0.6, the superconductive phase is not the main phase any longer. The dominant phases of this sample were $(Yb,Lu)_2BaCuO_5$ and $BaCuO_2$. Furthermore, as shown in Fig. 3.3.1.-3 a $CuBa_2LuCu_2O_{7-\delta}$ sample was synthesized for revealing the synthesis limit of a

superconductive phase in terms of $r(RE^{III})$. The obtained sample was multi-phasic containing $(Yb,Lu)_2BaCuO_5$ phase, $BaCuO_2$, LuO and BaO.

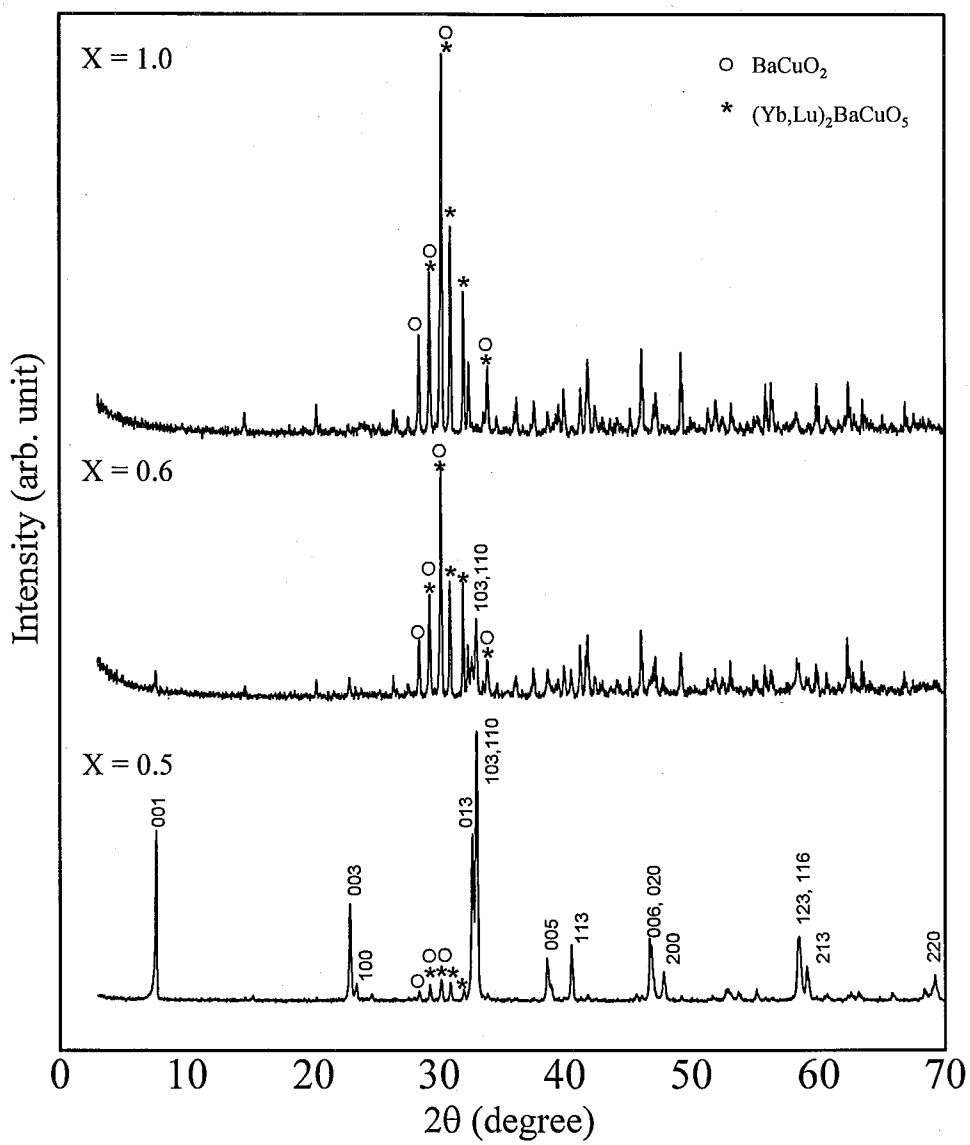

Fig. 3.3.1.-3 XRD patterns for the as-synthesized $CuBa_2(Yb_{1-x}Lu_x)Cu_2O_{7-\delta}$ samples with various Lu concentrations.

In Fig. 3.3.1.-4, the *a* and *b* lattice parameters of $CuBa_2RECu_2O_{7-\delta}$ show lanthanide contraction tendency linearly, only down to *RE* = Yb, while for the Yb/Lu samples the lanthanide contraction seems to be saturated. The *c* axis behaviour is supposed to be complicated since with decreasing $r(RE^{III})$, *c* axis is shortened due to smaller *RE* but at the same time, *c* axis is affected very sensitively by the oxygen content. These two factors, *i.e.*, *RE* size and oxygen content determine the length of the *c* axis. It was thus considered that the results of *c* lattice parameter are reasonable.

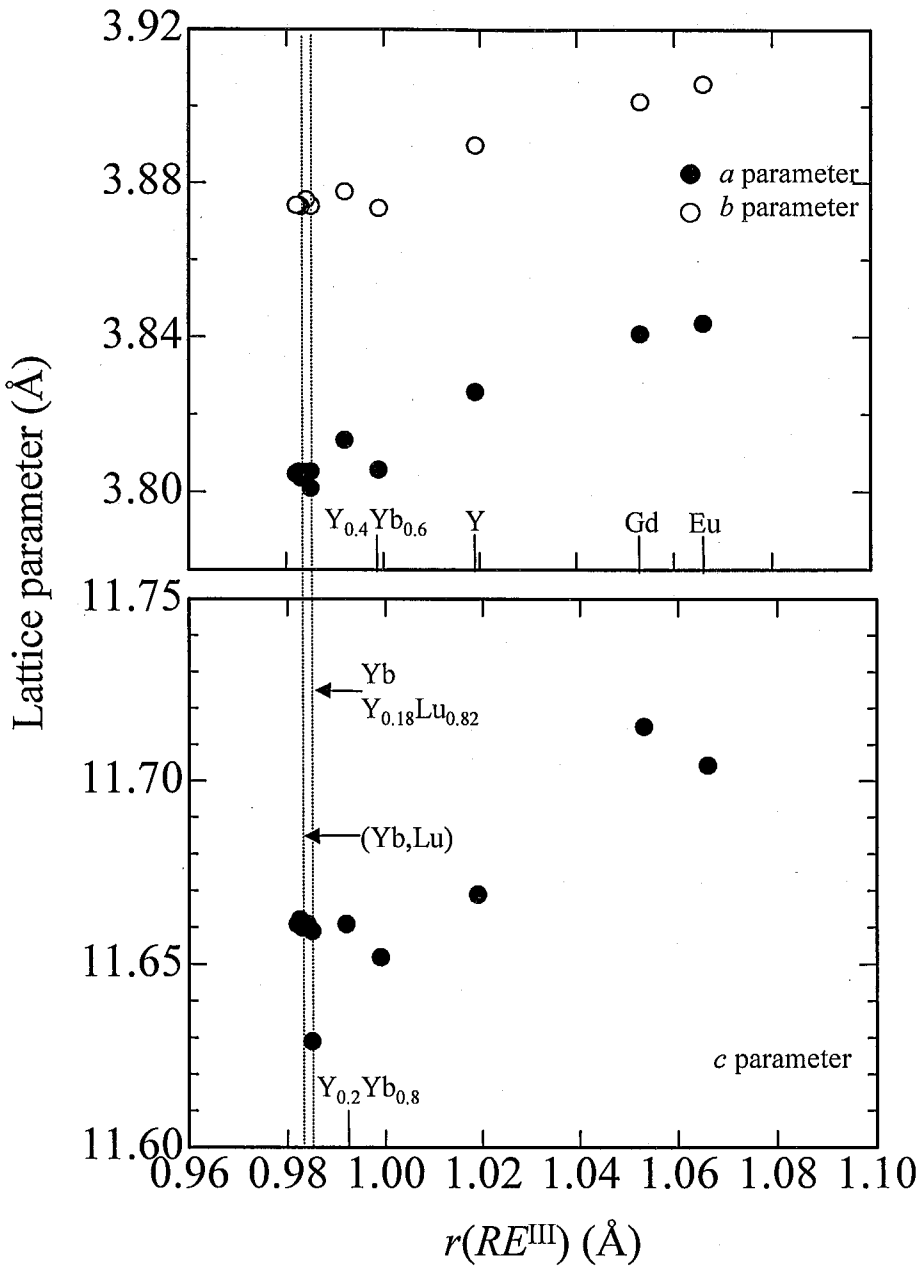

Fig. 3.3.1.-4 Lattice parameters for the fully-oxygenated $CuBa_2RECu_2O_{7-\delta}$ ($6.91 \leq 7-\delta \leq 6.94$) samples as a function of the ionic radius of the rare-earth element, $r(RE^{III})$, in trivalent state.

Considering the phase formation of the $CuBa_2(Yb_{0.6}Lu_{0.4})Cu_2O_{7-\delta}$ sample synthesized at various temperatures, XRD patterns of the $CuBa_2(Yb_{1-x}Lu_x)Cu_2O_{7-\delta}$ (x = 0.5, 0.6 and 1.0) samples and the lattice parameters of fully-oxygenated $CuBa_2RECu_2O_{7-\delta}$ series of samples, it seems that in terms of the size of the *RE* constituent *RE* = $Yb_{0.6}Lu_{0.4}$ is close to the lower limit as being stabilized under the present synthesis conditions.

Moreover, it has been reported that by starting with compositions excess in copper, it is possible to prevent the formation of the RE_2BaCuO_5 impurity phase and starting with the composition corresponding to $REBa_2Cu_{3.2}O_{7-\delta}$, the pure phase of $CuBa_2RECu_2O_{7-\delta}$ was successfully obtained with smaller $r(RE^{III})$ [34,43,44] since the excess amount of copper worked as a flux. However, the excess amount of copper did not contribute enough, in this study.

Fig. 3.3.1.-5 shows the T_c values of the fully-oxygenated $CuBa_2RECu_2O_{7-\delta}$ samples.

When r(Ba) and $r(RE^{III})$ are close, *i.e.* in the case of large *RE*, there is a possibility that a part of *RE* substitutes for a part of Ba site [45]. Therefore, the largest *RE* in this study, Eu might be substitutes for a part of Ba because r(Eu) is approximately 1.07 Å and that of Ba is 1.52Å for *CN* is 10 thus the r(Eu) and r(Ba) are close. However, based on Fig. 3.3.1.-5, T_c value depression was not observed for *RE* = Eu, thus the substitution of Ba site by Eu is not applicable. Although all the samples possess precisely the same oxygen content, *i.e.* $6.91 \leq 7\text{-}\delta \leq 6.94$ (except $CuBa_2GdCu_2O_{6.98}$), it was found that the T_c values are different among the samples. However, the difference among the samples is only $r(RE^{III})$s. This result implies that each sample has a different under-doped, optimal-doped and over-doped range as a function of the oxygen content. Thus, even though the oxygen content is fixed among the samples, their T_c values are different. However, the most crucial point in this study is the doping levels of over all crystals are the same among samples since all the samples have the same oxygen content. This means that under-doped, optimally-doped and over-doped states depend not only on the doping level but also on the size of *RE*. Since the overall doping level was fixed among the samples, this result implies that samples with the smaller *RE*'s tend to be move over-doped than those with the larger *RE*'s, inducing lower T_c values than those for the larger *RE* samples. It is important to note that this is due to the *RE* size effect only.

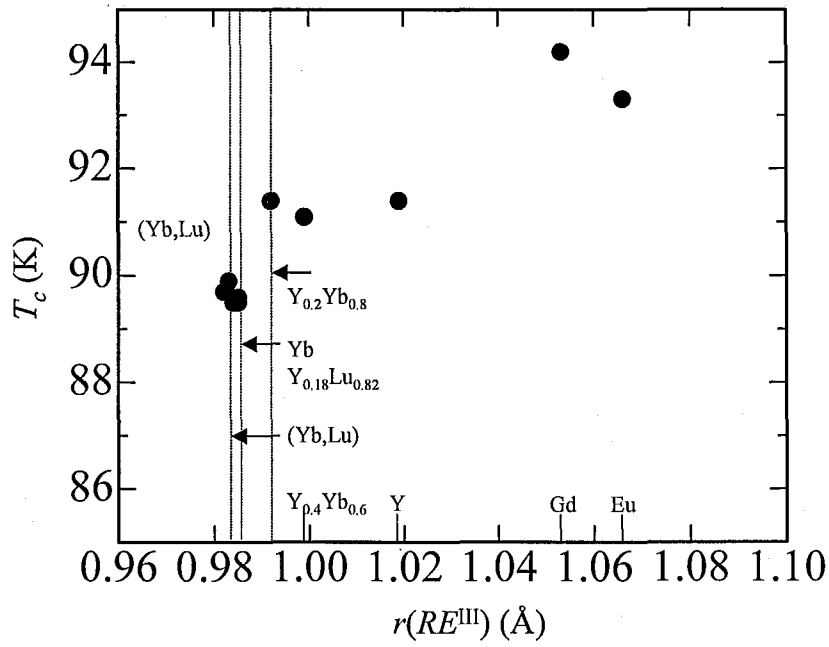

Fig. 3.3.1.-5 T_c values for the fully-oxygenated $CuBa_2RECu_2O_{7-\delta}$ ($6.91 \leq 7\text{-}\delta \leq 6.94$) samples plotted against $r(RE^{III})$.

3.3.2. Microstructures

The aim in this study was to reveal the intrinsic H_{irr} properties in samples of the $CuBa_2RECu_2\text{-}O_{7-\delta}$ phase without any extrinsic pinning centers. Therefore, the following thing

needed to be confirmed for the samples studied: whether some tiny impurity particles, *e.g.* RE_2BaCuO_5, are melted and grown together with melted $CuBa_2RECu_2O_{7-\delta}$ matrix during the synthesis process or not. If this melt-grown process is realized, the tiny melted impurity particles may act as active vortex pinning centers that might affect the H_{irr} characteristics. Thus, to confirm the existence of such kind of melt-grown superconductive phase and impurity particles, and if it is so, to check the effects of the impurity phase/particles, a SEM study with EDS analysis was carried out.

Fig. 3.3.2.-1 shows the results of the SEM observations for the most fundamental $CuBa_2YCu_2O_{6.93}$ sample and $CuBa_2(Yb_{0.6}Lu_{0.4})Cu_2O_{6.92}$ sample that has the smallest $r(RE^{III})$ in the present study. The both samples, *i.e.* mono-*RE* system of $CuBa_2YCu_2O_{6.93}$ and solid-solution-*RE* system of $CuBa_2(Yb_{0.6}Lu_{0.4})Cu_2O_{6.92}$, were found not to be melt-grown.

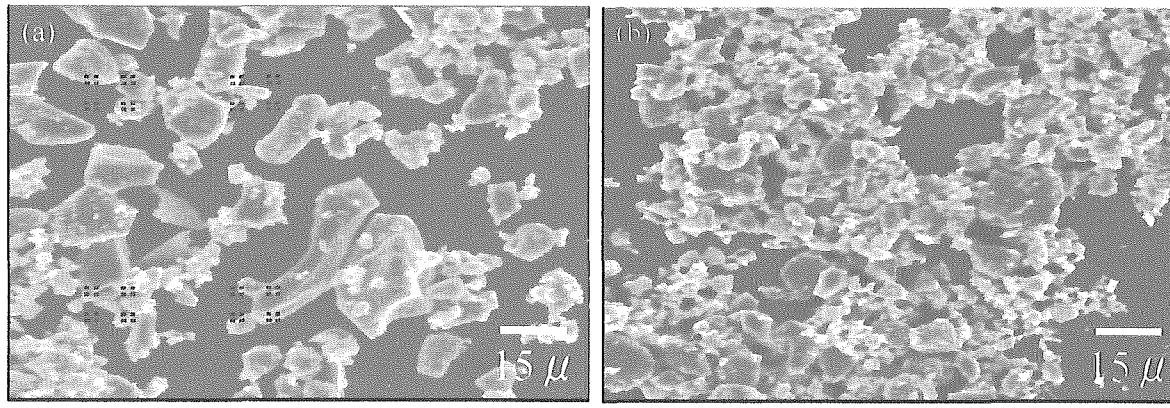

Fig. 3.3.2.-1 SEM images for the (a) $CuBa_2YCu_2O_{6.93}$ and (b) $CuBa_2(Yb_{0.6}Lu_{0.4})Cu_2O_{6.92}$ samples.

For a detailed microstructural study, the observations of the $CuBa_2(Yb_{0.6}Lu_{0.4})Cu_2O_{6.92}$ sample and composition analysis were carried out. The results of the SEM observation and the EDS analysis of grain of the $CuBa_2(Yb_{0.6}Lu_{0.4})Cu_2O_{6.92}$ sample which was the most difficult to synthesize in pure phase in this work, *i.e.* a sample with the highest probability to include the impurity phase of $(Yb, Lu)_2BaCuO_5$ is shown in Fig. 3.3.2.-2. A local spot (a) of the grain was concluded to be of the $CuBa_2(Yb_{0.6}Lu_{0.4})Cu_2O_{6.92}$ composition because of the grain shape. On the other hand, a local spot (b) was concluded to be of the $(Yb,Lu)_2BaCuO_5$ impurity particle from its spherical form. However, it was revealed that both local spots of the grain (a) and (b) possess the compositions of *RE*:Ba:Cu = 1.0:1.5:2.8 and *RE*:Ba:Cu = 1.0:1.7:3.0, respectively, thus it was confirmed that the composition of this sample is approximately $CuBa_2(Yb_{0.6}Lu_{0.4})Cu_2O_{6.92}$ from EDS analysis. These results imply that there are hardly any impurities in the $CuBa_2(Yb_{0.6}Lu_{0.4})Cu_2O_{6.92}$ sample and there is no possibility that tiny impurity particles are melted and grown together with melted superconductive phase.

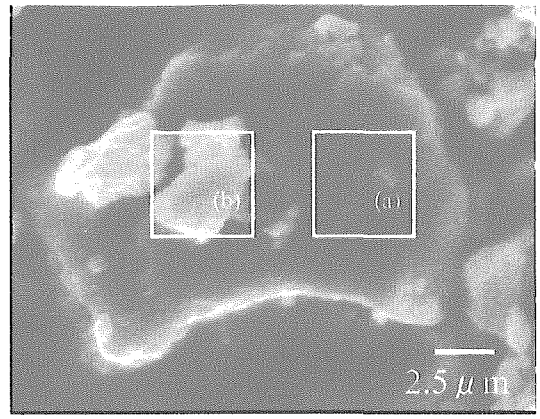

Position / Atomic %	(a)	(b)
Lu	5.85	7.3
Yb	12.64	10.22
sum of *RE*	18.49	17.52
Ba	29.65	29.45
Cu	51.85	53.03
RE : Ba : Cu	1.0:1.5: 2.8	1.0:1.73.0

Fig. 3.3.2.-2 SEM image and results of EDS analysis at corresponding spots for the $CuBa_2(Yb_{0.6}Lu_{0.4})Cu_2O_{6.92}$ sample.

Comparing superconductivity properties of the mono-*RE* and solid-solution-*RE* systems requires a careful study. It is because in the solid solution of two different *RE*'s, *i.e.* RE_a and RE_b, some atomic disorder or concentration modulation along the *ab* plane may occur, possibly resulting in some kind of weak pinning centers to yield better H_{irr} characteristics. These two kinds of *RE* may be clustered such that the regions of $CuBa_2RE_aCu_2O_{7-\delta}$ and $CuBa_2RE_bCu_2O_{7-\delta}$ in the sample might result in concentration modulation which induces a source of weak pinning centers. On the other hand, the two kinds of *RE* species may tend to order mutually, *i.e.* they order RE_a and RE_b in turn. In this case, there is hardly any macroscopic concentration modulation in the sample, thus weak pinning centers due to atomic disorder or concentration modulation may not exist. The third possibility is that RE_a and RE_b order randomly. Besides, the fully-oxygenated $CuBa_2RECu_2O_{7-\delta}$ samples possess many twin boundaries in each grain, in general. It has been reported that in the case that there is oxygen deficiency at the twin boundaries or RE_2BaCuO_5 impurity particles are trapped at the twin boundaries, these would work as pinning centers [46] and they affect the H_{irr} characteristics. Therefore, the TEM observations were indispensable to confirm these possibilities mentioned in above for the $CuBa_2(Yb_{0.6}Lu_{0.4})Cu_2O_{6.92}$ sample which was the most difficult to synthesize consisting of solid-solution-*RE* systems thus it was the most likely to include and trap $(Yb,Lu)_2BaCuO_5$ impurity particles at the twin boundaries.

Fig. 3.3.2.-3 (a) shows a TEM micrograph of a grain in the $CuBa_2(Yb_{0.6}Lu_{0.4})Cu_2O_{6.92}$ sample. It shows only twins due to fully oxygenation but no impurity particles. This implies that pinning centers owing to trapped RE_2BaCuO_5 impurity particles at the twin boundaries, do not exist in this sample. Moreover, a TEM electron diffraction pattern from a $CuBa_2(Yb_{0.6}Lu_{0.4})Cu_2O_{6.92}$ grain is shown in Fig. 3.3.2.-3 (b). Electron diffraction spots with streaks would originate from the atomic disorder of microstructure. Moreover, when the concentration modulation exists in the grain, the modulation structure induces a long periodic structure results in lattice super of electron diffraction. However, each spot in this diffraction pattern for the *ab* plane is round without streaks or lattice super. The double spots indicate the existence of twin structures. Thus the possibility of effective pinning centers due to the disorder

of atoms or modulation can be ruled out for this sample [III].

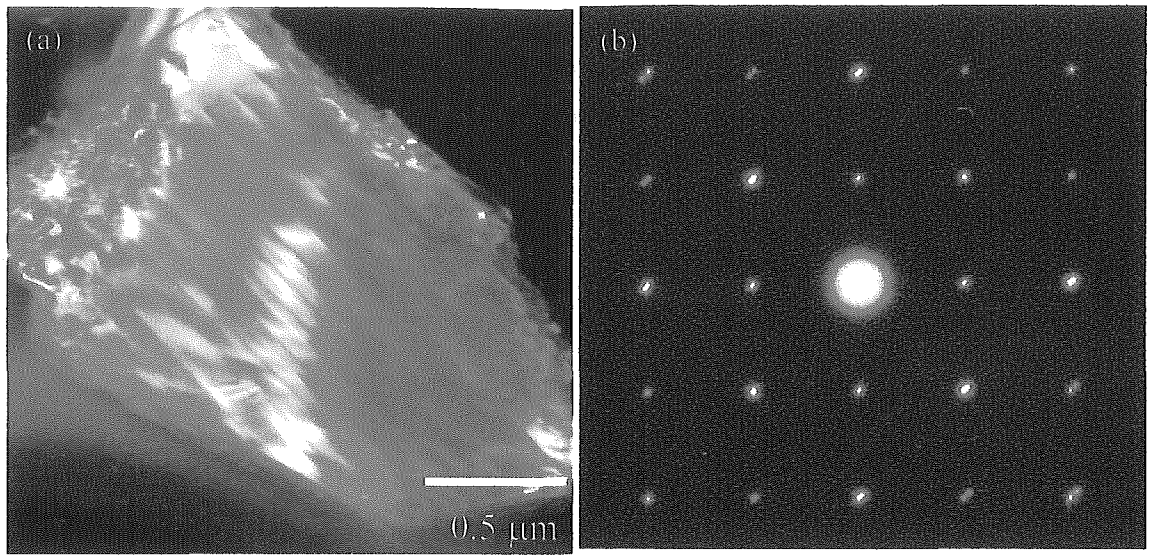

Fig. 3.3.2.-3 Dark-field image for the $CuBa_2(Yb_{0.6}Lu_{0.4})Cu_2O_{6.92}$ crystal with the incident electron beam parallel to the [001] direction (a), and (b) the ED pattern taken for the same crystal-grain from the same direction of the incident electron beam [III].

Furthermore, HRTEM observations were carried out for the same $CuBa_2(Yb_{0.6}Lu_{0.4})Cu_2O_{6.92}$ sample to reveal the possible ordering of atoms directly. The result is shown in Fig. 3.3.2.-4. In the case there would be concentration modulation, the HRTEM pattern would not show homogeneous pattern, like Fig. 3.3.2.-4, but a modulated pattern.

In conclusion, the microstructural study confirmed that the $CuBa_2(Yb_{0.6}Lu_{0.4})Cu_2O_{6.92}$ sample possesses homogeneous microstructures with twin boundaries without effective pinning centers.

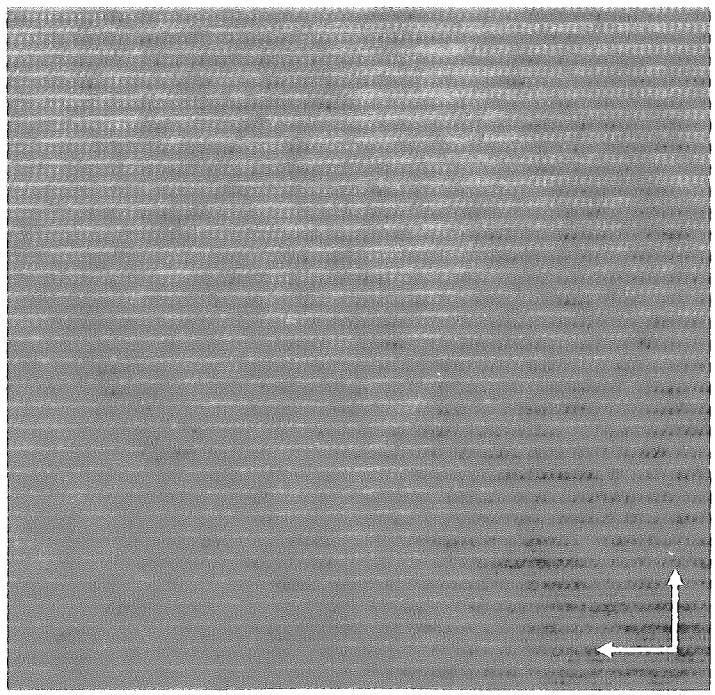

Fig. 3.3.2.-4 High resolution (HR) TEM image for the $CuBa_2(Yb_{0.6}Lu_{0.4})Cu_2O_{6.92}$ sample.

3.3.3. Magnetic Irreversibility-Field Characteristics [II,III]

In section 3.1.4, it was mentioned minutely that H_{irr} characteristics must be determined the fixed experimental parameters, criteria of H_{irr} determination, measurement rate and the grain size of the samples [47]. Therefore, in this study, the H_{irr} characteristics were evaluated for samples with a precisely controlled grain sizes, *i.e.* 3.0±0.5 μm from SEM observations and precisely fixed experimental conditions.

In Fig. 3.3.3.-1, the H_{irr} values determined for the fully-oxygenated series of $CuBa_2RECu_2O_{7-\delta}$ (*RE* = Eu, Gd, Y, Yb, $Yb_{0.9}Lu_{0.1}$, $Yb_{0.8}Lu_{0.2}$, $Yb_{0.7}Lu_{0.3}$ and $Yb_{0.6}Lu_{0.4}$) samples ($6.91 \leq 7-\delta \leq 6.94$; except for the sample with *RE* = Gd) are plotted against the reduced temperature, $1-T/T_c^{(e)}$. It is evident that for the samples of the $CuBa_2RECu_2O_{7-\delta}$ ($6.91 \leq 7-\delta \leq 6.94$) series with a constant oxygen content, the H_{irr} characteristics strongly depend on $r(RE^{III})$ [II,III]. Namely, the smaller the *RE* constituent is the higher is the H_{irr} field. For the $CuBa_2(Yb_{0.6}Lu_{0.4})Cu_2O_{6.92}$ sample that has the smallest $r(RE^{III})$ in this study, the value of H_{irr} was the highest among the present samples.

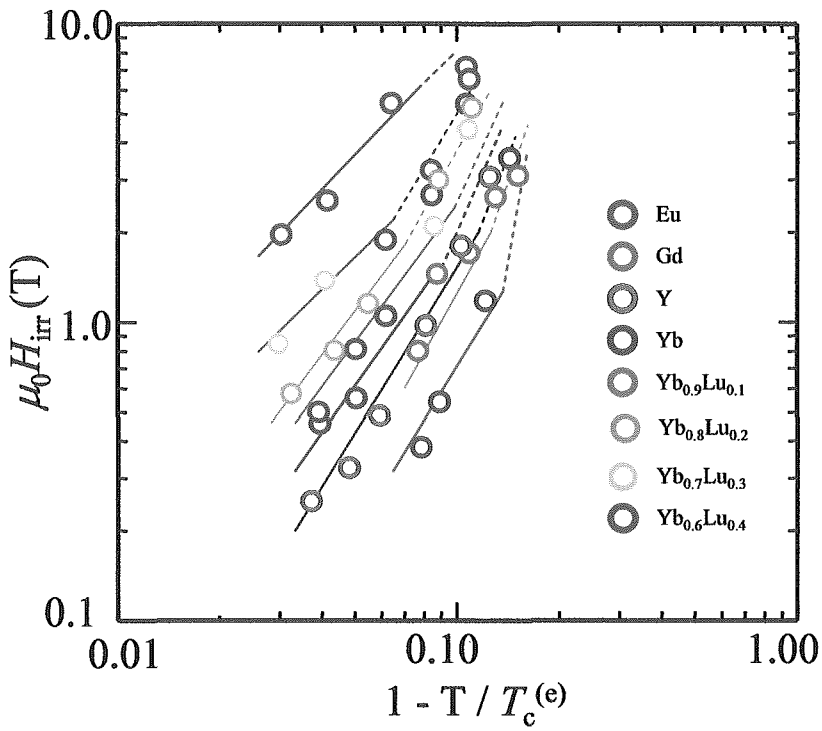

Fig. 3.3.3.-1 H_{irr} characteristics for the fully-oxygenated $CuBa_2RECu_2O_{7-\delta}$ ($6.91 \leq 7-\delta \leq 6.94$) samples.

Fig. 3.3.3.-2 shows more precise results, *i.e.* H_{irr} characteristics of the $CuBa_2(Yb_{0.6}Y_{0.4})Cu_2O_{6.93}$ and $CuBa_2(Yb_{0.6}Lu_{0.4})Cu_2O_{6.92}$ samples. The oxygen contents for the two samples are essentially same. Therefore, the difference between these two samples is only the substitutive *RE* spices of the Yb based *RE* site, *i.e.* Y and Lu. The amount of Yb is fixed at 0.6, and the substituted Y/Lu amount thus 0.4. Moreover, the formal valences of Y and Lu are +III, *i.e.* they are the "isovalent" cations. Thus, it is possible to think that the difference between the samples is only the $r(RE^{III})$. Fig. 3.3.3.-2 shows that with decreasing $r(RE^{III})$, the H_{irr}

characteristics were enhanced. Comparing these two samples, their H_{irr} characteristics are different by a factor of 2.

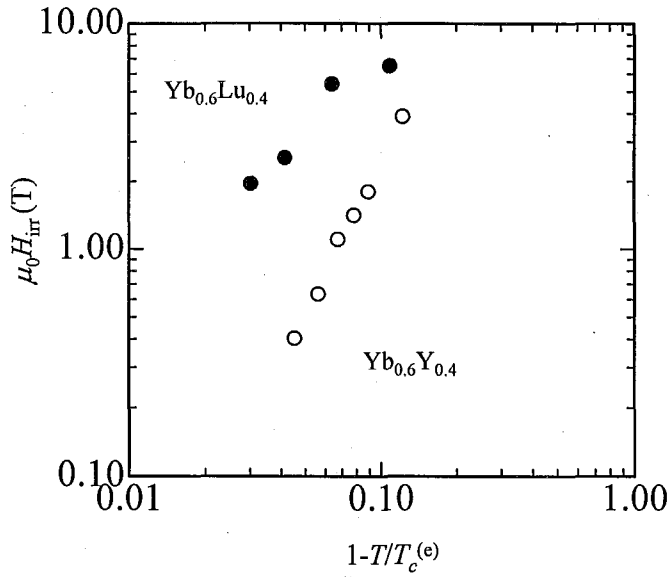

Fig. 3.3.3.-2 Comparison of H_{irr} characteristics between $CuBa_2(Yb_{0.6}Lu_{0.4})Cu_2O_{6.92}$ and $CuBa_2(Yb_{0.6}Y_{0.4})Cu_2O_{6.93}$ samples.

Fig. 3.3.3.-3 also shows the H_{irr} characteristics as a function of $1\text{-}T/T_c^{(e)}$ of the $CuBa_2(Yb_{0.8}Y_{0.2})Cu_2O_{6.91}$ and $CuBa_2(Yb_{0.8}Lu_{0.2})Cu_2O_{6.94}$ samples. Similarly to $CuBa_2(Yb_{0.6}Y_{0.4})Cu_2O_{6.93}$ and $CuBa_2(Yb_{0.6}Lu_{0.4})Cu_2O_{6.92}$ samples, the difference between the two samples in Figs. 3.3.3.-3 is only the $r(RE^{III})$ of Y and Lu. Considering results of Figs. 3.3.3.-1, 3.3.3.-2 and 3.3.3.-3, it indicates that the H_{irr} characteristics depend on $r(RE^{III})$ clearly in $CuBa_2RECu_2O_{7-\delta}$ ($6.91 \leq 7-\delta \leq 6.94$) system at a fully-constant oxygen content [II,III]. It should be emphasized that the superb H_{irr} characteristics of $CuBa_2RECu_2O_{7-\delta}$ ($6.91 \leq 7-\delta \leq 6.94$) samples with small *RE* was derived from the effects of isovalent-cation substitution only, *i.e.* $r(RE^{III})$ affects the H_{irr} characteristics. If these experimental results and the conclusion are correct, following assumption must be revealed; from Figs. 3.3.3.-1, 3.3.3.-2 and 3.3.3.-3, it was found that in the case of isovalent-cation substitution in $CuBa_2RECu_2O_{7-\delta}$ system, $r(RE^{III})$ largely affects the H_{irr} characteristics. If it is correct, $CuBa_2RECu_2O_{7-\delta}$ samples with the same $r(RE^{III})$/same oxygen content, are supposed to possess the same H_{irr} values/characteristics.

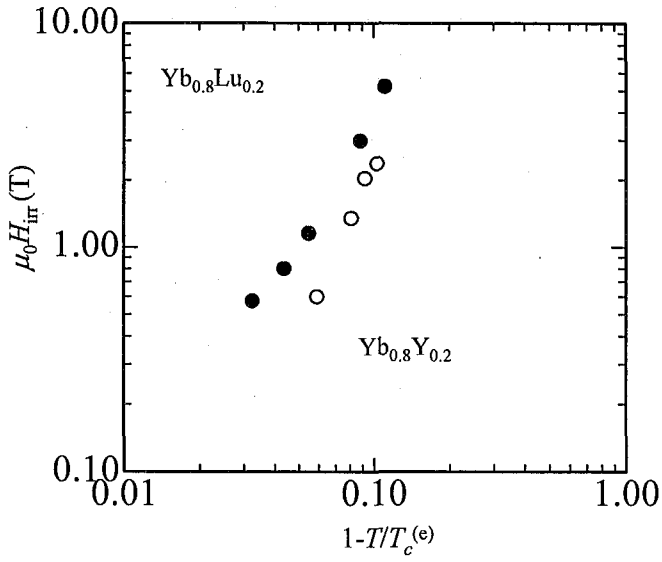

Fig. 3.3.3.-3 H_{irr} characteristics for the $CuBa_2(Yb_{0.8}Lu_{0.2})Cu_2O_{6.94}$ and $CuBa_2(Yb_{0.8}Y_{0.2})Cu_2O_{6.91}$ samples.

To confirm this point, a sample with a composition of $CuBa_2(Y_{0.18}Lu_{0.82})Cu_2O_{6.93}$ was synthesized. The average ionic radius of the *RE* site of this sample, *i.e.* $r(Y_{0.18}Lu_{0.82})$, corresponds to that of Yb. Furthermore, the oxygen contents of the two samples were exactly the same at 6.93. Interestingly, the optimum synthesis temperature for the $CuBa_2(Y_{0.18}Lu_{0.82})Cu_2O_{6.93}$ sample was determined at 900 °C that is the optimized synthesis temperature for the $CuBa_2YbCu_2O_{6.93}$ sample, too. Table 3.2.-1 (see section 3.2.) shows the detailed synthesis conditions and basic properties of both samples. Fig. 3.3.3.-4 shows the XRD patterns for the samples. It was found that the basic properties of these two samples having the same $r(RE^{III})$s, were very similar. Furthermore, the H_{irr} characteristics of $RE = Y_{0.18}Lu_{0.82}$ and Yb at the oxygen content 6.93 samples were determined and further compared in Fig. 3.3.3.-5. It is obviously seen that the samples with the same $r(RE^{III})$ and fixed oxygen content possess exactly similar H_{irr} values/characteristics. Therefore, these experimental results clearly revealed that the differences in the H_{irr} characteristics among the various $CuBa_2RECu_2O_{7-\delta}$ ($6.91 \leq 7-\delta \leq 6.94$) samples are derived from the effects of isovalent-cation substitution only in this system, with fixed oxygen contents.

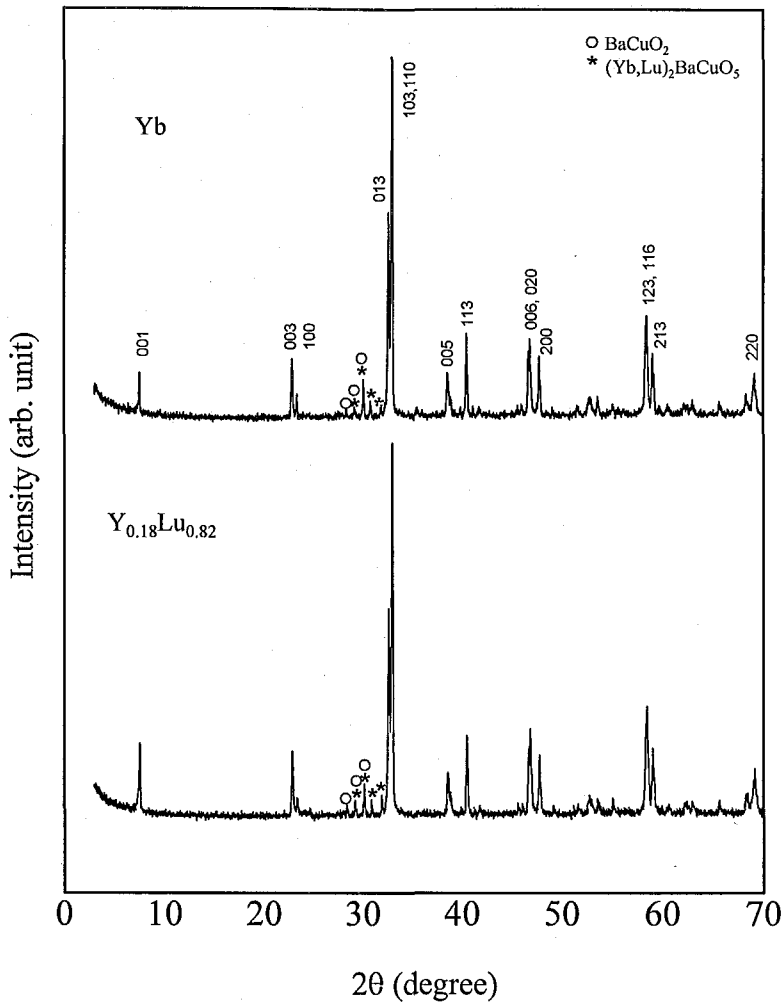

Fig. 3.3.3.-4 XRD patterns for the $CuBa_2YbCu_2O_{6.93}$ and $CuBa_2(Y_{0.18}Lu_{0.82})Cu_2O_{6.93}$ samples possessing the same oxygen contents, 7-δ of 6.93 and the same $r(RE^{III})$ values of 0.985 Å.

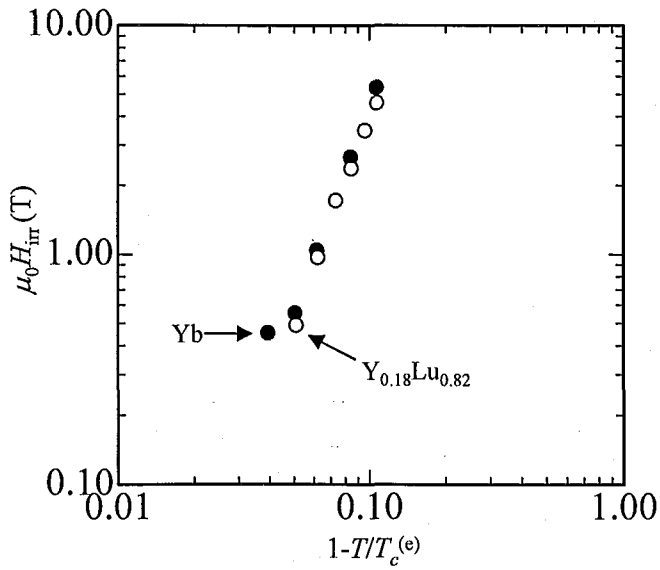

Fig. 3.3.3.-5 H_{irr} characteristics for the $CuBa_2YbCu_2O_{6.93}$ and $CuBa_2(Y_{0.18}Lu_{0.82})Cu_2O_{6.93}$ samples.

Moreover, to progress this study more quantitative aspect, the value of H_{irr} at 77 K was calculated [III]. Fig. 3.3.3.-6 shows these H_{irr} (77 K) values for each fully-oxygenated

$CuBa_2RECu_2O_{7-\delta}$ ($6.91 \leq 7-\delta \leq 6.94$) sample. It is seen that the magnitude of H_{irr} (77 K) strongly depends on $r(RE^{III})$ when the oxygen content is constant. With decreasing $r(RE^{III})$, the H_{irr} (77 K) values is strongly enhanced. For the $CuBa_2(Yb_{0.6}Lu_{0.4})Cu_2O_{6.92}$ sample that has the smallest *RE* constituents among the present samples, the value of H_{irr} (77 K) was as high as ~9.0 T. For further comparison, the H_{irr} values estimated for the $CuBa_2RECu_2O_{7-\delta}$ ($6.91 \leq 7-\delta \leq 6.94$) samples at $T = 0.92\ T_c^{(e)}$ are plotted against $r(RE^{III})$ in Fig. 3.3.3.-7 [II]. Note that, at high temperatures, *i.e.* $T = 0.92\ T_c^{(e)}$, the contribution from the vortex pinning to the value of H_{irr} may be considered negligible. Thereby the "intrinsic" H_{irr} values/characteristics can be evaluated.

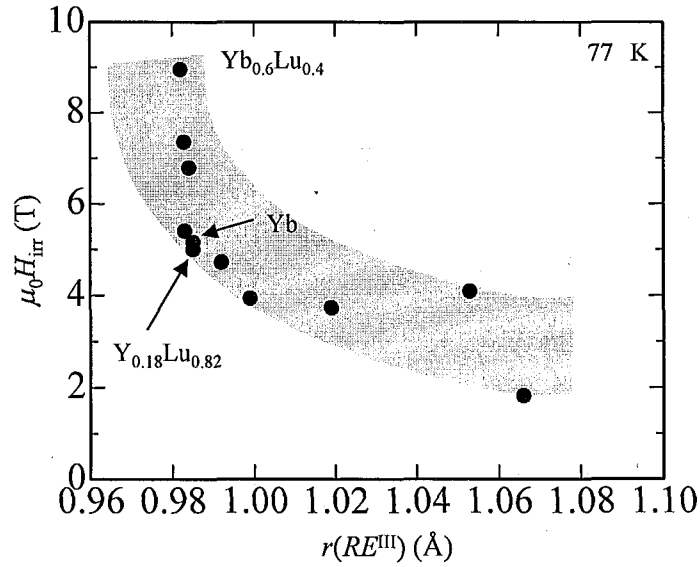

Fig. 3.3.3.-6 Correlation between H_{irr} (at 77 K) and $r(RE^{III})$ in the fully-oxygenated $CuBa_2RECu_2O_{7-\delta}$ ($6.91 \leq 7-\delta \leq 6.94$; except $CuBa_2GdCu_2O_{6.98}$) system [III].

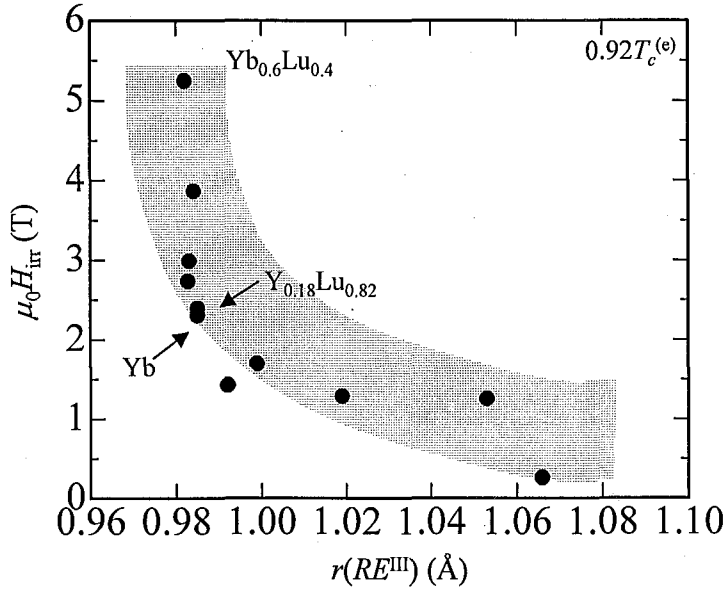

Fig. 3.3.3.-7 H_{irr} ($T = 0.92\ T_c^{(e)}$) of the $CuBa_2RECu_2O_{7-\delta}$ ($6.91 \leq 7-\delta \leq 6.94$; except $CuBa_2GdCu_2O_{6.98}$) samples with respect to $r(RE^{III})$ [II].

Recently it has been reported that a seeded-melt processed $CuBa_2NdCu_2O_{7-\delta}$ sample containing 15 mol% $Nd_4Ba_2Cu_2O_{10}$ has a superb H_{irr} characteristics, *i.e.* ~9.0 T in the case of

H//*c* at 77 K and ~10.5 T in the case of H⊥*c* at 88 K [43]. However, this is probably caused by "extrinsic" pinning centers, rather than an "intrinsic" nature of the electronic structure of the compound. Other studies for $CuBa_2RECu_2O_{7-\delta}$ (*RE* = Nd, Sm, Eu) superconductors synthesized by an oxygen-control-melt-growth (OCMG) process has been studied. When B_{irr} lines (irreversibility line) are scaled as a function of $(1 - t^2)^{1.5}$, since the slope of B_{irr}-*vs*-$(1 - t^2)^{1.5}$ was much steeper for the samples OCMG-processed in lower oxygen partial pressure, it was concluded that the flux pinning of these samples is much stronger thus the better B_{irr} values were obtained [44]. Moreover, to reveal the correlation between irreversibility-field line and the flux pinning, it has been reported that the irreversibility-field lines of OCMG-processed flux-grown $CuBa_2NdCu_2O_{7-\delta}$ single crystal, OCMG-processed melt-grown $CuBa_2NdCu_2O_{7-\delta}$ bulk and the MPMG-processed melt-grown $CuBa_2YCu_2O_{7-\delta}$ bulk were compared. Among these samples, OCMG-processed melt-grown $CuBa_2NdCu_2O_{7-\delta}$ bulk sample exhibited the highest irreversibility line. This study was concluded that the secondary phase inclusions existing in the OCMG-processed melt-grown $CuBa_2NdCu_2O_{7-\delta}$ bulk sample induced enhanced irreversibility property [24]. Furthermore, although the studied systems were different from $CuBa_2RECu_2O_{7-\delta}$ system, it has been reported that the effect of carrier doping on the irreversibility lines in $(La,Sr)_2CuO_{4-\delta}$ and $Bi_2Sr_2CaCu_2O_{8+\delta}$ single crystal were summarized. As a function of Sr or oxygen contents, systematic and dramatic widening of the irreversibility regions in the *B-T* diagram was observed in both systems. This result was concluded that the critical importance of carrier concentration which directly affects the interlayer coupling strength and dimensionality of the flux line lattice thereby results in improved irreversibility-field line in all the layered HTSC compounds as a universal feature [48].

It is clear that the studies of H_{irr} characteristics for $CuBa_2RECu_2O_{7-\delta}$ system has been progressed by a standpoint of flux pinning or secondary phase inclusions. However, the standpoint of present work is *RE* size-only-dependent effects on H_{irr} characteristics with free from extrinsic pinning centers. The H_{irr} value of ~9.0 T at 77 K for $CuBa_2(Yb_{0.6}Lu_{0.4})Cu_2O_{6.92}$ obtained in the present study is the highest H_{irr} value among those of the $CuBa_2RECu_2O_{7-\delta}$ compounds ever studied not containing any extrinsic pinning centers. The superb H_{irr} characteristics of the present $CuBa_2(Yb_{0.6}Lu_{0.4})Cu_2O_{6.92}$ sample is derived from size-only-dependent substitution [II,III].

Furthermore, it is required to consider and reveal the reasons why the smaller *RE* possessive $CuBa_2RECu_2O_{7-\delta}$ ($6.91 \leq 7-\delta \leq 6.94$) samples have the better H_{irr} properties. The possible reasons are follows [III]: (*i*) some tiny impurity particles, *e.g.* RE_2BaCuO_5, may act as vortex pinning centers that might induce the better H_{irr} characteristics. (*ii*) some atomic disorder or concentration modulation along the *ab* plane may work as weak pinning centers to yield the better H_{irr} characteristics. (*iii*) some other factors affect the H_{irr} characteristics.

From SEM observations with EDS analyses, it was revealed [III] that the possibility (*i*) is not applicable to the present samples. Similarly, possibility (*ii*) may not be applicable either, based on TEM and HRTEM observations. Therefore, there must be another reason for superior H_{irr} properties with small $r(RE^{III})$. Consequently, XANES measurements were carried out to

make clear the local hole-density distribution over the crystals for fully oxygenated $CuBa_2RECu_2O_{7-\delta}$ ($6.91 \leq 7-\delta \leq 6.94$; except $CuBa_2GdCu_2O_{6.98}$) samples (see Chapter 6). Furthermore, in order to evaluate the amount of holes in the CuO_2 plane and $CuO_{1-\delta}$ chain respectively, BVS calculation was investigated for fully oxygenated $CuBa_2RECu_2O_{7-\delta}$ system with reliable structural data obtained from neutron diffraction experiments by other group.

3.3.4. Importance of Hole-Density Distribution

3.3.4.-1 Effects of Size of *RE* on the Hole Distribution in the $CuBa_2RECu_2O_{7-\delta}$ System

In the previous section, the drastic differences in the superconductivity characteristics as a function of the ionic size of *RE* were revealed for the fully-oxygenated series of $CuBa_2RECu_2O_{7-\delta}$ ($6.91 \leq 7-\delta \leq 6.94$) samples. Since the overall hole concentration are fixed through the samples, it should be paid attention to "distribution" of hole density over the crystal for such outstanding differences in superconductivity properties observed. If each sample possesses individual and clear tendency of distribution of hole concentration, it is possible to consider $r(RE^{III})$ affects the hole-density distribution but keeping the total amount of holes constant. Then such a unique hole-density distribution from sample to sample can be considered that the origin of different superconductivity properties obtained as a function of $r(RE^{III})$. Thus, estimation of the hole-density distribution is one of the most crucial processes to be able to discuss the correlation between the superconductivity properties and hole-density distribution over the high-T_c superconductor crystals of the present isovalent-*RE* system.

Systematic study on BVS calculation from reliable structural data for a certain-compound system is a powerful way to investigate a tendency of the oxidation states of cations thereby to estimate the hole-density distribution. Using neutron diffraction data obtained for "optimized" $CuB_2RECu_2O_y$ samples [49], BVS reveals that with decreasing $r(RE^{III})$, the density of holes in the CuO_2 plane increases, while that in the $CuO_{1-\delta}$ chain decreases. For $CuBa_2RECu_2O_{7-\delta}$ phases with large *RE*'s, the hole density in the $CuO_{1-\delta}$ chain is much larger than that in the CuO_2 plane, *i.e.* the difference in the hole density between the CuO_2 plane and the $CuO_{1-\delta}$ chain is quite large [50]. Moreover, BVS calculation was carried out for revealing the hole amount in the CuO_2 plane from neutron diffraction data [51] collected for $CuBa_2RECu_2O_7$ with various *RE* constituents. The density of holes in the CuO_2 plane was calculated in accordance with P_{BVS} value described in Eqs. 2.2.1.-3 and 2.2.1.-4. As shown in Fig. 3.3.4.-1-1, the result revealed that with decreasing $r(RE^{III})$, the number of holes in the CuO_2 plane increased in spite of overall hole concentration is fixed. Thus it is deducible that holes in the $CuO_{1-\delta}$ chain decreased. These studies indicates that the hole distribution along the *c* axis becomes more homogeneous in proportion to decrease $r(RE^{III})$ in the $CuBa_2RECu_2O_{7-\delta}$ system. Previously, it was established [15] that the more homogeneous the hole-density distribution along the *c* axis is, the better is the H_{irr} characteristics. Thus the reason for superior H_{irr} properties with small $r(RE^{III})$

probably originate more homogeneous the hole-density distribution. The concept of hole-density distribution for better H_{irr} properties is shown in Fig. 3.3.4.-1-2.

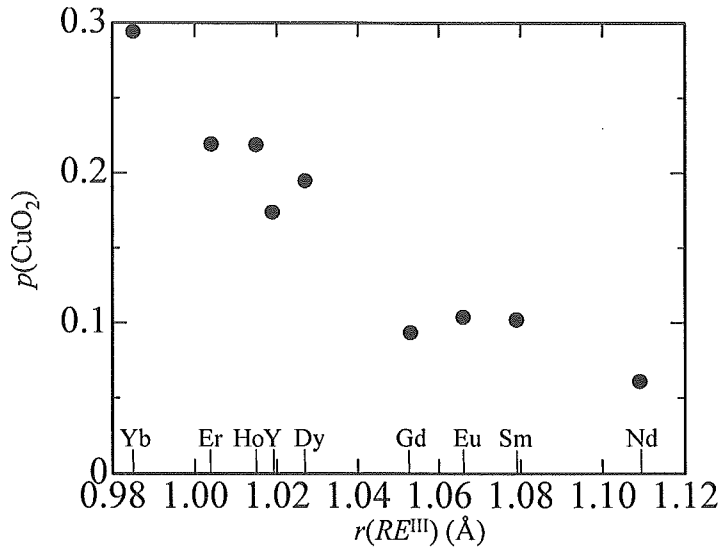

Fig. 3.3.4.-1-1 Hole concentration in the CuO_2 plane, $p(CuO_2)$ as a function of $r(RE^{III})$. The value of $p(CuO_2)$ was calculated based on neutron diffraction data [51], and on BVS concept, *i.e.*, Eqs. (2.2.1.-3) and (2.2.1.-4).

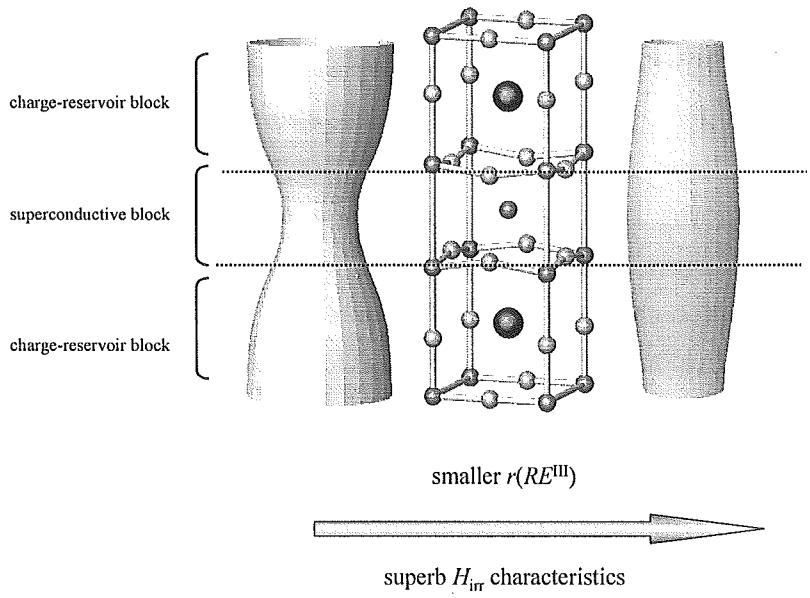

Fig. 3.3.4.-1-2 Schematic representation of the relationship between hole-density distribution and H_{irr} characteristics for the $CuBa_2RECu_2O_{7-\delta}$ system.

3.3.4.-2 Hole Distribution in Multi-layered Copper Oxides

In the isovalent substituted $CuBa_2RECu_2O_{7-\delta}$ (Cu-1212), $Cu_2Ba_2RECu_2O_{8+\delta}$ (Cu-2212) and $(Cu_{0.75}Mo_{0.25})Sr_2RE_3Cu_2O_{11+\delta}$ [(Cu,Mo)-1232] high-T_c superconductors with fully-oxygenated states, it has been established that T_c values decrease as the ionic radius of *RE* decreases in the $CuBa_2RECu_2O_{7-\delta}$ system [31,51], while the enhancements of T_c were

demonstrated in the $Cu_2Ba_2RECu_2O_{8+\delta}$ [52,53] and $(Cu_{0.75}Mo_{0.25})Sr_2RE_3Cu_2O_{11+\delta}$ [54] systems. For $CuBa_2RECu_2O_{7-\delta}$ the isovalent smaller-for-larger RE^{III} substitution is believed to induce a transfer of holes from the $CuO_{1-\delta}$ chain to the CuO_2 plane on the basis of Seebeck [55]/O *K*-edge XANES [56] measurements and BVS data [50,II,IV] as described above paragraphs. The increase in the hole concentration in the CuO_2 plane suppresses the T_c value [50,51,II,IV] because fully-oxygenated samples of the $CuBa_2RECu_2O_{7-\delta}$ phase are in a slightly overdoped state [54]. Contrary, the $r(RE^{III})$ dependence of T_c in the $Cu_2Ba_2RECu_2O_{8+\delta}$ and $(Cu_{0.75}Mo_{0.25})Sr_2RE_3Cu_2O_{11+\delta}$ phases may indicate that the substituting smaller *RE* for larger *RE* makes the systems to be closer to the optimum states of hole amounts thereby the T_c values are increased implying the underdoped states for fully-oxygenated $Cu_2Ba_2RECu_2O_{8+\delta}$ and $(Cu_{0.75}Mo_{0.25})Sr_2RE_3Cu_2O_{11+\delta}$ compounds.

The dependence of the H_{irr} fields on the amount of excess oxygen and the hole distribution was investigated in the systematic series of $Cu(Ba_{0.8}Sr_{0.2})_2YbCu_2O_{7-\delta}$ (Cu-1212:P), $CuBa_2Ca_2Cu_3O_{9-\delta}$ (Cu-1223:P), $CuBa_2Ca_3Cu_4O_{11-\delta}$ (Cu-1234:P), $HgBa_2Ca_2Cu_3O_{9-\delta}$ (Hg-1223:RS) and $Bi_2Sr_2(Ca_{1-x}Y_x)Cu_2O_{8+\delta}$ (Bi-2212:RS) phases [57]. It was found that the H_{irr} characteristics was shifted in a continuous manner to higher magnetic fields in accordance with increasing oxygen content for the n = 2 to 4 members of the Cu-12(n-1)n:P homologous series and for the $HgBa_2Ca_2Cu_3O_{9-\delta}$ samples with various oxygen contents. The better H_{irr} characteristics is realized for a sample with high doping level of the overall-hole concentration (Fig. 3.3.4.-2-1). This suggests there is no-overdoped region for the H_{irr} property. In the $Bi_2Sr_2(Ca_{1-x}Y_x)Cu_2O_{8+\delta}$ system however, the oxygen content was slightly increased by substituting traivalent-Y-for-divalent Ca, *i.e.*, aliovalent substitution. δ was increased due to increases in the x concentration. Different from other systems, increases in x ($0 \le x \le 0.5$) resulted in the depression of H_{irr} values, though the oxygen content increased ($0.25 \le \delta \le 0.36$) in the series of $Bi_2Sr_2(Ca_{1-x}Y_x)Cu_2O_{8+\delta}$ samples. Furthermore, the wet-chemical redox analysis clarified that the valences of both copper and bismuth decrease in proportion to the Y-substitution level/oxygen content in this system and the valences of copper and bismuth would have "positive" correlations in terms of the hole concentrations in the superconductive CuO_2-$(Ca_{1-x}Y_x)$-CuO_2 and non-superconductive SrO-$Bi_2O_{2+\delta}$-SrO blocks, respectively. These results clearly demonstrated that neither the oxygen content itself nor the thickness of the charge-reservoir block (the non-superconductive blocking block was shrunk by increasing the oxygen content) is the most important parameter for the magnetic-irreversibility lines. On the other hand, the hole concentrations in the superconductive and non-superconductive blocks, *i.e.*, the hole distribution in the crystal along the piling direction of different blocks, determines the H_{irr} characteristics, primary. This is consistent with the reports that *Mm*2(*n*-1)*n*:P/RS compounds exhibiting homogeneous hole distribution along the *c*-axis possess the superb H_{irr} characteristics [15,25].

By considering these experimental facts and the behaviours of T_c-*vs*-$r(RE^{III})$ mentioned above, substituting smaller-sized *RE* for larger *RE* might generate enhanced H_{irr} fields in the $Cu_2Ba_2RECu_2O_{8+\delta}$ and $(Cu_{0.75}Mo_{0.25})Sr_2RE_3Cu_2O_{11+\delta}$ systems because these systems are shifted

from underdoped states toward to optimum states by the effect of isovalent substitution.

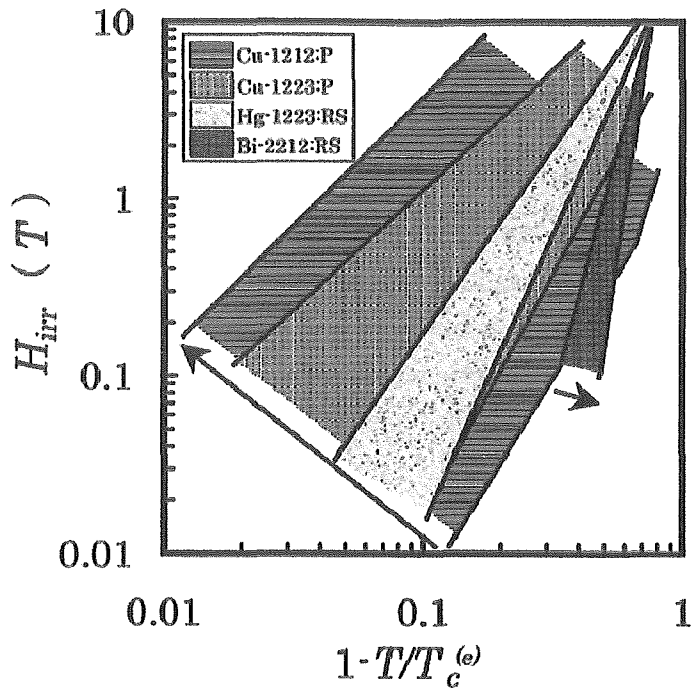

Fig. 3.3.4.-2-1 H_{irr} characteristics for the systems, $Cu(Ba_{0.8}Sr_{0.2})_2YbCu_2O_{7-\delta}$, $CuBa_2Ca_2Cu_3O_{9-\delta}$, $HgBa_2Ca_2Cu_3O_{9-\delta}$ and $Bi_2Sr_2(Ca_{1-x}Y_x)Cu_2O_{8+\delta}$ with increasing oxygen content. The effect of excess oxygen in each system is indicated by the two arrows. The increase in the oxygen content shifts the irreversibility-field lines to higher magnetic region within the shaded areas for the systems in which the oxygen content is varied through post-annealing treatments, *i.e.*, $Cu(Ba_{0.8}Sr_{0.2})_2YbCu_2O_{7-\delta}$, $CuBa_2Ca_2Cu_3O_{9-\delta}$ and $HgBa_2Ca_2Cu_3O_{9-\delta}$. For the $Bi_2Sr_2(Ca_{1-x}Y_x)Cu_2O_{8+\delta}$ system, the H_{irr} characteristics are depressed with increasing oxygen content. In this system, the increase in the oxygen content is realized by the Y^{III}-for-Ca^{II} isovalent substitution [57].

3.3.5. Effects of Isovalent Substitutions in the Layered Superconductive $M_mA_2Q_{n-1}Cu_nO_{m+2+2n\pm\delta}$ [IV]

In the previous section, importance of the homogeneity of the hole distribution for the superior H_{irr} characteristics was discussed in the $CuBa_2RECu_2O_{7-\delta}$ system. However, through out studies on the effects of isovalent substitutions it was demonstrated that the homogeneous hole distribution contributes enhancing the H_{irr} characteristics not only in the $CuBa_2RECu_2O_{7-\delta}$ system but also in the layered superconductive $M_mA_2Q_{n-1}CunO_{m+2+2n\pm\delta}$ or M-$m^{(A)}2^{(Q)}(n\text{-}1)n$ crystal [IV].

The importance of the homogeneity of the hole distribution may also be revealed from the data obtained for single-crystal $(Hg,Pb)(Ba_{1-x}Sr_x)_2Ca_2Cu_3O_{8+\delta}$ ($0 \leq x \leq 0.75$) [(Hg,Pb)-$1^{(Ba,Sr)}2^{(Ca)}23$] samples possessing 100-200 μm in size. The Sr content of the crystals was found to be nominal Sr concentration for each sample from the analyses of inductively coupled plasma (ICP) and energy-dispersive X-ray (EDX). Even though the crystals were too small to determine accurate oxygen content by wet-chemical redox analysis methods, it was found that the T_c values remained unchanged upon various post-annealings suggesting that for each $(Hg,Pb)(Ba_{1-x}Sr_x)_2Ca_2Cu_3O_{8+\delta}$ cation composition the amount of excess oxygen δ is

essentially constant. 70-100 crystals were utilized to measure the superconductivity characteristics of the samples with a SQUID magnetometer having the *c*-axis of the crystal parallel to the applied magnetic field. The H_{irr} lines for the Sr-substituted samples were superior to that obtained for the non-substituted $HgBa_2Ca_2Cu_3O_{8+\delta}$ crystals, such that the higher the Sr content is the higher is the H_{irr} line [58]. The enhancement in the irreversibility characteristics of this system through Sr^{II}-for-Ba^{II} substitution may be attributed to the overall increase in the hole concentration and the improvement of the hole-distribution homogeneity in the superconductive CuO_2-Ca-CuO_2-Ca-CuO_2 block: BVS calculation from the structural data obtained by four-circle single-crystal X-ray diffraction analysis for the present $(Hg,Pb)(Ba_{1-x}Sr_x)_2Ca_2Cu_3O_{8+\delta}$ samples [59] show that the hole concentration increases in both the inner $[p(CuO_2)_{inner}]$ and outer $[p(CuO_2)_{outer}]$ CuO_2 planes in proportion to increase the Sr content, but $p(CuO_2)_{outer}$ increase more strongly.

Furthermore, the effects of isovalent substitution at *A* sites on the H_{irr} characteristics of polycrystalline $Cu(Ba_{1-y}Sr_y)_2YbCu_2O_{7-\delta}$ ($0 \leq y \leq 0.4$) samples were investigated [60,61].Based on BVS calculations and measurements of O *K*-edge XANES spectroscopy it was revealed that isovalent substitution of Ba^{II} by a smaller Sr^{II} in this system results in an inter-block hole sift from the (Ba,Sr)O-$CuO_{1-\delta}$-(Ba,Sr)O blocking block to the superconductive CuO_2-*RE*-CuO_2 block. The oxygen contents of the samples were fixed at $\delta \approx 0.07$, such that the overall hole-doping level remained constant. Nevertheless, partial replacement of Ba by Sr was found to rather suppress the values of H_{irr} [60,61] in the contrast to the $(Hg,Pb)(Ba,Sr)_2Ca_2Cu_3O_{8+\delta}$ system. The suppression of H_{irr} values is believed to be due to the fact that Sr-substitution breaks the charge-reservoir copper-oxygen chains by promoting the charge-reservoir oxygen to partly occupy the *a*-axis site instead of the characteristics *b*-axis site. Owing to the shift of part of the *b*-axis oxygen atoms to the *a*-axis site the copper-oxygen chains are broken and also some of the Cu atoms in the chains get extra O atoms into the coordination polyhedron. These changes are believed to result in a decrease in the number of mobile holes in the charge-reservoir block, thus providing a possible explanation for the suppression of H_{irr} characteristics in the $Cu(Ba_{1-y}Sr_y)_2YbCu_2O_{7-\delta}$ system with increasing Sr content. The suppression of superconductivity characteristics derived from breakage of the charge-reservoir copper-oxygen chains by means of isovalent substitution of Ba^{II} by Sr^{II} was also observed in a series of samples of the $Cu(Ba_{1-y}Sr_y)_2YCu_2O_{7-\delta}$ ($0 \leq y \leq 1$) by other group [62]. In this system, it was found that the Sr substitution induces a displacement δ of O atom in the *a*-axis site from the *b*-axis. This displacement was mainly attributed to the size difference of Sr and Ba. Furthermore, according to the BVS calculations the Sr substitution released the stress of the Ba/Sr-O layers and this relaxation prevent the charge transfer from the Cu in the chain site of the charge-reservoir copper-oxygen chains to the Cu in the CuO_2 planes. Therefore, it was suggested that the stress of the Ba layer plays an important role in the charge transfer. This model is based on the assumption that the hole concentration on the CuO_2 planes is the dominant factor for the determination of T_c value. The authors concluded that this reduction of charge transfer is the origins of the decrease of T_c values as a function of Sr concentration.

From studies on the effects of isovalent substitutions at Q and A sites on the superconductivity properties of polycrystalline $CuBa_2RECu_2O_{7-\delta}$, $Cu(Ba,Sr)_2YbCu_2O_{7-\delta}$ and further $Cu(Ba,Sr)_2YCu_2O_{7-\delta}$ systems it is thus clear that the superconductivity characteristics of the Cu-1212 phase is not-at least primarily-controlled by the lattice dimension only. Isovalent-cation substitutions are effective in order to realize the homogeneity of the hole distribution, which is advantageous in terms of enhancing the H_{irr} characteristics in the layered superconductive $M_mA_2Q_{n-1}Cu_nO_{m+2+2n\pm\delta}$.

3.4. Conclusion

In conclusion of this chapter, the isovalent-cation effect on the H_{irr} characteristics in $CuBa_2RECu_2O_{7-\delta}$ ($6.91 \leq 7-\delta \leq 6.94$; except for the sample with RE = Gd) was systematically studied [II,III] in terms of the RE ionic radius using samples with RE = Eu, Gd, Y, $Y_{0.4}Yb_{0.6}$, $Y_{0.2}Yb_{0.8}$, Yb, $Y_{0.18}Lu_{0.82}$, $Yb_{0.9}Lu_{0.1}$, $Yb_{0.8}Lu_{0.2}$, $Yb_{0.7}Lu_{0.3}$ and $Yb_{0.6}Lu_{0.4}$. The H_{irr} characteristics was clearly enhanced in a monotonic way in proportion to decrease $r(RE^{III})$. For the $CuBa_2(Yb_{0.6}Lu_{0.4})Cu_2O_{6.92}$ sample with the smallest RE constituent among the samples prepared in the present work, a record-high H_{irr} value of ~9.0 T was obtained at 77 K. This is the highest H_{irr} value ever reported for the $CuBa_2RECu_2O_{7-\delta}$ phase freed from extrinsic origins of better H_{irr} value at 77 K. The superb H_{irr} characteristics of the present $CuBa_2(Yb_{0.6}Lu_{0.4})Cu_2O_{6.92}$ sample was derived from size-only-dependent effect of cation substitution at the RE site. Through a study of isovalent-RE effects in this system, it was found that the size of RE was a crucial factor for the H_{irr} properties. Namely, the same ionic radius of RE constituent for both mono-RE and solid-solution-RE system exhibited the same H_{irr} values at the same temperature and the same H_{irr} characteristics.

The hole doping-route scheme based on the BVS concept has been demonstrated to be extremely valuable in both understanding the relationship between the local atomic arrangement and the macroscopic properties of high-T_c superconductivity and tailoring the multi-layered copper oxides from the view point of materials chemistry. The result obtained in this work is also possible to explain by hole-doping route Π(3) [63]. Hole-doping route Π(3) functions only when changes of effective cation-anion length are focused at the Q-cation layer. In Fig. 3.4.-1, the data calculated for the oxygen-deficient $CuBa_2(RE_{1-x}Ca_x)Cu_2O_{7-\delta}$ phase ($\delta \approx 1$) is presented [63]: partial substitution of trivalent RE by divalent Ca introduces holes into the CuO_2 plane by increasing the effective distance, *i.e.* $(d_{ij} - R^0_{ij})$ value of the O-(RE,Ca) bond according to route Π(3). Considering obtained results from the BVS calculation and XANES measurements in the present study, hole-doping route Π(3) might be the same mechanism as this work, *i.e.* the mechanism of RE-size effect on the H_{irr} characteristics. These introduced holes around the CuO_2 plane by route Π(3) might be drifted from the holes in the $CuO_{1-\delta}$ chain to the CuO_2 planes retaining the total amount of holes. In other words, with decreasing the size of RE, holes in the $CuO_{1-\delta}$ chain would be moved towards CuO_2 plane by route Π(3) thus hole-density distribution

in the $CuO_{1-\delta}$ chain and CuO_2 plane changes to become more homogeneous over the crystal.

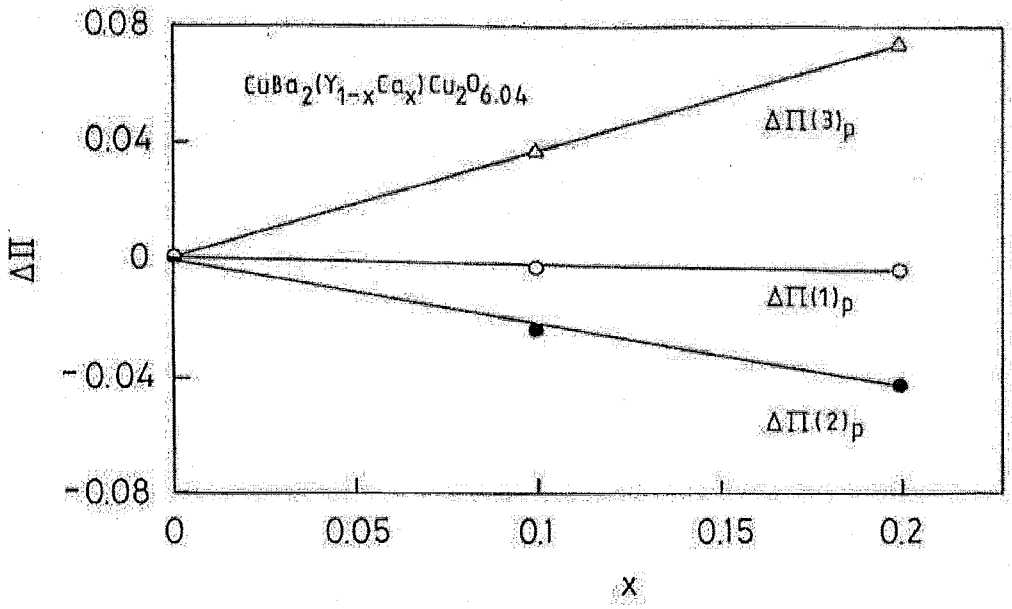

Fig. 3.4.-1 Function of the different hole-doping routes, Π(1)p, Π(2)p and Π(3)p with substitution of the *Q*-site Y^{III} by Ca^{II} in the $CuBa_2(Y_{1-x}Ca_x)Cu_2O_{6.04}$ phase. The contributions from the hole-doping routes are standardized against a sample with x = 0 [63].

For $CuBa_2RECu_2O_{7-\delta}$ with large *RE*'s, the difference in the hole density between the CuO_2 plane and the $CuO_{1-\delta}$ chain is quite large [50], *i.e.* less homogeneous distribution of holes. The hole distribution along the *c* axis is considered to become more homogeneous with smaller $r(RE^{III})$ in the $CuBa_2RECu_2O_{7-\delta}$ system. It has been established [15] that the more homogeneous the hole-density distribution along the *c* axis is, the better is the H_{irr} characteristics. Therefore, it was considered that the smaller sized *RE* induced more homogeneous hole-density distribution along the *c* axis by route Π(3) and thus the H_{irr} characteristics was enhanced as schematically shown in Fig. 3.3.4.-2.

From the material designing and tailoring points of view, the multi-layered copper-oxide structures the more homogeneous the hole distribution is along the piling direction of different blocks, the more enhanced is the H_{irr} characteristics, while the opposite is believed to apply in terms of increasing the value of T_c. In order to make clearer this concept, further study on the "quantitative" evaluation of hole distribution by means of O *K*-edge XANES measurements is an important challenge for further works. Moreover, an evaluation of "active" hole density, *i.e.*, hole density presiding over the superconductive properties, is one of the final aims in terms of research topic in high- T_c superconductive materials.

References

1. J.G. Bednorz and K.A. Müller, *Z. Phys. B* **64**, 189 (1986).
2. S. Uchida, H. Takagi, K. Kitazawa, and S. Tanaka, *Jpn. J. Appl. Phys.* **26**, L1 (1987).
3. K. Kishio, K. Kitazawa, S. Kanbe, I. Yasuda, N. Sugii, H. Takagi, S. Uchida, K. Fueki, and S.Tanaka, *Chem. Lett.* (2), 429 (1987).
4. M.K. Wu, J.R. Ashburn, C.J. Torng, P.H. Hor, R.L. Meng, L.Gao, Z.J. Huang, Y.Q. Wang, and C.W. Chu, *Phys. Rev. Lett.* **58**, 908 (1987).
5. S. Kondoh, Y. Andoh, M. Onoda, M. Sato, and J. Akimitsu, *Solid State Commun.* **65**, 1329 (1988).
6. Z.Z. Sheng and A.M. Hermann, *Nature* (London) **332**, 55 (1988).
7. Z.Z. Sheng and A.M. Hermann, *Nature* (London) **332**, 138 (1988).
8. H. Ihara, R. Sugise, M. Hirabayashi, N. Terada, M. Jo, K. Hayashi, A. Negishi, M. Tokumoto, Y.Kimura, and T. Shimomura, *Nature* (London) **334**, 510 (1988).
9. M. Uehara, T. Nagata, J. Akimitsu, H. Takahashi, N. Mori and K. Kinoshita, *J. Phys. Soc. Jpn.* **65**, 2764 (1996).
10. Y. Tokura, Kotaibutsuri, **25**, 618 (1990). (*in Japanese*)
11. T. Wada, A. Ichinose, H. Yamauchi, and S. Tanaka, *J. Ceram. Soc. Jpn. Int. Ed.* **99**, 420 (1991).
12. H. Yamauchi, *New Ceramics* **3**(10), 47 (1990). (*in Japanese*)
13. H. Yamauchi, M. Karppinen, and S. Tanaka, *Physica C* **263**, 146 (1996).
14. H. Yamauchi and M. Karppinen, *Superlatt. Microstructr.* **21A**, 127 (1997).
15. M. Karppinen and H. Yamauchi, *Mater. Sci. Eng. R* **26**, 51 (1999).
16. J. Akimitsu, S. Suzuki, M. Watanabe, and H. Sawa, *Jpn. J. Appl. Phys.* **27**, L347 (1988).
17. Y. Tokura, H. Takagi, and S. Uchida, *Nature* (London) **337**, 345 (1989).
18. M. Karppinen and H. Yamauchi, *Philos. Mag. B* **79**, 343 (1999).
19. M. Karppinen and H. Yamauchi, *J. Supercond.* **11**, 39 (1998).
20. R.D. Shannon, *Acta Cryst. A* **32**, 751 (1976).
21. T. Matsushita, E.S. Otabe, T. Matsuno, M. Murakami, and K. Kitazawa, *Physica C* **170**, 375 (1990).
22. T. Matsushita, E.S. Otabe, T. Nakane, M. Karppinen, and H. Yamauchi, *Physica C* **322**, 100 (1999).
23. R.S. Liu, C.Y. Chang, and J.M. Chen, *Inorg. Chem.* **37**, 5527 (1998).
24. K. Waki, T. Higuchi, S. I. Yoo, and M. Murakami, *Appl. Supercond.* **5**, 133 (1997).
25. H. Yamauchi, M. Karppinen, K. Fujimami, T. Ito, H. Suematsu, H. Sakata, K. Matsuura, and K. Isawa, *Supercond. Sci. Technol.* **11**, 1006 (1998).
26. Y.K. Du, G.C. Che, S.L. Jia, and Z.X. Zhao, *J. Solid. State. Chem.* **112**, 406 (1994).
27. T. Sakurai, T. Wada, N. Suzuki, S. Koriyama, T. Miyatake, H. Yamauchi, N. Koshizuka, and S. Tanaka, *Phys. Rev. B* **42**, 8030 (1990).
28. R. Pinto, L.C. Gupta, R. Sharma, A. Sequiera, and K.I. Gnanasekar, *Physica C* **289**, 280 (1997).
29. K.I. Gnanasekar, R. Pinto, A.S. Tamhane, L.C. Gupta, S.P. Pai, P.R. Apte, M. Sharon, and R. Vijayaraghavan, *Phys. Rev. B* **52**, 1362 (1995).
30. P.H. Hor, R.L. Meng, Y.Q. Wang, L. Gao, Z.J. Huang, J. Bechtold, K. Forster, and C.W. Chu, *Phys. Rev. Lett.* **58**, 1891 (1987).
31. J.M. Tarascon, W.R. McKinnon, L.H. Greene, G.W. Hull, and E.M. Vogel, *Phys. Rev. B* **36**, 226 (1987).
32. A. Oota, Y. Sasaki, M. Ohkuba, and M. Hioki, *Jpn. J. Appl. Phys.* **27**, L1425 (1988).
33. A.R. Moodenbaugh, M. Suenaga, T. Asano, R.N. Shelton, H.C. Ku, R. McCallum, and P. Klavins, *Phys. Rev. Lett.* **58**, 1885 (1987).
34. P. Somasundaram, A.M. Ram, A.M. Umarji, and C.N.R. Rao, *Mater. Res. Bull.* **25**, 331 (1990).
35. R. Balakrishnan, U.V. Varadaraju, and G.V. Subba Rao, *Modern. Phys. Lett. B* **3**, 653 (1989).
36. E. Hodorowicz, S.A. Hodorowicz, and H.A. Elick, *J. Alloys Compounds* **181**, 442 (1992).
37. V.R. Janovski, V.I. Voronkova, I.V. Vodolazskaja, L.N. Leont'eva, and T.P. Petrovskaya, *Supercond. Phys. Chem. Tech.* **2**, 30 (1989).
38. J.Z. Liu, L. Zhang, M.D. Lan, R.N. Shelton, and M.J. Flush, *Phys. Rev. B* **46**, 9123 (1992).
39. A.N. Lavrov and L.P. Kozeeva, *Physica C* **248**, 365 (1995).
40. R. Pinto, K.I. Gnanasekar, H.V. Keer, A.S. Tamhane, L.C. Gupta, and R. Vijayaraghavan, *Physica C* **227**, 120 (1994).
41. K.I. Gnanasekar, P. Selvam, H.V. Keer, R. Pinto, S.C. Purandare, A.S. Tamhane, L.C. Gupta, and R. Vijayaraghavan, *Appl. Phys. Lett.* **65**, 1296 (1994).
42. S.V. Samoylenkov, O.Yu. Gorbenko, I.E. Graboy, A.R. Kaul, and Y.D. Tretyakov, *J. Mater. Chem.* **6**, 623 (1996).
43. C. Michel and B. Raveau, *J. Solid. State. Chem.* **43**, 73 (1982).
44. A.M. Umarji and K.S. Nanjundaswamy, *J. Physics.* **29**, L611 (1987).

45. J. Shimoyama, Ph. D. Thesis, University of Tokyo, Tokyo 1998, p. 9.
46. H. Suematsu, M. Kawano, T. Onda, T. Akao, M. Hayakawa, H. Ogiwara, M. Karppinen and H. Yamauchi, *Physica C* **324**, 161 (1999).
47. K. Waki, T. Higuchi, S.I. Yoo, and M. Murakami, *Advances in Superconductivity XI*, In: *Proceedings of the 11th ISS'98*, B. Deaver and J. Ruvalds (Ed), Plenum, New York 1999, p.p. 521-524.
48. K. Kishio, J. Shimoyama, T. Kimura, Y. Kotaka, K. Kitazawa, K. Yamafuji, Q. Li, and M. Suenaga, *Physica C* **235-240**, 2775 (1994).
49. H.B. Radousky, *J. Mater. Res.* **7**, 1917 (1992).
50. S.V. Samoylenkov, O.Yu. Gorbenko, and A.R. Kaul, *Physica C* **278**, 49 (1997).
51. M. Guillaume, P. Allenspach, W. Henggerler, J. Mesot, B. Roessli, U. Staub, P. Fischer, A. Furrer, and V. Trounov, *J. Phys.: Condens. Matter* **6**, 7963 (1994).
52. D.E. Morris, J.H. Nickel, J.Y.T. Wei, N.G. Asmar, J.S. Scott, U.M. Scheven, C.T. Hultgren, A.G. Markelz, J.E. Post, P.J. Heaney, D.R. Veblen, and R.M. Hazen, *Phys. Rev. B* **39**, 7347 (1989).
53. Y. Yaegashi, S. Adachi, T. Wada, S. Takano, and H. Yamauchi, *Physica C* **190**, 433 (1992).
54. M. Karppinen, Y. Morita, J.M. Chen, R.S. Liu and H. Yamauchi, *Phys. Rev. B* **72**, 012501 (2005).
55. W.N. Kang and M.-Y. Choi, *Phys. Rev. B* **42**, 2573 (1990).
56. J.M. Chen, S.J.Liu, C.F. Chang, J.-Y. Lin, Y.S. Gou, and H.D. Yang, *Phys. Rev. B* **67**, 14502 (2003).
57. M. Karppinen, H, Yamauchi, T. Nakane, and M. Kotiranta, *Physica C* **338**, 18 (2000).
58. N. Kiryakov, S. Lee, M. Karppinen, H. Yamauchi, K. Yamawaki, and S. Sasaki, *Physica C* **357-360**, 350 (2001).
59. K. Yamawaki, Ph. D. Thesis, Tokyo Institute of Technology, Tokyo 2000.
60. T. Nakane, Y. Yasukawa, E.S. Otabe, T. Matsushita, M. Karppinen, and H. Yamauchi, *Physica C* **338**, 25 (2000).
61. T. Nakane, M. Karppinen, and H. Yamauchi, *Physica C* **357-360**, 226 (2001).
62. F. Licci, A. Gauzzi, M. Marezio, G. Radaelli, R. Masini, and C. Chaillout-Bougerol, *Phys. Rev. B* **58**, 15208 (1998).
63. M. Karppinen and H. Yamauchi, *Inter. Jour. Inorg. Mater.* **2**, 589 (2000).

4. CONTROL OF VALENCE MIXING IN A_2FeMoO_{6-w}

4.1. Introduction

4.1.1. *B*-site Ordered Double Perovskites

Research on double-perovskite compounds with the chemical formula of $A_2B'B''O_6$ (A= alkaline earth element, B', B'' = transition metal element) was initiated in the early 1950s [1-3] and expanded in the late 1950s [4,5]. From the late 1950s to the middle of 1970s many of the double perovskites were discovered and studied. The widest variation of double-perovskite compounds is possible when the B' and B'' cations have an average valence of four. Many compounds have been synthesized corresponding to the formulas, $A^{II}{}_2B'^{I}B''^{VII}O_6$, $A^{II}{}_2B'^{II}B''^{VI}O_6$ and $A^{II}{}_2B'^{III}B''^{V}O_6$ [6].

There are three B'/B'' sublattice types known for double perovskites: random, rock salt and layered as shown in Fig. 4.1.1.-1. The latter two sublattice structures are ordered arrangements. In general, if the charge difference between the B' and B'' cations is greater than two, complete ordering of these cations is observed. Therefore, the $A^{II}{}_2B'^{I}B''^{VII}O_6$ and $A^{II}{}_2B'^{II}B''^{VI}O_6$ compounds have shown complete ordering of the B'/B'' cations, whereas the $A^{II}{}_2B'^{III}B''^{V}O_6$ compounds have shown various degrees of order of B'/B'' cations. The actual degree of order of B'/B'' cations depends both on synthesis conditions and the particular A, B' and B'' cation species [7].

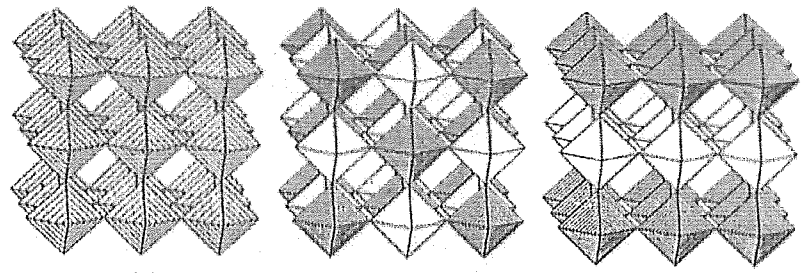

Fig. 4.1.1.-1 Typical sublattice types: (a) random, (b) rock-salt and (c) layered arrangements of B cations. (b) and (c) represent ordered structures.

In general, four factors control the B'/B'' arrangements in $A_2B'B''O_6$: difference in charge, ionic radius, atomic position and the ratio of A/B size, *i.e.*, the tolerance parameter. Among these factors, it is known that the difference in charge is the most influential parameter [1]. In order to quantify the effect of size and charge on sublattice type, many of the literature on $A_2B'B''O_6$ perovskites was reviewed [*e.g.*, 2,8,9] and a plot of B'/B'' charge difference *versus* B'/B'' ionic radius difference was concluded [1], see Fig. 4.1.1.-2. As Fig. 4.1.1.-2 shows, the cation arrangement on the B'/B'' sublattice of a stoichiometric double perovskite is controlled

primarily by the charge difference and secondarily by the size difference of the *B*'/*B*" cations. The figure clearly reveals that the rock-salt arrangement is dominant when the charge difference of *B*'/*B*" is greater than two, and the random arrangement is dominant when the charge difference is less than two.

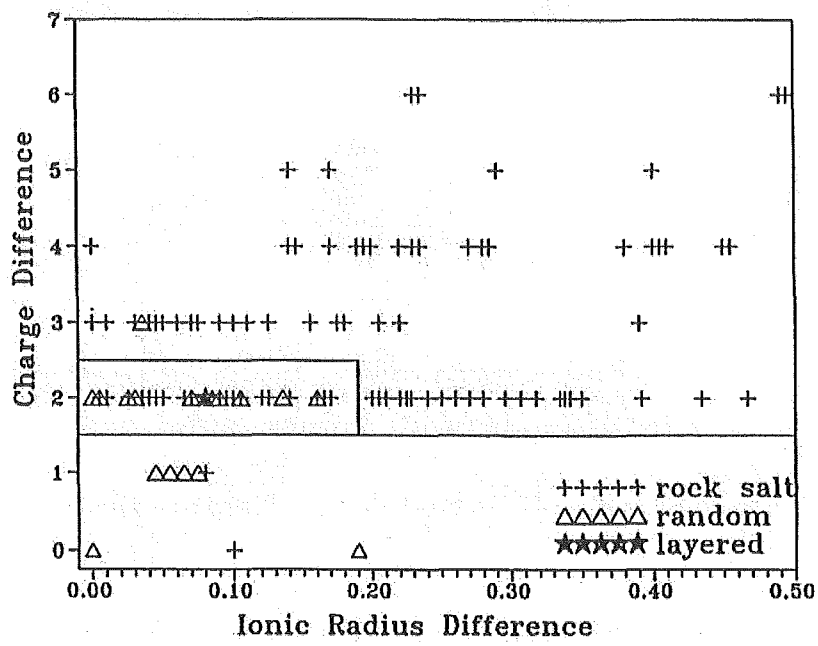

Fig. 4.1.1.-2 Differences of charge *versus* ionic radius of *B*'/*B*" cations for the $A_2B'B''O_6$ perovskites [1].

Ionic radius differences, electronic configuration differences and other aspects of crystal chemistry such as *A*/*B* size ratio also affect the sublattice type. As shown in Fig. 4.1.1.-3, the ionic radius difference between *B*' and *B*" affects the *B*'/*B*" arrangement and phase stability. With the exception of La_2CuMnO_6, the random arrangement is observed when the difference in the size of the *B*'/*B*", *i.e.*, $[r(B''^{IV})\text{-}r(Cu^{II})]$ where *B*' is Cu^{II} and *B*" represents various cation constituents with the valence value of IV, is less than 0.01 Å (Ln_2CuTiO_6, *Ln* = from La to Gd and Ln_2CuMnO_6, *Ln* = from Nd to Tm). The rock-salt arrangement is obtained when the size of *B*" is greater than 0.01 Å but less than 0.08 Å larger than copper (Ln_2CuIrO_6, *Ln* = from La to Nd). The layered arrangement is observed when the *B*" ion is greater than 0.08 Å but less than 0.12 Å larger than copper (La_2CuSnO_6). The tolerance factor also affects the *B*'/*B*" sublattice type, phase stability, crystal system, structure type and the degree of isotropic compression of the *B*'/*B*"-O bonds. As the lanthanide ionic radius decreases for any $Ln_2CuB''O_6$ series, the tolerance factor decreases. As the tolerance factor decreases, the limit of the stability field is reached and a mixture of phases or conversion to a non-perovskite structure appears. The perovskite-stability field is indicated by a dashed line in Fig. 4.1.1.-3. With increasing the difference of ionic radius of *B*'/*B*", *i.e.*, $[r(B''^{IV})\text{-}r(Cu^{II})]$, the stability field is reached at larger and larger values of the tolerance factor. This reflects the coupling of the increased two-dimensional *B*'/*B*" mismatch with the three-dimensional *A*/*B* size mismatch [1].

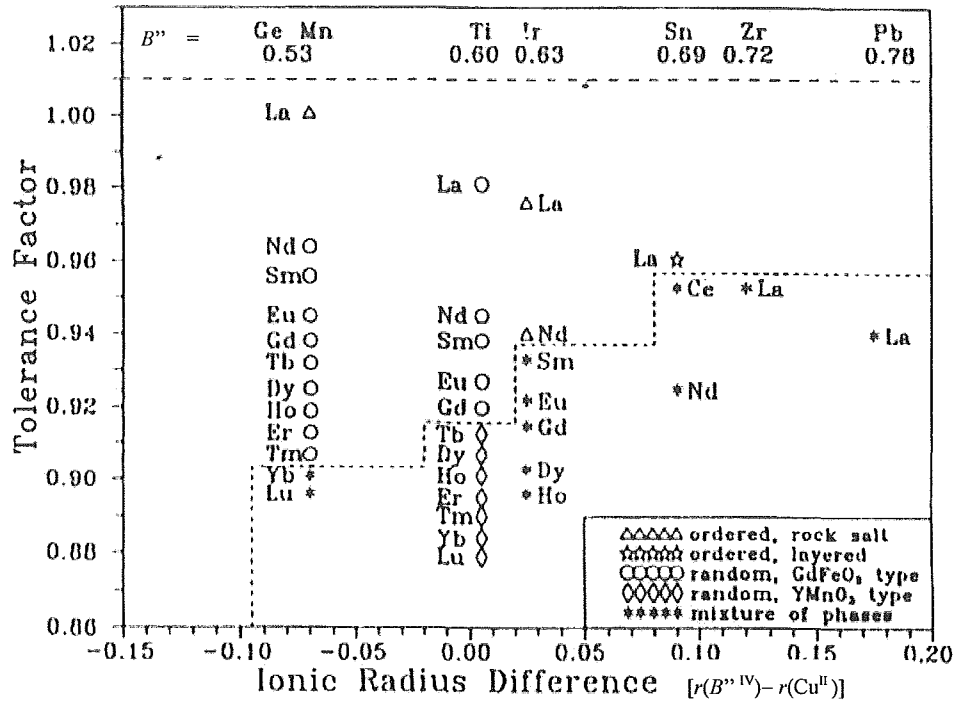

Fig. 4.1.1.-3 *B*-cation sublattice type for $Ln_2CuB''O_6$ as a function of tolerance factors and differences of ionic radius of *B*-cations [1].

Over three hundred *B*-site ordered double-perovskite compounds were synthesized from about 1950 to the present in total [1] and revealed that their physical properties are surprisingly various and complicated. For examples, this system exhibits magnetism/non-magnetism, conductivity/non-conductivity and shows various values of magnetic transition temperatures. Origins of these complicated properties are still open questions. Even categorizations of the physical properties in terms of the composition has not been established yet.

4.1.2. Magnetoresistivity and Halfmetallicity in A_2FeMoO_{6-w}

Halfmetallic compounds, *i.e.*, compounds with only one spin direction present at the Fermi level (E_F), are interesting for their potential applications at room temperature in spin electronics [10], *i.e.*, "spintronics", such as magnetic storage devices. These devices utilize low-field switching of the magnetization of adjacent decoupled ferromagnetic regions which are separated by barrier. Electrons may pass without losing their spin polarization across the barrier. Planar tunnel junctions with an insulating barrier [11,12], polycrystalline material with grain boundaries [11,13] and pressed powder with interparticulate contacts [11,14] are examples of device applications.

In the $Ln_{1-x}A'_xMnO_3$ manganites and Sr_2FeMoO_6 double perovskite, these compounds show two kinds of magnetoresistivity (MR) behaviour [15] originating from different mechanisms, *i.e.*, intrinsic intragrain-MR which can be observed in the vicinity of T_C and

extrinsic intergrain-MR (IMR) occurring below T_C. For the double-perovskite Sr_2FeMoO_6 and its related compounds, the tunneling across a barrier, *i.e.*, a grain boundary, of the spin-polarized carriers is the very root of MR property. Even in low magnetic fields, the MR characteristics are seen in this system. Domain structures of typical polycrystalline sample are schematically shown in Fig. 4.1.2.-1.

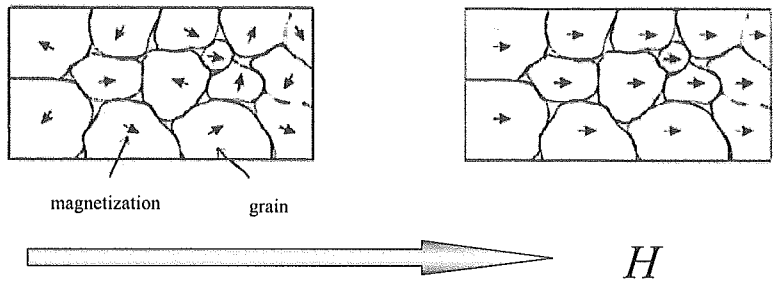

Fig. 4.1.2.-1 Schematic domain structures of polycrystalline sample.

A direction of magnetization in each grain is random without external field resulting in electrons with up spins and/or down spins are scattered at the grain boundary. However, low magnetic field value is possible to control the relative angle of magnetization of grains. Thereby the tunneling between two adjacent grains through a grain boundary would be probable when the canting angle of magnetization is relatively small [15-19] inducing the magnitude of resistivity among adjacent grains would be decreased. This is so-called "tunneling magnetoresistivity (TMR)" thereby IMR and TMR are regarded as the same process and this mechanism is believed to be origins of negative MR in this system. Henceforth in order to denote the intergrain-MR process, "TMR" is utilized in this thesis. Single-crystal thin film of (001)-oriented Sr_2FeMoO_6 have been epitaxially deposited to measure the grain-boundary resistance by utilizing a Wheatstone bridge [20]. The investigation found that only a high-field, weak MR, was observed through a bicrystal boundary demonstrating the low-field TMR observed below T_C in polycrystalline Sr_2FeMoO_6 is primarily due to spin-dependent transfer across grain boundaries and not to an intragranular effect. This tunneling-current phenomenon is due to highly spin polarized carriers [*e.g.*,21], *i.e.*, the highly polarized itinerant electrons, in A_2FeMoO_6 materials. Since the d^1 electron of Mo^V is expected to hop freely on one of the three half-filled t_{2g} orbitals of neighbouring Fe^{III}, the high spin polarization of the carriers are also assumed in this system [15]. Actually, a large TMR value at room temperature of ~5 % under ~1 T [17,21] in Sr_2FeMoO_6 has been reported. Hall coefficient measurements were carried out on Sr_2FeMoO_6 and Ca_2FeMoO_6 at 100 K [22] and the obtained result, especially for Ca_2FeMoO_6, found that the carrier concentration is quite different from those of manganite compounds which show MR properties [22,23]. This study suggests that the carrier concentration, and further, the influences of carrier on the material might be different from that of manganite oxides with MR properties. Also, the MR effect in Sr_2FeMoO_6 represents positive in epitaxial films of Sr_2FeMoO_6, while the polycrystalline samples show a negative effect [16]. This kind of "sample-state-dependence of MR", *i.e.*, changes in positive to negative MR due to the sample state, has not been reported in the manganite system.

Recently, there has been intense researches related to doped manganites, sparked by the observation of a drastic decrease in resistance in such samples on the application of an external magnetic field. This negative MR effect is now well known as the CMR effect. A huge CMR property has been observed mostly in $La_{1-x}Ca_xMnO_3$ and related compounds. However, there are two fundamental issues for widespread technological use of CMR manganite oxides. These are the low temperature and the high magnetic field required to obtain an appreciable negative MR response from these manganites. Since the CMR effect is the most significant close to the magnetic ordering temperature, there has been many studies for compounds with magnetic ordering temperature higher than the T_C (200 ~ 350 K) in manganites [24] but it was revealed that Curie temperatures of mixed-valence manganites of the type $Ln_{1-x}A_xMnO_3$ can not be increased above 400 K by applying any manipulation of the composition or stoichiometry [25]. Thus, it is questionable whether these compounds would be useful for the industrial applications. In this sense, oxides with high spin-polarization, high Curie temperature and exhibiting MR effect at low external fields are desirable [26].

In the *B*-site ordered double perovskites, the combination of *B*' of 3*d* element and *B*" of 4*d* or 5*d* element makes it easy to synthesize well ordered compounds because of large difference in the atomic radius between *B*' and *B*" [27-29]. In the 1960s, Galasso *et al.* [27] studied some compounds of the type A_2FeMoO_6 and reported that all the A_2FeMoO_6 members such as Ba_2FeMoO_6, Sr_2FeMoO_6 and Ca_2FeMoO_6 show high T_C values as well as a maximum value of T_C for A = Sr ($T_C \approx 420$ K). Based on this former study of A_2FeMoO_6, the iron based *B*-site ordered double perovskites have attracted a great deal of attention again with expectation of showing appreciable MR effect at room temperature. In 1998, it was reported that Sr_2FeMoO_6 [17] has a T_C of about 415 K and exhibits a pronounced negative MR at lower magnetic fields and higher temperatures compared to the doped manganites [24]. After this re-highlightment of the Sr_2FeMoO_6 compound, a huge number of studies related to iron based *B*-site ordered double perovskites were followed.

One of the theoretical researches established that the magnetic and MR properties of $A_2B'MoO_6$ and $A_2B'ReO_6$ double-perovskite compounds stem from an outstanding electronic structure where the itinerant electrons of Mo^V ($4d^1$: t_{2g}^1)/Re^V($5d^2$: t_{2g}^2) and localized electrons of Fe^{III} ($3d^5$: $t_{2g}^3 eg^2$) are antiferromagnetically coupled to give rise to a halfmetallic ground state with a high degree of spin polarization at E_F [17,19]. Although a correlation between halfmetallicity and TMR property has not been established yet, halfmetallicity is a favorable feature for TMR effect. If a material has high T_C value and is halfmetallic, it may exhibit MR effect even at room temperature. Therefore, the driving interest in the investigation of Sr_2FeMoO_6-type compounds derives from the fact that their high T_C values and high degree of spin-polarization promising candidates for applications as magnetoresistive materials and in devices.

It was found that a large low-field MR has been observed in polycrystalline samples with the *B*'/*B*" elements being not only Fe/Mo but also Fe/Re [19,21,30] and Cr/W [31]. Besides, the oxygen-deficient $LnBaCo_2O_{5+\delta}$ ordered perovskite shows superb MR properties [15].

4.1.3. Unique Physical Properties in A_2FeMoO_{6-w}

Only a very few of materials exhibit both metallicity and magnetism in the $A_2B'B''O_6$ double perovskites [32]. In early investigations, it was concluded that A_2FeMoO_6 [28] and A_2FeReO_6 [29] are the only ordered perovskites which show metallic conductivity. Later on, a study of thermoelectric power found that the metallicity of $(Sr_{1-x}Ca_x)_2FeMoO_6$ compounds deriving from Sr_2FeMoO_6 would be n-type [33]. It was attributed the origin of metallic behaviour in A_2FeMoO_6 to a valence degeneracy, *i.e.*, the overlapping of Fe $3d$ t_{2g} and Mo $4d$ t_{2g} orbitals such as Fe^{III}-Mo^{V} and Fe^{II}-Mo^{VI} [29]. The overlapping of these orbitals inducing the electron transfer from Fe^{II} to Mo^{VI}, rather than changes in the band width [34] would be a dominating factor for the conductivity in this system. The double-exchange interaction is regarded as an explanation for the metallicity of this system [35] and results of band-structure calculations predicted the metallicity, also [36]. In order to clarify the origin of metallicity in the A_2FeMoO_6 system from a different standpoint, the ρ-T measurements on the $Sr_2(Fe_{1-z}Mn_z)MoO_6$ melted-grown crystals with nearly the stoichiometric oxygen content were carried out. The measurements revealed that the magnitude of ρ gradually increased as z increases, *i.e.*, as the Mo $4d$-electron number decreases, and a metal-insulator transition occurred at z = 0.2. Since this metal-insulator behaviour correlated with the magnetic properties of $Sr_2(Fe_{1-z}Mn_z)MoO_6$, it might be summarized that the Mo $4d$-carriers are responsible for both the magnetic and transport properties in the A_2FeMoO_6 material [37].

The most unexpected physical properties of A_2FeMoO_6 system is an outstanding high magnetic transition temperature. It is because the magnetic Fe^{III} ions locate far apart each other which suggest a weak magnetic interaction in this compound. Generally, a high T_C values originated from a weak magnetic interactions is unusual and compounds with interactions between $3d^5$ ions mediated via different nonmagnetic species tend to be antiferromagnets due to the superexchange mechanism. The closely related antiferromagnetic Sr_2FeWO_6 system with $T_N \approx 37$ K [24,38] is one of the examples of this generalization. Besides, the Weiss constant θ was found to change from $\theta < T_C$ to $\theta > T_C$ with applying field in the $(Sr_{1-x}Ca_x)_2FeMoO_6$ system [33]. The value of θ is larger than that of T_C in the ferromagnetic compounds, whereas a $\theta < 0$ is normally found in a ferrimagnet. Varying a θ value with applying H is unprecedented, so far. Therefore, these backgrounds might imply novel and unique origins of magnetism in the A_2FeMoO_6 compounds [24].

4.1.4. Open Issues in A_2FeMoO_{6-w}

In the perovskite mixed valent manganites, it is believed that the double exchange mechanism in the presence of strong electron-phonon couplings arising from Jahn-Teller distortion is responsible for the CMR properties [39]. On the other hand, in the contrast to the manganites, it is more important to note that there is not any Jahn-Teller distortion and lattice

does not play any significant role in the Sr_2FeMoO_6 compound. Furthermore, the system is a cation-stoichiometric one in contrast to the manganites. Therefore, Sr_2FeMoO_6 is in principle a simpler system than $AMnO_3$. In spite of this apparent simplicity, there are surprisingly many open issues concerning the basic electronic and magnetic structures of this compound.

Among the ferromagnet halfmetallic compounds the best known materials are the mixed-valence manganites, *i.e.*, $(RE_{1-x}A_x)MnO_3$. Characteristics of ferromagnets in this system are observed when x = 0.3 [40,41]. CrO_2 is also the representative ferromagntic metal at room temperature [40,42]. In contrast to these examples, there has been an intense search for issue whether Sr_2FeMoO_6 and its related compounds are ferromagnets or ferrimagnets but a sufficient conclusion in this matter has not been obtained, yet. In the earliest proposed model for the magnetic structure of Sr_2FeMoO_6 consisting of nominally Fe^{III} ($3d^5$, S = 5/2) and Mo^V ($4d^1$, S = 1/2), the magnetic moments were considered to be ordered parallel inducing a ferromagnetic structure in which the moment of Mo^V is subtracted from that of Fe^{III}. Since the expected magnetic moments are approximately 5 μ_B for Fe^{III} and 1 μ_B for Mo^V, respectively, the saturated net magnetic moment of less than 4 μ_B usually observed from the *M-H* measurement at the highest external field implied a ferrimagnetic ordering model [43]. This ferrimagnetic modeling was reported by Nakayama *et al.* in1968 [44] based on neutron diffraction data. Such a ferrimagnetic model was attributed to Fe^{III} magnetic moments antiferromagnetically coupled with Mo^V spins. Fe^{III} forms the high-spin state splitting the *d* orbitals into spin-up and spin-down states. The empty spin-down states (π^*-β) of Fe^{III} degenerate to the one electron occupied spin-down states (π^*-β) of Mo^V which may lead to the formation of a narrow band. The electrons in this band have their spins antiparallel to the localized spins in the spin-up states (σ^*-α and π^*-α) of Fe^{III} [29,45]. However, these initial suggestions [17] of the ferrimagnetic arrangement model was claimed to be doubtful [46] from the later neutron investigations. It was because no magnetic moment could be observed on the Mo sites [46]. Nevertheless, a subsequent study reported the existence of the magnetic moment of 1 μ_B on the Mo site [47]. Not only neutron studies but also recent investigations applying many experimental techniques lead various conclusions in terms of ferromagnetic/ferrimagnetic issue in this compound. The critical behaviour of Sr_2FeMoO_6 was searched through measurements of the magnetization, susceptibility and temperature derivative of the resistivity by Yanagihara *et al.* [36]. They found that this material belongs to three-dimensional Heisenberg ferromagnet such as Ni or Fe, rather than a typical ferrimagnet [36,48,49]. The ferromagnetic modeling was also supposed by an ESR study [50] suggesting an origin of the ferromagnetic ordering is derived from a double exchange-like interaction as in the CMR manganites. Against these considerations, quite new theory has been reported. Resultants of x-ray magnetic circular dichroism (XMCD) which detects the magnetic moments at the Mo site as well as at the Fe and O sites directly, clarified [51] that the dichroic signal of XMCD spectra at the Mo 3*p* edge was negligible indicating the magnetic moment at the Mo sites was below the detection limit. This study also demonstrated that the delocalized states are not solely Mo 4*d* derived states but a substantial admixture of O 2*p* states. On the basis of experimental facts in this research, the delocalized electron spin density

coupling antiferromagnetically to the localized Fe spins was concluded to delocalize over several sites including the neighbouring FeO_6 octahedra. This indicates a novel origin of magnetism [24,52] which is different from the conventional double-exchange mechanism. Namely, the localized Fe S = 5/2 state couples antiferromagnetically with the spin density of delocalized S = 1/2 state to form S = 2 state. A series of these investigations indicates that the identification of ferromagnetism/ferrimagnetism of this compound is extremely complicated and is still open question.

Even though arguments about the ferromagnetic/ferrimagnetic states are under the discussion and magnetization measurements have not so far been able to provide conclusive evidence of this problem [53] in the A_2FeMoO_6, the isovalent substitution at *A* site in this system might generate an influence not only on the *M-T* and *M-H* properties (which are described in the following section) but also on the ferromagnetic/ferrimagnetic state. From studies of neutron powder diffraction [26], the magnetic moment in Ba_2FeMoO_6 amounted to μ_{Fe} = 4.06(9) μ_B, whereas no magnetic moment was detected on the Mo site within the experimental error, *i.e.*, μ_{Mo} = -0.1(1) μ_B. In the case of $BaSrFeMoO_6$ possessing a cubic structure, the values of magnetic moment were determined as μ_{Fe} = 4.32(8) μ_B and μ_{Mo} = 0.06(10) μ_B. Ca_2FeMoO_6 showed different magnetic structure from that of Ba_2FeMoO_6 and $BaSrFeMoO_6$ cubic compounds since a significant moment was refined on the Mo site orienting antiparallel to the Fe moments, *i.e.*, the moment amounted to μ_{Fe} = 3.91 (7) μ_B and μ_{Mo} = -0.7(3) μ_B at 2 K. These moment values are in agreement with refinement results obtained from other group [22] in this compound revealing a small ordered magnetic moment on the Mo site of μ_{Mo} = -0.76 ± 0.06 μ_B antiferromagnetically coupled with the Fe magnetic moments (μ_{Fe} =3.2(1) μ_B) at 2 K resulting in a ferrimagnetic configuration. In the case of Sr_2FeMoO_6, the magnetic structure was refined as μ_{Fe} = 3.72(6) μ_B and μ_{Mo} = -0.54(7) μ_B, respectively [26] thus it would be possible to consider that this tetragonal compound possesses intermediate characteristics of magnetism between that of cubic and monoclinic compounds.

4.2. Experimental Procedure

Many of the perovskite-type oxides can be synthesized through a high-temperature solid-state reaction between binary oxide powders which are stable in air. However, it is often advantageous to choose carbonates and nitrates, *etc.*, instead of the oxides as starting materials, if they can be obtained in smaller particle sizes to insure quicker reactions or if they are much purer. On the other hand, some of the perovskite-type compounds can only be obtained applying special synthesis techniques. Fresia *et al.* [54] found that in the preparation of the provskite compounds with the general formula $A_2B'^{II}WO_6$ where *A* is Ba or Sr and *B'* is Fe, Co, Ni or Zn, alkaline earth tungstates always could be detected in the final products. Similar results have been observed for molybdenum compounds. Regrinding and refiring of samples often enable us reduce the amount of tungstates or molybdates present in the products but each compound has to

be treated as a separate case for which the best sintering temperature and sintering time must be determined.

In synthesizing perovskites containing Fe^{II} and Co^{II} the valence state is retained by sintering the sample in an evacuated sealed silica/quartz capsule or in a non-oxidizing atmosphere. Divalent Fe or Cr ions can be obtained in a compound by the mixtures of equal amounts of metallic Fe and Fe_2O_3 or Cr and Cr_2O_3, respectively with the other oxide constituents. For example, Galasso *et al.* [54] prepared $Ba_2Fe^{II}_{0.66}Ta_{1.34}O_6$ by means of mix the reactants according to the reaction:

$$BaO + 1/9\ Fe_2O_3 + 1/9\ Fe + 1/3\ Ta_2O_5 \rightarrow Ba_2Fe_{0.66}Ta_{1.34}O_6. \qquad (4.2.\text{-}1)$$

compressing the sample and sintering it at 1000 °C for 24 hours in an evacuated sealed silica capsule. Furthermore, Patterson *et al.* [54] demonstrated that they could prepare the $A_2B'^{III}WO_6$ and $A_2B'MoO_6$ compounds with a mixture of the metal trioxides and the metals as starting materials in order to obtain pentavalent tungsten and pentavalent molybdenum, respectively.

For the synthesis of the *B*-site ordered double-perovskite samples a reduced oxygen partial pressure in the range of about $10^{-9.8} \sim 10^{-13.5}$ atm at 1200 °C were required in order to obtain these phases [55]. In an encapsulation synthesis technique with a metallic oxygen-getter, it is possible to control oxygen-partial pressure by varying the getter of oxygen component or sintering temperature. The oxygen-partial pressure is calculated from the standard-free energy for the oxidation reaction of the metal species. Thus, the mixtures of sample powders were sintered together with Fe grains at 1150 °C. Under these conditions the oxygen partial pressure is expected to be appropriate for the synthesis of *B*-site ordered double-perovskites. Therefore, an oxygen-getter-controlled low-O_2-pressure encapsulation technique [56] was applied for the synthesis of *B*-site ordered double-perovskites, in this study.

A series of A_2FeMoO_{6-w} samples with A = Ba, $Ba_{0.8}Sr_{0.2}$, $Ba_{0.5}Sr_{0.5}$, $Ba_{0.2}Sr_{0.8}$, Sr, $Ca_{0.2}Sr_{0.8}$, $Ca_{0.8}Sr_{0.2}$ and Ca, was prepared by means of an oxygen-getter-controlled low-O_2-pressure encapsulation technique [56] from stoichiometric mixtures of high-purity (99.9 - 99.99 %) powders of ACO_3 (A = Ba, Sr and Ca, Fe_2O_3 and MoO_3. The powder mixtures were calcined in air at 900 °C for 15 hours in order to remove the carbonate included in the starting materials. Then the calcined powders were pelletized and sintered in an evacuated and sealed fused-quartz ampoule that contained the sample pellets together with fine Fe grains (99.9 % up). The Fe grains absorb the oxygen evolved from the samples during the sintering, *i.e.*, Fe act as a getter for oxygen. The empty space inside the ampoule was filled with a fused-quartz rod in order to create a more homogeneous atmosphere in the ampoule. Each sample was fired at 1150 °C for 50 hours. Under these conditions the oxygen partial pressure is expected to equilibrate at 2.6×10^{-13} atm due to the redox couple of Fe/FeO [57]. After synthesis the ampoule was quenched onto a thick Cu plate immediately from the synthesis temperature.

Additionally, for the ^{57}Fe Mössbauer measurements four samples with the *A*-site composition of A = Sr, $Ca_{0.25}Sr_{0.75}$, $Ca_{0.5}Sr_{0.5}$ and $Ca_{0.75}Sr_{0.25}$ were synthesized in Taiwan using a

flowing H_2/N_2 gas technique [45]. For these samples, the final sintering was carried out in a 5 % H_2/N_2 gas mixture in order to crate a reduction atmosphere at 1000 °C for 26 hours and then 12 hours after an intermediate grinding. This technique is one of the common synthesis methods employed for Sr_2FeMoO_6 system and related compounds. Employment of these two different techniques enable us to compare the dependence of the valence of iron and the electrical-magnetic characteristics on the synthesis method.

The magnetic properties of a sires of A_2FeMoO_{6-w} samples are studied by measuring *M-H* with various temperatures and *M-T* at fixed *H*. The saturation magnetization (M_S) value of the compound was determined by extrapolating the obtained *M* value at $H = 5$ T that satisfies the magnetic saturation of this system to the $H = 0$ T level from the resultant of *M-H* plots. In the magnetization measurements, the sample amount was kept relatively large and essentially constant, *i.e.* at 30 ± 10 mg for double-perovskite compounds, in order to obtain sufficient magnetization signal.

Particularly, a condition of grains, *i.e.*, whether the sample grains are melt-grown or not, influences the electrical transport properties. Since the melt-grown particles affect the distance of electron tunneling, the observation of grains of A_2FeMoO_{6-w} samples with MR properties induced by the tunneling magnetoresistance is required. For this compound, the grain size is also important since each particle possesses magnetic boundary. The boundary acts as a barrier of the tunneling of electrons. To confirm the particle size and to check whether the sample grains are melt-grown or not, the field-emission scanning electron micrographs (SEM; Hitachi FE-SEM S-45500) with EDS were taken for the A_2FeMoO_{6-w} samples at an accelerated voltage of 15 kV.

Statistical evaluation, *i.e.*, Plani-metric method, was applied for the estimation of the grain size for the double-perovskite compound because of non-anisotropy of the grain shape. In the Plani-metric method, the analyzed circle area (area *A*) was determined on the printed grain image photograph and the amount of grain in the circle (n_c) and on the circle (n_j) was counted, respectively. The amount of grain in a unit area (N_G) was calculated as

$$N_G = \frac{n_c + 0.5n_j}{\frac{A}{m^2}}, \qquad (4.2.-2)$$

where *m* represents magnification. Therefore, the average grain size $d_{ave.}$ is determined as following formula:

$$d_{ave.} = \frac{2}{(\pi N_G)^{1/2}}. \qquad (4.2.-3)$$

The grain size of each sample was confirmed to lie in a narrow range of 2 to 6 μm for A_2FeMoO_{6-w} samples.

For the magnetic compounds the microstructures related to magnetism, *i.e.*, magnetic

boundaries/domains, are crucial crystallographic parameters for the physical properties. Thus, the direct observation of magnetic boundaries/domains and revealing the correlation between magnetic structures and antiphase boundaries (APBs) are interesting research topics.

The magnetic boundaries/domains and APB for fundamental compound, *i.e.*, Sr_2FeMoO_6 sample, was observed by means of Lorentz TEM (HITACHI HF-3000) at an accelerating voltage of 300 kV in National Institute for Materials Science (NIMS) in Tsukuba, Japan. The magnetic structures were observed in the Lorentz mode without an external field meanwhile the APB was observed in the dark-field mode. For the observation, sample was made into thin film by means of ion milling technique.

4.2.1. Determination of Valence of Iron

Robin and Day have divided mixed-valence compounds such as these into three different classes, *i.e.*, class I, class II and class III [58]. Class I categorized compounds are localized and have a very large barrier to electron transfer between the different valences with a gradual rate of transfer. Compounds with a feature of class III are delocalized with no barrier to electron transfer and ultrafast rates, while class II compounds possess properties intermediate those of class I and III. The first case is that only one element takes some valence states in relation to the element of the same kind. This is observed in *A*-site ordered double perovskites, *e.g.*, $BaSm(Cu_{0.5+x}Fe_{0.5-x})O_{5+\delta}$ [59]. In this case, Fe takes two different valence states. The class III is that the mixed-valence state is taken in between the different kind of elements, *e.g.*, *B*-site ordered perovskite compounds such as Sr_2FeMoO_6 [60]. For instance, the valence of Fe can be taken $Fe^{II/III}$ (and $Mo^{V/VI}$) state and the other is Fe^{III} and Mo^{V}.

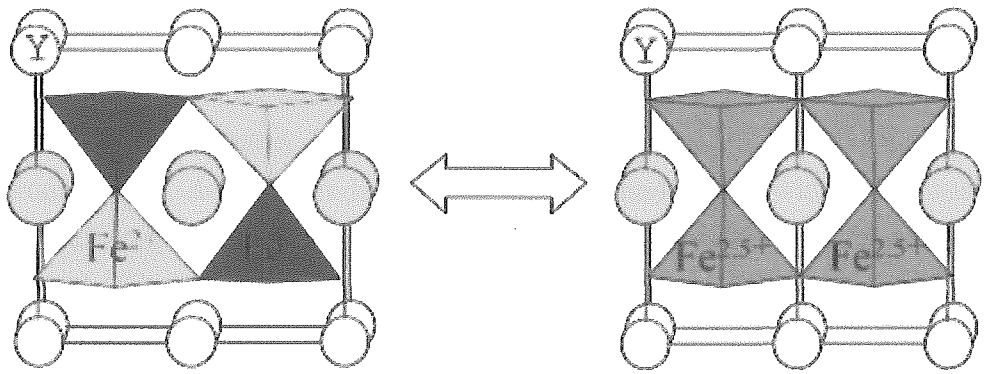

Fig. 4.2.1.-1 Typical examples of the class II (left) and class III (right) mixed-valence state for the *A*-site ordered double-perovskite $YBaFe_2O_5$. Below the Verway transition temperature, Fe takes two different valence states, *i.e.*, Fe^{II} and Fe^{III}, exhibiting a feature of the class II mixed-valence state. On the other hand, Fe possesses $Fe^{2.5+}$ (or $Fe^{II/III}$) above the Verway temperature resulting in class III mixed valency. The mixed valence transition is induced at Verway temperature in this compound.

There are several methods to evaluate the valence value of Fe for A_2FeMoO_6 samples, *e.g.*, BVS calculation from neutron powder diffraction (NPD) data [61], the measurements of XANES spectroscopy [VI], photoemission spectroscopy (PES) [62] and ^{57}Fe Mössbauer

spectroscopy [60] *etc.* So far, the mixed-valency of Fe in the Sr_2FeMoO_6 has been accepted in ^{57}Fe Mössbauer studies [43,63], though trivalent interpretations has been reported as well [64]. Furthermore, study of the Fe $L_{2,3}$-edge XANES spectra for Sr_2FeMoO_6 have been proposed both Fe^{III} [51,65] and $Fe^{II/III}$ [62]. In terms of Mo, a mixed-valence state, $Mo^{V/VI}$ [66] was suggested by a NMR study. Based on these various experimental facts in terms of valence states of Fe/Mo, the valence distribution of Fe/Mo should be clarified. Using a series of samples of the A_2FeMoO_{6-w} system we are able to know the influence of $r(A^{II})$ on the Fe valence (V_{Fe}), and further, are able to evaluate the charge distribution of *B*'/*B*"-sites that might be the most dominant factor for the physical properties of this compound.

In this study, two techniques were employed for the confirmation of the valence of Fe for a series of A_2FeMoO_{6-w} sample, *i.e.*, the measurements of ^{57}Fe Mössbauer spectroscopy and Fe *K*- and $L_{2,3}$-edge XANES.

4.2.1.-1 ^{57}Fe Mössbauer Measurement

The ^{57}Fe Mössbauer spectra of the A_2FeMoO_{6-w} samples were recorded at 77 K in transmission geometry. The absorbers were made by spreading the sample materials mixed with epoxy resin evenly on an Al foil. A linear Doppler velocity sweeping from –11.15 to 11.15 mm/s was used. A Cyclotron Company ^{57}Co:Rh (25mCi, January 2002) source was used for producing the 14.4 KeV Mössbauer γ quanta. For the fit of the obtained data the following hyperfine parameters were applied: the internal magnetic field experienced by the Fe nucleus (*B*), the chemical isomer shift relative to α-Fe (δ), the quadrupole coupling constant (eQV_{zz}), the resonance line width (Γ), and the relative intensity of the component (*I*) [60]. The full Hamiltonian of combined electric and magnetic interaction was used to fit the spectra by these parameters.

The following conditions and constrains were applied: (*i*) for each component a certain variation in the parameter *B* was allowed in order to simulate the fact that the internal fields have a certain spread. A Gaussian distribution was assumed and its width (ΔB) was also introduced as a fit parameter. (*ii*) the θ angle between the wave vector of the γ quanta and the direction of *B* was fitted. This angle depends on how the applied field B_{ext} manages to align the magnetization the three main components. The asymmetry parameter, η, and the additional angles α and ϕ were fixed at zero. (*iii*) all spectral components were constrained to have equal line width Γ.

4.2.1.-2 X-ray Absorption Near-Edge Structure (XANES) Measurement

All the XANES measurements were performed at National Synchrotron Radiation Research Center (NSRRC) in Taiwan with an electron beam energy of 1.5 GeV and maximum stored current of 240 mA [34]. For the XANES measurement the sample was ground to pass

through 400-mesh sieve to fulfill the requirement that the size of the particles of the sample was smaller than the absorption length in the material. The resultant powder was rubbed onto Scotch tape with homogeneous thickness. The measurements were performed in transmission mode at the Wiggler beamline BL-17C with a double-crystal Si (111) monochromator. Gas-ionization chambers filled with gas mixtures of N_2-He and N_2-Ar were used as detectors to measure the incident (I_0) and transmitted (I) photon intensities. On the other hand, as a reference for the calibration at the Fe K edge, the spectrum of Fe metal foil was simultaneously monitored. The Fe $L_{2,3}$-edge spectra were recorded by measuring the sample drain current in an ultrahigh vacuum chamber with 10^{-9} Torr atmosphere. The incident photon flux (I_0) was monitored at the same time by using a Ni mesh located after the exit slit of the monochromatic beam. The absorption measurements were normalized to I_0. The reproducibility of the absorption spectra of the same sample in different experimental runs was found to be good. All the measurements were performed at room temperature [VI].

4.2.2. Physical Property Measurement System (PPMS)

In order to study the electrical transport properties, a standard four-point probe technique was employed in this work. The resistance (ρ) and the magnitude of MR were carefully evaluated for fundamental B-site ordered double-perovskite compounds, *i.e.*, samples with A = Ba, Sr and Ca. The values of ρ and MR were calculated from the measured electrical resistivity (R) values with Physical Property Measurement System (Quantum Design PPMS-9) apparatus.

In order to investigate the conductivities of the samples and the field-dependence of ρ/MR properties, resistivities were measured in a field-scanning mode at constant various temperatures. The scanning in field steps of 0.05 T, 1 T from H = 0 to 1 T, form H = 1 to 7 T, respectively, was carried out since this compound is expected to show low field MR properties thus the precise measurement would be required for the low H region. The magnitude of MR was evaluated as follows:

$$\mathrm{MR}(H,T_{\mathrm{fixed}})(\%)=\left[\frac{\rho(H,T_{\mathrm{fixed}})-\rho(H_0,T_{\mathrm{fixed}})}{\rho(H_0,T_{\mathrm{fixed}})}\right]\times 100 \quad . \qquad (4.2.2.\text{-}1)$$

In this measurement the samples were shaped into pellets with a cross-section 2 to 3 mm^2 with Au wires as electrodes.

4.2.3. Multivariate Data Analysis

On the basis of long research history of B-site ordered double-perovskite compounds it has been prospected that the crystallographic fine structure of the compounds might correlate

with the physical properties such as electromagnetic properties and conductivities. Concerning the detailed crystallographic structure, bond lengths of cation-oxygen, *i.e.*, distances between *A*-O, *B*'/*B*"-O, thereby valences of *B*'/*B*" cations, ionic radius of *A*, *B*' and *B*" cations, degree of order at *B*'-/*B*"-site, *B*'-O-*B*" bond angles, spin state of *B*' cation, lattice parameters, bond angle of lattice, tolerance factor and so on must be correlated to each other and be dominant parameters for the properties of the material. Consequently, the appearance of various and complicated properties of *B*-site ordered double perovskites can be considered a multivariate problem.

Multivariate analysis has the following advantages: it may (*i*) handle many variables and few observations, (*ii*) handle few variables and many observations, (*iii*) handle almost square matrices of any size, (*iv*) cope with missing data. Thus, multivariate data analysis is versatile and useful [67]. Multivariate programs, *i.e.*, the "principal component analysis (PCA)" and the "Projection to Latent Structures by means of partial least squares (PLS)" methods, can be approached by so-called projection methods which allow both qualitative and quantitative examination of correlations between variables [68]. PCA analysis can be utilized for searching trends, outliers, dominating variables, groups and clusters among the data. The PLS method is an extension of the PCA analysis and is used when information on the dependence between X (cause) and Y (response) variables is desired. The relative importance of each X variable on a selected Y can be evaluated and furthermore, quantitative prediction of Y value is possible for a new observation.

In the present work, PCA was applied for the qualitative evaluation of relations between fine structural variables (X variables) mentioned above and values of T_C in the ferrimagnetic $A_2B'B''O_6$ phases. Quantitative modeling in the $A_2B'B''O_6$ system was also performed by PLS analysis. Moreover, in order to find essential factors for magnetism in the $A_2B'B''O_6$ compounds, "PLS discriminate analysis (PLSDA)" was carried out for two distinct groups, *i.e.*, magnetic (ferrimagnetic and antiferromagnetic) compounds and paramagnetic (paramagnetic) compounds, of various compositional $A_2B'B''O_6$ phases. All the data utilized for these analyses were adopted from a number of room temperature neutron/x-ray diffraction studies published for these phases. In this study, searching trends, outliers, quantitative modeling for T_C value and qualitative evaluation of the type of magnetism in the $A_2B'B''O_6$ system was discussed in terms of structural parameters only.

4.2.3.-1 General Consideration of Multivariate Data Analysis

The basics of multivariate data analysis are outlined in terms of the projections of multidimensional spaces. With regard to projections, the most fundamental aspect is that a row in a data table can be interpreted as point swarm in a multidimensional space. This allows multivariate data and models to be understood and analyzed in terms of spaces and geometrical configurations within these spaces [67] which are represented as points, lines and hyper-planes in these spaces. Multivariate data analysis has a good ability to comprehend structures in two- and

three-dimensions. The understanding of these few dimensions can then be generalized to higher dimensional space spanned by many variables.

In the multivariate data analysis we have a *K*-dimensional coordinate system with *K* variables. For instance, if we have a data table **X** with $K = 3$ variables denoted by x_1, x_2 and x_3, a three-dimensional coordinate system consists of three-coordinate axes. In this case, each observation in **X** is then characterized by three numerical values. The three values of an observation are represented by one point in this space. Then the first principal component (PC 1) of the data set is available by computing the data. This component is the line in the *K*-dimensional space that the best approximates the data in the least square sense. This line goes through the average point of the data. Each observation can now be projected onto this line in order to get a coordinate value along the PC-line. Usually, one principal component is insufficient to model the systematic variation of a data set. Thus, a second principal component, PC 2, is required. The second PC is also a line in the *K*-dimensional variable space which is orthogonal to the first PC. This line also passes through the average point and improves the approximation of the X-data as much as possible. When two PCs have been derived they together define a plane, *i.e.*, a window, into the *K*-dimensional space. By projecting all the observations onto this low-dimensional sub-space and plotting the results, a visualize structure of the investigated data set can be obtained. The coordinate values of the observations on this plane are called scores [67]. This conversion process of data table is called projection. Through the projection, all the observations of **X** are displayed in *K*-space as a swarm of points. This window oriented such that it provides a good overview of the data and hence enables their interpretation. We have accomplished a projection from the original three-dimensional space down onto a two-dimensional window. The idea of projections can now mathematically be extended from two and three dimensions to any number of dimensions, *i.e.*, any number of variables.

The information in the data is seen as patterns along these lines, planes, and hyper-planes. The direction of the projection plane gives information about which variables are important, which are not and how the important variables combine to separate the clusters of observations, or to define trends among the observations [69]. PCA and PLS methods give a summary of data table which can be analyzed graphically by means of two plots, the "score" and the "loading" plots. The score plot is a summary of the relationship among the observations, while the loading plot is a similar summary of the variables [67]. In the score/loading plots observations/variables contributing similar characteristics/information are grouped together, *i.e.*, they are correlated. When observations/variables are negatively correlated they are positioned on opposite sides of the plot origin, in diagonally opposed quadrants. Furthermore, the distance to the origin also conveys information. The further away from the plot origin, the stronger impact that variable has on the model in the loading plot. Thus, un-influential variables are existed around the origin of the plot (0, 0).

Abbreviations and notation of multivariate data analysis is listed in Appendix 1. In the multivariate data analysis, bold upper case, *e.g.*, **X**, represents matrices, whereas column vectors are denoted by bold lower case characters, *e.g.*, **t**.

4.2.3.-2 PCA and PLS

PCA describes the correlation structure in **X** [67]. This overview reveals the relationship between observations and variables and among variables themselves [67]. Clarifying the relationships among the variables with PCA analysis it is possible to get information of (*i*) which variables contribute similar information to the PCA model and (*ii*) which provide unique information about the observations [67]. Thus, PCA analysis is useful for generalizing a data table [67]. PLS method also has this ability but PLS has an extended ability compared with PCA. PLS can analyze data with strongly correlated, noisy and numerous X-variables and also simultaneously model several response variables, **Y**.

Assumptions underlying the PLS method are (*i*) latent variables: the PLS modeling supposes that the investigated system is influenced by underlying LV's, (*ii*) alternative derivation: this means the foundation of LV-model is a Taylor expansion, (*iii*) homogeneity: the investigated system is thought to be in a similar state throughout all the investigation and (*iv*) non-linear PLS: a transforming selected X-variables/X-scores to qualitative variables coded as sets of dummy variables is assumed to be possible [69].

With appropriate data and a workable PLS model, it is possible to find out (*i*) how the X-variables influence the Y-variables, (*ii*) how the Y-variables correlate with each other and (*iii*) how to adjust the X-variables to get a desired profile of the Y-variables. The main objectives of PLS analysis are (*i*) to model **X** and **Y** and (*ii*) to predict **Y** from **X** for new observations.

Similar to PCA, the **X** matrix can be represented as N observations with K dimensions in the PLS. Moreover, Y-variables possessing M dimensions denoted by $\mathbf{y}_m$ (m = 1, 2, ..., M) consists of the whole data set of PLS. Therefore, data set from the two matrices **X** and **Y** of dimensions (N * K) and (N * M), respectively are utilized for this analysis [69]. The X-scores, *i.e.*, $\mathbf{t}_a$, derived by the PLS analysis are predictors of **Y** and also model **X**. The X-scores are estimated as linear combinations of the original variables $\mathbf{x}_k$ with the coefficients, *i.e.*, weights, represented by w^*_{ka} (a = 1, 2, ..., A). The correlations employed by the PLS method are described in Appendix 2.

PLS score plots of the t/u-type provide information about deviations from the dominating **X/Y** correlation structure. As well as detecting outliers in the **X/Y** relationship, the PLS **t/u** scores are useful in identifying departures from linearity between **X** and **Y**. Moreover, by plotting the t-vectors against each other and the u-vectors against each other, we may examine the patterns in the X- and Y-space, separately [67]. Large Y-residuals indicate that the model is poor. Residuals for X estimates the part not used in the modeling of **Y** in the PLS [67,69]. Geometrically, the tighter the scatter around the dotted diagonal, the stronger the correlation between **X** and **Y** in the second PLS-model dimension [67].

4.2.3.-3 Predictions Based on PLS

When a PLS-model is judged reliable through the interpretation of model parameters, *i.e.*, diagnostic tools, cross-validation, *etc.*, it is possible for predicting the Y-data for new observations. A new observation to be predicted is judged similar to the observations of training set if it is located inside the cylindrical tolerance volume in the X-space. Then, its projection on the X-model, t, can be entered into the t/u inner relation, thus producing a u-value for that dimension. This u-value (or several u-values if there is more than one component) defines a location on the Y-space model. This location corresponds to a predicted value for each response variable [67].

4.3. Results and Discussion

For the A_2FeMoO_{6-w} system, it has been reported that the grain size [70,71] and the degree of Fe/Mo order at the *B*-cation site [72,73] strongly affect the magnetotransport characteristics. In order to investigate "intrinsic characteristics" of the A_2FeMoO_{6-w} system, the grain size, the oxygen content and the degree of Fe/Mo order are required to be controlled for all the samples. A systematic study on the A_2FeMoO_{6-w} sample series (A = Ba, $Ba_{0.8}Sr_{0.2}$, $Ba_{0.5}Sr_{0.5}$, $Ba_{0.2}Sr_{0.8}$, Sr, $Ca_{0.2}Sr_{0.8}$, $Ca_{0.25}Sr_{0.75}$, $Ca_{0.5}Sr_{0.5}$, $Ca_{0.75}Sr_{0.25}$, $Ca_{0.8}Sr_{0.2}$ and Ca) is reported for the present study aiming at clarifying the A size-only-dependent effects, *i.e.* isovalent-cation-substitution effects, on the magnetotransport characteristics and further the valence of Fe in this chapter.

4.3.1. Confirmations of Synthesized Samples

The absolute values of the oxygen content of the A_2FeMoO_{6-w} with A-site elements consisting of Ba, Sr and Ca were determined by the $Fe^{2+/3+}$ coulometric titration method. According to several parallel experiments, the precise oxygen content of the samples of Ba_2FeMoO_{6-w}, Sr_2FeMoO_{6-w} and Ca_2FeMoO_{6-w} was determined at $6-w$ = 5.98(1), 5.97(1) and 5.99(1), respectively [V]. Since the oxygen contents of these edge members of samples were fixed at 5.98±0.02, it might be possible to assign other A_2FeMoO_{6-w} samples with various A's synthesized by an oxygen-getter-controlled low-O_2-pressure encapsulation technique to stoichiometric oxygen content, in the present work. Henceforth in order to denote the oxygen content ($6-w$) of the samples, "6" is utilized in this thesis.

In order to identify the phase and to check the phase purity, the XRD measurements for the A_2FeMoO_6 with various A constituents obtained by an oxygen-getter-controlled low-O_2-pressure encapsulation technique were performed. Crystal structures and space groups were referred from literatures for Ba_2FeMoO_6 [26], Sr_2FeMoO_6 [74] and Ca_2FeMoO_6 [22]

samples then Rietveld simulations of the peak position, diffraction profile and broadening of profile for these compounds were carried out. By comparing the simulated profiles and obtained diffraction patterns in this work, the most reasonable crystal structures and space groups for the present samples were determined. The samples were believed to be of their space groups as $Fm\bar{3}m$ [26], $I4/mmm$ [74] or $I4/m$ [43], and $P2_1/n$ [22], for A = Ba, Sr and Ca, respectively, in this study. Comparison of simulated diffraction profiles and the measured XRD patterns of these compounds are shown in Fig. 4.3.1.-1(a) to (c).

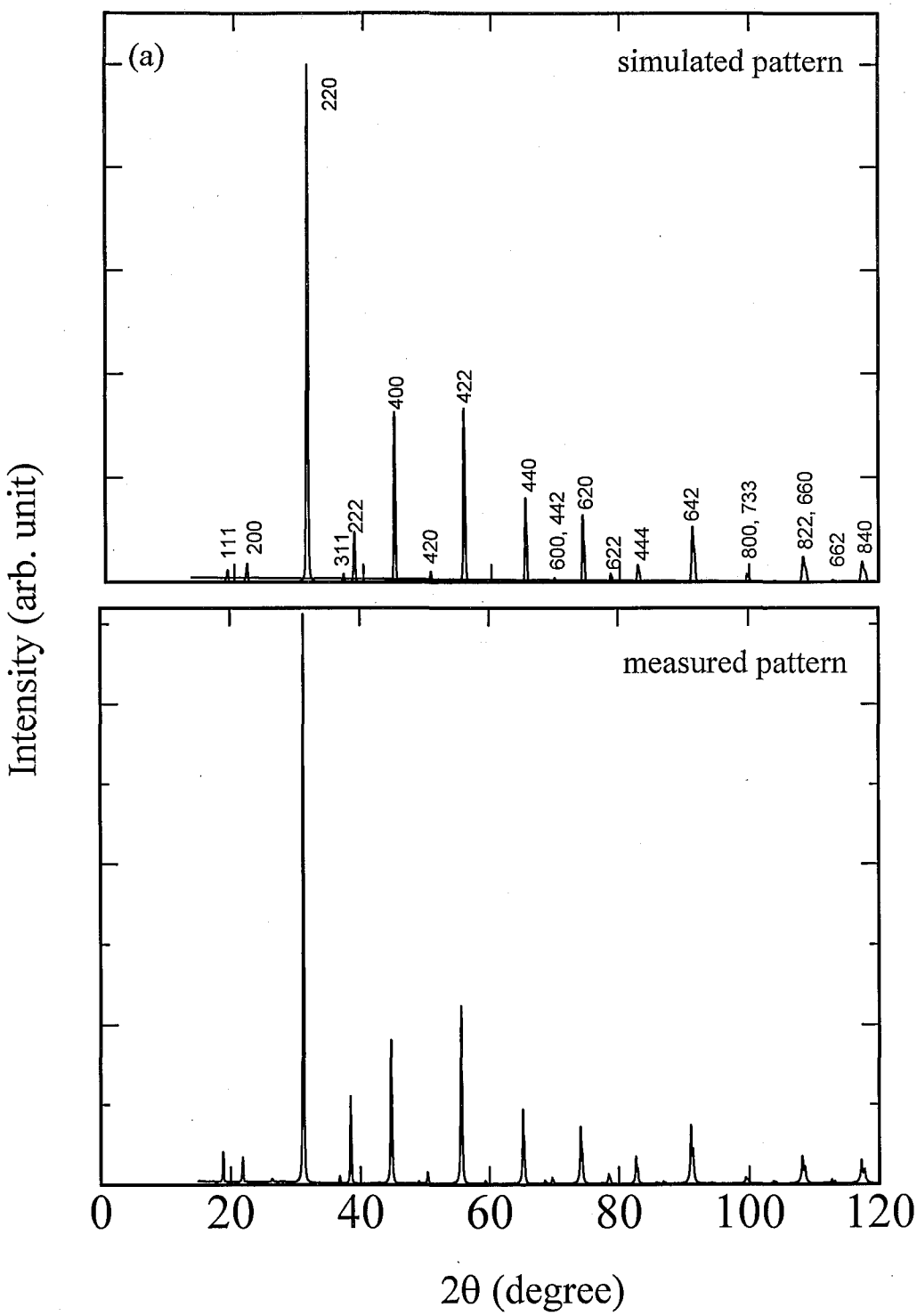

Fig. 4.3.1.-1 Comparison of simulated diffraction patterns and the measured XRD patterns for the (a) Ba_2FeMoO_6 (cubic, $Fm\bar{3}m$ [26]), (b) Sr_2FeMoO_6 (tetragonal, $I4/mmm$ [74]) and (c) Ca_2FeMoO_6 (monoclinic, $P2_1/n$ [22]) samples synthesized by an oxygen-getter-controlled low-O_2-pressure encapsulation technique. The simulated patterns are obtained by assuming the perfect Fe/Mo orders, *i.e.*, degrees of order at *B* site (*S* values) are assumed to be 1.

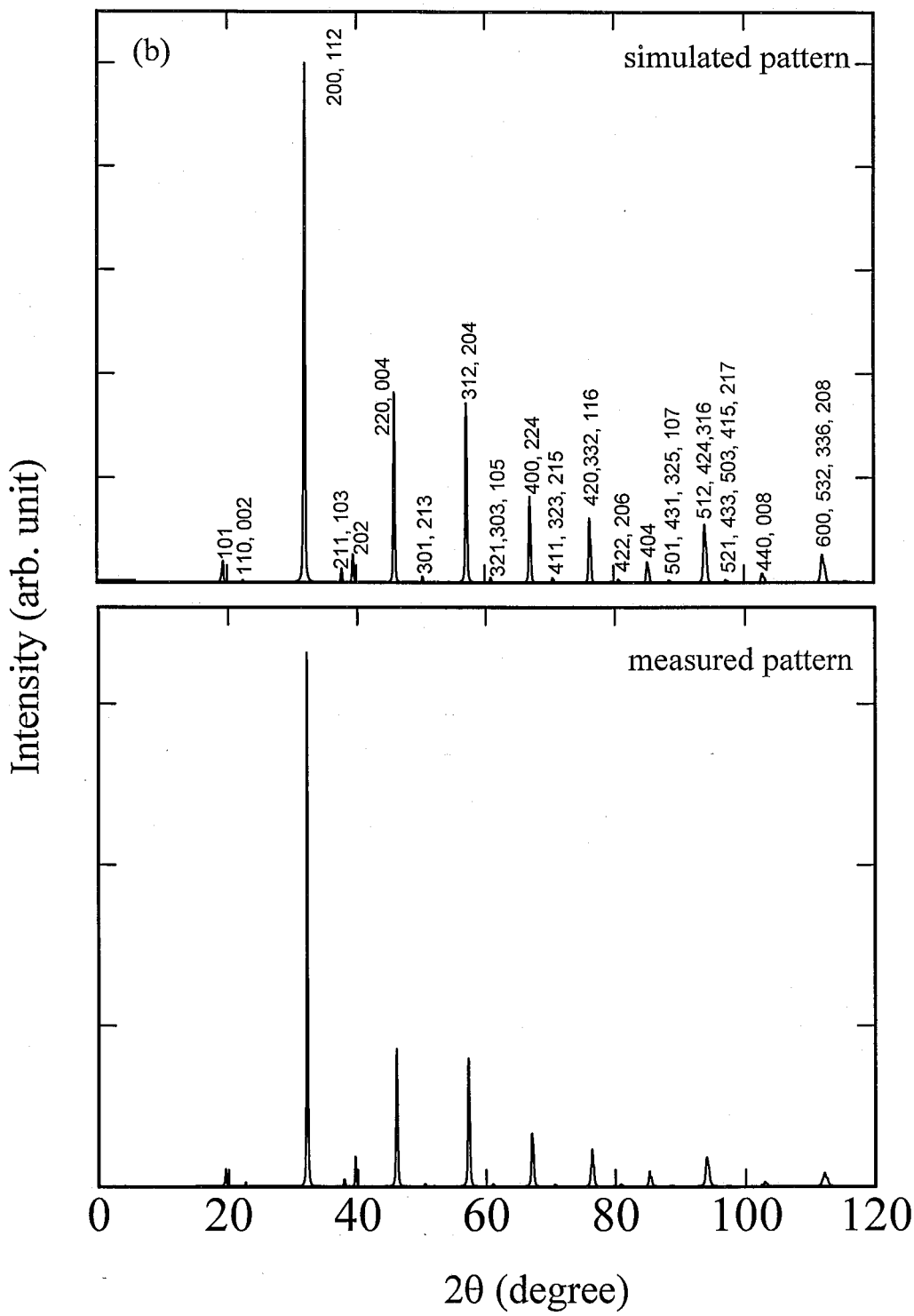

Fig. 4.3.1.-1 (Continued)

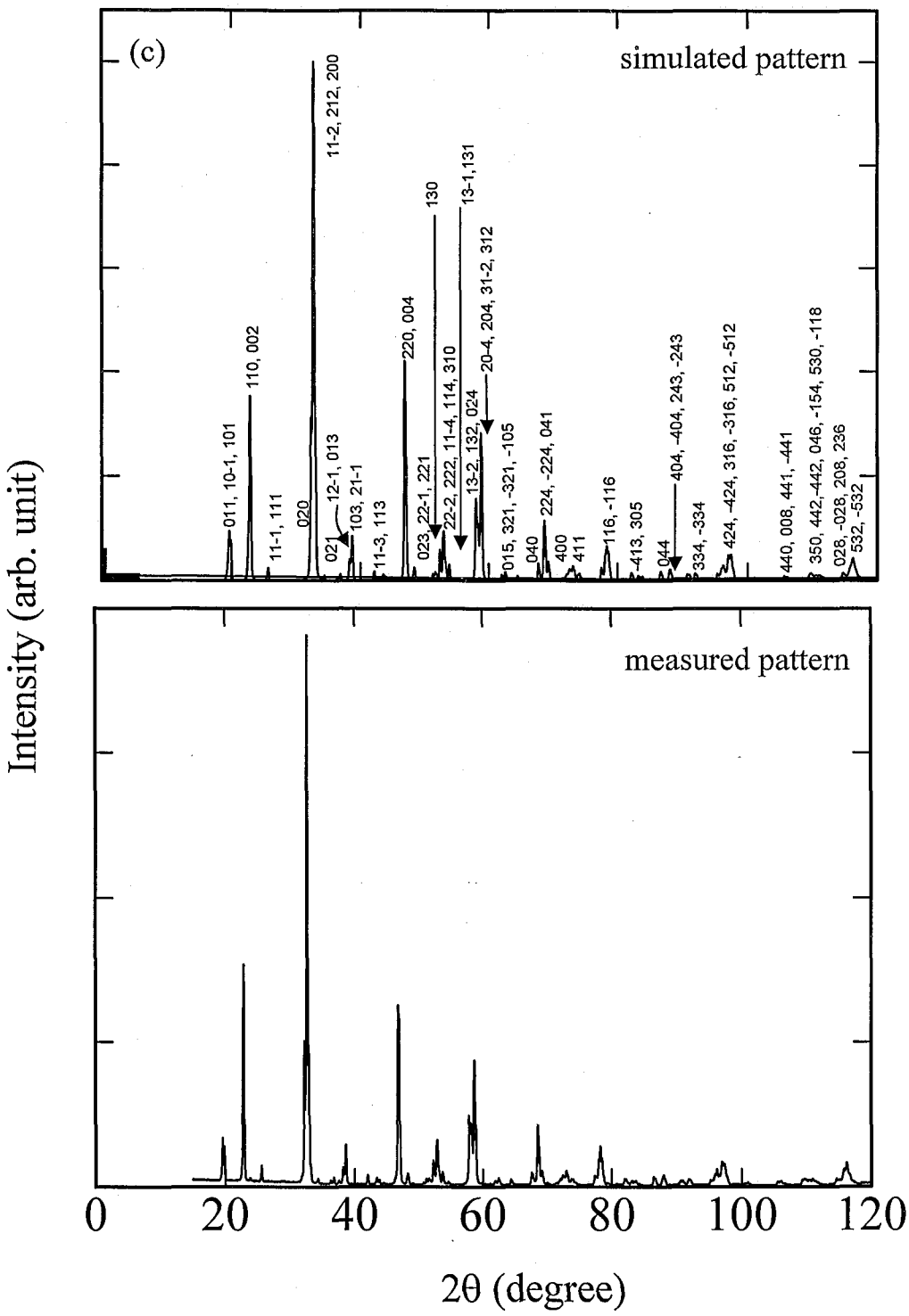

Fig. 4.3.1.-1 (Continued)

Each simulated/measured pattern is well consistent for each compound. The occupancy of *B*' (Fe) and *B*'' (Mo) was assumed to be perfect, *i.e.*, it was supposed that all the Fe/Mo atoms locate in correct Fe/Mo sites, in the simulations. From Fig. 4.3.1.-1, visible two weak peaks existing in ~19.6° and ~38° in all the samples give evidence of the supercell arising from the ordering of Fe and Mo sites alternatively [72]. Thus, it is possible to judge cell edges to be doubled for these compounds. Also, it was revealed that with a further increase in ionic radius of

A element, the more symmetric crystal structure of A_2FeMoO_6 phase can be obtained. In general, the cubic symmetry with $Fm\bar{3}m$ space group is tend to be obtained for $Ba_2B'B''O_6$ compounds from both single crystals and polycrystals [*e.g.*,29]. On the other hand, crystal structures of $Ca_2B'B''O_6$ samples are highly distorted originating from considerably tilted $B'O_6$ and $B''O_6$ octahedra due to the relatively small size of the Ca^{II} cations [*e.g.*,22]. This is clarified by Fig. 4.3.1.-2 showing the XRD patterns for all the A_2FeMoO_6 samples synthesized by an oxygen-getter-controlled low-O_2-pressure encapsulation technique.

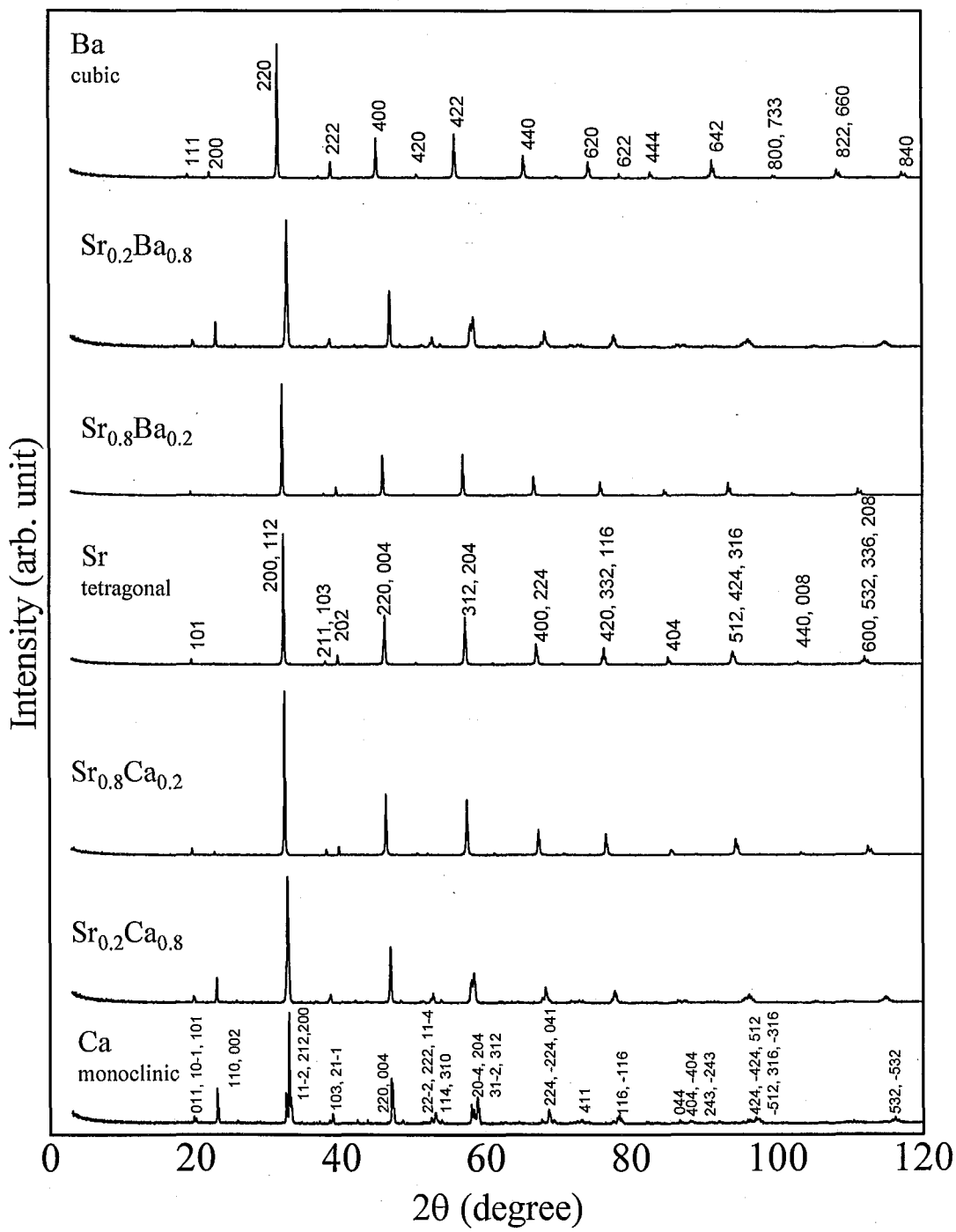

Fig. 4.3.1.-2 XRD patterns for a series of A_2FeMoO_6 samples synthesized by an oxygen-getter-controlled low-O_2-pressure encapsulation technique. Each sample was fired at 1150 °C for 50 hours in the ampoule together with fine Fe grains.

Many groups have been investigated $(Sr,Ca)_2FeMoO_6$ compounds from a stand point of crystal structure. In the case of $(Sr_{1-x}Ca_x)_2FeMoO_6$ ($0 \leq x \leq 1$) samples with $x < 0.5$ and $x > 0.75$, it has been determined their structures as the tetragonal *I*4/*m* and as the monoclinic $P2_1/n$ space groups, respectively from the XRD measurements. In the range of $0.5 \leq x \leq 0.75$, the structural transitions from the tetragonal to the monoclinic were observed [34]. Moreover, other group proposed that the changes in the space groups from the tetragonal to the primitive-tetragonal, *i.e.*, P-tetragonal structures, for $0.3 < x < 0.65$ in a series of $(Sr_{1-x}Ca_x)_2FeMoO_6$ samples, whereas the structures were identified as the primitive-monoclinic for the case of $0.65 \leq x \leq 1.0$ [33]. It has been attributed the chemical pressure by substituting Ca^{II} for Sr^{II} to bending the Fe-O-Mo angles rather than the decreasing of the Fe/Mo-O bond lengths in the $(Sr_{1-x}Ca_x)_2FeMoO_6$ system [34]. A driving force of symmetrizing the crystal structures in the A_2FeMoO_6 system would be complicated and different mechanisms would affect the symmetry of structures among samples: in the case of *A* constituents of Ba, BaSr and Sr compounds, these phases are cubic ($Fm\bar{3}m$) at 500 K, while Ca_2FeMoO_6 adopts the monoclinic $P2_1/n$ structure through all the temperature range. For the Ba_2FeMoO_6 and $BaSrFeMoO_6$ phases, both compounds maintain cubic structure down to 2 K [26]. However, a structural phase transition from the cubic ($Fm\bar{3}m$) to the tetragonal (*I*4/*m*) occurred at ~400 K in the Sr_2FeMoO_6 compound upon cooling. With decreasing the temperature, the FeO_6 and MoO_6 octahedra rotate continuously around the *c* axis in the tetragonal structure which induces a continuous structural phase transition of this sample [43]. The temperature dependence of this phase transition revealed that the tetragonal distortion tends to be zero as the ferromagnetic moment vanishes. Increase in the magnetic moment seems to depend on the increase of structural distortion [43]. Considering these facts, each independent mechanism would settle each crystal structure of A_2FeMoO_6 compounds having various *A*-site constituents. Furthermore, many space groups has been suggested for Sr_2FeMoO_6 sample such as tetragonal *I*4/*mmm* [*e.g.*,17,74], *I*4/*m* [43], *P*4/*mmm* [11], $P4_2/m$ [26] and even the cubic symmetry, $Fm\bar{3}m$ [20,75] has been proposed at room and high temperatures. It was found from the neutron measurements that the size of the FeO_6 and MoO_6 octahedra was only different in the *c*-direction with Fe-O3 = 2.027(7)Å and Mo-O3 = 1.935(7)Å. The in-plane cation-oxygen distance was found to be equivalent, *i.e.*, Fe(Mo)-O = 1.979(1)Å [26]. These experimental facts might be origin of difficulties of structural determination of Sr_2FeMoO_6. Besides, in a polycrystalline Sr_2FeMoO_6, a cubic phase possessing a lower T_C of ~390 °C with a value of M_S at 5 K of ~2.84 μ_B/f.u. has been stabilized by a short annealing at 1200 °C followed by cooling at the rate of 3°C/min. Concerning a tetragonal phase, it was obtained from a longer annealing times at 1200 °C. Thereby a T_C value was about 415 °C exhibiting M_S at 5 K of ~3.0 μ_B/f.u. with higher degree of order than that of the cubic phase [20]. From the measured XRD pattern for the present Sr_2FeMoO_6 sample and resultants of simulation of diffraction profile, the tetragonal structure with *I*4/*m* space group was found to be the most satisfied structure for the present Sr

sample.

After crystal structures and space groups were established, the Rietveld refinements were fulfilled using RIETAN program. The lattice parameters were determined by the the refinements and the ordering state at Fe(*B*')/Mo(*B*") sites for the present Ba_2FeMoO_6, Sr_2FeMoO_6 and Ca_2FeMoO_6 samples was evaluated based on Fe/Mo occupancies. This detailed Rietveld refinement was carried out for the most fundamental members, *i.e.*, *A* = Ba, Sr and Ca samples only, because the precise crystal structures, symmetries and space groups have not been established for the intermediate $(Ba,Sr)_2FeMoO_6$ and $(Sr,Ca)_2FeMoO_6$ samples. For these fundamental members, each peak obtained was indexed through the refinement and all the peaks were identified. Thus, Ba_2FeMoO_6, Sr_2FeMoO_6 and Ca_2FeMoO_6 samples synthesized by the present work were confirmed to be of high quality. In the structural refinement, the powder-diffraction pattern was calculated taking into account instrument-related factors, *i.e.*, the instrumental profile function, zero position, background, wave length and sample holder, *etc.* Starting values for all the atomic positions and isotropic thermal displacement parameters were set at literature values for each sample (Ba: [26], Sr: [74], and Ca: [22]). The cell parameters were taken from the measured XRD results, and were refined together with parameters such as the background and the total scaling factor. The occupancies of all the atoms were fixed at full for the initial refinements then the occupancies of Fe and Mo were set as changeable parameters and refined in the last stage of the Rietveld analysis, in the present study. Based on the final refinement, the miss-occupancy of Fe at the Mo sites denoted by ν, was evaluated as 0.015(1), 0.047(1) and 0.040(1) for *A* = Ba, Sr and Ca samples, respectively [V]. Through out the Rietveld analysis for fundamental compounds, it was found: (*i*) samples have ordered arrangements at Fe/Mo sites. Thus, these compounds form the double-perovskite structure (*ii*) these compounds possess almost perfect ordered structure at *B* sites but tiny amount of miss-occupancy of Fe and Mo elements exist in samples. The agreement factors in the Rietveld analysis is listed in Table 4.3.1.-1. These factors indicate that refinements are possible to consider to be reasonable. As described in section 4.1.1, differences in charge at *B*'- and *B*"-cation is the most influential parameter [1] for *B*-site arrangements in the $A_2B'B''O_6$ compounds. According to the present Rietveld refinement, all the fundamental compounds consisting of *A* = Ba, Sr and Ca have ordered structure thereby they form the rock-salt arrangement at Fe/Mo sites. Therefore, it is possible to prospect that the charge differences between Fe/Mo atoms are, at least, greater than two for these samples. This subject is discussed in section 4.3.3.-1 in detail.

Table 4.3.1.-1 The results and agreement factors obtained from the present Rietveld refinements.

Sample	Ba_2FeMoO_6	Sr_2FeMoO_6	Ca_2FeMoO_6
R_{wp}	8.71	6.71	7.19
R_p	6.67	4.57	4.91
RR	8.80	5.39	6.83
R_e	3.29	2.44	3.37
R_{wp}/R_p	1.31	1.47	1.46
g	0.985	0.953	0.960
S	0.970	0.906	0.920
ν	0.015	0.047	0.040

4.3.2. Microstructures

For the A_2FeMoO_6 system, it has been reported that the grain size [70,71] strongly affect the MR characteristics. Furthermore, a condition of grains, *i.e.*, whether the sample grains are melted-grown or not, influences the electrical transport properties. Since the melted-grown particles affect the distance of electron tunneling, the MR properties generated by the tunneling MR mechanism would be influenced whether the sample grains are melted-grown or not. If this melt-grown process is realized during the synthesis process, the melted A_2FeMoO_6 particles might induce extrinsic electronic-transport/MR characteristics. Therefore, the observation of grains of A_2FeMoO_6 samples showing the tunneling MR properties is required. The aim in this study was to reveal the intrinsic effects of $r(A^{II})$ in the A_2FeMoO_6 phase without any extrinsic factors. For this compound, the grain size is also important since each particle possesses magnetic boundary. The boundary acts as a barrier of the tunneling of electrons. Namely, a sample with small average grain size may show high electrical resistivities. Thus, to check a condition of the sample grain and to confirm the particle size, a SEM study with EDS analysis was performed on the A_2FeMoO_6 samples synthesized by an oxygen-getter-controlled low-O_2-pressure encapsulation technique.

Fig. 4.3.2.-1 shows the results of the SEM observations for all the A_2FeMoO_6 samples that has various $r(A^{II})$ in the present study. There are not any melted-grown particles in all the samples and particle-growths seem to be sufficient. This direct observation of sample grains agrees with the resultants of XRD measurements for the present samples, *i.e.*, the more symmetric crystal structure of A_2FeMoO_6 phase can be obtained for larger $r(A^{II})$ constituents. It is because samples that have large $r(A^{II})$ form more spherical-shaped grains due to more symmetric crystal structures compared to samples consisting of smaller $r(A^{II})$elements. Judging from the present resultants of SEM observation only, a sample with $A = Ca_{0.8}Sr_{0.2}$ might be a boundary of crystal symmetry between less Ca containing samples and Ca-rich samples from a shape of grains.

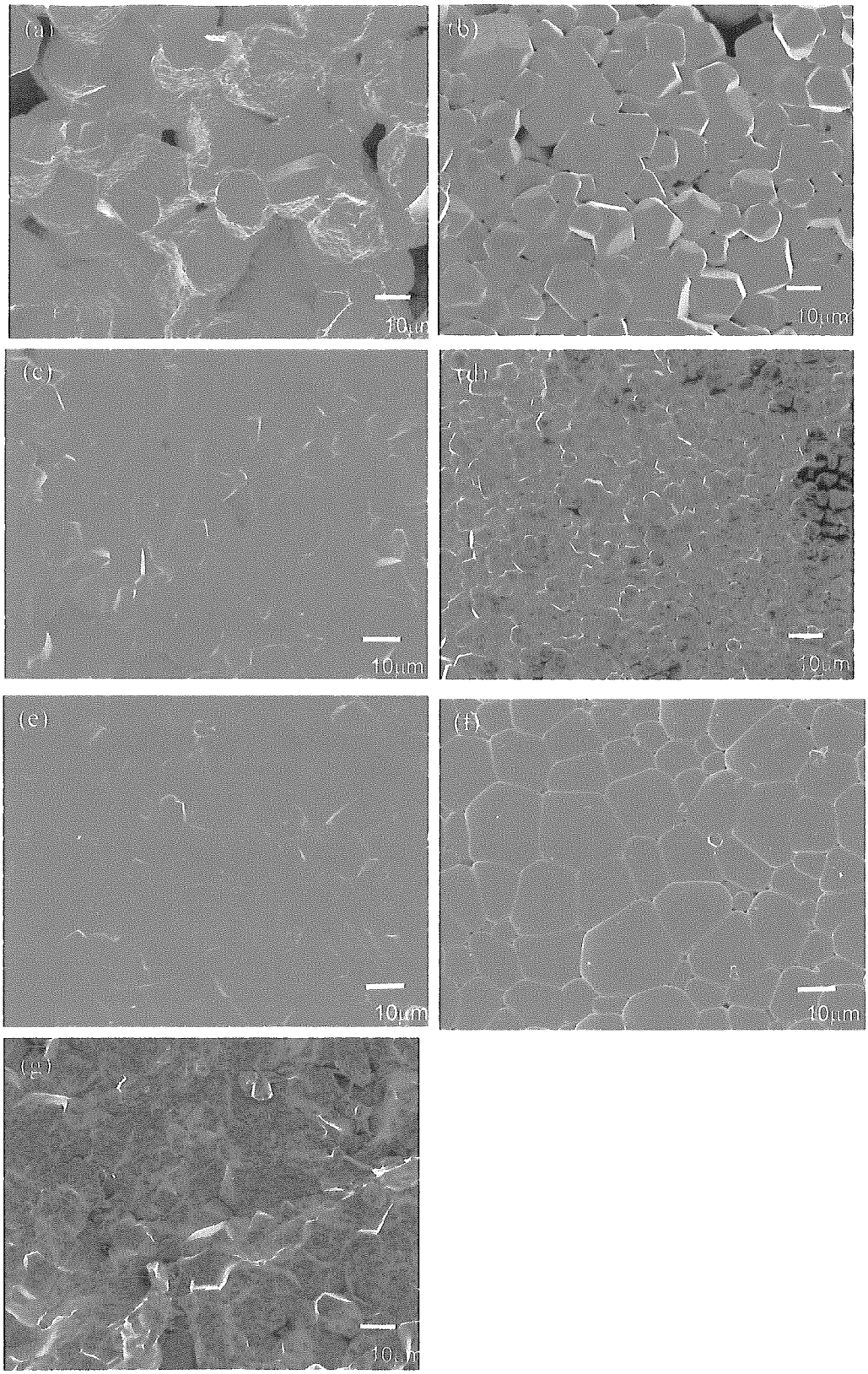

Fig. 4.3.2.-1 SEM images for the A_2FeMoO_6 samples with A = (a) Ba, (b) $Sr_{0.2}Ba_{0.8}$, (c) $Sr_{0.8}Ba_{0.2}$, (d) Sr, (e) $Sr_{0.8}Ca_{0.2}$, (f) $Sr_{0.2}Ca_{0.8}$ and (g) Ca constituents.

The average grain size, d_{ave}, was calculated by applying the Plani-metric method. Six local spots for each sample were selected and calculated the d_{ave} values. The grain size of each sample was confirmed to lie in a narrow range of 2 to 6 μm for A_2FeMoO_6 samples. For a

detailed microstructural study, SEM micrographs for the most fundamental members of Ba_2FeMoO_6, Sr_2FeMoO_6 and Ca_2FeMoO_6 are shown in Fig. 4.3.2.-2. This study emphasizes that a sample with the large $r(A^{II})$ constituent has large grain size.

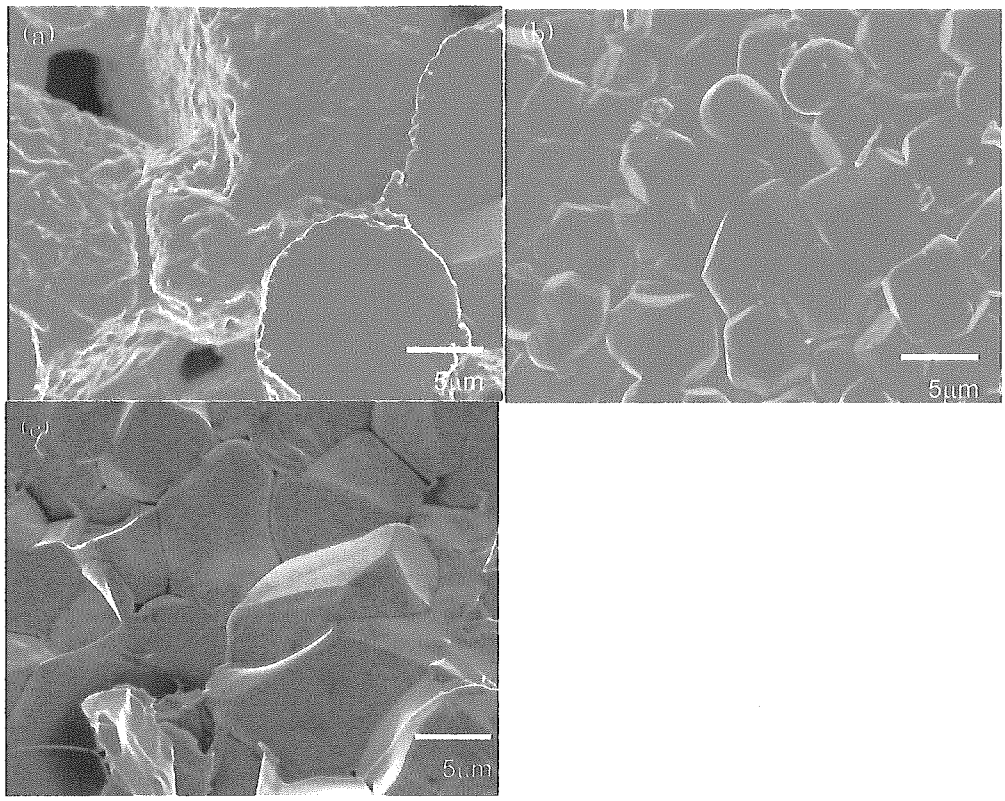

Fig. 4.3.2.-2 SEM images for the (a) Ba_2FeMoO_6, (b) Sr_2FeMoO_6 and (c) Ca_2FeMoO_6 samples.

Moreover, the EDS analysis of grains for all the samples was carried out in order to reveal the cation compositions. The analysis was performed for four local spots of each sample and obtained the average composition ratio of cations. All the analyzed local spots of the grain was concluded to be approximately the stoichiometric A_2FeMoO_6 possessing the compositions of A:Fe:Mo = 2.0:1.0:1.0 with small standard deviations.

The microstructural study concludes that there are hardly any melted particles in all the A_2FeMoO_6 samples with homogeneous grain sizes and cation compositions so that it is possible to deduce that the samples show intrinsic properties induced by the size effects of $r(A^{II})$, only.

4.3.3. Iron Valence [V,VI,VII]

4.3.3.-1 Determination of Iron Valence

The valence state of iron was investigated by ^{57}Fe Mössbauer spectroscopy measurement was performed for all the samples, *i.e.*, samples synthesized by an oxygen-getter-controlled low-O_2-pressure encapsulation technique and by a flowing H_2/N_2 gas technique [V]. In Table 4.3.3.-1-1, the resultant values of hyperfine parameters obtained from the

computer fittings of the spectra are listed for the samples synthesized by the encapsulation technique. By considering the fitting results, the main component was found to be $Fe^{II/III}$ (denoted M1). The second component (denoted AS) was assigned to derive from the antisite Fe atoms. This component represents the Fe atoms locating at the Mo site with the V_{Fe} of III. The existence of antiphase boundaries (APB) was first seen for Sr_2FeMoO_6 [VII] and all the experimental facts indicated that all the present A_2FeMoO_6 samples possess the APBs. Thus, the third component (denoted AP) was assignable to the Fe atoms at APBs. The fourth component (denoted M2) was considered to be a satellite of the main component originating from the Fe atoms located adjacent to the antisite Fe atoms. Since the influence of nearest-neighbour (oxygen) atoms only gives rise to unique components in Mössbauer spectra for perovskite oxides usually, this component M2 is rather unusual. Namely, Fe atoms with different oxygen coordination spheres appear as well-resolved components even when spin and valence states are identical, whereas any variation at the next-nearest-neighbour (cation) site(s) only causes line broadening of the components. However, in the present phase the nearest-neighbour oxygen configuration is identical for each Fe atom but the delicate charge balance between the next-nearest-neighbour atoms, *i.e.* Mo or Fe, affect the Mössbauer spectra, *i.e.* $Fe^{II/III}$ (component M1) or pure Fe^{III} (component AS). Therefore, the M2 component is indeed believed to reflect $Fe^{II/III}$ atoms adjacent to an antisite Fe atom. Both M2 and AS hence indicate the presence of antisite Fe atoms. Although only AS really originates from the Fe atoms at the Mo site, the component M2 measured only indirectly, would reflect the concentration of antisite Fe.

The isomer shift is the best hyperfine parameter to judge the valence state of iron. It has been established [76] that the average isomer-shift values for Fe^{III} in oxides are expected to show 0.20-0.55 mm/s. At 77 K, a typical value for high-spin (HS) Fe^{III} in a 5- or 6-coordination is ~0.3 mm/s [77], whereas for HS Fe^{II} values of ~1.0 mm/s are expected [76]. In accordance with a previous Mössbauer study [35] on the $Sr_2Fe(Mo,W/Ta)O_6$ system, it was revealed that replacing Mo with W^{VI} (Ta^{V}) enhances the formation of pure Fe^{II} (Fe^{III}) at the expense of mixed-valence $Fe^{II/III}$ species. It was also reported that the partially W(Ta)-substituted samples exhibited various mixtures of Fe^{II}(Fe^{III}) and $Fe^{II/III}$. Typical isomer-shift values for these in the paramagnetic state at 300 K were: 1.00 mm/s for Fe^{II}, 0.33 mm/s for Fe^{III} and 0.55~0.70 for $Fe^{II/III}$. Judging from these facts, the valence state of Fe atoms that contributes to component M1 (with isomer-shift value in the range of 0.7 to 0.85 mm/s at 77-K as listed in Table 4.3.3.-1-1 was concluded to show in between II and III in this study. Component M1 may thus be concluded to $Fe^{II/III}$ in accordance with earlier reports [43,60].

Table 4.3.3.-1-1 Hyperfine parameters obtained from the computer fittings of ^{57}Fe Mössbauer spectra at 77 K for the samples synthesized by the encapsulation technique [V].

		A element							
Comp.		Ba	$Ba_{0.8}Sr_{0.2}$	$Ba_{0.5}Sr_{0.5}$	$Ba_{0.2}Sr_{0.8}$	Sr	$Sr_{0.8}Ca_{0.2}$	$Sr_{0.2}Ca_{0.8}$	Ca
M1	*B* (T)	43.66(3)	44.58(3)	45.43(3)	45.88(1)	45.24(4)	45.46(1)	45.36(3)	44.76(5)
	δ (mm/s)	0.849(4)	0.823(3)	0.766(4)	0.719(1)	0.700(6)	0.703(1)	0.731(4)	0.684(5)
	I (%)	80(4)	80(2)	87(3)	84(1)	77(4)	82(1)	67(2)	80(3)
	e*QV*zz (mm/s)	-0.01(3)	-0.5(2)	-0.06(2)	-0.5(1)	-1.0(2)	-0.4(1)	-0.9(1)	-0.8(2)
M2	*B* (T)	46.8(3)	46.1(2)	47.1(2)	47.52(8)	45.6(3)	47.5(1)	46.19(3)	46.7(5)
	δ (mm/s)	0.66(1)	0.66(2)	0.57(3)	0.43(1)	0.50(4)	0.56(1)	0.50(1)	0.51(3)
	I (%)	8(2)	7(1)	8(1)	7.8(5)	11(2)	9.3(2)	22(2)	8(2)
	e*QV*zz (mm/s)	0.46(3)	0.7(2)	0.7(2)	0.61(8)	1.5(3)	0.0(1)	0.76(6)	1.2(2)
AS	*B* (T)	50.6(5)	51.9(5)	52(fix)	52.4(2)	51.7(2)	52.2(3)	51.1(2)	52.3(4)
	δ (mm/s)	0.32(fix)	0.21(6)	0.3(1)	0.18(3)	0.4(4)	0.28(3)	0.41(2)	0.51(5)
	I (%)	2(1)	1.6(6)	1.4(9)	2.5(4)	2.3(4)	4.0(4)	7.4(5)	3(1)
	e*QV*zz (mm/s)	0.2(3)	-0.1(2)	-0.1(4)	-0.3(1)	-1(2)	-0.3(1)	-0.24(6)	-0.4(2)
AP	*B* (T)	1.9(4)	2.6(1)	0.8(6)	2.4(1)	1.2(3)	3.4(2)	2.6(4)	1.6(3)
	δ (mm/s)	0.38(5)	0.39(2)	0.18(5)	0.37(2)	0.34(4)	0.23(6)	0.14(3)	0.38(4)
	I (%)	10(1)	11.2(5)	3.7(6)	5.7(3)	9(1)	5.1(3)	3.6(2)	9.1(8)
	e*QV*zz (mm/s)	-0.8(2)	-0.48(9)	1.0(2)	0.3(1)	-0.8(1)	1.1(2)	1.1(2)	1.2(1)

Prominent effects of *A*-site cation on the actual isomer-shift value of M1 were observed in the present results. The dependence is illustrated in Fig. 4.3.3.-1-1 for all the samples (synthesized by the two different techniques). The isomer-shift value is plotted as a function of $r(A^{II})$ in the figure. The straightforward interpretation is that the higher the isomer-shift value is, the lower is the valence of the mixed-valence Fe in the sample, *i.e.* closer to II. Thus, there is a systematic shift towards divalency with increasing $r(A^{II})$, especially within the A = (Sr,Ba) regime upon increasing the Ba content. The difference of some 0.15 mm/s between the extreme isomer-shift values is rather large and significant. Even though the actual values are somewhat scattered, a similar trend can be seen for the isomer-shift values of component M2 as listed in Table 4.3.3.-1-1. The scattered values of component M2 may originate from a partially resolution of component M1. The higher isomer-shift value seen for component M1 in Ba_2FeMoO_6 in comparison to that in Sr_2FeMoO_6 is consistent with the results of two earlier Mössbauer studies [63,78]. On the other hand, authors in other group suggested [63] that A = Ba must be a pure mixed-valence state of $Fe^{II/III}$, whereas Ca- and Sr-based samples are closer to pure trivalency. However, based on the present isomer-shift value of M1, it would be reasonable to interpret that for A = Ca sample rather indicates that an Fe valence state close to "pure II/III". The recent XANES study [62] in the Fe *L*-edge portion, authors concluded that the ground states of Ba_2FeMoO_6 and Sr_2FeMoO_6 compounds possess the mixed-valence $Fe^{II/III}$ configuration but with a larger Fe^{II} contribution for Ba_2FeMoO_6 than for Sr_2FeMoO_6. This is consistent with the obtained results in this study. Note that component M1 dominates all spectra thus high accuracy of the fitting for the isomer shift for all the six lines of M1 component is expectable. It is also possible to fit reliably even for component M2 because of the clear distinguishable spectra deriving from M2 contribution.

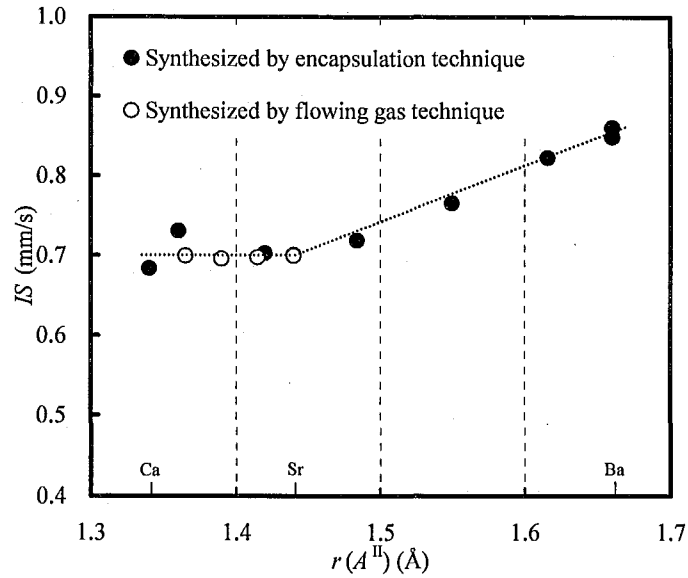

Fig. 4.3.3.-1-1 Isomer-shift value of component M1 *versus* ionic radius of the alkaline-earth element, $r(A^{II})$, in 12 coordinated state [V].

Component AS covers just a few per cent of the total intensity and only lines 1 and 6 are visible in the data. Accordingly it is not possible to fit the isomer shift reliably. This induces the somewhat scattered isomer-shift values for component AS as listed in Table 4.3.3.-1-1. The change in the isomer shift of component AS seems partly opposite to that for M1 (and M2) but AS iron would be free from a strong compensation for changes in the valence of the majority Fe atoms. It is because the overall concentration of AS is low in each sample. For component AP, the possible change, if any, is parallel to that seen for components M1 and M2. Thus, the valence balance $Fe^{II/III}$-$Mo^{V/VI}$ may gradually shift closer to that of Fe^{II}-Mo^{VI} for larger size of A constituents in the A_2FeMoO_6 samples. By considering these experimental results, the chemical pressure would be the most plausible explanation of the A-site constituent dependence of valence-mixing state found in the present A_2FeMoO_6 samples. If this is correct, the density of state(DOS)s of B constituents might be varied with $r(A^{II})$ because the electric structure of compound and its valence state can be correlated closely with each other. Thus, the variation of DOS may induce the difference of valence states of B cations, *i.e.*, Fe and Mo valences. Therefore, it is interesting to refer to the band-structure calculations based on the LDA method [79]. The calculations were focused on Ba_2FeMoO_6, Sr_2FeMoO_6 and Ca_2FeMoO_6 which are established their crystal structures and space groups by reliable/detailed neutron studies (for A = Ba and Sr [80], for A = Ca [22]). Nevertheless the difference of A-cation species, all the calculated DOSs show clear halfmetallic features (Fig. 4.3.3.-1-2).

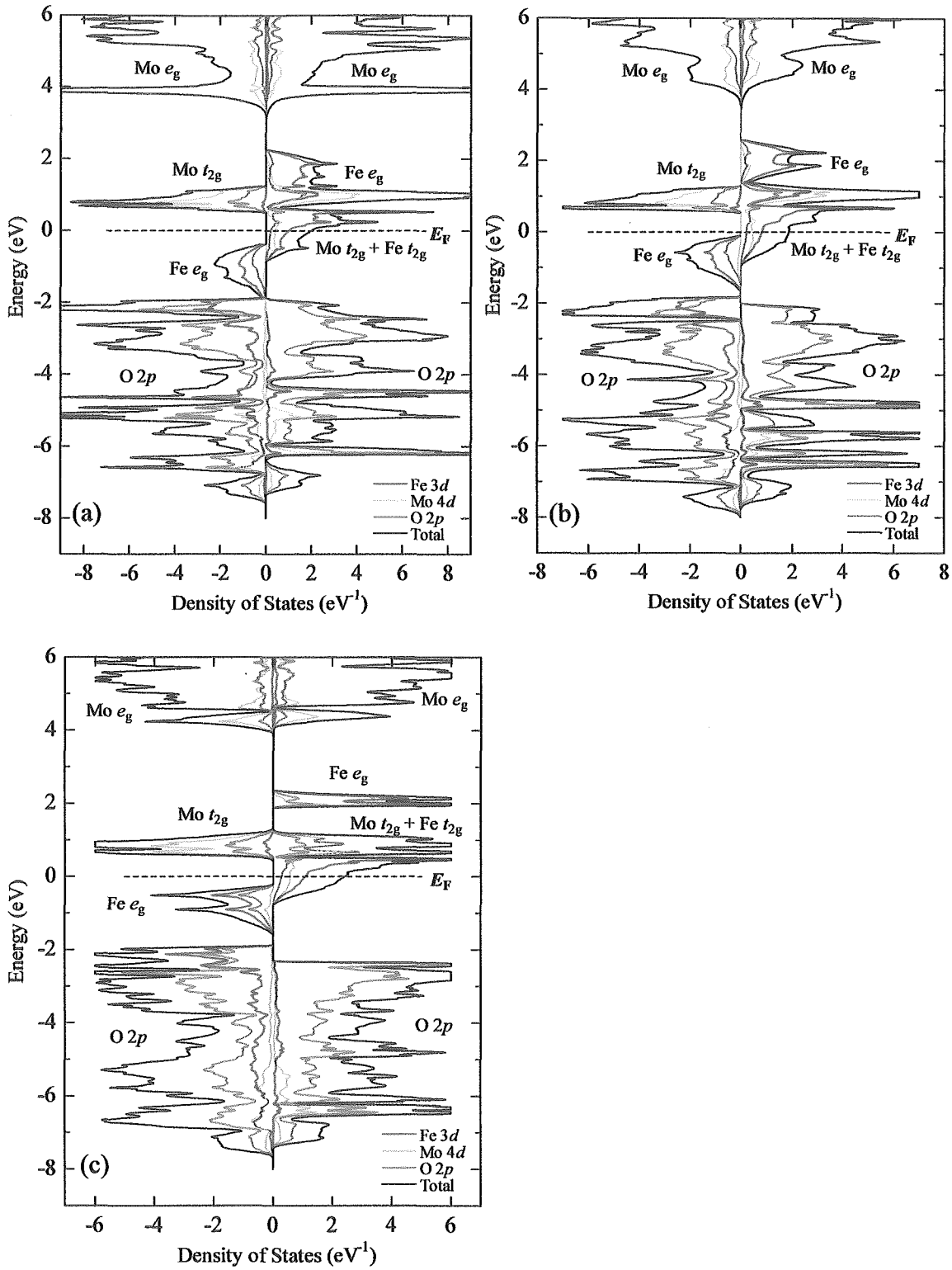

Fig. 4.3.3.-1-2 Density of states (DOS) for the (a) Ba_2FeMoO_6, (b) Sr_2FeMoO_6 and (c) Ca_2FeMoO_6 compounds calculated based on the LDA method [79].

On the up-spin channel, there is an apparent gap in the DOS, whereas the conducting state on the down-spin channel crosses the Fermi level (E_F) for all the samples. The halfmetallicity is due to the hybridization of both Fe and Mo t_{2g} states [17,79,80]. From the obtained results shown in Fig. 4.3.3.-1-2, the DOS existing in the down-spin side and crossing the E_F is composed of the hybridization of Fe 3*d*, Mo 4*d* and O 2*p* down spins. A clear difference in

the electronic structure originating from the size difference at *A* site is seen in Fig. 4.3.3.-1-3, a partial DOS of Mo 4*d* existing below the Fermi level. By integrating the partial DOS of Mo 4*d* below the E_F, the area was evaluated and it was found that the calculated area is relatively small in the case of Ba_2FeMoO_6, while those for Sr_2FeMoO_6 and Ca_2FeMoO_6 are mostly equivalent [79]. Since decreases in the area imply a lessen electron density of the Mo 4*d*; t_{2g}, charge and spin density of the itinerant electron of Mo 4*d*, tend to shift easily to Fe 3*d*, *i.e.*, transferring from Mo^V to Fe^{III}. Concomitant with this shift, the valence of Fe ought to decrease towards II as the V_{Mo} increases to VI in Ba_2FeMoO_6. Actually, this is in accordance with the results of Mössbauer analyses: the behaviours of isomer-shift value/the calculated area of partial DOS of Mo 4*d* below the E_F in terms of $r(A^{II})$ are parallel correlation, as represented in Fig. 4.3.3-1-4.

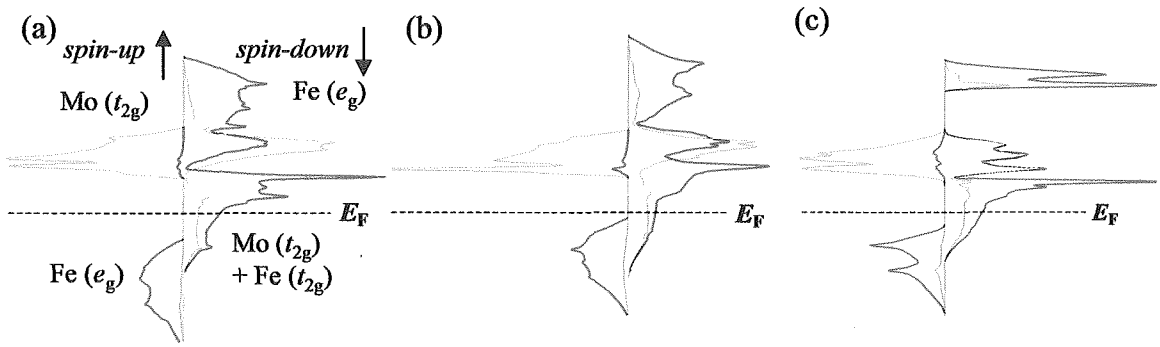

Fig. 4.3.3.-1-3 DOS of Fe 3*d* and Mo 4*d* for the (a) Ba_2FeMoO_6, (b) Sr_2FeMoO_6 and (c) Ca_2FeMoO_6 compounds calculated based on the LDA method [79]. In this figure, only the Fe and Mo states are extracted from the Fig. 4.3.3.-1-2 for the sake of clarify. The spin densities are explained in Fig. 4.3.3.-1-3 (a).

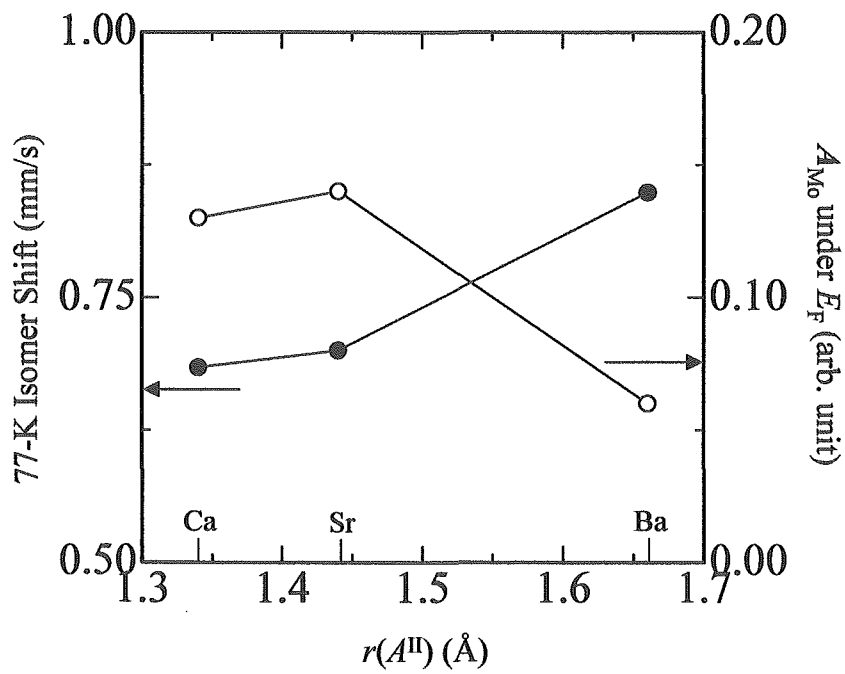

Fig. 4.3.3.-1-4 The isomer-shift values from the present ^{57}Fe Mössbauer analyses [V] and the partial density of states of Mo areas under E_F from band calculations [79] as a function of $r(A^{II})$ for the Ba_2FeMoO_6, Sr_2FeMoO_6 and Ca_2FeMoO_6 compounds. The partial Mo area of DOS below the Fermi level (A_{Mo}) was calculated by integrating data of the density of states point by point [79].

In Table 4.3.3.-1-1, not only the isomer shift but also other hyperfine parameters differ rather little for the A = (Sr,Ca) samples. For all the samples, the internal-field values indicate typical HS Fe^{II} or Fe^{III}, except for component AP. The component AP has an abnormally small internal field because of the spins of the APB atoms orient perpendicularly to the bulk magnetization which confirms the antiferromagnetic coupling between the Fe atoms within the antiphase boundary [VII], *i.e.*, strong magnetic frustration. The internal field value of the APB iron atoms is of only ~2.8 T at 77 K [VII], while a typical $Fe^{II}/^{III}$ main component usually shows ~46 T. Component AS exhibits the highest internal field as it originates from pure Fe^{III}. High-spin Fe^{III} with a 5- or 6-coordination usually has a saturation field of over 50 T. In the present measurements it is demonstrated that the internal field of component M1 is somewhat decreased with a value of lower than 50 T owing to the valence mixing. By considering the isomer-shift values it was judged that the valence and spin states of the mixed-valence Fe atoms are the lowest in A = Ba sample. This reasonably leads to the fact that the strongest decrease in the field value for this sample. However, a further discussion is required for the overall behaviour of the field induced by component M1 as follows (see Fig. 4.3.3.-1-5). In the Ca-for-Sr substituted samples the isomer-shift values indicate a constant V_{Fe}. The local maximum in the internal field around 30 % Ca-substitution level is thus best explained such that the transition from the tetragonal to cubic symmetry occurs in this region [33]. The variation of the internal field in the (Sr,Ca) regime might be purely due to the changes in the lattice symmetry. Also it may be attributed the first increasing of field in the (Sr,Ba) region to the high symmetry of the samples, *i.e.*, the fact that the samples again become cubic in this regime. With increasing the Ba content, the strong decrease in field was observed. This is clearly due to the fact that the valence of Fe approaches II. In terms of component M2, it exhibited field values intermediate between those for components, M1 and AS, as expected based on the isomer-shift values for M2.

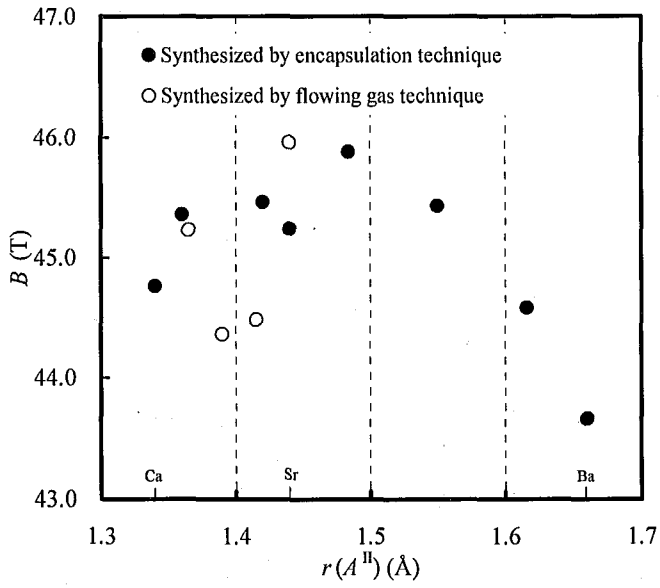

Fig. 4.3.3.-1-5 Internal field of component M1 plotted against $r(A^{II})$ [V].

Since the component M2 is assigned to the Fe atoms adjacent to antisite Fe atoms, it

would be possible to expect a constant intensity ratio of M2 to AS. Thus, the intensity ratio, calculated as I(M2)/I(AS), is plotted against the intensity of AS for all the A_2FeMoO_6 samples in Fig. 4.3.3.-1-6. Nevertheless the plot includes data for samples synthesized by the encapsulation technique under slightly different synthesis conditions, an obvious trend was found. It can be seen a decreasing trend for I(M2)/I(AS) as the concentration of anti-site atoms increases. Only for samples with the smallest concentration of anti-site atoms the theoretical intensity ratio, *i.e.*, 6:1, was obtained. The most possible explanation for this trend is clustering of antisite atoms, *i.e.*, the anti-site defects at the B-cation site tend to cluster as their concentration increases.

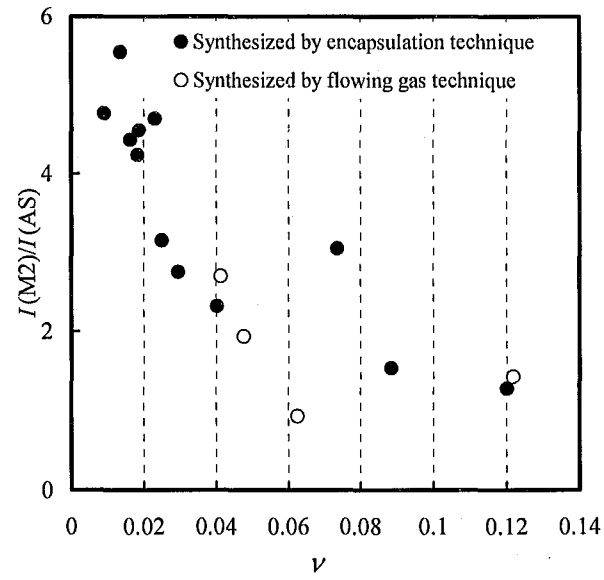

Fig. 4.3.3.-1-6 Intensity ratio of component M2 to AS, *i.e.*, I(M2)/I(AS), as obtained from the fitted 77-K Mössbauer spectra for the A_2FeMoO_6 samples [V].

The V_{Fe} was also investigated by the Fe $L_{2,3}$-edge XANES measurements for the present A_2FeMoO_6 samples (A = Ba, $Ba_{0.8}Sr_{0.2}$, $Ba_{0.2}Sr_{0.8}$, Sr, $Ca_{0.2}Sr_{0.8}$, $Ca_{0.8}Sr_{0.2}$ and Ca) synthesized by an oxygen-getter-controlled low-O_2-pressure encapsulation method. The $L_{2,3}$-edge of Fe attributed the main spectral features to dipole transitions from the core Fe $2p$ level to the empty Fe $3d$ states [81,82]. The spectra are derived from a core-hole spin –orbit interaction, *i.e.*, Fe $2p_{3/2}$ (L_3 edge; 705 ~ 715 eV) and Fe $2p_{1/2}$ (L_2 edge; 715 ~ 730 eV), so that the spectra are separated into two regions. Moreover, transitions $2p \rightarrow 4s$ are possible but they are much weaker, contributing the background only. Thus, these transitions can be neglected. In the L_3 portion of the Fe $L_{2,3}$-edge X-ray absorption spectra, there are two outstanding peaks originated from the Fe^{II} species in an octahedral crystal field in the A_2FeMoO_6 system as shown in Fig. 4.3.3.-1-7 (a). Fe^{II} component typically shows a main peak or a shoulder at ~707 eV, while a weaker peak or a shoulder at ~709 eV followed in the region of L_3 absorption edge [81,82]. The order of the peaks represent Fe^{III} species [VI]. Although both peaks at the photon energies ~707 eV and ~709 eV derive from Fe^{II}, it has been established [VI] that if the contribution of Fe^{III} is stronger than Fe^{II} in terms of Fe atoms in the sample, the intensity and area of peak at ~709 eV are intensified, while those of peak at ~707 eV are weakened and *vice versa*. By

considering these empirical facts, it would be possible to discuss the V_{Fe} in the samples from these two peaks. For discussing the area of spectra peak, all the measured spectra were fitted by Gaussian function. All the Gaussian fitting might be reliable with fitting-standard errors of 10^{-12} ~ 10^{-15} order. Fig. 4.3.3.-1-7 (b) shows the area ratio, *i.e.*, A_{709}/A_{707}, of the two peaks at ~707 and ~709 eV as a function of $r(A^{II})$. Each A_{709}/A_{707} value was calculated from Gaussian fitted peak area. Clearly, the obtained results show that with increasing the $r(A^{II})$, the A_{709}/A_{707} ratio decreases suggesting much contribution of Fe^{II} rather than Fe^{III} in the samples. This tendency agrees with conclusion obtained by the Mössbauer analyses. However, it is difficult to deduce the absolute values of V_{Fe} from the results of XANES measurements.

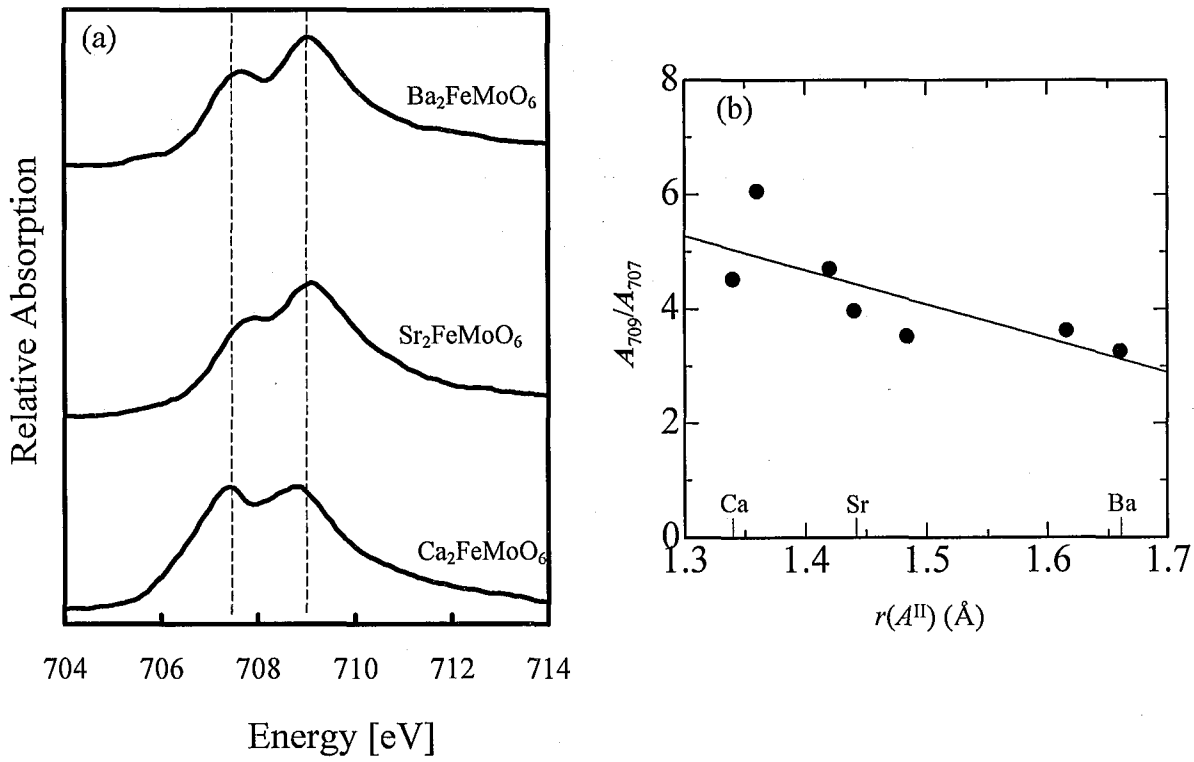

Fig. 4.3.3.-1-7 (a) Fe L_3 edge XANES spectra of Ba_2FeMoO_6, Sr_2FeMoO_6 and Ca_2FeMoO_6 samples synthesized by the oxygen-getter-controlled low-O_2-pressure encapsulation method in the present work. Eventhough the measurements were carried out for all the present A_2FeMoO_6 samples synthesized by the encapsulation technique, the spectra for the most fundamental compounds only are shown for a sake of clarify. (b) The area ratio, A_{709}/A_{707}, of the two peaks at ~707 and ~709 eV as plotted against the ionic radius of A-cation constituents. The line in the figure represents the data approximation in the least square sense.

It has been investigated the valence of iron for extended B-site ordered double-perovskite systems, *i.e.*, $Sr_2Fe(Mo,W/Ta)O_6$ sample series, freed from the oxygen deficiency [VI]. Thus, it is possible to suppose the relative correlations of V_{Fe} among samples, and further, by comparing these relationships of V_{Fe} values, it would be deducible an absolute V_{Fe} value for each sample. Form the Fe $L_{2,3}$-edge absorption spectra of $Sr_2Fe(Mo,W/Ta)O_6$ systems, authors found that the ~707 eV peak is stronger than the ~709 eV peak for heavily W^{VI}-substituted samples and weaker for heavily Ta^{V}-substituted ones. This implies much contribution of Fe^{II} species than Fe^{III} species in the W-substituted samples and *vice versa* in the

Ta^{V}-substituted samples. The Sr_2FeMoO_6 sample showed intermediate spectral features as compared with those for the strongly W- and Ta-substituted samples. Thus, the XANES investigation also concluded that the Sr_2FeMoO_6 sample is in the $Fe^{II/III}$ mixed-valence state. This is shown in Fig. 4.3.3.-1-8. Furthermore, the Fe *K*-edge absorption spectra were obtained for the whole series of $Sr_2Fe(Mo,W/Ta)O_6$ samples. Clearly, from the energy shift of the absorption edge, the expected valence of Fe increased from II (for $Sr_2Fe(Mo,W)O_6$ regime) to III (for $Sr_2Fe(Mo,Ta)O_6$ regime). Through out the XANES studies utilizing full series of double-perovskite samples, it was concluded that the observed behaviour might indicate that the actual valence of Fe in Sr_2FeMoO_6 is not precisely 2.5 but a little higher from the studies of *K* edge. In the isovalent substituted $(Sr_{1-x}Ca_x)_2FeMoO_6$ (x = 0, 0.25, 0.5 and 0.75) samples, the Fe *L*-edge XANES spectra showed [34] two multiple structures due to the orbit splitting of Fe $2p_{3/2}$ and $2p_{1/2}$. The obtained spectra were deduced that the Fe valence is much higher than +II but less than +III over the range of Ca substitution. This is well accordance with the present obtained Mössbauer conclusion. Besides, the same group measured the Mo *M*-edge absorption spectra of these $(Sr_{1-x}Ca_x)_2FeMoO_6$ (x = 0, 0.25, 0.5 and 0.75) compounds. The valence of Mo reduction with the increasing Ca content was seen from the spectra which would cause the increase of valence of Fe with x.

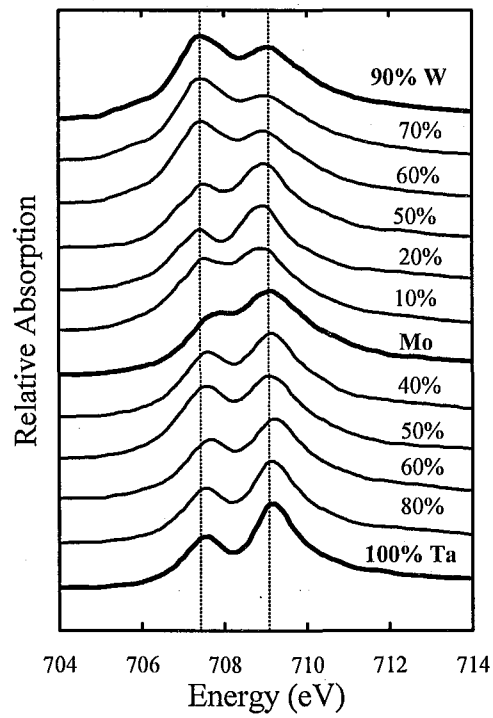

Fig. 4.3.3.-1-8 Fe L_3 edge XANES spectra for a series of $Sr_2Fe(Mo,W/Ta)O_6$ samples in the energy range of 704-714 eV [VI].

In conclusion of valence of iron for the present A_2FeMoO_6 sample series, two techniques were employed such as ^{57}Fe Mössbauer and Fe XANES spectroscopies to show that iron in the halfmetallic A_2FeMoO_6 possesses an $Fe^{II/III}$ mixed-valence state. Not only these experimental facts but also band-structure calculation [17] confirmed for the mixed valency of Fe for Sr_2FeMoO_6. The neutron diffraction data for this system also demonstrated that reducing

of magnetic-moment values for the Fe and Mo sites compared with the values expected for higher-spin Fe^{III} and Mo^{V} [43] indicates the valence mixing of Fe and Mo species.

4.3.3.-2 Role of the Valence of Iron for Properties

Based on the hyperfine parameters obtained for component M1, it was concluded that with increasing the ionic radius of *A* element, the valence balance $Fe^{II/III}$-$Mo^{V/VI}$ gradually shifts closer to that of Fe^{II}-Mo^{VI} as described in section 4.3.3.-1. It means that the difference between the charges of the two *B*'/*B*" cations increases as $r(A^{II})$ increases. For $A_2B'B''O_6$ double-perovskite compounds consisting of two *B*' and *B*" cations with equal atomic fractions, the degree of *B*-site order has been believed to be controlled by the size of the cation *A* and the charges of the cations *B'* and *B"*. In the present study, the concentration of antisite defects, *i.e.*, miss-occupancy of Fe at the Mo site, ν, was calculated by means of three independent ways such that (*i*) the XRD data through Rietveld refinement (which has already been revealed in section 4.3.1.), (*ii*) the results of magnetization experiments, and (*iii*) the analysis of Mössbauer data. The obtained values of ν are plotted against $r(A^{II})$, for the samples synthesized by the encapsulation technique as presented in Fig. 4.3.3.-2-1. As already mentioned, the Rietveld refinement clarified the ν values of 0.015(1), 0.047(1) and 0.040(1) for the (*A*',*A*") = Ba, Sr and Ca samples, respectively. The magnitude of saturation magnetization (M_S) value was determined as the magnetization value *per* formula unit at 5 T and 5 K. The M_S value was calculated from the measured magnetization data and are determined 3.9(1) μ_B, 3.8(1) μ_B and 3.6(1) μ_B for the *A* = Ba, Sr and Ca samples, respectively. Other samples with mixtures of Ba, Sr and Ca at the *A* site were confirmed to lie in a range of 3.4~3.9 μ_B as M_S values. The reduction in M_S as compared with the maximum value of 4 μ_B is believed to originate from the antisite defects [74,83]. Therefore, it is possible to estimate a relationship between the concentration of antisite defects and M_S values [63]: $M_S = (4 - 8\nu)$. Moreover, it is possible to calculate ν from the intensity of component AS [*I*(AS)] by Mössbauer analysis: $\nu = I(AS)/100$. The numbers of ν obtained from the three different approaches are consistent and all the samples possess high degrees of order as shown in Fig. 4.3.3.-2-1. It has been reported [7] that (*i*) decreasing the (average) size of *A*, and (*ii*) increasing the charge difference between the *B*'/*B*" cations, would promote the ordering. However, a tendency of slightly increased ν values is seen upon decreasing $r(A^{II})$, in this study. This is opposite to (*i*), but agrees with (*ii*). This may imply that the influence of (*ii*) might be stronger than that of (*i*) for the concentration of antisite defects. Therefore, the trend seen in Fig. 4.3.3.-2-1 is reasonable with an interpretation of the Mössbauer parameters in terms of the precise V_{Fe}.

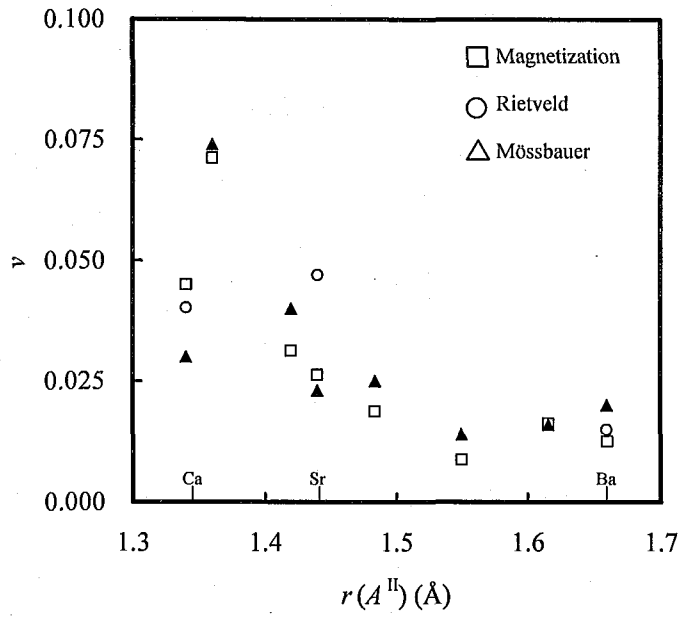

Fig. 4.3.3.-2-1 Concentration of anti-site defects (v) *versus* $r(A^{II})$. The value of v is estimated based on the M_S value from the magnetization measurement, the result of Rietveld refinement of XRD data and the observed relative intensity of component AS in the 77-K ^{57}Fe Mössbauer spectrum [V].

4.3.3.-3 Valence of Iron in Other *B*-site Ordered Double-Perovskite Compounds

A_2FeReO_6 can be regarded as the closest B-site ordered double-perovskite system of the A_2FeMoO_6 compounds. In this system, ^{57}Fe Mössbauer measurements showed [30] that iron is present mainly in the high spin (S = 5/2) Fe^{III} state in the Ca_2FeReO_6 compound, whereas an intermediate state between high spin Fe^{II} (S = 2) and Fe^{III} but closer to the latter was revealed in the Ba_2FeReO_6. For the A = Sr sample, the values of isomer shift and hyperfine field for this sample clarified that these values showed intermediate between those for the Ba and Ca compounds. However, the obtained Mössbauer parameters of Sr_2FeReO_6 were closer to Ca_2FeReO_6, rather than Ba_2FeReO_6 in terms of the valence state. This is the same tendency in the present A_2FeMoO_6 system in terms of A-site constituent though the absolute values of V_{Fe} are different between Ba_2FeMoO_6/Ba_2FeReO_6, Sr_2FeMoO_6/Sr_2FeReO_6 and Ca_2FeMoO_6/Ca_2FeReO_6 compounds. It was also found in this research that the transport properties and variation in the crystal structures in the A_2FeReO_6 system are coincident with the variation of V_{Fe} because a changing in the A-cation species exerted a metal-insulator transition in this system. The strong correlation between the physical properties and valence mixing of B cations in A_2FeMoO_6 has been clarified in the present work, too. However, another Mössbauer investigation revealed [84] that the main component of iron atoms in a series of $(Sr,Ca)_2FeReO_6$ samples is composed of mixed-valent $Fe^{II/III}$ state but a linear Ca-substitution level dependence of isomer-shift value was observed, *i.e.*, the higher the concentration of Ca was, the closer was the valence value of Fe^{III} keeping the valence mixing state of iron up to Ca_2FeReO_6. This is shown in Fig. 4.3.3.-3-1.

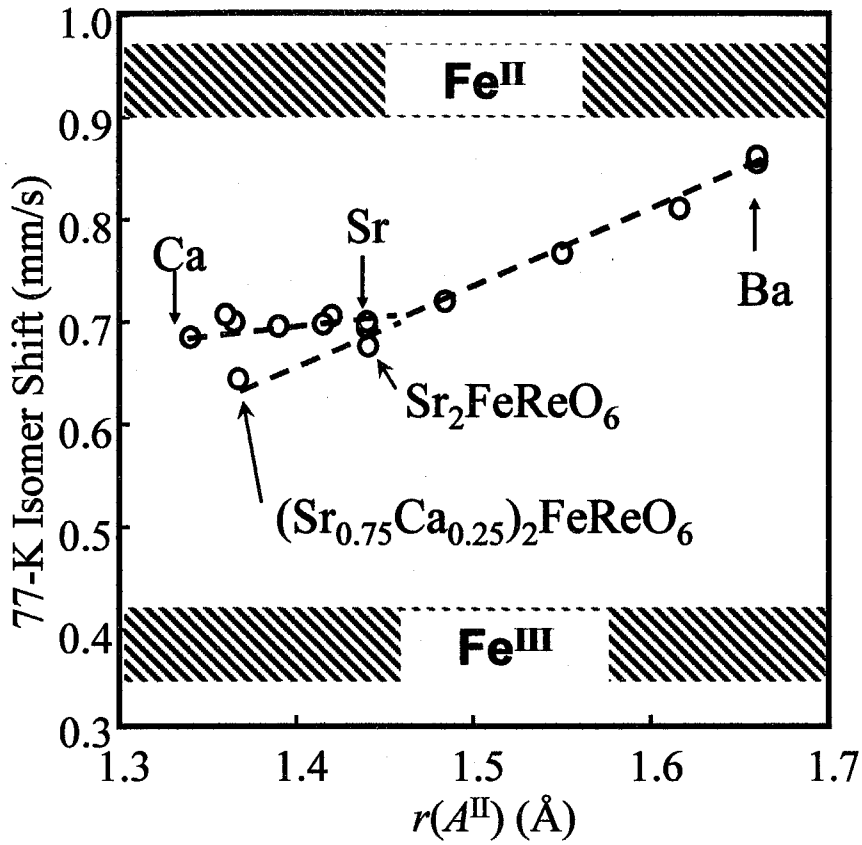

Fig. 4.3.3.-3-1 Comparison of isomer-shift value of component M1 between the present A_2FeMoO_6 [V] and A_2FeReO_6 [84] systems as a function of $r(A^{II})$ measured at 77 K.

4.3.4. Magnetic Boundaries/Domains and Anti Phase Boundaries

The APB is defined as a crystallographic boundary at which the phase shift of the *B*-site ordering occurs. It has been found that APB strongly affects the physical properties such as magnetic properties and MR characteristics in *B*-site ordered perovskites [85,86]. So far, the observations of APBs with high-resolution electron microscopy (HREM) have been reported by Navarro *et al.* [85] but they performed the Fourier transformation on the HREM image, *i.e.*, they presented "indirect" observations.

In the study of V_{Fe} by the Mössbauer measurements for the present samples, extremely low internal-field values were obtained for component AP so that the existence of Fe atoms at APBs was expected in this study. It is because antisite defects are believed to promote some magnetic frustration [85] results in small internal-field values of Fe nuclei. Therefore, "direct" observations of APBs at room temperature were tried on the most basic *B*-site ordered double perovskite, Sr_2FeMoO_6, by a TEM technique, in this study. The utilized ceramic Sr_2FeMoO_6 sample was synthesized by an oxygen-getter-controlled low-O_2-pressure encapsulation technique and made into thin film by means of ion milling technique. The concentration of APB was estimated 8 % from the Mössbauer analysis, while a long-rang order (*S*) at Fe/Mo sites was calculated ~0.92 by a refinement of Rietveld analysis for this sample.

Figs. 4.3.4.-1 (a) to (d) show TEM micrographs of a grain in the Sr_2FeMoO_6 sample taken with an incident electron beam of the [001] direction. Structural defects observed in a bright-field image (Fig. 4.3.4.-1 (a)) and dark-field images (002 and 200 spots: Figs. 4.3.4.-1 (b) and (c)), were considered to be original structural defects exist in the grain or to be defects derived from the ion-milling process. This structural defect is indicated by "defect" with arrows in Fig. 4.3.4.-1 (e). On the other hand, there are some defects observed only in a dark-field image (101 spot) as shown in Fig. 4.3.4.-1 (d). They can be seen in a dark-field image (101 spot) but invisible in bright-field and dark-field images (002 and 200 spots). The 101 spot is a superstructure spot which reflects the ordering of Fe/Mo atoms in *B'/B"* site. Therefore, defects observed in a dark-field image (101 spot) only, are reasonable to conclude disturbances of ordering of Fe/Mo atoms, *i.e.*, defects originate from APB. The APBs are indicated with arrows in schematic Fig. 4.3.4.-1 (e). This direct TEM observation revealed the existence of APBs that were expected by Mössbauer measurements, see section 4.3.3.-1. These results demonstrated that the assignment of component AP as APB is reasonable.

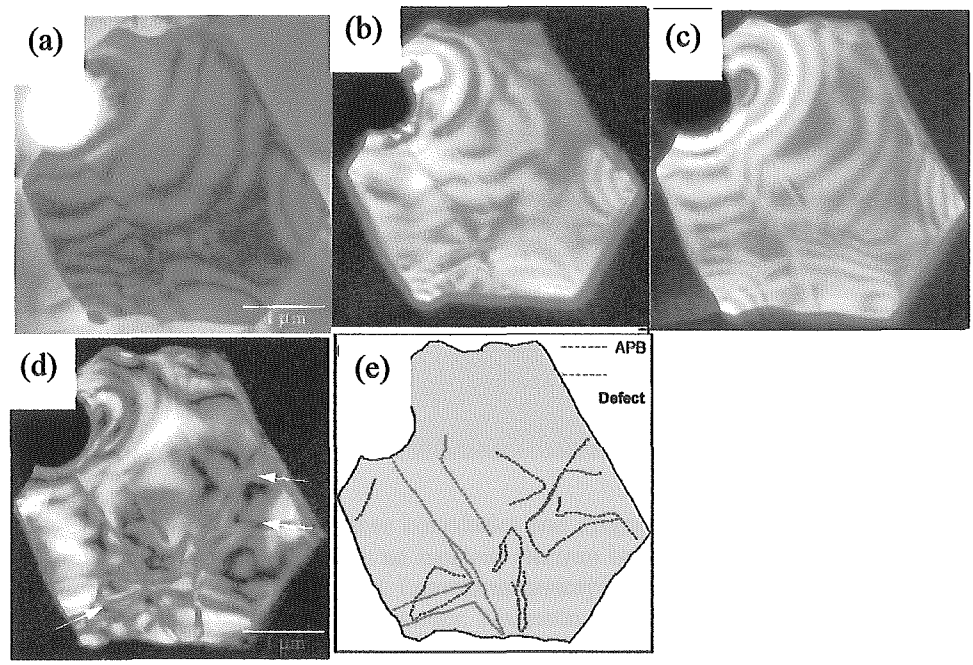

Fig. 4.3.4.-1 Electron microscopic observations of antiphase boundaries. (a) bright-field image, (b) dark-field image (002 spot), (c) dark-field image (200 spot) and (d) dark-field image (101 spot) for the Sr_2FeMoO_6 sample. The image is taken with an incident electron beam of the [001] direction. (e) schematic drawing for the corresponding crystal grain.

Since APB is a crystallographic defect, APB may act as pinning site that might affect the magnetic boundaries/domains in the structure of sample. By combining the results of observations of magnetic domain boundaries and APB, the relationship between them was studied. The results of correlation between APB and magnetic domain boundaries in a Sr_2FeMoO_6 grain are shown in Figs. 4.3.4.-2 (a) to (e). Fig. 4.3.4.-2 (a) shows the same figure as Fig. 4.3.4.-1 (d), a dark-field image (101 spot) taken with an incident electron beam of the [001]

direction indicating APBs. The magnetic boundaries are shown in Figs. 4.3.4.-2 (b) and (c) in accordance with the Fresnel method. Figs. 4.3.4.-2 (d) and (e) show the magnetic domains applied by Foucault method. All the observations were performed in the same grain, in the same position. Considering all the results, it can be seen that magnetic boundaries/domains and APB correlate each other, *i.e.*, magnetic domain boundaries are "trapped" by APBs as shown by arrows in Figs. 4.3.4.-2 (a) to (e). This implies that APBs have a possibility to work as weak pinning site. If this pinning site is realized, the physical properties might be influenced because the magnetic boundaries/domains in the sample grain are changeable through the changes in position/concentration of APB.

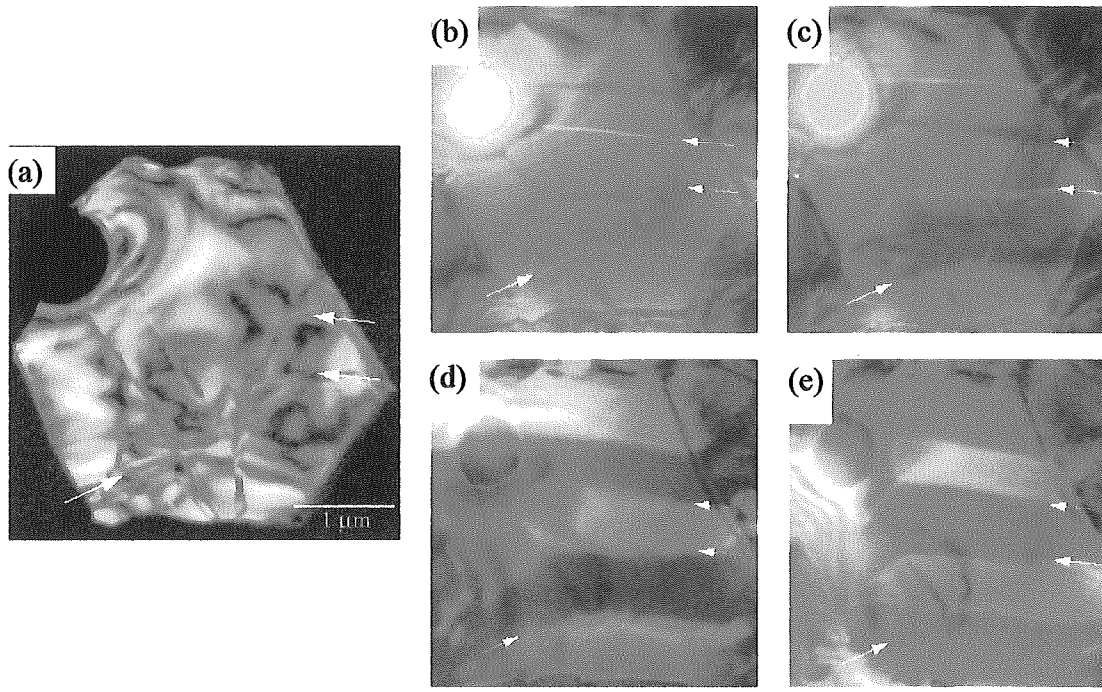

Fig. 4.3.4.-2 Correlation between antipahse boundaries and magnetic domain boundaries in a Sr_2FeMoO_6 grain. (a): dark-field image (101 spot) taken with an incident electron beam of the [001] direction. Arrows indicate the positions of antiphase boundaries. (b) and (c): Lorentz microscopic images by the Fresnel method. The images were taken with the over-(b) and under-(c) focus modes. Magnetic boundaries are indicated with arrows. (d) and (e): Lorentz microscopic images by the Foucault method. The images were taken with the over-(d) and under-(e) focus modes. Magnetic domain boundaries are indicated with arrows.

4.3.5. Electromagnetic Properties

4.3.5.-1 Electric Properties

Temperature dependence of resistivity is shown in Fig. 4.3.5.-1-1 for the present A = Ba, Sr and Ca compounds synthesized by the oxygen-getter-controlled low-O_2-pressure encapsulation technique. Samples show essentially metallic characteristics in accordance with the previous reports.

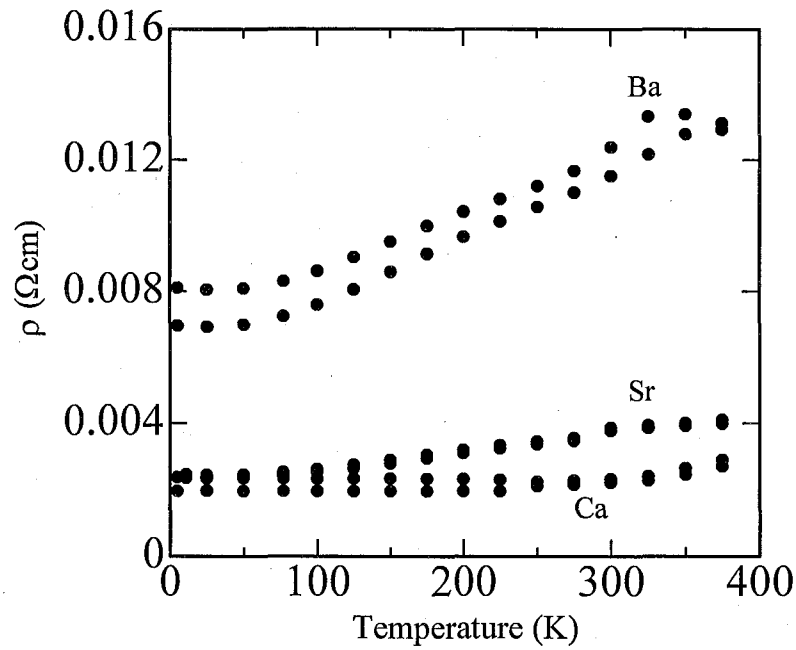

Fig. 4.3.5.-1-1 Resistivity measurements as a function of temperature and applied magnetic field (zero field and 7 T) for the Ba_2FeMoO_6, Sr_2FeMoO_6 and Ca_2FeMoO_6 samples synthesized by the oxygen-getter-controlled low-O_2-pressure encapsulation technique.

Outstanding features of transport properties of A_2FeMoO_6 are high residual resistivity at low temperatures and much weaker temperature dependence than conventional ferromagnetic metals [36,47,74,87,88]. Thus, this system is deducible to be unique magnetic material [36]. It has been reported that insulating [17,43,89], semimetallic or metallic [43] Sr_2FeMoO_6 samples could be obtained from various annealing conditions as shown in Fig. 4.3.5.-1-2. Since the charge ordering of the Fe^{III} and Mo^{V} combination is expected to give rise to insulating properties only, the observation of various conducting properties is quite unusual. An insulating Sr_2FeMoO_6 was obtained from a post-annealing of metallic sample in a vacuum-sealed quartz tube [89] thus this behavioral change would be originated from the improvement of conductivity of the grain-boundary or from the homogenization of the composition [43].

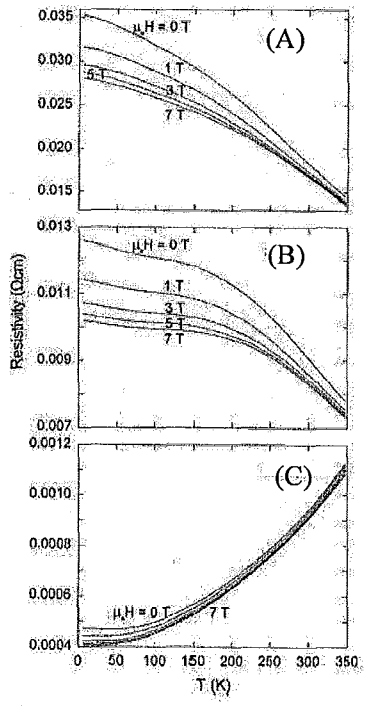

Fig. 4.3.5.-1-2 Temperature dependence of resistivity measured at various external fields for the Sr_2FeMoO_6 samples synthesized by different synthesis conditions. At zero field, samples A, B and C exhibit insulating, semimetallic and metallic properties, respectively [43].

It was found in the Ba_2FeMoO_6 sample that the temperature dependence of resistivity was affected by the grain size [71]. The ρ-T indicated a metallic behaviour for the various grain-sized Ba_2FeMoO_6 samples but the magnitude of ρ decreased with an increase in the grain size. The observed large variation of ρ values would be derived from a consequence of grain boundary scattering originated from the different grain size. That is, a sample possessing a larger grain size showed better connectivity between grains than a smaller sized sample. This suggests that an intergrain resistivity becomes lower for a larger sized sample. The conductivity was also found to depend sensitively on the precursor history and annealing time in the Sr_2FeMoO_6 sample [43]. The importance of the thermal treatment was also revealed in the Ca_2FeMoO_6 exhibiting the resistivity values in the range of 1-10000 mΩm by various heat treatments [11]. These reports demonstrated that the synthesis conditions of samples ought to strongly affect the conductivity properties of A_2FeMoO_6 compounds. Furthermore, different synthesis conditions generate various values of degree of Fe/Mo order, S, in this compound [90] thereby the various conductivity properties have been reported in accordance with variety values of S.

It has been well established that the substitution of different sized cations into the A site of $A'MnO_3$ exerts a chemical pressure on the system. This chemical pressure induced by the isovalent substitution causes changes in physical properties of $A'MnO_3$ system such as value of T_C and CMR property [21,32,91]. It is natural to consider that the isovalent substitution at A site might generate an influence on the electric property in the A_2FeMoO_6 system, also. Actually, $r(Sr^{II})$ and lattice parameters of Sr_2FeMoO_6 showed intermediate values between those of Ba and Ca thus it would be possible that the Sr compound shows intermediate conducting properties such as metallic/semiconducting behaviour depending on the synthesis conditions [19,30].

Besides, Ba_2FeMoO_6, Sr_2FeMoO_6 and Ca_2FeMoO_6 have the positive temperature coefficient of resistivity indicating a feature of metallic characteristic but absolute values of resistivity of these samples are different [11]: A polycrystalline Ca_2FeMoO_6 sample exhibited a metallic behaviour over the whole temperature range [22] and the observed $\rho_{(300\ K,\ 0\ T)}$ of 1.8×10^{-4} Ωcm was the smallest value compared to that of the Ba and Sr samples, *i.e.*, $\rho_{(300\ K,\ 0\ T)} = 2 \times 10^{-3}$ and 8×10^{-3} Ωcm, respectively [22,46,92]. This tendency agrees with the present results displayed in Fig. 4.3.5.-1-1 that Ca_2FeMoO_6 has the smallest absolute values of resistivity over the whole temperature range. Other two samples have a different trend compared to above-mentioned case: the magnitude of resistivity seen in Sr is closer to that of Ca, rather than Ba, in the present study. It was proposed [22] that the resistivity of the Ba_2FeMoO_6 and Sr_2FeMoO_6 samples would be dominated by the carrier scattering at the grain boundaries inducing the high ρ values. This suggestion was experimentally demonstrated. The (001)-oriented single crystal of Sr_2FeMoO_6 thin film showed about two orders of magnitude higher conductivity than that of a polycrystalline phase [17,20] implying the transport property of polycrystalline Sr_2FeMoO_6 is dominated by a strong electron scattering at the grain boundaries [20].

Although $r(A^{II})$ dependence of the conductivity property has not been theoretically explained in A_2FeMoO_6, an electronic itinerancy is considered to be one of the crucial factors for conductivity: in spite of highly distorted structure of the Ca_2FeMoO_6 and a consequence of lower degree of orbital overlapping, a good metallicity was observed in this material suggesting an importance of electronic itinerancy. The higher the degree of electronic itinerancy would be, the better is metallicity in the A_2FeMoO_6 compounds [22].

4.3.5.-2 Magnetic Properties

Fig. 4.3.5.-2-1 represents the temperature dependence of magnetic moment for A = Ba, Sr and Ca compounds synthesized by the encapsulation technique measured under an external field of 0.5 T. In the low temperature region, all the samples show the features of spontaneous magnetization deriving from the magnetic ordering. At higher temperature such as around 330 ~ 380 K, the magnitude of magnetic moment of Ba and Ca samples drastically decreases. This reveals a destruction of magnetic ordering, while paramagnetism appears. For the Sr sample, the paramagnetic behaviour can not be seen up to 400 K, at which the maximum-measurement temperature of SQUID apparatus, thus T_C value of this compound is clearly the highest among these samples. Obviously the A_2FeMoO_6 and A_2FeReO_6 ordered perovskites are very similar compounds. The T_C for A_2FeMoO_6 and A_2FeReO_6 with A = Ba are nearly the same, 330 K [26] and 300 K [93], respectively. In the Sr composed samples at A site, 420 K [43] and 405 K [93,94] were reported for both the B" = Mo and Re samples. The values of T_C for Ca_2FeMoO_6 and Ca_2FeReO_6 however, show a large difference, *i.e.*, 320 K [22] and 540 K [30,93-95], respectively. These magnetic ordering temperatures are much higher than any other ordered perovskites possess regardless of whether ferrimagnetism or antiferromagnetism is considered

[29]. All the compounds showed T_C values of 378-418 K from the paramagnetic inverse susceptibility χ^{-1} in the isovalent-substituted $(Sr_{1-x}Ca_x)_2FeMoO_6$ samples [33]. It is known that T_C values are strongly affected by the synthesis conditions even in the same compositional samples but a tendency to decrease T_C values with substituting Sr by Ca can be seen, generally.

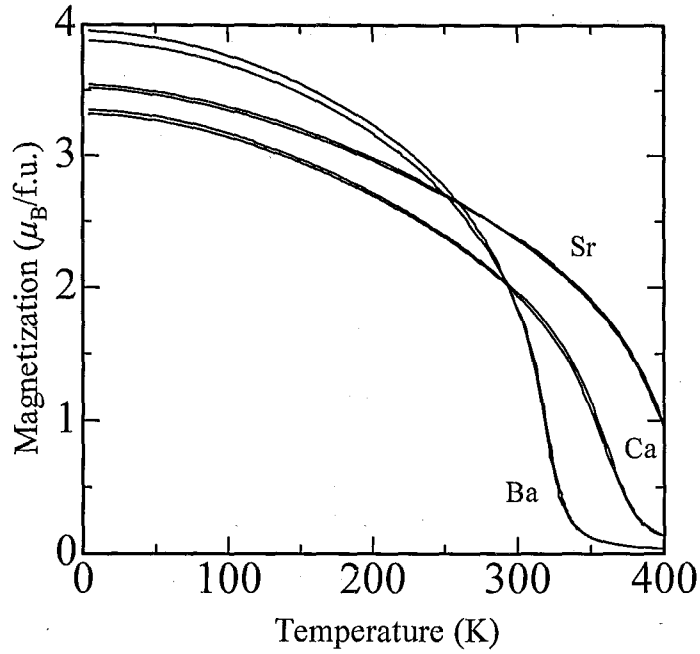

Fig. 4.3.5.-2-1 *M-T* curves for the Ba_2FeMoO_6, Sr_2FeMoO_6 and Ca_2FeMoO_6 samples with the applied magnetic field of 0.5 T.

Even though influences of $r(A^{II})$ by the isovalent substitution at A site on the T_C in the A_2FeMoO_6 system has not been clearly understood, it can be seen causal relationships. From a study of the T_C value and crystallographic structures as a function of the average ionic radius of $r(A^{II})$ in the A_2FeMoO_6 (A = Ba, BaSr, Sr and Ca) system, the symmetry of the structure increased as $r(A^{II})$ increases [21,26]. This effect causes an impact on structural parameters which are important for the electronic structure and consequently for the electron hopping [21]. The electronic band width/strength of the electron hopping, W which is sensitive to the structural parameters might be an influential parameter on the T_C values [26]. In the case of single perovskites, ABX_3, the empirically obtained formula of W has been successfully employed [96,97] as

$$W \approx \frac{\cos\omega}{d^{3.5}_{B-X}}, \qquad (4.3.5.-2-1)$$

where ω is the tilting angle, *i.e.*, given by $\omega = (\pi - \langle B\text{-}X\text{-}B\rangle)/2$, and $d_{B\text{-}X}$ is the bond length between cation B and anion X. In the A_2FeMoO_6 system, the $r(A^{II})$ dependence of the band width W and of the T_C value clearly showed that a remarkable correlation between the values of W/T_C and $r(A^{II})$ [21,26] as shown in Fig. 4.3.5.-2-2.

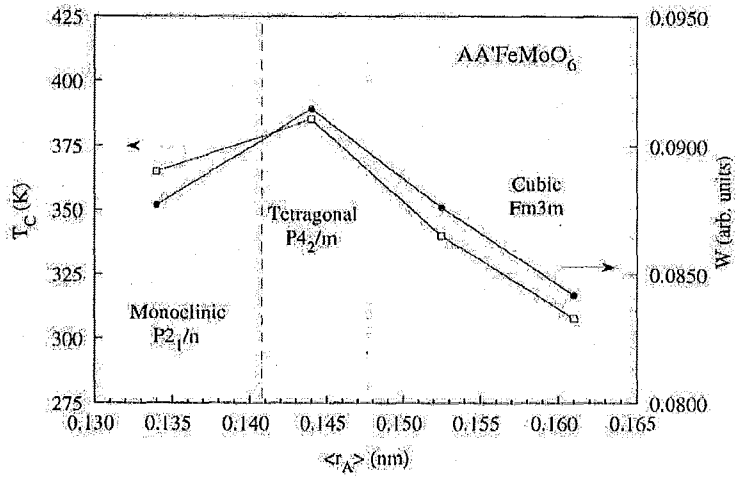

Fig. 4.3.5.-2-2 Electronic bandwidth, W, and the Curie temperature plotted against the average ionic radius $<r_A>$ [26].

By increasing chemical pressure with the composition from Ba_2FeMoO_6 to $(Sr_{0.95}Ca_{0.05})_2FeMoO_6$, bond angles of Fe-O-Mo and Mo-Mo did not change drastically maintaining about 180° [21]. On the other hand, decreases in bond lengths of Fe-O-Mo/Mo-Mo induced by the pressure and thus an increase in the value of W may be realized. This agrees with the enhancement of T_C observed for these compounds [21]. Upon further increasing chemical pressure from $(Sr_{0.95}Ca_{0.05})_2FeMoO_6$ to Ca_2FeMoO_6, not only bond distances but also bond angles would be largely influenced by the changes in the structure. Since the electron hopping can be reduced in Ca_2FeMoO_6 sample with monoclinic structure, the value of T_C in the Ca_2FeMoO_6 ought to be decreased. In the ρ-T property revealing a good metallicity of Ca_2FeMoO_6 described in section 4.3.5.-1, the low resistivity value of this compound was attributed to the high degree of electronic itinerancy. On the other hand, above discussion claims the decreases in the electron hopping induces the suppression of T_C value of Ca_2FeMoO_6 in the $(Sr,Ca)_2FeMoO_6$ regime. These considerations seem to have some contradictions because materials with high electronic itinerancy probably have strong electron hoppings. Thus, the discussion of the electromagnetic properties from the respect of electronic itinerancy only/electron hopping only, might be too simple in the A_2FeMoO_6 materials.

The external-field dependence of the magnetic moment, *i.e.*, Moment-H curve, was measured for all the samples synthesized by the oxygen-getter-controlled low-O_2-pressure encapsulation technique as shown in Figs. 4.3.5.-2-3 (a) to (c).

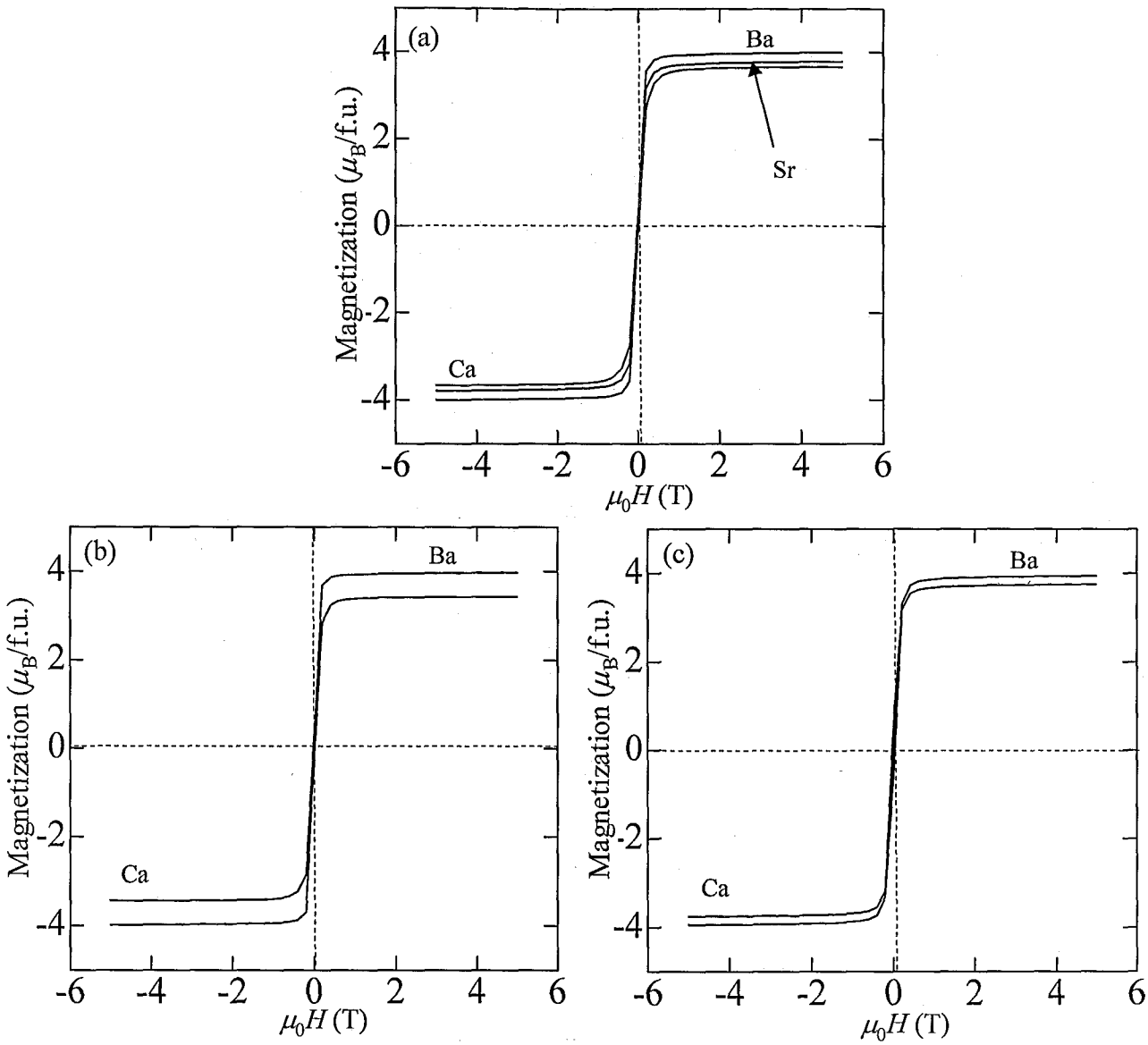

Fig. 4.3.5.-2-3 Field dependence of the magnetic moment, M, for the (a) Ba_2FeMoO_6, Sr_2FeMoO_6 and Ca_2FeMoO_6, (b) $(Sr_{0.2}Ba_{0.8})_2FeMoO_6$ and $(Sr_{0.2}Ca_{0.8})_2FeMoO_6$, and (c) $(Sr_{0.8}Ba_{0.2})_2FeMoO_6$ and $(Sr_{0.8}Ca_{0.2})_2FeMoO_6$ samples measured at 5 K, respectively. All the samples are synthesized by the oxygen-getter-controlled low-O_2-pressure encapsulation technique.

Basically, the magnetic behaviour of all the samples are quite similar. Extremely tight hysteresis loops representing a low remanence M_r, small corecivity H_{ci} (the value of H_{ci} has been reported less than 160 Oe [33] in a literature, but it is hard to determine the value in this study) and the attainment of saturation moment within a low applied field are observed in all the samples at 5 K. This suggests that the samples in this system are soft magnetic materials. Ba_2FeMoO_6 is considered to be magnetically soft because a steeper increase in the low-field magnetization of the Ba sample than those of the Sr_2FeMoO_6 and Ca_2FeMoO_6 samples has been generally observed from the *M-H* measurements [21]. The *M-H* curves measured at various temperatures exhibited that this system to be magnetic even at room temperature. Fig. 4.3.5.-2-3 (a) displays the *M-H* curves of the present A_2FeMoO_6 with *A*-site elements consisting of Ba, Sr and Ca. Similar magnetic behaviour can be seen among these samples but the magnitude of M_S values are

different. One of the puzzling facts about this system is the wide dispersion of values of the M_S [73]. The reported values of saturation magnetizations are 3.5-3.9 μ_B/formula for $(Ba,Sr,Ca)_2FeMoO_6$, generally [11] but M_S were reported to vary from $\approx$ 2.6 to 3.7 μ_B/formula at low-temperature for Sr compound due to different synthesis conditions among samples [17,50]. In the case of Ca_2FeMoO_6, M_S value is usually reported to be $\approx$ 3.6 μ_B/formula at low temperature [*e.g.*,22,40] which agrees with a result obtained in this study (see Fig. 4.3.5.-2-3 (a)). Ba sample possesses the highest M_S value, whereas Sr and Ca samples show closer values in M_S in the present measurements. According to a research [21] for the A_2FeMoO_6 samples consisting of A = Ba, Sr and Ca, Ba_2FeMoO_6 showed the highest magnetization value under 0.5 T among three compounds, while Ca_2FeMoO_6 showed the smallest magnitude of the magnetization. In the case of Sr sample, the magnetization lain in between those of Ba and Ca which is a similar trend to the ρ-T property of Sr_2FeMoO_6 compound mentioned in section 4.3.5.-1, *i.e.*, Sr_2FeMoO_6 possibly shows intermediate conductivity properties. The study reporting the magnetic behaviour of Sr sample and the results observed in the present magnetic measurements can be regarded the same tendency. Moreover, M_S value was determined at 3.5 μ_B/formula in the $(Sr_{1-x}Ca_x)_2FeMoO_6$ ($0 \leq x \leq 0.5$) samples at 5 K [33]. This system showed the magnetization increased from x = 0 to 0.25 and then slightly decreased from x = 0.25 to 0.5 from the *M-H* measurements [45]. It would be possible to attribute the complex behaviour of *M-H* characteristics in these phases to the reduction of Fe-O-Mo bond angle [45] as also suggested in the chemical pressure dependence of T_C value in this system, described in above paragraph.

Figs. 4.3.5.-2-3 (b) and (c) represent the correlation between moment and applied field of $(A'_{0.8}Sr_{0.2})_2FeMoO_6$ and $(A'_{0.2}Sr_{0.8})_2FeMoO_6$ samples with A' = Ba or Ca, respectively. These results agree with Fig. 4.3.5.-2-3 (a) since the magnitude of magnetic moment of Ba samples always larger than that for Ca. This tendency may originate from the isovelnt effect at A-site cation. When A' consists of Ba or Ca, the average ionic radius at A site varies larger in $(A'_{0.8}Sr_{0.2})_2FeMoO_6$ samples rather than in $(A'_{0.2}Sr_{0.8})_2FeMoO_6$ samples. This is well demonstrated in Figs. 4.3.5.-2-3 (b) and (c). The larger the difference of average ionic radius at A site is, the larger is the difference of the magnitude of magnetic moment of Ba and Ca samples. Further detailed discussion about the M_S values and constituents of A-site cation spieces was already described in section 4.3.3.-2.

In addition to the effects of isovalent substitution at A site on the M_S value, another crucial factor for the magnitude of M_S is ordering state of B site, *i.e.*, degree of order at Fe and Mo sites. Experimentally obtained M_S values suggest an antiferromagnetic coupling between the Fe and Mo sublattices resulting in ferrimagnetic structure [29,53] thereby $M_S = 4$ μ_B is predicted for antiferromagnetic coupled Fe $3d^5$ and Mo $4d^1$ electrons. However, M_S value is commonly reduced, less than 4 μ_B, that is believed to be caused by antisite defects arising from miss-occupancy of Fe sites by Mo species and *vise versa* [17,53,98,99]. Thus, the superb M_S value must be arisen from an improvement of B-site ordering [*e.g.*,100]. It was investigated [98] for clarifying the origins of various values of M_S in Sr_2FeMoO_6 and concluded that the various levels of antisite disorder at the Fe and Mo sites induces different values of M_S.

The antisite disorder was proposed to be located in the surroundings of the antiferromagnetic Fe-O-Fe antisite patches, that via next near neighbor interactions impede the complete ferromagnetic ordering of the Fe^{III} sublattice in the stoichiometric volume [73]. On the other hand, another group proposed a different model [33] which consists of two ordered domains: nucleation of ordered domains in a *B*-site ordered double-perovskite compound may order Fe atoms on *B*' sites in one domain and Fe atoms on *B*" sites in another. Where two such ordered domains meet, an antiphase interface is created across which are antiferromagnetic Fe-O-Fe interactions. Such interfaces would couple antiparallel the ferromagnetic domains on opposite sides of the interface. It was concluded that the different domains would be the different volumes thus there would be a residual magnetization on suppressing the field to zero from the saturation value. However, as described in sections 4.3.1 and 4.3.3.-2, the evaluated values of the miss-occupancy of Fe at the Mo sites are quite small in the present synthesized $(Ba,Sr,Ca)_2FeMoO_6$ samples. Therefore, differences observed in *M-T* and *M-H* properties can be mainly originated from the effects of isovalent substitution, in this work.

4.3.5.-3 Magnetoresistivity Properties

Fig.s 4.3.5.-3-1 (a) to (c) show the dependence of MR effect on the strength of applied external-magnetic field measured at various temperatures for the Ba_2FeMoO_6, Sr_2FeMoO_6 and Ca_2FeMoO_6 samples synthesized by the encapsulation technique. The magnitude of MR was calculated from Eq. 4.2.2.-1 with T_{fixed} = 5 K and H = 7 T. All the MR characteristics clearly represent tunneling-type MR curves at low temperatures/fields. The magnitude of MR at 5 K for A = Ba sample is smaller than those for A = Sr and Ca, *i.e.*, 14.1 % for A = Ba, and 17.4~17.5 % for A = Sr or Ca. The difference in the magnitude of MR, MR which is derived from the halfmetallicity, may be attributed to the difference in the electronic structure/the V_{Fe} value in Ba_2FeMoO_6, (closer to Fe^{II}) and in Sr_2FeMoO_6/Ca_2FeMoO_6 (closer to $Fe^{II/III}$). Halfmetallicity in principle should depend on the electronic structure thereby should also depend on the degree of valence mixing. Not only the isovalent-substituted system presented in this study but also in the *B*-site substituted $Sr_2Fe(Mo_{1-x}T_x)O_6$ (T = W, Ta and $0 \leq x \leq 1$) systems, with increasing x, *i.e.*, the decreases in the $Fe^{II/III}$ concentration, the magnetization, the conductivity and 300-K MR properties, were found to be rather similar in general [35] in both the Ta- and W-substituted systems. At 300 K Ba_2FeMoO_6 exhibits a larger MR effect than the A = Sr and Ca samples. Thus, this largest magnitude of MR for Ba sample may originate from CMR effect and it is supported by the fact that the shape of the MR curve for Ba_2FeMoO_6 at 300 K lacks the typical steep low-field dependence, while it is still present for the 300-K MR curves of the A = Ca and Sr samples.

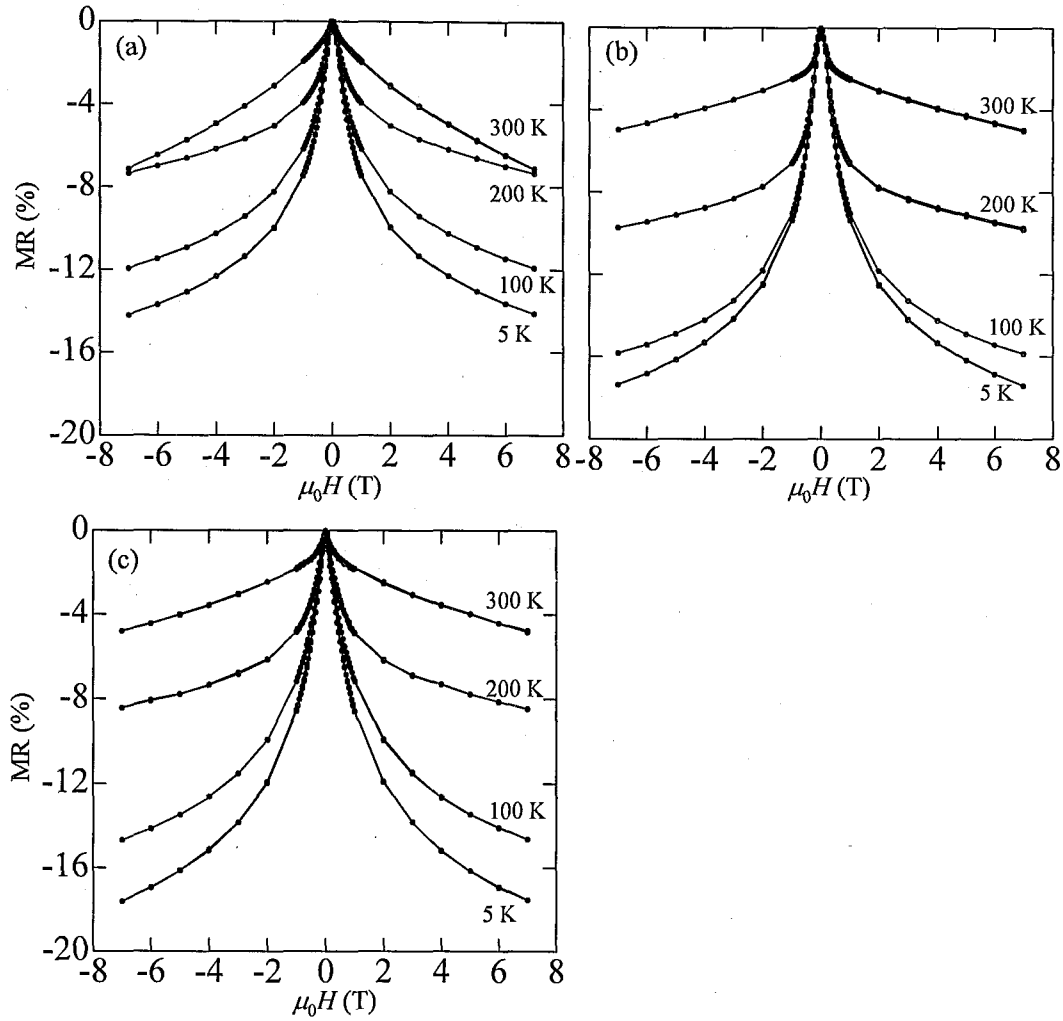

Fig. 4.3.5.-3-1 Field dependence of MR effect for the samples: (a) Ba_2FeMoO_6, (b) Sr_2FeMoO_6, and (c) Ca_2FeMoO_6, synthesized by the encapsulation technique [V].

Temperature dependence of absolute MR values measured at 7 T for the present A = Ba, Sr and Ca samples synthesized by an capsulation technique are displayed in Fig. 4.3.5.-3-2. TMR behaviours are observed for all the samples in the low temperature region, whereas MR peaks observed at high temperatures in Ba and Ca samples would correspond to their magnetic transition temperatures. This is so-called "CMR effect" at T_C. Two different origins of MR effects, *i.e.*, the intrinsic intragrain-MR and the extrinsic TMR [92], are seen in the present Ba_2FeMoO_6 and Ca_2FeMoO_6 in Fig. 4.3.5.-3-2. The MR effect which possesses a maximum at 5 K decreased with increasing the temperature. This would be a TMR behaviour which is derived from the tunneling current at the grain boundaries in low field region [15]. In the present Ba_2FeMoO_6, Sr_2FeMoO_6 and Ca_2FeMoO_6 samples, the TMR responses commonly possess the maxima at 5 K but the magnitude of maxima are seemed to be affected by $r(A^{II})$. Ba_2FeMoO_6 exhibited the smallest absolute value of the TMR maximum as seen in Fig. 4.3.5.-3-2, whereas those for A = Sr and Ca compounds are similar. This agrees with the resultant obtained by the ρ-T property (Fig. 4.3.5.-1-1), *i.e.*, the values of ρ at whole temperature range are mostly equivalent for Sr_2FeMoO_6 and Ca_2FeMoO_6 but that of Ba_2FeMoO_6 is different. The TMR ought

to correlate the resistivity strongly, thus the observed consistency would be essential and crucial. Another maximum of MR can be seen ~330 K and ~350 K, respectively, *i.e.*, the vicinity of T_C, for Ba and Ca samples in Fig. 4.3.5.-3-2. The second MR maximum can not be a TMR but rather a scattering reduction of the spin-polarized carries near T_C, *i.e.*, the intrinsic intragrain-MR. On the other hand, the present Sr_2FeMoO_6 sample shows the first MR maximum only in the MR-*T* property implying the absence of intrinsic intragrain-MR in the measured temperature region.

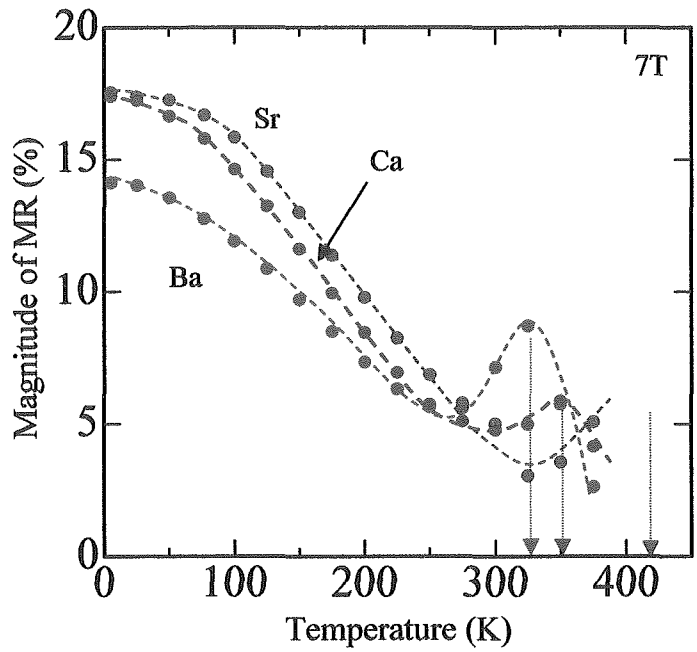

Fig. 4.3.5.-3-2 Temperature dependence of MR effect for the (a) Ba_2FeMoO_6, (b) Sr_2FeMoO_6 and (c) Ca_2FeMoO_6 samples synthesized by the encapsulation technique. Arrows indicate the magnetic transition temperatures established in published papers for these compounds.

Other than the intrinsic intragrain-MR and extrinsic intergrain-MR, several "material parameters" are known to affect the MR properties in A_2FeMoO_6 double perovskites. Among the material parameters, the most influential factor would be a degree of order at *B* site. For example, the highest MR ratio appeared in a sample with a low Fe/Mo antisite disorder and the highest magnetization in the $(Sr_{1-x}Ca_x)_2FeMoO_6$ compounds [34]. A detailed investigation was carried out [72] by preparing crystallographically ordered/disordered Sr_2FeMoO_6 specimens and studying their MR behaviour.

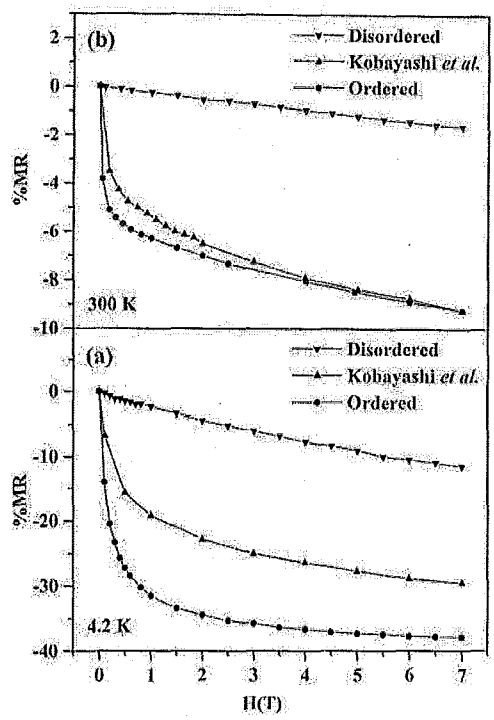

Fig. 4.3.5.-3-3 Comparisons of MR effect between the ordered and disordered Sr_2FeMoO_6 samples as well as the result presented in ref. [17] at (a) 4.2 K and (b) 300 K [72].

As can be seen in Figs. 4.3.5.-3-3 (a) and (b), the ordered sample exhibited the sharp MR responses under the low field at 4.2 and 300 K but no response at low field was characterized in the disordered sample, though a substantial negative MR was seen in the disordered sample. Conversely, the MR properties in the two samples at high field were similar being approximately parallel at both the temperatures which implies that there must be a common intragrain origin of high-field MR behaviour for two samples. It was attributed the MR response at high field to the overall magnetic nature of the sample, even in absence of the halfmetallic state. The low-field MR response however, depends crucially on the halfmetallic ferro(ferri)magnetism. It was concluded that the origins of the halfmetallic ferro(ferri)magnetic state and the resulting intergrain spin-dependent scattering are led by the long-range order of Fe/Mo atoms. The band-structure calculations studied by the same group showed [72] that a metallic state in the disordered system, though the system remains to be a ferrimagnet. It was argued that the halfmetallic ferro(ferri)magnetic ground state is not realized for any disordering of the Fe and Mo sublattices. Besides, grain boundaries are one of the material parameters which affect the MR characteristics. The barriers between two grains were controlled by the post-annealing treatments to improve the low-field MR [15]. Through the attempt, a drastic degradation of both the ρ-T property (from metal to insulator) and of magnitude of resistivity was achieved. This demonstrates the suppression of the quality of grain boundaries. By the post-annealing treatments, the low-field TMR was enhanced but the intragrain MR characteristics were maintained. The results obtained by this study would be one of the evidences for the field dependent tunneling of carriers through the grain boundaries in the A_2FeMoO_6 system [15]. In relation to the grain-boundary effects on the MR, a polycrystalline Ca_2FeMoO_6 sample

possessing a good connectivity (it is because the sample has a small absolute value of the resistivity) between grains showed an abrupt increase of MR above 270 K, *i.e.*, close to T_C [22]. In this sample, the grain-boundary effects at lower temperature regime were suggested to be less influential thereby the intragranular derived MR around T_C would dominate in this sample. Besides, the effect of grain size on MR response has been also clarified. The temperature dependent magnetization was found to be insensitive to grain size but ρ-T and MR properties were affected by the grain size [71], *i.e.*, with decreasing the grain size, the magnitude of ρ-*T* and the MR value increased. In the MR-*T* curvature, MR has been enhanced especially at low temperature for smaller grain sized samples. In the present studied samples in this work, the average grain size of Ba_2FeMoO_6 was determined to be larger compared to those of Sr_2FeMoO_6 and Ca_2FeMoO_6 samples from the plani-metric method. Conversely, Ba_2FeMoO_6 exhibited the smallest absolute MR value at 5 K under 5 T among the samples consisting of A = Ba, Sr and Ca, as shown in Fig. 4.3.5.-3-1. These observations would imply a correlation between the size of grain and MR characteristics. However, it might not be explained the MR response from a standpoint of grain size, only. It is because the average grain size of A = Sr and Ca samples were evaluated at 2.14 μm and 4.10 μm, respectively but those compounds possess quite similar absolute values of MR at 5 K under 5 T, as can be seen in Fig. 4.3.5.-3-1. Another group claimed [43] that Sr_2FeMoO_6 samples with various conductivity properties obtained by different synthesis conditions showed different MR effects, *i.e.*, a metallic sample exhibited a negligible MR effect, whereas significant MR response were detected for semimetallic and insulating samples. This might represent an interrelation between the grain size derived from various synthesis processes and MR characteristics, also. In the actual materials, a balance of intrinsic intragrain-MR, extrinsic intergrain-MR and material parameters mentioned above would determine the MR characteristics in this system.

Furthermore, the low-field TMR in the polycrystalline A_2FeMoO_6 compounds have a high tunability by means of isovalent substitution at A site [21]. Through out a study of polycrystalline $(Ba,Sr,Ca)_2FeMoO_6$ compounds, it was found that the optimal value of low-field TMR among all the samples was observed for a sample in the composition of $(Sr_{0.2}Ba_{0.8})_2FeMoO_6$. The low-field TMR varied nonmonotonically with the variation of chemical pressure in both $(Sr_{1-x}Ca_x)_2FeMoO_6$ and $(Sr_{1-y}Ba_y)_2FeMoO_6$ regions. In a series of $(Sr_{1-x}Ca_x)_2FeMoO_6$, the low-field TMR was maximized at the composition of $(Sr_{0.95}Ca_{0.05})_2FeMoO_6$ but the absolute value of low-field TMR is relatively small in comparison with that of $(Sr_{0.2}Ba_{0.8})_2FeMoO_6$. This study revealed a tendency that the absolute values of low-field TMR were relatively small in the $(Sr_{1-x}Ca_x)_2FeMoO_6$ series compared to those of $(Sr_{1-y}Ba_y)_2FeMoO_6$ samples. However, effects of isovalent substitution at A site on the MR has not been well established yet in the in the A_2FeMoO_6 system.

4.3.5.-4 Interrelation Between Magnetic Properties and Magnetoresistivities Derived by the Halfmetallicity

Figs. 4.3.5.-4-1 (a) and (b) show the field dependence of MR effect/the magnetic moment for these samples. Steep negative MR behaviours at low field region are observed for all the samples at 5 K (Fig. 4.3.5.-4-1 (a)). These drastic decreases in the MR values well correspond to a steep increasing of the magnetic moment at low field region as shown in the lower figure of Fig. 4.3.5.-4-1 (a). Even at room temperature, steep negative MR and corresponding steep increases in the magnetic moments are observed for *A*-cation constituents of Sr and Ca samples, as shown in Fig. 4.3.5.-4-1 (b). It has been reported [101] that a sharp drop in the MR at the low field corresponds to that associated with of magnetic-domain-rotation process in the magnetization curve. On the other hand, the high field reduces the magnetic scattering by aligning the spins thus the resistivity decreases slowly with increasing magnetic field thereby the MR curve has the gentle slope [101]. In Fig. 4.3.5.-4-1 (b), the MR behaviour of Ba sample is not steep but rather round and the absolute value of MR at 5 T is the largest among the samples, while M_S value at 5 T is the smallest at 300 K. Thus, the magnetic transition temperature of this sample is close to the room temperature. Fig. 4.1.2.-1 well explains the experimental results demonstrated in Figs. 4.3.5.-4-1 (a) and (b).

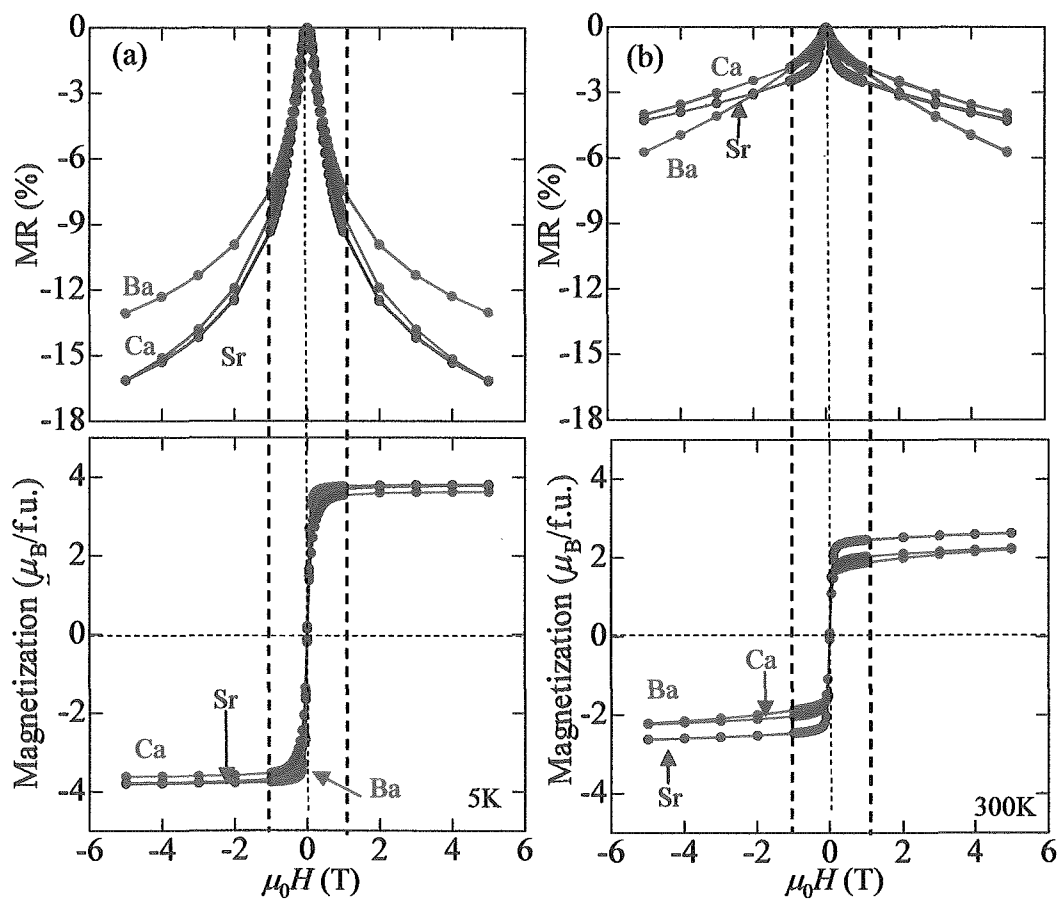

Fig. 4.3.5.-4-1 Field dependence of magnetoresistivity and magnetic properties for the Ba_2FeMoO_6, Sr_2FeMoO_6 and Ca_2FeMoO_6 samples measured at (a) 5 K and (b) 300 K. The fixed experimental condition is employed for MR-*H* and *M*-*H* measurements: the scanning in field steps of 0.05 T from $H = 0$ to 1 T and of 1 T form $H = 1$ to 7 T, respectively.

The detailed electromagnetic properties in the A_2FeMoO_6 (A = Ba, Sr and Ca) synthesized in this work were studied in order to establish an interrelation between transport properties and magnetic properties. In the case of A = Ba sample, TMR behaviour is seen from 5 K to 250 K as shown in Fig. 4.3.5.-3-2. However, the maximum value of MR was observed at 325 K and it suppresses rapidly higher than 325K. At 375 K, MR behaviour is mostly disappeared. The field dependence of the magnetic moment of A = Ba sample at 325 K and 375 K are shown in Fig. 4.3.5.-4-2. The spontaneous magnetic moment is observed at 325 K but the magnetic curvature is quite ambiguous suggesting that the sample is in the border of paramagnetism and ferrimagnetism (ferromagnetism). Thus, the magnetic moment at 5 T is low, *i.e.*, less than 2 μ_B/f.u. The *M-H* curvature obviously shows that the sample is in the paramagnetic state at 375 K. This is in good accordance with the feature of MR at 375 K. Since the T_C value of Ba_2FeMoO_6 has been well established [92] to be around 330 K, the observed strong suppression of MR value and paramagnetic characteristics are reasonable.

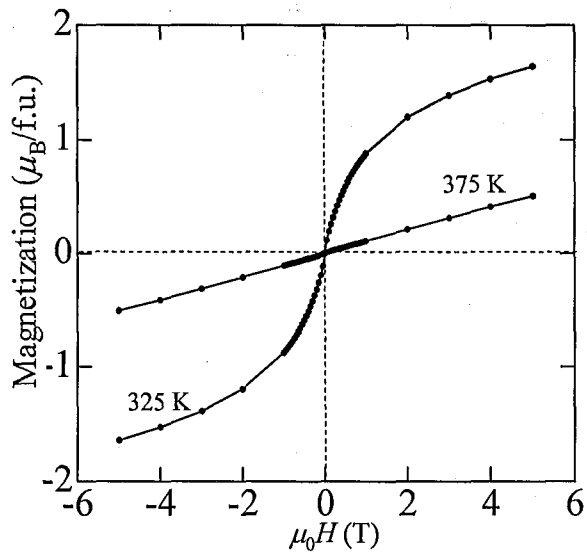

Fig. 4.3.5.-4-2 *M-H* curves for the Ba_2FeMoO_6 sample synthesized by the encapsulation technique.

For the case of Sr_2FeMoO_6, even though the *M-H* curvature is dull compared to that of low temperature, the spontaneous magnetic moment can be observed even at 375 K originating from the magnetic ordering as shown in Fig. 4.3.5.-4-3. This result is consistent with the MR bahaviour exhibited in Fig. 4.3.5.-3-2, *i.e.*, it can not be seen the maximum MR value up to 375 K. From Fig. 4.3.5.-3-2, TMR behaviour can be seen, at least, up to 325 K for this sample. Obtained experimental facts from the MR-*T* and the M-*H* suggest the sample with A = Sr would have higher T_C value than T = 375 K. This supports well established fact that the Sr_2FeMoO_6 has $T_C \approx$ 415 K [17].

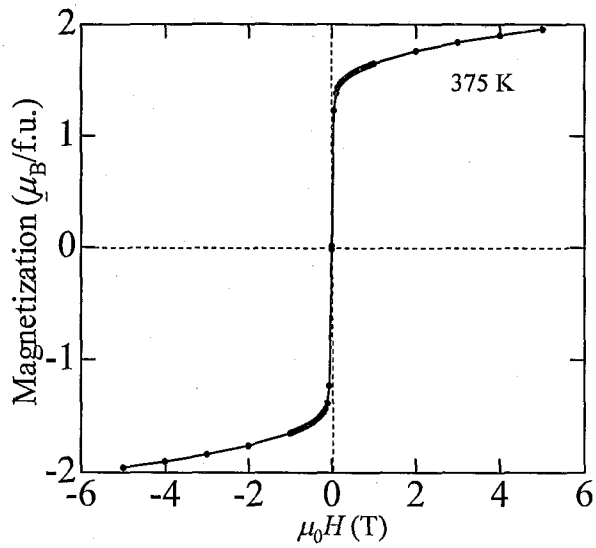

Fig. 4.3.5.-4-3 *M-H* curve for the Sr_2FeMoO_6 sample synthesized by the encapsulation technique.

An obvious TMR effect was observed up to $T \approx 300$ K in the case of A = Ca compound, as implied in Fig. 4.3.5.-3-2. At the MR maximum temperature, *i.e.*, 350 K in the Fig. 4.3.5.-3-2, an ambiguous behaviour of the magnetic moment was obtained, as represented in Fig. 4.3.5.-4-4. The figure shows that this sample is still magnetic state at 350 K. This is reasonable because the T_C value of Ca_2FeMoO_6 has been reported to be ~380 K [22]. At 375 K, the suppression of MR value resulting in the randomly oriented spin moment was revealed from Fig. 4.3.5.-3-2. However, the *M-H* curve at this temperature shown in Fig. 4.3.5.-4-4 exhibited small and ambiguous but clear spontaneous magnetic moment. These experimental results observed by MR-*T* and *M-H* at 375 K are contradiction. In the M-*H* measurement process by means of SQUID, even a small portion of magnetic moment can be detected as a magnetic signal, while the detection limit of magnetic moment of PPMS apparatus is insensitive than that of SQUID. Thus, the spontaneous magnetic moment observed in *M-H* properties measured by SQUID might be originated from some impurity phases with the magnetic moment in the Ca_2FeMoO_6 compound but it is not an intrinsic property of this compound. From the *M-T* and *M-H* measurements, it was found [22] the existence of a weak ferromagnetism with a significant saturation moment of 0.07 μ_B in the polycrystalline Ca_2FeMoO_6 sample at 700 K. They could not determine the origin of this anomalous but it could be due to a small impurity of Fe_3O_4 or Fe metal or FeMo alloy which present as small particles with amorphous state probably. Therefore, the spontaneous magnetic moment seen in Fig. 4.3.5.-4-4 might be originated from the impurity phase(s) mentioned above which could not be detected by the diffraction methods in the present Ca_2FeMoO_6 sample.

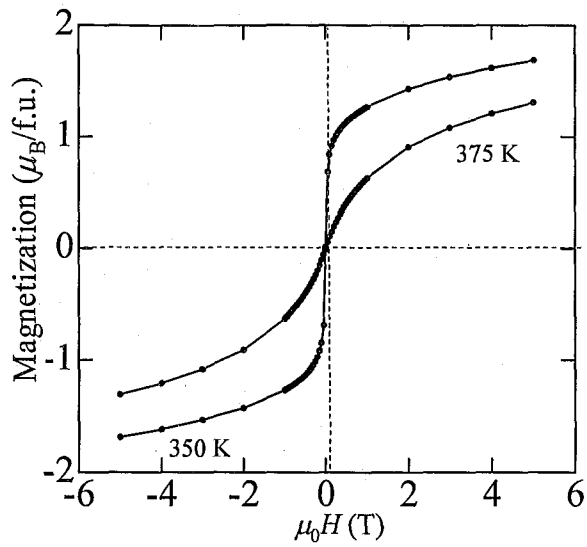

Fig. 4.3.5.-4-4 *M-H* curves for the Ca_2FeMoO_6 sample synthesized by the encapsulation technique.

Generally, MR originating from the spin-polarized tunneling at the grain or magnetic domain boundaries is possible to scale by the $(M/M_S)^2$ [5,17,19,20,101]. In the Ba_2FeMoO_6 sample, MR was proportional to the $(M/M_S)^2$ at room temperature [101] suggesting the origin of MR in the spin-polarized tunneling. An detailed investigation for general patterns that explain the low-field MR at low temperatures in the A_2FeMoO_6 system clarified a relationship between MR effect and magnetic moment [73]. In this study, a broad set of A_2FeMoO_6 samples through different synthesis routes have explored. It was found that there are two different regimes in the behaviour of the measured $R(H)/R(0)$ *versus* H: MR with a steeper slope in the low-field region ($H < 2$ T) and the high-field MR effect with a less pronounced slope. The low-field MR per unit of applied field *vs* M_S was plotted because differences between samples were prominent in the differences of low-field MR rather than in the high-field behaviour shown in Fig. 4.3.5.-4-5. It can be seen an essentially linear dependence of low-field MR on M_S.

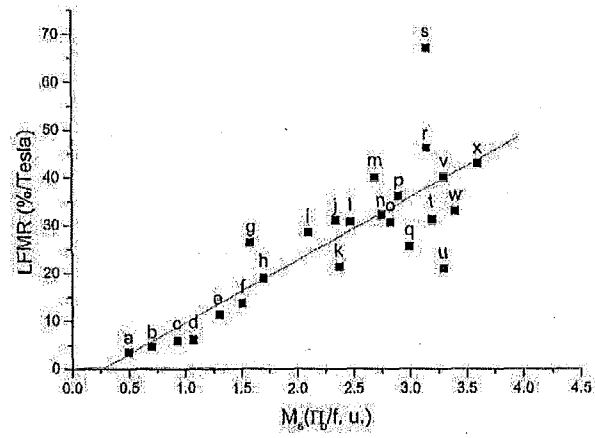

Fig. 4.3.5.-4-5 Low-field MR (LFMR) per unit of applied field *versus* saturated magnetic moment, M_S [73].

The study claimed that this dependence is further connected with the relative degree of antisite disorder at the B site. This was explained in terms of a spin dependent crossing of intragranular

barriers originated from the presence of antiferromagnetic $SrFeO_3$ patches that naturally develop when antisite disorder occurs in the double perovskites. The presence of a moderate levels of antisite disorder would be at the very root of low-field MR in A_2FeMoO_6 double perovskites. The scattering of $(M/M_S)^2$ as a function of the field confirms an electron spin dependent crossing of barriers as the mechanism responsible for the low-field MR [17,73]. The observed dependence seen in Fig. 4.3.5.-4-5 further correlates to relative ordering of Fe and Mo as seen in Fig. 4.3.5.-4-6. In contrast with the remarked dependence of low-field MR on M_S, high-field MR was found to be independent of the M_S value. Furthermore, based on experimental facts only, the low-field TMR can be enhanced as A_2FeMoO_6 materials become magnetically soft [21].

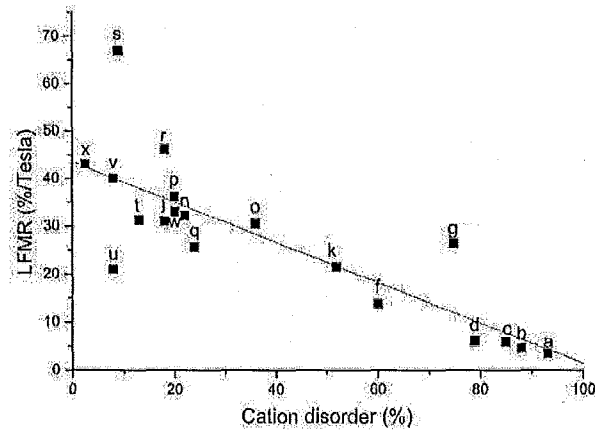

Fig. 4.3.5.-4-6 LFMR per unit of applied field as a function of percentage cation disorder [73].

4.3.5.-5 The Dominating Factors for the Type of Magnetism and for the Magnetic Transition Temperatures in the *B*-site Ordered Double-Perovskite Systems

As described in the previous sections, A_2FeMoO_6 shows various complicated magnetic characteristics that can not be explained theoretically. General *B*-site ordered double perovskites, *i.e.*, $A_2B'B''O_6$, as well as A_2FeMoO_6 have extensive types of magnetism such as ferrimagnet, antiferromagnet, paramagnet, spin glass and coexisting with ferromagnet and antiferromagnet in a sample. The previous investigations reported that the ferrimagnetism are established for example, A_2MnReO_6, A_2NiReO_6, A_2FeReO_6 (A = Ba) [29,30], A_2CrMoO_6 (A = Sr, Ca) [30,102], A_2CrReO_6 (A = Sr, Ca) [30,103] and ALaMnReO$_6$ (A = Ba, Sr, Ca) [30,104], while the antiferromagnetic characters were found in, *e.g.*, A_2CoReO_6 (A = Ba) [29,30], A_2FeWO_6 (A = Sr) [33,105-107], A_2MnMoO_6 (A = Sr) [19,24,75,108,109], A_2CoMoO_6 (A = Sr) [19,24,108,109]. Other group however, claimed that A_2MnMoO_6 (A = Sr) and A_2CoMoO_6 (A = Sr) are paramagnetic compounds [75]. $A_2B'B''O_6$ with B' = Cr, Fe and B'' = Mo, W and Re [11,29,54,102,103,110], A_2FeReO_6 (A = Sr) and A_2CrMoO_6 (A = Sr) were reported to be ferromagnetic [24], against the previous reports on ferrimagnetism for these compounds which is mentioned above. The types of magnetism of these compounds and related magnetic properties, *e.g.*, values of T_C and T_N *etc.*, have not been systematically classified in terms of general sample

compositions. In order to obtain some sort of rules for the type of magnetism and revealing the origins of complicated magnetic properties in the *B*-site ordered double-perovskite compounds, multivariate data analysis was carried out. It is because clarifying these rules and origins may provide us with an apparent indicator for tailoring desirable materials, *e.g.*, compounds possessing high magnetic-transition temperatures, from a standpoint of industrial application.

In the initial stage of analysis, crucial structural parameters (X variables) for the type of magnetism of $A_2B'B''O_6$ were extracted by means of PLSDA analysis. A list of observations which consist of ferrimagnets, antiferromagnets and paramagnets for the PLSDA study is tabulated in Table A.3.-1 (see Appendix A.3.). Two groups were categorized, *i.e.*, magnetic compounds consisting of ferri/antiferromagnetic phases and paramagnetic phases. All the basic structural data of these phases were reported in the published papers on the basis of the neutron/x-ray diffraction studies measured at room temperature. The extended structural parameters such as values of bond valence and BVS were calculated from the atomic positions and space groups *etc.* in the published literatures, while the ionic radii of cations were referred from a paper reported by Shanon [111]. The obtained score plot of PLSDA analysis which represents an interrelation between observations is shown in Fig. 4.3.5.-5-1 with the reliability of this analysis of ~73 %. Two distinct groups which consist of the magnetic compounds and the paramagnetic compounds are clearly seen in the figure. Though several paramagnetic compounds are grouped in the magnetic phases as dispersions of the analysis, it would not be serious because the majority of paramagnetic compounds are well analyzed in the same group and are well distinguished from the magnetic group.

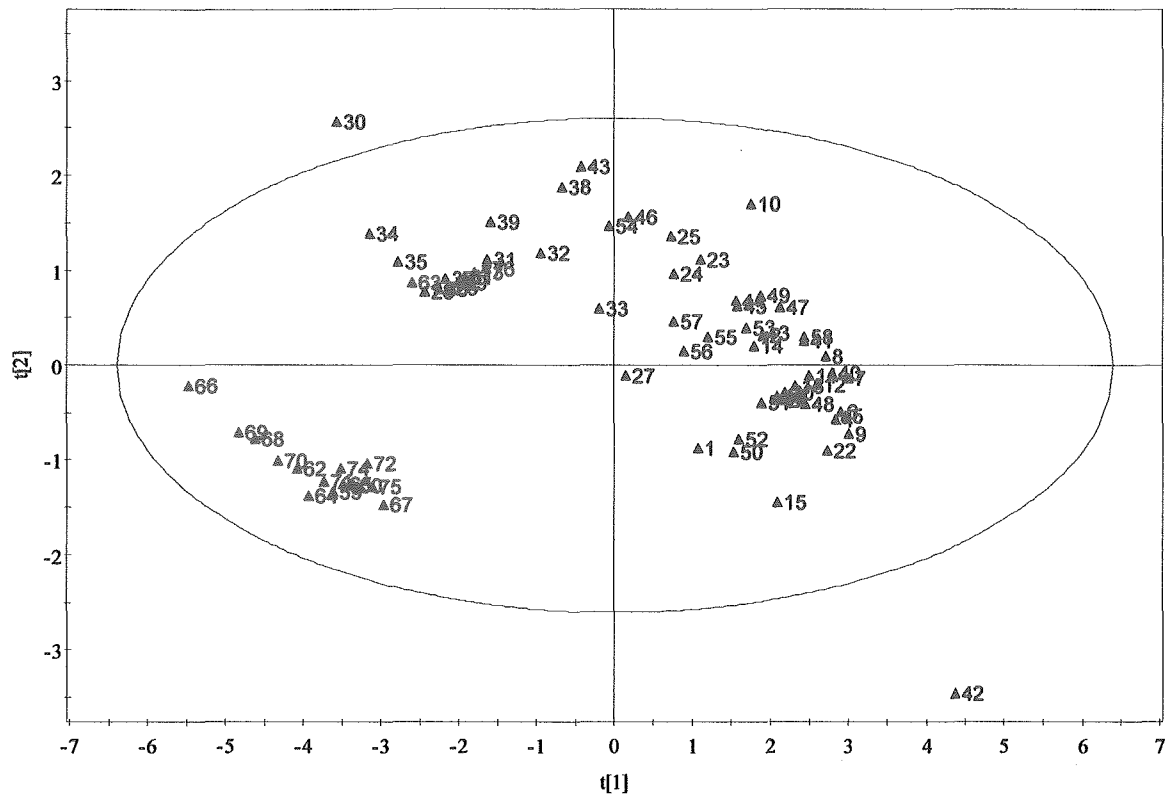

Fig. 4.3.5.-5-1 PLSDA score plot for the structural data of various *B*-site ordered double-perovskite compounds. The plot explains relationships between observations. Each observation is represented by number (see, Table A.3.-1): blue marks are magnetic compounds, whereas red one represents paramagnetic compounds.

Through out the PLSDA investigation, ionic radius of *B*", valence of *B*", bond length between *B*"-O and valence of *B*' were concluded to be the dominating X variables in this order for the type of magnetism of *B*-site ordered double perovskites. Note that this issue was analyzed in terms of "objective" structural parameters only without taking into account theoretical parameters such as electron-hopping strength, effects of exchange interactions or superexchange interactions *etc.* In spite of ferromagnetism/ferrimagnetism in the A_2FeMoO_6 has not been determined, this compound is classified as ferrimagnetic compound in the study of multivariate data analysis because a consideration of ferrimagnetism of this compound has been gaining ground, rather than ferromagnetism.

After the important structural parameters for the type of magnetism in the *B*-site ordered double-perovskites were clarified, key structural factors for the superb T_C values of ferrimagnetic $A_2B'B''O_6$ were tried to extract by PLS analysis based on the resultants of PLSDA study. Table 4.3.5.-5-1 shows ferrimagnetic observations utilized for the PLS investigation. Since a condition of the observation selection is very restricted in the present study, *i.e.*, observations for the analysis were selected when they have detailed/precise structural information and T_C values measured at 300 K, the number of observation is quite small unfortunately.

Table 4.3.5.-5-1 List of observations for the PLS analysis.

Number	Obsevation	Reference
1	Ba_2FeMoO_6	J. Magn. Magn. Mater. **242-245**, 747-750 (2002).
2	Ba_2FeReO_6	J. Phys.: Condens. Matter **12**, 965-973 (2000).
3	Ca_2FeMoO_6	Chem. Mater. **12**, 161-168 (2000).
4	Ca_2FeReO_6	J. Phys.: Condens. Matter **12**, 965-973 (2000).
5	$Ca_2Fe_{0.94}MoO_6$	J. Phys.: Condens. Matter **12**, 8295-8308 (2000).
6	$Sr_2CoMoO_{5.86}$	Chem. Mater. **14**, 812-818 (2002).
7	Sr_2CrMoO_6	J. Solid State Chem. **155**, 233-237 (2000).
8	Sr_2FeMoO_6	Phys. Rev. B **62**, 14197-14206 (2000).
9	Sr_2FeMoO_6	Phys. Rev. B **62**, 14197-14206 (2000).
10	Sr_2FeMoO_6	Phys. Rev. B **62**, 14197-14206 (2000).
11	Sr_2FeMoO_6	Phys. Rev. B **61**, 422–427 (2000).
12	$Sr_2Fe_{0.97}Mo_{0.94}O_{5.81}$	J. Phys.: Condens. Matter **12**, 8295-8308 (2000).
13	Pb_2MnReO_6	Chem. Mater. **15**, 668-674 (2003).

Fig. 4.3.5.-5-2 represents a definition of O(1), O(2) and O(3) positions for the present analysis in a general unit cell of double-perovskite which has three non-equivalent oxygen positions. In the case of cubic symmetry, all the oxygen atoms exist in the same site, whereas tetragonal/monoclinic samples have two/three distinct oxygen positions.

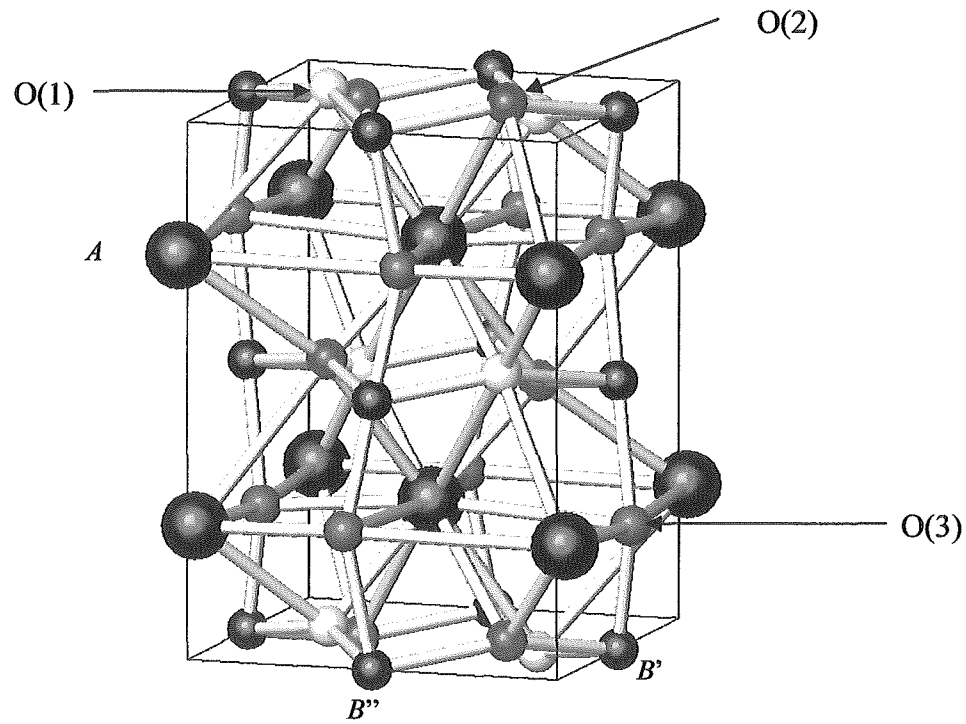

Fig. 4.3.5.-5-2 Definition of O(1), O(2) and O(3) positions for a compound with three non-equivalent oxygen sites in the present multivariate data analysis.

A list of structural parameters adopted for the analysis is tabled in Table 4.3.5.-5-2. More

detailed structural factors were employed for this analysis than a case of PLSDA because crucial X variables for the type of magnetism in this system have already revealed in the previous analysis. Thus, X variables are composed of detailed structural parameters and a value of T_C is settled on Y variable as a response variable. A score plot obtained by the analysis is displayed in Fig. 4.3.5.-5-3.

Table 4.3.5.-5-2 List of original variables and their explanations for the PLS analysis. All the variables are composed of structural-derived parameters only. "X" and "Y" represent cause/response variables, respectively.

	Variable	Explanation
X	$r(A)$, $r(B')$, $r(B'')$	Ionic radii of A, B' and B''
	AV. $r(B',B'')$	(Average) ionic radius of B' and B''
	V(B'), V(B'')	Valences of B' and B''
	V(B')$_{BVS}$, V(B'')$_{BVS}$	Valences of B' and B'' calculated by BVS method
	V(B')$_{BVS}$-2.5	Valence difference from 2.5 for B' (calculated by BVS method)
	a, b, c	Lattice parameters
	t.f.	Tolerance factor
	A-O(1), A-O(2)	Cation-oxygen bond lengths
	B'-O(1), B'-O(2), B'-O(3)	
	B''-O(1), B''-O(2), B''-O(3)	
	A-O, B'-O, B''-O	(Average) caion-oxygen bond lengths
	B'-O(1)-B'', B'-O(2)-B'', B'-O(3)-B''	Cation-oxygen bond angles
	B'-O-B''	(Average) cation-oxygen bond angle
	sA-O(3)	Cation-oxygen bond valences
	sB'-O(1), sB'-O(2), sB'-O(3)	
	sB''-O(1), sB''-O(2), sB''-O(3)	
	sA-O, sB'-O, sB''-O	(Average) cation-oxygen bond valences
Y	T_C	Magnetic transition temperature for ferrimagnetic compounds

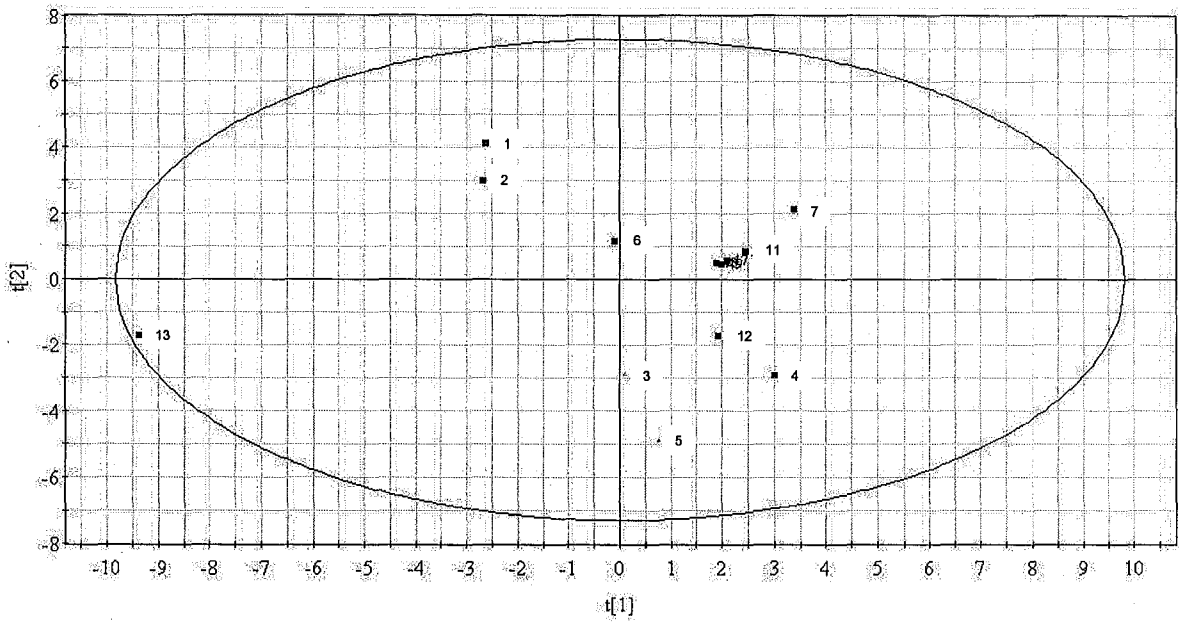

Fig. 4.3.5.-5-3 PLS score plot for the ferrimagnetic *B*-site ordered double perovskites.

In the beginning of PLS, the analysis was tried for 40 observations of ferrimagnetic compounds but it was found there are many outliers due to unreliable and inaccurate structural data through out the analyzing process. All the outliers were excluded from the observations in order to obtain reliable analysis results. Thus, only 13 compounds which would be a minimal number of observations were utilized for this study. All the observations are well dispersed in the score plot suggesting that there are various characteristics in the observations which is composed of various compositions. On the other hand, compounds consisting of the same composition represent similar characteristics, *i.e.*, it can be seen a cluster of Sr_2FeMoO_6 observations in the score plot. In the present study, there are four different Sr_2FeMoO_6 observations reported by two different groups but they show close relationships due to their common compositions. This also demonstrates that the PLS analysis in this work is reliable. The reliability factor of this analysis is ~91 %. The loadings plot of the present analysis is shown in Fig. 4.3.5.-5-4. This plot clarifies correlations between variables, *i.e.*, relationships between X- and Y-variables as well as relationships between X-variables each other, in this study. All the variables utilized for the analysis are located far from the plot origin and the most of coordinates of each variable in this plot are independent indicating all the variables are effectively working for the analysis.

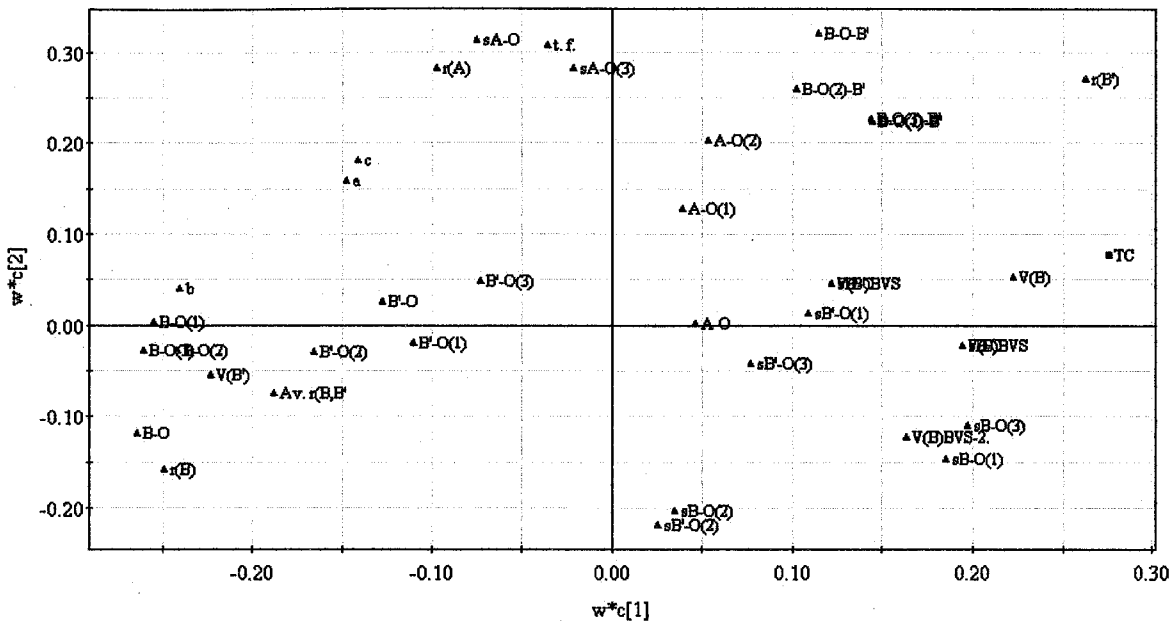

Fig. 4.3.5.-5-4 PLS loadings plot for the ferrimagnetic *B*-site ordered double perovskites. The plot represents interrelations between variables.

Fig. 4.3.5.-5-5 shows an interrelation between experimentally obtained T_C values, *i.e.*, reported values of T_C in the literatures, and predicted T_C values from the present PLS analysis. A good linear relationship was obtained implying that the PLS analysis and the following prediction is reliable. It was found that the reliability factor of prediction is ~72 %. It should be noted that T_C values of the ferrimagnetic $A_2B'B''O_6$ compounds were well analyzed and predicted by structural parameters only, in the same way as the analysis of type of magnetism for $A_2B'B''O_6$. The highest T_C value was reported [108] and expected Sr_2CrMoO_6 which has a reported T_C value of 450 K and the predicted T_C value form the present analysis of 457 K, respectively.

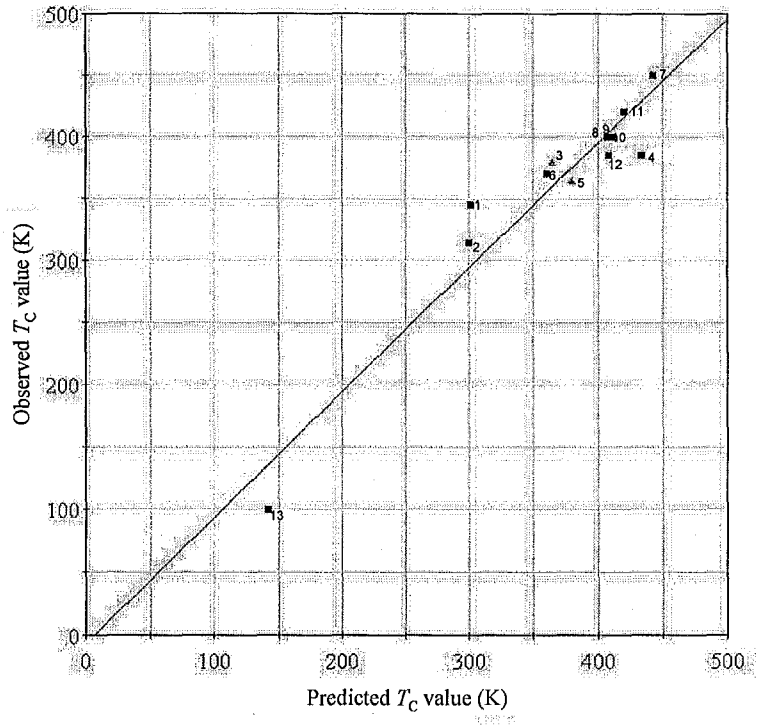

Fig. 4.3.5.-5-5 Observed *versus* predicted T_C for the ferrimagnetic *B*-site ordered double-perovskite compounds. The predicted T_C values are obtained from the present PLS analysis, while the observed values are referred from literatures.

The coefficient plot is shown in Fig. 4.3.5.-5-6 which reveals crucial structural parameters for the T_C value in this system. The variables have large coefficients would strongly affect the value of T_C, while the variables with small coefficients would not be dominant factors of T_C value. The obtained results imply that the bond distance between *B*' and O, ionic radius of *B*", *B*'-O(3) and *B*'-O(1) bond lengths, ionic radius of *B*', bond length between *B*' and O(2), lattice parameter *b*, valence of *B*' and valence of *B*" *etc.* may be crucial X-variables for the determination of T_C value, in this order.

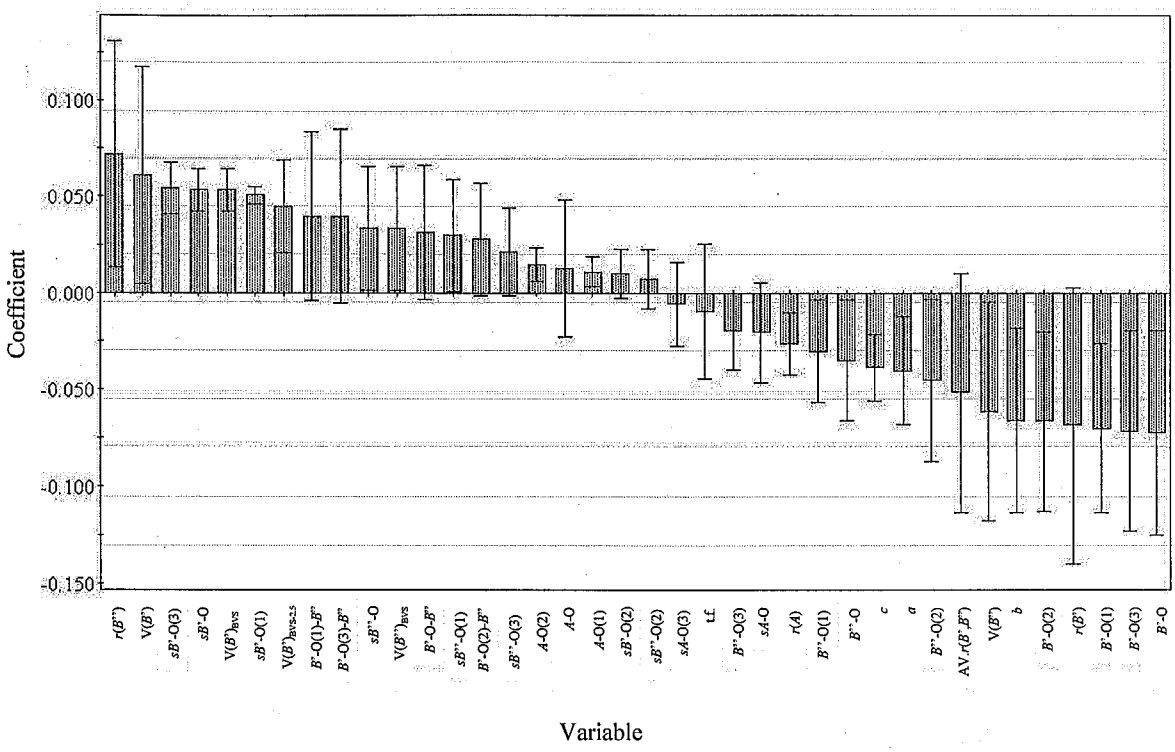

Fig. 4.3.5.-5-6 Relative importance of variables in terms of T_C obtained from the PLS analysis for the ferrimagnetic *B*-site ordered double-perovskite compounds.

By comparing the obtained results of PLSDA and PLS analyses, the most dominant structural parameters are the same, *i.e.*, ionic radius and valence of *B*", for the type of magnetism and the value of T_C. Also, the valence of *B*' was found to be one of the most important factors for both the type of magnetism and the T_C value. These agreements seem important because a magnetic transition temperature of $A_2B'B''O_6$ is derived from the magnetism of the compound. Generally, the magnetism and the value of T_C must be close relationship in magnetic compounds. This generalization is demonstrated by the present PLSDA and PLS analyses for the *B*-site ordered double perovskites. In the coefficient plot shown in Fig. 4.3.5.-5-6, X-variables possessing positive coefficients may enhance the value of T_C but variables with negative coefficients would suppress the T_C value. For instance, when the ionic radius of *B*" and valence of *B*' increase the values of T_C might be risen. Contrary, if average-bond length of *B*'-O, bond lengths between *B*' and O(1), O(2) and O(3), ionic radius of *B*', valence of *B*" and lattice parameter *b* increase T_C value might be decreased in this system. Thus, the present result indicates that for tailoring a new magnetic $A_2B'B''O_6$ compound with a high T_C value, the most straightforward way might be selecting a larger sized *B*" cation, choosing a high valent *B*' cation and designing to "decrease" the *B*'-O bond length *etc.* In this study, qualitative evaluation of the type of magnetism and quantitative modeling for T_C value in the $A_2B'B''O_6$ system is discussed in terms of structural parameters only. In fact, the Curie temperature seems to be controlled by structural parameters [26] through affecting the electronic bandwidth. Even though the present accomplishment provide us with just a first step for aims of this investigation, revealing essential

factors for the type of magnetism/the magnetic transition temperature by means of multivariate data analysis has not been tried, ever.

4.4. Conclusion

In conclusion of this chapter, the isovalent-cation effect on the electromagnetic properties and valence of iron in A_2FeMoO_6 was systematically studied in terms of the ionic radius of A site using samples with A = Ba, $Ba_{0.8}Sr_{0.2}$, $Ba_{0.5}Sr_{0.5}$, $Ba_{0.2}Sr_{0.8}$, Sr, $Ca_{0.2}Sr_{0.8}$, $Ca_{0.25}Sr_{0.75}$, $Ca_{0.5}Sr_{0.5}$ $Ca_{0.75}Sr_{0.25}$, $Ca_{0.8}Sr_{0.2}$ and Ca [V]. In the sample synthesis by means of an oxygen-getter-controlled low-O_2-pressure encapsulation technique [56], special care was taken to keep the samples as akin as possible in terms of the grain size (2 to 6 μm), oxygen content (determined at 5.98±0.02 for samples consisting of A = Ba, Sr and Ca: it might be possible to assign other samples to stoichiometric oxygen content. Thus, the oxygen content was denoted "6" in this thesis.) and the (high) degree of Fe/Mo order ($S_{ave.}$ of ~0.94 for all the samples studied) which strongly affect the physical properties and the valence of iron.

The electromagnetic properties in particular derived from the halfmetallicity, *i.e.*, MR effect and the valence mixing of iron, were influenced by the effect of isovalent-cation substitution at A site [V]. This is reasonable because the MR characteristics and Mössbauer spectra revealed a feature of high degree of halfmetallicity and valence mixing between Fe and Mo by the chemical pressure at A site. Thereby the halfmetallicity induced properties would be strongly depended on the substitution. A systematic shift from the II/III mixed valence state towards pure II was observed for Fe with increasing Ba concentration at the A site, though even for the end phase with A = Ba a considerable degree of valence mixing was concluded from the hyperfine parameters obtained from the Mössbauer measurements. Parallel to the shift of the valence balance from $Fe^{II/III}$-$Mo^{V/VI}$ closer to that of Fe^{II}-Mo^{VI}, the degree of Fe/Mo order was found relatively to increase. On the other hand, a significant valence shift was not observed for Fe with Ca substitution at the A site. In this regime, the valence of iron was revealed to be almost constant up to the end phase with A = Ca maintaining the II/III mixed valence state of iron [V]. The valence-mixing state of B site in the present A_2FeMoO_6 sample manifested by Mössbauer and XANES studies [VI] was considered to derive from size-only-dependent effect of cation substitution at the A site. Thereby the density of state of B cations might be varied through the chemical pressure. From band structure calculations on the basis of the LDA method, density of states were revealed to clearly represent a halfmetallic feature for the most fundamental compounds consisting of A = Ba, Sr and Ca [79]. An outstanding difference originated from size difference at A-site cation could be seen in a partial density of state of Mo 4*d* existing below the Fermi level. The calculated area of partial DOS of Mo 4*d* was found to be relatively small in the case of Ba_2FeMoO_6, while those for Sr_2FeMoO_6 and Ca_2FeMoO_6 were mostly equivalent. Since decreases in the area suggest a lessen electron density of the Mo 4*d* state, charge and spin density of the itinerant electron of Mo 4*d* tend to be transferred easily to Fe 3*d*, *i.e.*, transferring from

Mo^{V} to Fe^{III}, would be a plausible explanation. Through out this shift, the valence of Fe ought to decrease resulting in closer to II (keeping the valence state of II/III) in proportion to the V_{Mo} toward VI in the Ba_2FeMoO_6. This resultants were agreed with the experimental facts of Mössbauer study: the behaviour of isomer-shift value in terms of $r(A^{II})$ was accord with the results of the area of partial DOS of Mo 4*d* below the E_F as a function of $r(A^{II})$.

The intergain-magnetoresistivity as well as the field dependence of MR effects measured at various temperatures which are derived from the halfmetallic characteristics showed an apparent *A*-cation size dependence, also. In the most fundamental members of A_2FeMoO_6 which consist of *A* = Ba, Sr and Ca, the intergain-magnetoresistivity responses were commonly observed possessing its maxima at the lowest temperature in the present study but the magnitude of maximum was affected by $r(A^{II})$. Ba_2FeMoO_6 exhibited the smallest absolute value of the maximum of the intergrain MR from the MR-*T* curve, whereas those for *A* = Sr and Ca compounds were similar [V]. Although the presence of a moderate levels of antisite disorder would be required for low-field MR in A_2FeMoO_6 double perovskites [73] and a tendency of slightly increased the concentration of miss-occupancy of Fe at the Mo site was seen with decreasing $r(A^{II})$, the antisite-defect value was found to be small in each sample [V]. Thus, the degrees of Fe/Mo order would be possible to regard as almost constant for the present samples. Consequently, the effect of small difference of *B*-site ordering among samples studied might be rule out and be possible to conclude that the isovalent-substitution at *A* site would be the most dominant parameter for the difference in the intergrain MR. The magnitudes of ρ-*T* property at whole temperature range and of *M-H*/MR-*H* properties measured at low temperature applying high field as well as the MR characteristics demonstrated that the relatively equivalent values were obtained for Sr_2FeMoO_6 and Ca_2FeMoO_6 compounds in this work [V]. In the Ba_2FeMoO_6, these property-derived values were dissimilar from those of Sr_2FeMoO_6 and Ca_2FeMoO_6. This is in good agreement with the conclusions of *A*-site size dependences of V_{Fe} and of the electronic structure described above. In the present investigation, these common experimental tendencies seen in the physical properties related to the halfmetallicity are considered to have their origin of the cation-size difference at *A* site by the isovalent substitution. It is because the prominent material parameters which possibly affect the physical properties and the valence of iron were carefully fixed in the present work.

From the material designing and tailoring points of view, the multivariate data analyses were tried in order to (*i*) find out some rules and classifications of the type of magnetism based on the composition of compounds and (*ii*) to obtain an indication for a brand new compound which has a potential of the industrial application with high magnetic transition temperature in the general *B*-site ordered double perovskites. The common parameters were extracted to be important factors for both the type of magnetism and values of T_C such as the valence of *B*', ionic radius and valence of *B*". Since a magnetic transition temperature of $A_2B'B"O_6$ is derived from the magnetism of the compound, the results revealing the same parameters as essential factors for both matters would be reasonable and intrinsic. Even though these issues argued in the present study were discussed without considering the "subjective factors", *e.g.*,

electron-hopping strength/width, effects of exchange interactions or superexchange interactions *etc.*, which are often concluded to be important to determine the type of magnetism and/or T_C in the $A_2B'B''O_6$ system, the variation of structural parameters might also induce the changes in these theoretical factors, also. Improvement of PLSDA and PLS analyses by increasing a number of observations is required to obtain more reliable conclusion in terms of the aim of this research.

References

1. M.T. Anderson, K.B. Greenwood, G.A. Taylor, and K.R. Poeppelmeier, *Prog. Solid State Chem.* **22**, 197 (1993).
2. R. Roy, *J. Amer. Ceram. Soc.* **37**, 581 (1954).
3. E.G. Steward and H.P. Rooksby, *Actra Crystallogr.* **4**, 503 (1951).
4. F.S. Galasso, L. Katz, and R. Ward, *J. Am. Chem. Soc.* **81**, 820 (1959).
5. E.J. Fresia, L. Katz, and R. Ward, *J. Am. Chem. Soc.* **81**, 4783 (1959).
6. L. Katz, and R. Ward, *Inorg. Chem.* **3**, 205 (1964).
7. P. Woodward, R.-D. Hoffmann, and A.W. Sleight, *J. Mater. Res.* **9**, 2118 (1994).
8. U. Amador, C.J.D. Hetherington, E. Moran, and M.A. Alario-Franco, *J. Solid State Chem.* **96**, 132 (1992).
9. T. Nakamura and J.-H. Choy, *J. Solid State Chem.* **20**, 233 (1977).
10. G. Prinz, *Science* **282**, 1660 (1998).
11. R.P. Borges, R.M. Thomas, C. Cullinan, J.M.D. Coey, R. Suryanarayanan, L. Ben-Dor, L. Pinsard-Gaudart, and A. Revcolevschi, *J. Phys.: Condens. Matter* **11**, L445 (1999).
12. J.M. DeTeresa, A. Barthélémy, A. Fert, J.P. Contour, R. Lyonnet, F. Montaigne, P. Seneor, and A. Vaurès, *Phys. Rev. Lett.* **82**, 4288 (1999).
13. H.Y. Hwang, S.-W. Cheong, N.P. Ong, and B. Batlogg, *Phys. Rev. Lett.* **77**, 2041 (1996).
14. J.M.D. Coey, *J. Appl. Phys.* **85**, 5576 (1999).
15. A. Maignan, C. Martin, M. Hervieu, and B. Raveau, *J. Magn. Magn. Mater.* **211**, 173 (2000).
16. L.S. Lobanovskiĭ, I.O. Troyanchuk, and H. Szymczak, *J. Exp. Theor. Phys.* **91**, 537 (2000).
17. K.-I. Kobayashi, T. Kimura, H. Sawada, K. Terakura, and Y. Tokura, *Nature* (London) **395**, 677 (1998).
18. T.H. Kim, M. Uehara, S.-W. Cheong, and S. Lee, *Appl. Phys. Lett.* **74**, 1737 (1999).
19. K.-I. Kobayashi, T. Kimura, Y. Tomioka, H. Sawada, K. Terakura, and Y. Tokura, *Phys. Rev. B* **59**, 11159 (1999).
20. H.Q. Yin, J.-S. Zhou, J.-P. Zhou, R. Dass, J.T. McDevitt, and J.B. Goodenough, *Appl. Phys. Lett.* **75**, 2812 (1999).
21. B.-G. Kim, Y.-S. Hor, and S.-W. Cheong, *Appl. Phys. Lett.* **79**, 388 (2001).
22. J.A. Alonso, M.T. Casais, M.J. Martínez-Lope, J.L. Martínez, P. Velasco, A. Muñoz, and M.T. Fernández-Díaz, *Chem. Mater.* **12**, 161 (2000).
23. Y. Shimakawa, Y. Kubo, and T. Manako, *Nature* (London) **379**, 53 (1996).
24. D.D. Sarma, *Cuur. Opin. Solid State Mater. Sci.* **5**, 261 (2001).
25. J.J. Blanco, T. Hernandez, L.M. Rodriguez-Martinez, M. Insausti, J.M. Barandiaran, J.-M. Greneche, and T. Rojo, *J. Mater. Chem.* **11**, 253 (2001).
26. C. Ritter, M.R. Ibarra, L. Morellon, J. Blasco, J. García, and J.M. De Teresa, *J. Phys.: Condens. Matter* **12**, 8295 (2000).
27. F.S. Galasso, F.C. Douglas, and R.J. Kasper, *J. Chem. Phys.* **44**, 1672 (1966).
28. T. Nakagawa, *J. Phys. Soc. Jpn.* **24**, 806 (1968).
29. A.W. Sleight and J.F. Weiher, *J. Phys. Chem. Solids* **33**, 679 (1972).
30. J. Gopalakrishnan, A. Chattopadhyay, S.B. Ogale, T. Venkatesan, R.L. Greene, A.J. Millis, K. Ramesha, B. Hannoyer, and G. Marest, *Phys. Rev. B* **62**, 9538 (2000).
31. J.B. Philipp, D. Reisinger, M. Schonecke, A. Marx, A. Erb, L. Alff, R. Gross, and J. Klein, *Appl. Phys. Lett.* **79**, 3654 (2001).
32. H.Y. Hwang, S.-W. Cheong, P.G. Radaelli, M. Marezio, and B. Batlogg, *Phys. Rev. Lett.* **75**, 914 (1995).
33. J.B. Goodenough, and R.I. Dass, *Int. J. Inorg. Mater.* **2**, 3 (2000).
34. T.S. Chan, R.S. Liu, G.Y. Guo, S.F. Hu, J.G. Lin, J.M. Chen, and J.P. Attfield, *Chem. Mater.* **15**, 425 (2003).
35. J. Lindén, T. Yamamoto, J. Nakamura, H. Yamauchi, and M. Karppinen, *Phys. Rev. B* **66**, 184408 (2002).
36. H. Yanagihara, W. Cheong, M.B. Salamon, Sh. Xu, and Y. Moritomo, *Phys. Rev. B* **65**, 092411 (2002).
37. Y. Moritomo, H. Kusuya, A. Machida, E. Nishibori, M. Takata, M. Sakata, and A. Nakamura, *J. Phys. Soc. Jpn.* **70**, 3182 (2001).
38. H. Kawanaka, I. Hase, S. Toyama, and Y. Nishihara, *Physica B* **281-282**, 518 (2000).
39. A.J. Millis, P.B. Littlewood, and B.I. Shraiman, *Phys. Rev. Lett.* **74**, 5114 (1995); A.J. Millis, B.I. Shraiman, and R. Mueller, *Phys. Rev. Lett.* **77**, 175 (1996).
40. L. Pinsard-Gaudart, R. Surynarayanan, A. Revcolevschi, J. Rodriguez-Carvajal, J.-M. Greneche, P.A.I. Smith, R.M. Thomas, R.P. Borges, and J.M.D. Coey, *J. Appl. Phys.* **87**, 7118 (2000).
41. J.M.D. Coey, M. Viret, and S. von Molnar, *Adv. Phys.* **48**, 167 (1999).
42. S.G. Lewis, P.B. Allen, and T. Sasaki, *Phys. Rev. B* **55**, 10253 (1997).
43. O. Chmaissem, R. Kruk, B. Dabrowski, D.E. Brown, X. Xiong, S. Kolesnik, J.D. Jorgensen, and C.W.

Kimball, *Phys. Rev. B* **62**, 14197 (2000).
44. S. Nakayama, T. Nakagawa, and S. Nomura, *J. Phys. Soc. Jpn.* **24**, 219 (1968).
45. R.S. Liu, T.S. Chan, S.F. Hu, J.G. Lin, and C.Y. Huang, *J. Magn. Magn. Mater.* **239**, 164 (2002).
46. B. García-Landa, C. Ritter, M.R. Ibarra, J. Blasco, P.A. Algarabel, R. Mahendiran, J. García, *Solid. State. Commun.* **110**, 435 (1999).
47. Y. Moritomo, S. Xu, A. Machida, T. Akimoto, E. Nishibori, M. Takata, M. Sakata, and K. Ohoyama, *J. Phys. Soc. Jpn.* **69**, 1723 (2000).
48. D.L. Connelly, J.S. Loomis, and D.E. Mapother, *Phys. Rev. B* **3**, 924 (1971).
49. D.S. Simons and M.B. Salamon, *Phys. Rev. B* **10**, 4680 (1974).
50. M.T. Causa, A. Butera, M. Tovar, and J. Fontcuberta, *Physica B* **320**, 79 (2002).
51. S. Ray, A. Kumar, D.D. Sarma, R. Cimino, S. Turchini, S. Zennaro, and N. Zema, *Phys. Rev. Lett.* **87**, 097204 (2001).
52. D.D. Sarma, P. Mahadevan, T. Saha-Dasgupta, S. Ray, and A. Kumar, *Phys. Rev. Lett.* **85**, 2549 (2000).; J. Kanamori and K. Terakura, *J. Phys. Soc. Jpn.* **70**, 1433 (2001).
53. B. Martínez, J. Navarro, Ll. Balcells, and J. Fontcuberta, *J. Phys.: Condens. Matter* **12**, 10515 (2000).
54. F.S. Galasso, *Structure, properties and preparation of perovskite-type compounds*, Pergamon, Oxford (1969).
55. T. Nakamura, K. Kunihara, and H. Hirose, Mater. Res. Bull. **16**, 321 (1981).
56. T. Yamamoto, J. Liimatainen, J. Lindén, M. Karppinen, H. Yamauchi, J. Mater. Chem. **10**, 2342 (2000).
57. F.D. Richardson and J.H.E. Jeffes, *J. Iron Steel Inst.* (London) **160**, 261 (1948).
58. M.B. Robin and P. Day, *Adv. Inorg. Chem. Radiochem.* **10**, 247 (1967).
59. J. Nakamura, J. Lindén, H. Suematsu, M. Karppinen, and H. Yamauchi, *Physica C* **338**, 121 (2000).
60. J. Lindén, T. Yamamoto, M. Karppinen, H. Yamauchi, and T. Pietari, *Appl. Phys. Lett.* **76**, 2925 (2000).
61. I.D. Brown and D. Altermatt, *Acta Cryst. B* **41**, 244 (1985).
62. J.-S. Kang, J.H. Kim, A. Sekiyama, S. Kasai, S. Suga, S.W. Han, K.H. Kim, T. Muro, Y. Saitoh, C. Hwang, C.G. Olson, B.J. Park, B.W. Lee, J.H. Shim, J.H. Park, and B.I. Min, *Phys. Rev. B* **66**, 113105 (2002).
63. J.M. Greneche, M. Venkatesan, R. Suryanarayanan, and J.M.D. Coey, *Phys. Rev. B* **63**, 174403 (2001).
64. P.A. Algarabel, L. Morellon, J.M. De Teresa, J. Blasco, J. García, M.R. Ibarra, T. Hernández, F. Plazaola, and J.M. Barandiarán, *J. Magn. Magn. Mater.* **226-230**, 1089 (2001).
65. M.S. Moreno, J.E. Gayone, M. Abbate, A. Caneiro, D. Niebieskikwiat, R.D. Sánchez, A. de Siervo, R. Landers, and G. Zampieri, *Solid State Commun.* **120**, 161 (2001).
66. Cz. Kapusta, P.C. Riedi, D. Zajac, M. Sikora, J.M. De Teresa, L. Morellon, and M.R. Ibarra, *J. Magn. Magn. Mater.* **242-245**, 701 (2002).
67. L. Eriksson, E. Johansson, N. Kettaneh-Wold, and S. Wold, *Multi- and Megavariate Data analysis Principles and Applications*, Umetrics Ab, Umeå (2001).
68. L. Eriksson, E. Johansson, N. Kettaneh-Wold, and S. Wold, *Introduction to Multi- and Megavariate Data analysis using Projection Methods (PCA & PLS)*, Umetrics Ab, Umeå (1999), p. 490.
69. S. Wold, M. Sjöström, and L. Eriksson, *Chemometrics and Intelligent Laboratory Systems* **58**, 109 (2001).
70. C.L. Yuan, S.G. Wang, W.H. Song, T. Yu, J.M. Dai, S.L. Ye, and Y.P. Sun, *Appl. Phys. Lett.* **75**, 3853 (1999).
71. H. Han, B.J. Han, J.S. Park, B.W. Lee, S.J. Kim, and C.S. Kim, *J. Appl. Phys.* **89**, 7687 (2001).
72. D.D. Sarma, E.V. Sampathkumaran, S. Ray, R. Nagarajan, S. Majumdar, A. Kumar, G. Nalini, and T.N. Guru Row, *Solid State Commun.* **114**, 465 (2000).
73. M. García-Hernández, J.L. Martínez, M.J. Martínez-Lope, M.T. Casais, and J.A. Alonso, *Phys. Rev. Lett.* **86**, 2443 (2001).
74. Y. Tomioka, T. Okuda, Y. Okimoto, R. Kumai, K.-I. Kobayashi, and Y. Tokura, *Phys. Rev. B* **61**, 422 (2000).
75. Y. Moritomo, Sh. Xu, A. Machida, T. Akimoto, E. Nishibori, M. Takata, and M. Sakata, *Phys. Rev. B* **61**, R7827 (2000).
76. N.N. Greenwood, T.C. Gibb, *Mössbauer Spectroscopy*, Chapman & Hall, London 1971, p. 91.
77. J. Lindén, A. Kjekshus, P. Karen, J. Miettinen, M. Karppinen, *J. Solid State Chem.* **139**, 168 (1998).
78. N. Nguyen, F. Sriti, C. Martin, F. Bourée, J.M. Grenèche, A. Ducouret, F. Studer, B. Raveau, *J. Phys.: Condens. Matter* **14**, 12629 (2002).
79. E.L. Rautama, Master Thesis, Helsinki University of Technology, Espoo 2005, pp. 70-99.
80. S.B. Kim, B.W. Lee, and C.S. Kim, *J. Magn. Magn. Mater.* **242-245**, 747 (2002).
81. J.P. Crocombette, M. Pollak, F. Jollet, N. Thromat, and M. Gautier-Soyer, *Phys. Rev. B* **52**, 3143 (1995).
82. M. Gautier-Soyer, *J. Eur. Ceram. Soc.***18**, 2253 (1998).
83. Z. Fang, K. Terakura, J. Kanamori, *Phys. Rev. B* **63**, R180407 (2001).
84. Y. Hirota, Master Thesis, Tokyo Institute of Technology, Tokyo, 2004, p. 44.
85. J. Navarro, Ll. Balcells, F. Sandiumenge, M. Bibes, A. Roig, B. Martínez, and J. Fontcuberta, *J. Phys.:*

Codens. Matter **13**, 8481 (2001).
86. H.Q. Yin, J.-S. Zhou, R.Dass, J.-P. Zhou, J.T. McDevitt, and J.B. Goodenough, *J. Appl. Phys.* **87**, 6761 (2000).
87. W. Westerburg, D. Reisinger, and G. Jakob, *Phys. Rev. B* **62**, 767 (2000).
88. H. Yanagihara, M.B. Salamon, Y. Lyanda-Geller, Sh. Xu, and Y. Moritomo, *Phys. Rev. B* **64**, 214407 (2001).
89. M. Itoh, I. Ohta, and Y. Inaguma, *Mater. Sic. Eng. B* **41**, 55 (1996).
90. T. Shimada, J. Nakamura, T. Motohashi, H. Yamauchi, and M. Karppinen, *Chem. Mater.* **15**, 4494 (2003).; Y.H. Huang, J.Lindén, H. Yamauchi, and M. Karppinen, *Chem. Mater.* **16**, 4337 (2004).
91. C.N.R. Rao, A.K. Cheetham, and R. Mahesh, *Chem. Mater.* **8**, 2421 (1996).
92. A. Maignan, B. Raveau, C. Martin, and M. Hervieu, *J. Solid State Chem.* **144**, 224 (1999).
93. J.M. De Teresa, D. Serrate, J. Blasco, M.R. Ibarra, and L. Morellon, *Phys. Rev. B* **69**, 144401 (2004).
94. T. Alamelu, U.V. Varadaraju, M. Venkatesan, A.P. Douvalis, and J.M.D. Coey, *J. Appl. Phys.* **91**, 8909 (2002).
95. W. Prellier, V. Smolyaninova, A. Biswas, C. Galley, R.L. Greene, K. Ramesha, and J. Gopalakrishnan, *J. Phys.: Condens. Matter* **12**, 965 (2000).
96. P.G. Radaelli, G. Iannone, M. Marezio, H.Y. Hwang, S.-W. Cheong, J.D. Jorgensen, and D.N. Argyriou, *Phys. Rev. B* **56**, 8265 (1997).
97. M. Medarde, J. Mesot, P. Lacorre, S. Rosenkranz, P. Fischer, and K. Gobrecht, *Phys. Rev. B* **52**, 9248 (1995).
98. A.S. Ogale, S.B. Ogale, R. Ramesh, and T. Venkatesan, *Appl. Phys. Lett.* **75**, 537 (1999).
99. Ll. Balcells, J. Navarro, M. Bibes, A. Roig, B. Martínez, and J. Fontcuberta, *Appl. Phys. Lett.* **78**, 781 (2000).
100. K.-I. Kobayashi, T. Okuda, Y. Tomioka, T. Kimura, and Y. Tokura, *J. Magn. Magn. Mater.* **218**, 17 (2000).
101. J.S. Park, B.J. Han, C.S. Kim, and B.W. Lee, *J. Magn. Magn. Mater.* **226-230**, 741 (2001).
102. F.K. Patterson, C.W. Moeller, and R. Ward, *Inorg. Chem.* **2**, 196 (1963).
103. A.W. Sleight, J. Longo, and R. Ward, *Inorg. Chem.* **1**, 245 (1962).
104. K. Ramesha, V. Thangadurai, D. Sutar, S.V. Subramanyam, G.N. Subbanna, and J. Gopalakrishnan, *Mater. Res. Bull.* **35**, 559 (2000).
105. G. Blasse, *Philips. Res. Repts.* **20**, 327 (1965).
106. T. Nakagawa, K. Yoshikawa, and S. Nomura, *J. Phys. Soc. Jpn.* **27**, 880 (1969).
107. H. Kawanaka, I. Hase, S. Toyama, and Y. Nishihara, *J. Phys. Soc. Jpn.* **68**, 2890 (1999).
108. A. Arulraj, K. Ramesha, J. Gopalakrishnan, and C.N.R. Rao, *J. Solid State Chem.* **155**, 233 (2000).
109. N. Hamada and Y. Moritomo In: 3rd Japan-Korea joint workshop on first-principles electronic structure calculations, 2000.
110. J.M. Longo and R. Ward, *J. Am. Chem. Soc.* **83**, 1088 (1961).
111. R.D. Shannon, *Acta Cryst. A* **32**, 751 (1976).

5. SUMMARY AND GENERAL CONCLUSIONS

In the present work, revealing the "essence" of isovalent-cation substitution in the strongly-correlated electron systems was the first objective through out the research. In order to accomplish this aim, the experiments were planned in such a way that all the other material parameters remained as little affected as possible. On the basis of knowledge obtained from the consequences of this study, providing an indication for a new functional material possessing a possibility of industrial usage was set so as to the final accomplishment of this work. Two target systems were selected from a standpoint of a material application, *i.e.*, the tunneling-type magnetoresistance compounds of A_2FeMoO_{6-w} possessing double-perovskite structure and the high-T_c superconductive compounds of $CuBa_2RECu_2O_{7-\delta}$ consisting of triple-perovskite structure.

Since the mixed-valence states are possible for transition metal/few heavy metals, perovskite structures often take oxygen non-stoichiometry for tuning the transition-metal valence. Therefore, the precise determination of the oxygen content of compounds and further, the fine tuning of the oxygen content and controlling the material properties, *i.e.*, "oxygen engineering", is one of the most crucial/interesting topics in the functional perovskite-related compounds [I].

There are three critical factors limiting the practical use of the high-T_c superconductive materials, *i.e.*, the critical current density (J_c), the critical temperature (T_c) and the magnetic irreversibility-field line [$H_{irr}(T)$]. By considering these factors, synthesis process and toxicity of materials, high-T_c superconductive materials consisting of Bi and Cu only would have a possibility for industrial usage in future. Among these critical parameters, effects of isovalent-cation substitution at *A*/*RE* sites on the T_c in the $CuBa_2RECu_2O_{7-\delta}$ system have been well established. The dependence of H_{irr} on the isovalent-cation substitution at the *RE* site has not been established yet; nevertheless, $CuBa_2YCu_2O_{7-\delta}$ was known to possess the most superb H_{irr} characteristics among the present high-T_c superconductive materials. Therefore, the isovalent-cation effect on the H_{irr} characteristics in $CuBa_2RECu_2O_{7-\delta}$ with the values of 7-δ ranging from 6.91 to 6.94 (except $CuBa_2GdCu_2O_{6.98}$) was systematically studied in terms of the *RE* ionic radius in the present study [II,III]. Through a study of isovalent-*RE* effects in this system, it was found that the size of *RE* crucially controls the H_{irr} properties. $CuBa_2YbCu_2O_{6.93}$ and $CuBa_2(Y_{0.18}Lu_{0.82})Cu_2O_{6.93}$ which are composed of the same $r(RE^{III})$ and the equivalent oxygen content showed exactly the same H_{irr} values at all the temperature measured. It was evident that the H_{irr} characteristics were clearly enhanced in a monotonic way in proportion to decrease $r(RE^{III})$ and a record-high H_{irr} value of ~9.0 T was obtained at 77 K in the $CuBa_2(Yb_{0.6}Lu_{0.4})Cu_2O_{6.92}$ which is a compound including the smallest $r(RE^{III})$ essentially freed from impurity phases. Detailed observations of SEM/EDS and TEM implied that an existence of effective pinning site which may work as an extrinsic factor for the superior H_{irr} characteristics can not be applicable for the $CuBa_2(Yb_{0.6}Lu_{0.4})Cu_2O_{6.92}$ sample. Thus, this is the highest H_{irr} value ever reported for the $CuBa_2RECu_2O_{7-\delta}$ phase at 77 K owing to a "pure"

size-only-dependent effect.

The calculations based on the BVS concept utilizing reliable neutron structural data revealed that the amount of holes in the CuO_2 plane increases in proportion to decrease in $r(RE^{III})$ in the fully oxygenated $CuBa_2RECu_2O_{7-\delta}$ system. In the present study, the oxygen content was fixed at full through the samples maintaining the overall-hole concentration to be constant. Therefore, these introduced holes around the CuO_2 plane might be transferred from the $CuO_{1-\delta}$ chain retaining the total amount of holes. In the $CuBa_2RECu_2O_{7-\delta}$ compounds with the large *RE*'s the $CuO_{1-\delta}$ chain is more heavily doped with holes than the CuO_2 plane and the difference is quite large and hence the distribution of holes is far from homogeneous. Thus, the hole distribution between the $CuO_{1-\delta}$ chain and the CuO_2 plane changes to become more homogeneous over the crystal for smaller sized *RE* constituent, and this is believed to be the reason for the superior H_{irr} characteristics of the $CuBa_2RECu_2O_{7-\delta}$ compounds with the smallest *RE*'s. Disturbance of the $CuO_{1-\delta}$ chain is known to suppress the H_{irr} characteristics. Although this was not investigated in the present study, this possibility should not be ruled out for samples having larger *RE* constituents. It is because there is a possibility of intermixing between Ba and *RE* elements for $CuBa_2RECu_2O_{7-\delta}$ with large *RE*'s and if this happens, part of the O(1)-site oxygen atoms shift to the O(5) site which may induce the depression of H_{irr} values. This would also lead to relatively superb H_{irr} characteristics of smaller *RE* included $CuBa_2RECu_2O_{7-\delta}$ samples.

The Fe-based *B*-site ordered double-perovskite compounds, A_2FeMoO_6, possess two outstanding characteristics of the high ferromagnetic transition temperature and the high degree of spin polarization of ~100%, which induces the large tunneling-type magnetoresistance (TMR) effect. Besides, TMR characteristics of this compound depend strongly on the external magnetic field in the low-field region in particular. Therefore, A_2FeMoO_6 is believed to be one of the candidates of "spintronics" materials in future, *e.g.*, magnetoresistive random access memory (MRAM), the magnetic head utilizing the MR effects of material and a kind of spin transistor *etc.*. The A_2FeMoO_6 system however, is interest not only for the applications of industrial usage but also for the fundamental science. For example, ^{57}Fe Mössbauer studies have shown that iron in this compound possesses a mixed-valence state which is often observed together with the halfmetallic ground state of compounds.

Intense investigations have been reported on the effects of the aliovalent-cation substitution at the *B* site in this compound and the aliovalent substitution found to induce influences on the physical properties. On the other hand, systematic consequences of isovalent-cation substitution at *A* site had not been well understood, yet. Therefore, the isovalent-cation effects on the charge distribution of *B*'/*B*" cations, *i.e.*, the valences of Fe and Mo ($V_{Fe/Mo}$), and on the electromagnetic properties in the A_2FeMoO_6 were systematically studied in the present work in terms of the *A* ionic radius [V]. It was revealed that the *A*-cation size is one of the influential factors for both the valence balance of Fe/Mo species and electric/magnetic properties for the A_2FeMoO_6 compound. The measurements of ^{57}Fe Mössbauer [V] and Fe L_3 edge XANES [VI] clarified that all the A_2FeMoO_6 samples studied possess the valence mixing of

$Fe^{II/III}$ and thereby $Mo^{V/VI}$ state. The valence of iron of $(Ca,Sr)_2FeMoO_6$ exhibited independent behaviour of $r(A^{II})$ showing the mostly the constant V_{Fe} values, while a straightforward $r(A^{II})$ dependence of V_{Fe} was observed for $(Sr,Ba)_2FeMoO_6$ compounds. The larger the A-cation size was, the closer was the V_{Fe} of II maintaining the iron-valence state of II/III for $(Sr,Ba)_2FeMoO_6$. The mixed-valence state of Fe and Mo would be related to the itinerancy of down spins, *i.e.*, the conductivity electrons of this compound, between the Fe t_{2g} and Mo t_{2g} orbitals. Actually, band structure calculations for Ba_2FeMoO_6, Sr_2FeMoO_6 and Ca_2FeMoO_6 carried out in our group revealed that the differences in $r(A^{II})$ exert the variation in the partial density of state (DOS) in Mo 4*d* which exists below the Fermi level retaining all the compounds to be halfmetals. The calculated area of partial DOS of Mo 4*d* below the E_F, *i.e.*, A_{Mo}, as a function of $r(A^{II})$ was in accord with the behaviour of the valence state of iron in terms of ionic radius of A demonstrating the strong interrelation between V_{Fe} and A_{Mo}. Ba_2FeMoO_6 which includes the largest size of A cation represented the smallest A_{Mo} value among the calculated three compounds, while almost the equivalent A_{Mo} values were obtained for Sr_2FeMoO_6 and Ca_2FeMoO_6. The smaller A_{Mo} would suggest a high possibility of transferring the charge and spin density of the itinerant electron of Mo 4*d* to Fe 3*d* resulting in the V_{Fe} value to be closer to II in proportion to the V_{Mo} towards VI.

Since the miss-occupancy of Fe at the Mo site was found to be small in all the present samples, it is possible to consider that the degrees of Fe/Mo order are high for samples studied. However, there was a tendency: with increasing the difference of valence between Fe and Mo, *i.e.*, A_2FeMoO_6 consisting of larger A's, the higher degree of Fe/Mo order and further, the superb magnetic properties were concluded [V] but the suppression of conductivity property was found. Temperature/field dependences of MR characteristics for the A_2FeMoO_6 samples were also revealed to depend on the size of A-cation constituents. Sr_2FeMoO_6 and Ca_2FeMoO_6 which represent relatively mostly the equivalent V_{Fe} values exhibited that the behaviours of MR characteristics were well agreed each other, whereas different MR values/responses were seen in Ba_2FeMoO_6 possessing relatively low valence value of iron [V]. These A-site size dependences of electromagnetic properties are considered to be induced by varying the charge distribution/electronic structure of B site by the isovalent-cation substitution at A site. The isovalent substitution affects the electric structure, thereby the degree of valence mixing between B'/B'' changes, *i.e.*, the halfmetallicity of A_2FeMoO_6 is influenced by the substitution. Thus, the halfmetallicity derived phenomena, *e.g.*, B-site order (because the degree of order at B site is determined by the valence balance of B'/B'' and the balance is strongly depended on the halfmetallicity of compounds), MR properties, and the magnetic properties were considered to be varied, also.

So far, a number of B-site ordered double-perovskite compounds have been investigated. By considering these resultants, it has been found that there is not a drastic difference in the crystal structures in this system but the physical properties are known to be sensitive to their chemical compositions and to slight differences in the structural parameters. Furthermore, the high magnetic transition temperature of $A_2B'B''O_6$ compound is indispensable

for the application of spintronic materials. Thus, in order to find out "hidden" structural parameters which dominate and induce the high magnetic transition temperature in the *B*-site ordered double perovskites were tried to reveal by means of multivariate data analyses on the basis of mathematical statistics. The analyses showed that the valence of *B*', ionic radius and valence of *B*" were found to be crucial structural factors for the magnetic transition temperature of this system. These structural factors were also extracted as the important parameters of $A_2B'B''O_6$ compounds to be magnetic materials which is essential for obtaining high magnetic transition-temperature value. This is the first investigation revealing which and how the structural parameters affect the physical properties in the *B*-site ordered double-perovskite compounds with statistical point of view. It was also found that the structural parameters related to *A* constituent may affect the parameters originated form the *B*-cation species, mentioned above. Thus, it would be possible to regard that the *A*-related parameters can control the type of magnetism and the value of T_C indirectly for the $A_2B'B''O_6$ compounds. Namely, the present analyses showed a possibility of tuning the functional properties by means of the isovalent-cation substitution at *A* site.

Through out the present investigation, the consequences of isovalent-cation substitutions were clarified for both double- and triple-perovskites in the strongly-correlated electron systems. Although it is impossible to compare the effects of isovalent substitutions on both systems directly, it would be possible to suggest that the substitution easily affects the double-perovskite compounds than the triple perovskites because of the simpler crystal structure of double perovskites, while the triple-perovskite compounds possess more complicated structures, *i.e.*, they are composed of the stacking layers along *c* axis. The aliovalent-cation substitution induces the changes in the physical properties or in the crystal structures by varying the overall charge/carriers in the crystal thus the influences of the aliovalent substitution on materials have been believed to be straightforward and more effective than the isovalent substitution. The isovalent-cation substitution however, it was clearly demonstrated by the present work that the substitution exerts changes in material properties effectively through controlling the distribution of charge/carriers retaining the total amount of charge/carriers for both double- and triple-perovskite compounds.

6. SUGGESTIONS FOR FUTURE WORKS

In this work, the importance of hole-density distribution was suggested from the obtained experimental results and BVS method in the present fully oxygenated $CuBa_2RECu_2O_{7-\delta}$ ($6.91 \leq 7-\delta \leq 6.94$) samples. BVS is a calculation approach for discussing the hole distribution over the crystal, while XANES measurement is one of the experimental techniques to reveal the amount of local hole in the crystal. NMR (Nuclear Magnetic Resonance) measurement, the measurement of Hall coefficient and Seebeck coefficient measurement based on TEP (thermoelectric power) measurement *etc.* are commonly utilized to evaluate the hole concentrations. Therefore, Cu L_{23}- and O *K*-edge XANES measurements were performed in the present fully oxygenated $CuBa_2RECu_2O_{7-\delta}$ samples, *i.e.* *RE* = Gd, Y, $Y_{0.4}Yb_{0.6}$, $Y_{0.2}Yb_{0.8}$, Yb, $Yb_{0.8}Lu_{0.2}$ and $Yb_{0.6}Lu_{0.4}$, respectively.

There are two distinct Cu sites in this system. In the Cu L_{23}-edge X-ray absorption spectra, the photon energy 932.2 eV, refers to the sum of holes in the CuO_2 plane and in the $CuO_{1-\delta}$ chain. Although it is difficult to discuss from the Cu L_{23}-edge X-ray-fluorescence yield spectra, since all the fully-oxygenated samples possess the constant oxygen content, it is possible to assume that total hole amount, *i.e.* sum of holes in the CuO_2 plane and in the $CuO_{1-\delta}$ chain over the crystal, is the same among the samples. All the peak amplitude at ~932.2 eV seemed to have the same from the obtained Cu L_{23}-edge measurement spectra, except for samples with Y and $Y_{0.2}Yb_{0.8}$ as *RE* constituents. Thus, it would be possible to consider that the total hole amount which exist in the CuO_2 plane and in the $CuO_{1-\delta}$ chain is the same among the present $CuBa_2RECu_2O_{7-\delta}$ samples with fixed oxygen contents, *i.e.*, the values of the oxygen content are in the narrow range of 6.91 ~ 6.94 except for the sample with *RE* = Gd, in accordance with the conclusions of the coulometric titrations. On the other hand, O *K*-edge X-ray absorption spectra refers to the amount of holes of CuO_3 ribbon ($CuO_{1-\delta}$ chain and apical oxygen) photon energy at ~527.7eV (peak 1), refers to the amount of holes of CuO_2 plane at ~528.3 eV (peak 2) and Upper Hubbard Band at ~529.3 eV (peak 3), respectively. The evaluation based on amplitude of spectra peak only, there was a tendency that accordingly decreasing $r(RE^{III})$, peak 1 decreased except for samples with *RE* = Y, $Y_{0.2}Yb_{0.8}$ and $Yb_{0.6}Lu_{0.4}$. The decrease of spectra peak for CuO_3 ribbon indicates that the amount of holes which locate at the ribbon become less. In the case of samples with *RE* consisting of Y, $Y_{0.2}Yb_{0.8}$ and $Yb_{0.6}Lu_{0.4}$, the exception tendencies may be due to the decomposition of these samples. It is because after the XANES measurement, the sample had decomposed, already. Considering all the results of XANES measurement, the total hole concentration in the crystal might be invariable at a fixed and fully-oxygenated $CuBa_2RECu_2O_{7-\delta}$ ($6.91 \leq 7-\delta \leq 6.94$; except $CuBa_2GdCu_2O_{6.98}$) system. Conversely, the amount of holes which locate $CuO_{1-\delta}$ chain and apical oxygen seem to be decreased in proportion to decrease $r(RE^{III})$ implying that with decreasing $r(RE^{III})$, the holes which locate at $CuO_{1-\delta}$ chain and apical oxygen move/drift to CuO_2 plane, but the total hole concentration is unchangeable. Thus, the hole distribution would be more homogeneous in the crystal when the *RE* is small.

However, it ought to regard that not only the amplitude of spectra peak but also the width of peak should be considered, be fitted to Gaussian function (or the more suitable function) and should be calculated the area of spectra peak for the quantitative discussion in terms of amount of holes. Unfortunately the detailed Gaussian fitting has not successfully accomplished in this work for both the Cu L_{23}- and O K-edge measurements due to the ambiguous spectra. Thus, it is inadequate to have the quantitative discussion in this matter. In order to make clearer this concept, further study on the "quantitative" evaluation of hole distribution by means of O K-edge XANES measurements is an important challenge for further works. Another candidate to clarify this point would be a Seebeck measurement.

Moreover, an evaluation of "active" hole density, *i.e.*, hole density presiding over the superconductive properties, is one of the final aims in terms of research topic in high- T_c superconductive materials. From the material designing and tailoring points of view, the multi-layered copper-oxide structures the more homogeneous the hole distribution is along the piling direction of different blocks, the more enhanced is the H_{irr} characteristics, while the opposite is believed to apply in terms of increasing the value of T_c. It should be emphasized important roles of the hole distribution/inhomogeneity in controlling the superconductivity properties of high-T_c superconductors. An opposite effect can be expected on the better H_{irr} characteristics and on the high T_c values in terms of the hole distribution, thus it would be interesting to find the most "optimized" or "balanced" hole distribution for both properties at the same time.

This work suggested the first resultants of the multivariate data analyses of general B-site ordered $A_2B'B''O_6$ compounds by revealing the some rules and classifications of the type of magnetism based on the composition and an indication for the superb magnetic transition temperature. These problems were discussed from the structural parameters only in this work but it should be also considered how the changes in the structural parameters correlate with the electron hoppings, the exchange interactions or superexchange interactions *etc.* which are generally regarded as the dominating factors to determine the type of magnetism and/or T_C in the $A_2B'B''O_6$, also. Besides, more reliable conclusion is required to be established by increasing the number of observations. It would be possible to find out an intrinsic tendency in the type of magnetism of $A_2B'B''O_6$ in terms of cation species because the PLSDA analysis was carried out about 80 observations. However, most of paramagnetic phases consist of the combination of B' = *RE* and B'' = Nb. In the multivariate data analysis, observations composed of various kinds of cation pairs are more desirable because this analysis method is based on the mathematical statistics. Furthermore, the number of observations adopted in the PLS study is small, thus this induces the obtained resultants less persuasiveness, unfortunately. On the basis of these points, increasing the number of observations which include various A/B cations is extremely important to accomplish the aiming of this study.

Designing desirable functional strongly-correlated electron oxides, particularly B-site ordered double-perovskite compounds such as halfmetallic antiferromagnetic compounds or new phases with surprisingly high magnetic transition temperature and so on, is one of the interesting

investigation topics in the aspect of material tailoring. In order to make a "plan" for a brand-new material, multivariate data analysis would provide us with very apparent indicators. By utilizing the obtained results from the analysis as a blueprint for a desirable compound and, comparing the actual material property and predicted material property from the analysis would pioneer the new investigation field of material science.

APPENDIX

A.1. Abbreviations and Notation of Multivariate Data Analysis

Table A.1.-1 Abbreviations and notation utilized in the present multivariate data analysis.

Abbreviation	Explanation
LV	Latent Variable
A	number of components in a PCA or PLS model
a	index of components, *i.e.*, dimensions of model; (a = 1, 2, …., A)
N	number of objects (cases, observations)
k	index of X-variables (k = 1, 2, …., K)
m	index of Y-variables (m = 1, 2, …., M)
$\mathbf{X}$	matrix of predictor variables with (N * K) in size
$\mathbf{Y}$	matrix of response variables with (N * M) in size
$\mathbf{c}_a$	PLS-regression Y-weights of component a
$\mathbf{p}_a$	PLS-regression X-loading vector of component a
R^2	multiple correlation coefficient, *i.e.*, amount Y "explained" in terms of sum of squares
R^2_X	amount X "explained" in terms of sum of squares
Q^2	cross-validated R^2, *i.e.*, amount Y "predicted"
$\mathbf{t}_a$	X-scores of component a
$\mathbf{u}_a$	Y-scores of component a
$\mathbf{w}_a$	PLS-regression X-weights of component a
$\mathbf{w}_a$ *	PLS-regression weights transformed to be independent between component

A.2. Basic Concepts Employed for the PLS Modeling

The correlations employed by the PLS method are described as follows:

$$t_{ia} = \sum_{k} W_{ka} * X_{ik} \quad . \tag{A.2.-1}$$

The X-scores have the following properties: (*i*) they are multiples by the loadings p_{ak} and summarizing appropriately the characteristics of **X** with small X-residual values of e_{ik}:

$$X_{ik} = \sum_{a} t_{ia} p_{ak} + e_{ik} \quad . \tag{A.2.-2}$$

With multivariate **Y** ($M > 1$), the corresponding Y-scores, *i.e.*, $\mathbf{u}_a$, are multiples by the weights c_{am}, and they are good summaries of Y possessing small residuals values of g_{im}:

$$y_{im} = \sum_{a} u_{ia} c_{am} + g_{im} \quad . \tag{A.2.-3}$$

(*ii*) the X-scores predict **Y** reasonable, *i.e.*:

$$y_{im} = \sum_{a} c_{ma} t_{ia} + f_{im} \quad . \tag{A.2.-4}$$

The Y-residuals, f_{im} express the deviation between the observed and modeled responses.

A.3. Lists of Observations and Variables for the Multivariate Data Analysis

Table A.3.-1 List of observations for the PLSDA analysis. A_2FeMoO_6 are categorized as ferrimagnetic compounds.

Magnetic compound		
Number	**Ferrimagnet**	**Reference**
1	Ba_2FeMoO_6	J. Magn. Magn. Mater. **242-245**, 747-750 (2002).
2	Ba_2FeReO_6	Phys. Rev. *B* **62**, 9538-9542 (2000).
3	Ba_2FeReO_6	J. Phys.: Condens. Matter **12**, 965-973 (2000).
4	Ca_2FeMoO_6	Chem. Mater. **12**, 161-168 (2000).
5	Ca_2FeMoO_6	Chem. Mater. **15**, 425-432 (2003).
6	$Ca_2Fe_{0.94}MoO_6$	J. Phys.: Condens. Matter **12**, 8295-8308 (2000).
7	Ca_2FeReO_6	Phys. Rev. *B* **62**, 9538-9542 (2000).
8	Ca_2FeReO_6	J. Phys.: Condens. Matter **12**, 965-973 (2000).
9	$CaLaFeVO_6$	J. Solid State Chem. **162**, 250-253 (2001).
10	Pb_2MnReO_6	Chem. Mater. **15**, 668-674 (2003).
11	$SrCaFeMoO_6$	Chem. Mater. **15**, 425-432 (2003).
12	$Sr_{0.5}Ca_{1.5}FeMoO_6$	Chem. Mater. **15**, 425-432 (2003).
13	$Sr_{1.5}Ca_{0.5}FeMoO_6$	Chem. Mater. **15**, 425-432 (2003).
14	$Sr_2CoMoO_{5.86}$	Chem. Mater. **14**, 812-818 (2002).
15	Sr_2CrMoO_6	J. Solid State Chem. **155**, 233-237 (2000).
16	Sr_2FeMoO_6	Phys. Rev. B **62**, 14197-14206 (2000).
17	Sr_2FeMoO_6	Phys. Rev. B **62**, 14197-14206 (2000).
18	Sr_2FeMoO_6	Phys. Rev. B **62**, 14197-14206 (2000).
19	Sr_2FeMoO_6	Phys. Rev. B **61**, 422–427 (2000).
20	Sr_2FeMoO_6	Chem. Mater. **15**, 425-432 (2003).
21	$Sr_2Fe_{0.97}Mo_{0.94}O_{5.81}$	J. Phys.: Condens. Matter **12**, 8295-8308 (2000).
22	$SrLaFeVO_6$	J. Solid State Chem. **162**, 250-253 (2001).

Table A.3.-1 (Continued)

Magnetic compound		
Number	**Antiferromagnet**	**Reference**
23	Ba_2CoMoO_6	Eur. J. Inorg. Chem. **9**, 2463-2469 (2002).
24	Ba_2CoWO_6	Eur. J. Inorg. Chem. **9**, 2463-2469 (2002).
25	Ba_2CuWO_6	J. Solid State Chem. **147**, 291-295 (1999).
26	Ba_2DyReO_6	J. Mater. Chem. **12**, 2361-2366 (2002).
27	Ba_2FeWO_6	Mater. Res. Bull. **37**, 1797-1813 (2002).
28	Ba_2GdReO_6	J. Mater. Chem. **12**, 2361-2366 (2002).
29	Ba_2HoReO_6	J. Mater. Chem. **12**, 2361-2366 (2002).
30	Ba_2LaRuO_6	J. Solid State Chem. **46**, 234-244 (1983).
31	Ba_2LuReO_6	J. Mater. Chem. **12**, 2361-2366 (2002).
32	Ba_2LuRuO_6	J. Solid State Chem. **78**, 108-116 (1989).
33	Ba_2MnWO_6	Mater. Res. Bull. **36**, 2215-2228 (2001).
34	Ba_2NdReO_6	J. Mater. Chem. **12**, 2361-2366 (2002).
35	Ba_2SmReO_6	J. Mater. Chem. **12**, 2361-2366 (2002).
36	Ba_2TbReO_6	J. Mater. Chem. **12**, 2361-2366 (2002).
37	Ba_2YReO_6	J. Mater. Chem. **12**, 2361-2366 (2002).
38	Ba_2YRuO_6	J. Solid State Chem. **52**, 138-145 (1984).
39	Ba_2YRuO_6	J. Solid State Chem. **78**, 108-116 (1989).
40	$BaLaMgRuO_6$	J. Solid State Chem. **150**, 383-390 (2000).
41	$BaLaZnRuO_6$	J. Solid State Chem. **150**, 383-390 (2000).
42	Ca_2FeSbO_6	Bull. Korean Chem. Soc. **18**, 91-97 (1997).
43	Ca_2LaRuO_6	J. Solid State Chem. **46**, 234-244 (1983).
44	Ca_2MnWO_6	Mater. Res. Bull. **36**, 2485-2496 (2001).
45	Ca_2MnWO_6	J.Phys.:Condes. Matter **14**, 8817-8830 (2002).
46	Ca_2YRuO_6	J. Solid State Chem. **54**, 245-250 (1984).
47	Sr_2CoMoO_6	Chem. Mater. **14**, 812-818 (2002).
48	$Sr_2CoSbO_{5.63}$	J. Solid State Chem. **157**, 76-85 (2001).
49	Sr_2CuWO_6	J. Solid State Chem. **147**, 291-295 (1999).
50	Sr_2FeSbO_6	J. Mater. Chem. 7, 459-463 (1997).
51	Sr_2FeSbO_6	J. Mater. Chem. **5**, 75-78 (1995).
52	Sr_2FeSbO_6	Bull. Korean Chem. Soc. **18**, 91-97 (1997).
53	Sr_2FeWO_6	Mater. Res. Bull. **37**, 1797-1813 (2002).
54	Sr_2LuRuO_6	J. Solid State Chem. **78**, 108-116 (1989).
55	Sr_2MnMoO_6	J.Phys.:Condes. Matter **14**, 8817-8830 (2002).
56	Sr_2MnWO_6	J.Phys.:Condes. Matter **14**, 8817-8830 (2002).
57	Sr_2MnWO_6	J. Magn. Magn. Mater., **237**, 124-134 (2001).
58	Sr_2NiWO_6	Mater. Res. Bull. **35**, 499-457 (2000).

Table A.3.-1 (Continued)

	Paramagnetic compound	
Number	**Paramagnet**	**Reference**
59	Ba_2DyNbO_6	J. Solid State Chem. **148**, 353-360 (1999).
60	Ba_2ErNbO_6	J. Solid State Chem. **148**, 353-360 (1999).
61	Ba_2ErReO_6	J. Mater. Chem. **12**, 2361-2366 (2002).
62	Ba_2EuNbO_6	J. Solid State Chem. **148**, 353-360 (1999).
63	Ba_2EuReO_6	J. Mater. Chem. **12**, 2361-2366 (2002).
64	Ba_2GdNbO_6	J. Solid State Chem. **148**, 353-360 (1999).
65	Ba_2HoNbO_6	J. Solid State Chem. **148**, 353-360 (1999).
66	Ba_2LaNbO_6	J. Solid State Chem. **148**, 353-360 (1999).
67	Ba_2LuNbO_6	J. Solid State Chem. **148**, 353-360 (1999).
68	Ba_2NdNbO_6	J. Solid State Chem. **148**, 353-360 (1999).
69	Ba_2PrNbO_6	J. Solid State Chem. **148**, 353-360 (1999).
70	Ba_2SmNbO_6	J. Solid State Chem. **148**, 353-360 (1999).
71	Ba_2TbNbO_6	J. Solid State Chem. **148**, 353-360 (1999).
72	Ba_2TmNbO_6	J. Solid State Chem. **148**, 353-360 (1999).
73	Ba_2TmReO_6	J. Mater. Chem. **12**, 2361-2366 (2002).
74	Ba_2YNbO_6	J. Solid State Chem. **148**, 353-360 (1999).
75	Ba_2YbNbO_6	J. Solid State Chem. **148**, 353-360 (1999).
76	Ba_2YbReO_6	J. Mater. Chem. **12**, 2361-2366 (2002).

Curriculum Vitae

Name:	Yukiko YASUKAWA
Sex:	Female
Birth:	July 19, 1975 in Tokyo, Japan
Nationality:	Japanese

Education :

1995.4 - 1999.3 : Department of Applied Chemistry, Faculty of Engineering, Kogakuin University.

1999.3 : Batchelor of Engineering (Kogakuin University).

1999.4 - 2001.3 : Department of Innovative and Engineered Materials, Interdisciplinary Graduate School of Science and Engineering, Tokyo Institute of Technology (Master Course).

2001.3 : Master of Engineering (Tokyo Institute of Technology).

2001.4-present : Department of Innovative and Engineered Materials, Interdisciplinary Graduate School of Science and Engineering, Tokyo Institute of Technology (Doctoral Course).

List of Publications :

1 T. Nakane, **Y. Yasukawa**, E.S. Otabe, T. Matsushita, M. Karppinen, and H.Yamauchi, "Effects of substitution on the magnetic-field irreversibility in superconductive $Cu(Ba_{1-y}Sr_y)_2YbCu_2O_{6+z}$", *Physica C* **338**, 25-28 (2000).

2 **Y. Yasukawa**, T. Nakane, H. Yamauchi, and M. Karppinen, "Consequence of isovalent rare earth substitution to magnetic irreversibility in cation-stoichiometric $CuBa_2RECu_2O_{6.93\pm0.01}$", *Appl. Phys. Lett.* **78**, 2917-2919 (2001).

3 **Y. Yasukawa**, T. Nakane, M. Karppinen, and H. Yamauchi, "Rare-earth-ion-size control on magnetic irreversibility field in $CuBa_2RECu_2O_{7-\delta}$", *Physica C* **357-360**, 230-233 (2001).

4 **Y. Yasukawa**, H. Yamauchi, and M. Karppinen, "Accurate oxygen-content determination method for decreased sample amounts of superconductive and other functional oxides", *Appl. Phys. Lett.* **81**, 502-504 (2002).

5 M. Karppinen, N. Kiryakov, **Y. Yasukawa**, T. Nakane, and H. Yamauchi, "Isovalent cation substitutions to control the intrinsic H_{irr} characteristics of superconductive copper oxides", *Physica C* **382**, 66-71 (2002).

6 J. Lindén, M. Karppinen, T. Shimada, **Y. Yasukawa**, and H. Yamauchi, "Observation of antiphase boundaries in Sr_2FeMoO_6", *Phys. Rev. B* **68**, 174415-1-5 (2003).

7 M. Karppinen, H. Yamauchi, **Y. Yasukawa**, J. Lindén, T.S. Chan, R.S. Liu, and J.M. Chen, "The valence state of iron in the $Sr_2Fe(Mo,Ta,W)O_{6.0}$ double-perovskite system: an Fe *K*-edge and $L_{2,3}$-edge XANES study", *Chem. Mater.* **15**, 4118-4121 (2003).

8 **Y. Yasukawa**, M. Karppinen, J. Lindén, T.S. Chan, R.S. Liu, and H. Yamauchi, "Iron valence in double-perovskite $(Ba,Sr,Ca)_2FeMoO_6$: isovalent substitution effect", *J. Solid State Chem.* **177**, 2655-2662 (2004).

List of Presentations :

1 T. Nakane, **Y. Morooka (Yasukawa)**, M. Karppinen, H.Yamauchi, E.S. Otabe, and T. Matsushita, The Japan Society of Applied Physics and Related Societies (The 60th Autumn Meeting), Sept. 1-4, 1999, Konan Univ.

2 T. Nakane, **Y. Yasukawa**, E.S. Otabe, T. Matsushita, M. Karppinen, and H.Yamauchi, 5th International Workshop on Chemical Designing and Proceedings of High-T_c Superconductor (Chem-HTSC V), Oct. 15-16, 1999, Tokyo Inst. Tech.

3 **Y. Yasukawa**, T. Nakane, M. Karppinen, and H. Yamauchi, The Japan Society of Applied Physics and Related Societies (The 47th Spring Meeting), Mar. 28-31, 2000, Aoyama Gakuin Univ.

4 T. Nakane, **Y. Yasukawa**, T. Matsushita, M. Karppinen, and H. Yamauchi, The Japan Society of Applied Physics and Related Societies The 47th Spring Meeting), Mar. 28-31, 2000, Aoyama Gakuin Univ.

5 **Y. Yasukawa**, T. Nakane, M. Karppinen, and H. Yamauchi, 13th International Symposium on Superconductivity, Oct. 14-16, 2000, Tokyo, Japan.

6 Y. Morita, T. Motohashi, T. Nakane, **Y. Yasukawa**, J. Sugihara, M. Karppinen, and H.Yamauchi, The Japan Society of Applied Physics and Related Societies (The 48th Spring Meeting), Mar. 28-31, 2001, Meiji Univ.

7 **Y. Yasukawa**, T. Nakane, Y. Morita, T. Motohashi, M. Karppinen, and H. Yamauchi, The Japan Society of Applied Physics and Related Societies (The 48th Spring Meeting), Mar. 28-31, 2001, Meiji Univ.

8 T. Nakane, **Y. Yasukawa**, T. Motohashi, M. Karppinen, and H. Yamauchi, The Japan Society of Applied Physics and Related Societies (The 48th Spring Meeting), Mar. 28-31, 2001, Meiji Univ.

9 **Y. Yasukawa**, J. Lindén, R.S. Liu, J.M. Chen, H. Yamauchi, and M. Karppinen, The Physical Society of Japan (The 58th Autumn Meeting), Sept. 6-9, 2002, Chubu Univ.

10 **Y. Yasukawa**, H. Yamauchi, and M. Karppinen, 8th International Workshop on Chemical Designing and Proceedings of High-T_c Superconductor (Chem-HTSC VIII), Nov. 8-9, 2002, Tokyo Inst. Tech.

Patent :

出願番号:特願 2000–314282 号 (公開番号: 特開 2002-128522 号)
発明の名称:臨界電密度特性および/または不可逆磁場特性に優れた高温超伝導酸化物および高温超伝導銅酸化物を含む高温超伝導材料
出願人:東京工業大学
発明者:山内尚雄、マーリット カルピネン、末松久幸、中根茂行、森田祐介、安川雪子、杉原淳

Study Visit :

A four-day study visit (May 27-30, 2001) at National Synchroton Radiation Research Center in Hsinchu, Taiwan, to learn "quantitative analysis of XANES spectroscopy data".